



Contract Number 260165

E-HUB

*Energy-Hub for residential and commercial districts and transport*

SEVENTH FRAMEWORK PROGRAMME

Grant Agreement No: NMP2-SL-2010-260165

Call identifier: FP7-2010-NMP-ENV-ENERGY-ICT-EeB

## **D3.2 Report on a combination of thermal storage techniques and components**

Due date of deliverable: 15 Nov 2013

Actual submission date: 18 March 2014

Start date of project: 01/12/2010

Duration: 48 months

Organisation name of lead contractor for this deliverable: ECN

Author(s):

*Dirk Vanhoudt, Bert Claessens, Fjo De Ridder, Glenn Reynders, VITO*

*Ruud Cuypers, Henk Oversloot, Christian Finck, Christiaan van Soest, Ardjan de Jong,  
Ellemieke Henquet, Hans van 't Spijker, Frans Koene, TNO*

*Robert de Boer, Simon Smeding, Herbert Zondag, ECN*

Dissemination Level:

Public

Revision: final

## History of document

date	status of document	by partner
January 8, 2014	draft distributed to partners for feedback	ECN
January 24, 2014	final draft sent to reviewer	ECN
February 5, 2014	document reviewed	Solintel
March 17, 2014	final version submitted to coordinator	ECN
March 17, 2014	final version submitted to the Commission	TNO

Effort by partners for this deliverable:

Partner	Personmonths
TNO	24
ECN	30
DAPP	
ACC	
VITO	23
Fraunhofer	
VTT	
TPG-DIMSET	
Solintel	
EDF	
ISPE	
Most	
Ertzb	
Cestec	
ICAX	
HSW	
PM total	77
PM planned (DOW)	85

# Content

<b>Executive Summary .....</b>	<b>5</b>
<b>1. Introduction .....</b>	<b>9</b>
<b>2. Heat storage system requirements and research approach.....</b>	<b>11</b>
2.1. Introduction .....	11
2.2. Distributed heat storage .....	11
2.3. Thermochemical heat storage .....	12
<b>3. Assessment of the performance of distributed heat storage in smart district heating networks.....</b>	<b>15</b>
3.1. Introduction .....	15
3.2. Assessment of the performance of distributed heat storage in smart district heating networks.....	15
Goal of the research .....	15
The studied district heating network during one week .....	16
Numerical models .....	17
The lab setup of the distributed buffers .....	22
The control algorithms .....	24
Results and discussion .....	26
Conclusions .....	31
3.3. Characterization of thermal storage buffers .....	32
Introduction .....	32
Generic grey-box heat buffer model .....	32
Estimation of buffer parameters .....	33
Minimization of the number of sensors in the buffer .....	36
Conclusion .....	43
<b>4. Thermochemical heat storage using open sorption.....</b>	<b>44</b>
4.1. Introduction .....	44
4.2. System design and construction .....	45
Open sorption heat storage Prototype 1.....	45
Open sorption heat storage Prototype 2.....	47
4.3. Numerical models .....	52
Sorbent reactor model .....	52
Heat exchanger model.....	54
4.4. Experiments and results.....	55
TCS performance measurements .....	55
4.5. Model validation .....	61
4.6. Discussion and conclusions .....	65
<b>5. ThermoChemical heat storage using closed sorption .....</b>	<b>67</b>
5.1. Introduction .....	67
Approach and overview .....	67
5.2. System design and construction .....	69
Specifications .....	69
Design considerations adsorber/desorber .....	70
Design considerations evaporator/condenser .....	71
Other aspects.....	72

5.3. Numerical models .....	73
Introduction .....	73
Modelling a TCS system .....	73
Iterative solution .....	74
Modelling results .....	75
5.4. Experiments and results .....	77
Characterisation experiments .....	77
Typical experiment .....	78
Effect of different desorption/condensation temperatures on heat storage capacity .....	83
Effect of different adsorption/evaporation temperatures on heat storage capacity .....	85
Heat losses to the environment .....	86
Pressure equilibration after opening of the valve (300 seconds experiment) .....	86
Comparison with design specifications .....	88
5.5. Model validation .....	88
Suggestions for future work .....	91
5.6. Design of 15 kWh reactor .....	91
Demands and principles .....	91
Solution possibilities .....	91
Further optimisation .....	94
Suggestions for future work .....	94
<b>6. Discussion and Conclusions .....</b>	<b>96</b>
<b>7. References .....</b>	<b>98</b>
<b>8. Annexes .....</b>	<b>100</b>
<b>Annex A: Literature review: distributed thermal storage for application in district heating networks .....</b>	<b>100</b>
<b>Annex B: Determination of the values of the building model parameters .....</b>	<b>117</b>
<b>Annex C: Description of the active control framework .....</b>	<b>119</b>
<b>Annex D: The buffer grey-box model .....</b>	<b>122</b>
<b>Annex E: Identification of the buffer parameters .....</b>	<b>125</b>
<b>Annex F: Kalman filter procedure .....</b>	<b>130</b>
<b>Annex G: Supporting information for design, modeling, construction and testing of the closed sorption TCS system .....</b>	<b>131</b>



## Executive Summary

The E-Hub project, funded under the FP7 programme “Energy efficient Buildings (EeB)” aims at developing smart energy systems for districts that are able to utilise the full potential of renewable energies available at district level.

Work Package 3 of the project is focused on the thermal energy part of the E-hub. The overall objective of the WP3 is to develop technologies and components that are crucial to realize an E-hub and that are not yet available at this moment, based on new working mechanisms, new design tools and renewable energy sources. Task 3.1 is devoted to the harvesting and the use of renewable heat via integrated renewable concepts such as thermo-active foundations and thermal road collector systems. Task 3.2 focuses on the development of components and techniques for thermal energy storage.

Heat storage is an important part of an E-hub system. The effectiveness of solar collectors systems is increased when long term thermal storage is added to the system. CHP systems (micro and macro) can also benefit from thermal storage, as they can be used more flexibly in the energy system. Long term heat storage might be realised for example in underground thermal energy storage or by innovative thermo chemical heat storage. Short term thermal energy storage can be realised in water storage tanks, using tanks with stratification or PCMs, or pit storage. The individual hot water storage vessels in dwellings can be used to create a ‘virtual collective heat storage’ system.

This report describes the activities performed and the results obtained within task 3.2. The aim of the task is to develop components and techniques which can bridge the gap between decentralized renewable energy production and consumption, i.e. storage techniques at the relevant scale. Based on the scenario studies in work package 2 and overall system modeling in work package 4, the general requirements and specifications for a flexible thermal storage system on district level are defined and serve as input for the further application developments of innovative heat storage technology.

The technologies selected for development are distributed heat storage, also known as virtual collective heat storage (VCS) and thermochemical heat storage (TCS). The distributed heat storage uses existing small scale hot water storages, distributed in individual dwellings within a district. The use of many of these small storages can be controlled by the E-hub to create a distributed heat storage system, that has the potential benefit of storing heat close the place where is used. Thermochemical heat storage uses the heat of reaction of a material combination to store and release heat. TCS technology allows to store heat for very long times with limited loss of energy, and it also stores heat more compact than water storages, creating more opportunities for building installation. TCS can be implemented as distributed or as central heat storage.

**Distributed heat storage:** The performance of distributed heat storage in a smart district heating network is assessed by simulation experiments. An experimental setup (Figure 1) was designed and built with 4 heat storage vessels, including the emulation of heat production and consumption. Different heat storage configurations for district heating grids fed by CHP are compared for energetic and economic performance, using the hardware-in-the-loop simulation model. The flexibility in the energy system resulting from the storage vessels is used to actively control the CHP, which in this way can produce electricity at times of high electricity prices.

Four scenarios were selected to evaluate the performance of different heat storage configurations. The results of the simulation program indicate that the developed control framework performs well. As reference case the CHP is simply controlled by following the heat demand, and surplus electricity is sold at actual price. Active control of the CHP, using the thermal mass of the building as a heat store, increases the profit of the CHP significantly compared to the reference case. The configuration with distributed heat storage buffer tanks performs best, slightly better than the active configuration without buffers. The results for the centralized large heat storage case are a little worse, but still a lot better than in the reference case without thermal storage and without active control. It was also found that the thermal mass of the buildings, representing also a large heat storage capacity when actively

used for thermal storage, provides even more flexibility to store heat compared to the central buffer case and as a result gives higher profits in running the CHP.

The models and control algorithms developed in this study to assess the performance of distributed heat storages can be integrated in the overall energy management system developed in WP4.

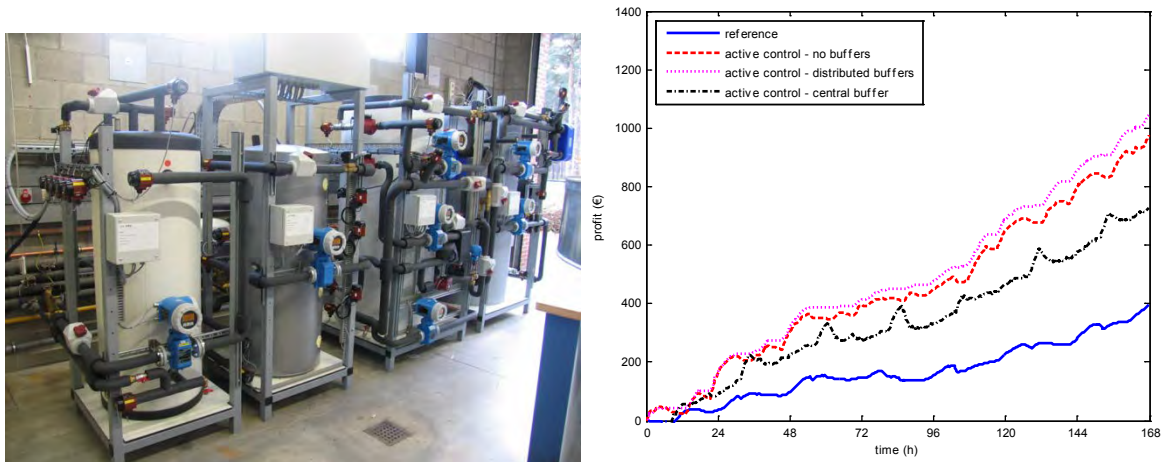


Figure 1-1: (left) experimental setup to study the performance of distributed heat storage (right) Result of the simulation program for active control of CHP system with thermal storage, showing an increased operational profit

To exploit the full potential of distributed heat storage, information on the actual State of Charge of a heat storage system is crucial to allow effective control in an E-hub system. A method is developed to reliably determine the State of Charge (SoC) of a water based storage vessel with a minimum number of temperature sensors. A model is developed together with an identification procedure based on measurements on the four different hot water vessels. The method to estimate the temperature profile in the storage tanks with a minimal number of sensors shows good results. (see figure 2) The position of the sensors is a very important parameter to get good results with only few sensors.

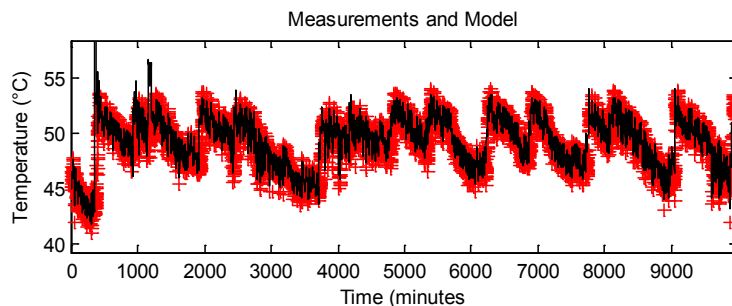


Figure 1-2 Comparison between the measured outlet temperature (red) and the predicted temperature (black) of thermal storage tank.

An extension of this method to a situation without a single temperature sensor in the buffer also gives good results with respect to the predication of the outlet temperature of the buffer. The estimation of the temperature profile in the buffers give good results during a very large period of the tests, however when the temperature changes rapidly, the last method is not able to reconstruct the temperature profile accurately.

**Thermochemical heat storage:** The performance of long term heat storage technology based on thermochemical reactions was studied experimentally. The materials to be used for thermochemical heat storage were selected, their properties characterized, and different reactor design were first tested on a small scale, in advance of the design and construction of the 15kWh storage prototype. Two different system concepts are developed and tested; the open sorption heat storage concept and the closed sorption system concept, (see Figure 1-3)

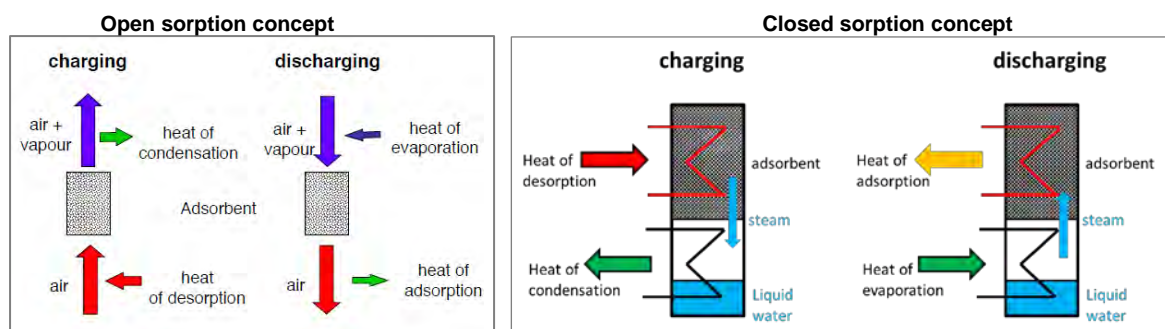


Figure 1-3: Basic system lay-out and operational scheme for the open and closed sorption heat storage concepts.

The open sorption system concept uses air as medium to transfer heat and to transfer the water vapour to and from the adsorbent. In the closed system concept the adsorbent and the water vapour are contained in a closed vessel with heat exchangers inside to transfer heat to and from the adsorbent and to condensate and evaporate the water. The water vapour is transported as a result of pressure differences between the adsorbent and the water reservoir.

Simulation models were developed for both system concepts to support the design of the prototypes and to simulate the performances. Based on results of small scale tests and system simulations the design and construction of the prototypes was undertaken, see also Figure 1-4

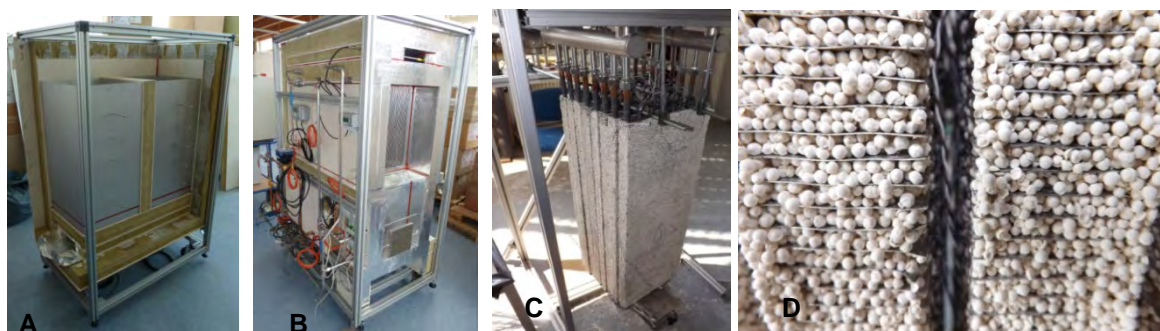


Figure 1-4: Pictures of the construction of prototypes of the thermochemical heat storage systems. **A** the storage containers for the adsorbent and **B** the air handling system of the open sorption system concept, **C** and **D** the closed sorption system under construction, with the adsorbent closely integrated with a heat exchanger.

The closed sorption system concept uses the sorption reaction of zeolite 5A with water vapour to store and release heat. In the closed sorption concept the water vapour is actively condensed and evaporated, requiring a sub-atmospheric system pressure and therefore a hermetically sealed containment. A heat exchanger is embedded in the zeolite mass to provide and subtract the heat of reaction (adsorption) for charging and discharging. Storage capacity, temperature levels, thermal powers and heat storage efficiency are experimentally determined. Model calculations are validated against the performance measurement.

The open sorption system concept aims to use salt hydrates as thermochemical materials, because of their high storage density. In the initial reactor tests the chemical stability of the salt hydrate appeared insufficient and zeolite 13X was used as stable replacement. In the open sorption system the water vapour as a reactant is carried by an air flow through the bed of zeolite. The system operates at atmospheric pressure and the air flow is used as heat transfer medium. Hot air is used to charge the system by desorption of the attached water from the zeolite, and the water vapour is carried away in the air flow. For heat release cool and humid air flows through the zeolite, the water vapour adsorbs in the zeolite and this produces hot air again. Storage capacity, temperature levels, thermal powers and heat storage efficiency are experimentally determined.



*Figure 1-5: Laboratory prototype systems of the open sorption (left) and the closed sorption (right) thermochemical storage concepts*

The open sorption system was able to release heat at temperature levels above 60°C, which is sufficient for domestic hot water and room heating purposes. The thermal power for charging and discharging were in the range of 500W. The long term storage capacity of the system was around 70MJ ( $\sim 0,35 \text{ GJ/m}^3$ ) and the storage efficiency 15%. Further improvements of the open sorption concept should focus on reduction of heat losses during charging and discharging process, and to minimize auxiliary electric usage. The closed sorption concept had a storage capacity of 10 MJ ( $\sim 0,12 \text{ GJ/m}^3$ ), and a heat storage efficiency of 35%. Thermal powers around 1 kW were reached with typical charge and discharge times of 4 hours.

In conclusion, the working principles of both concepts for thermochemical heat storage were successfully demonstrated. The performance characteristics are experimentally determined and are used for validation of the TCS system models. The models developed to simulate the performance of both the open and the closed TCS systems show a fair correspondence to the experimental results. The TCS simulation models form a useful tool for the analysis of improvement options and for the future design of open and closed sorption heat storage systems for different applications.



# 1. Introduction

## The Energy hub concept

An Energy Hub is a physical cross point, similar to an energy station, in which energy and information streams are coordinated, and where different forms of energy (heat, electricity, chemical, biological) are converted between each other or stored for later use.

The Energy Hub is a mechanism for exchanging energy via the grids between its members (households, renewable energy plants, offices, businesses), who may be both consumers and suppliers. The members exchange information on their energy production and energy needs with the Energy Hub. The E-Hub then distributes the available energy in the most efficient way.

To match supply and demand, the Energy Hub converts and stores energy and performs load shifting by controlling the E-hub components for managing energy flows within the district. The members are connected to the Energy Hub by means of bi-directional energy grids (low and high temperature heat grids, electrical grids (AC and DC) and gas grids (hydrogen, biogas, syngas).

Renewable energy may be generated by individual members (e.g. from solar thermal panels or PV on residences) or by central means (a ground source energy or a large combined heat and power plant) located within the district that may be fuelled by solar energy, biofuel or hydrogen.

## Thermal energy storage as part of an Energy Hub

Thermal energy storage is a critical asset for enabling a control system to match supply and demand of heat. Renewable heat can be stored underground via thermo-active foundations or in boreholes. Surplus heat can be collected in summer, stored and then used in winter using seasonal heat storage. Heat can also be stored in distributed heat storages or in thermochemical materials (TCMs) for later use in periods of high demand.

In a district with collective renewable energy production, for example a biomass fuelled CHP and a district heating network, the integration of short and long term thermal energy storage is important, and might be realised in different ways. Long term storage might be realised by for example underground thermal energy storage or thermochemical storage. Short term thermal energy storage can be realised in water storage tanks, using tanks with stratification or PCMs, or pit storage. The individual hot tap water storage vessels in the dwellings can be used to create a distributed heat storage system.

Also in times with large supply of renewable electricity from wind and solar, the conversion from power to heat by means of heat pumps and the storage of heat can be an effective way to store renewable energy.

Heat storage components and systems within an E-hub need to be developed to create a flexible combination of long and short term storage system at the district level. Based on the scenario studies in work package 2 and overall system modelling in WP4 the requirements and specifications for a flexible thermal storage system on district level will be defined.

The total storage system will be simulated as part of WP4. The goal of WP3 task 2 is to develop, build and test the essential heat storage components on lab-scale and to validate the heat storage models for the different technologies.

This report describes the development, construction and tests on three different lab-scale systems of innovative thermal storage techniques. The first technology deals with the development and test of distributed thermal energy storage. It studies the potential benefits of using multiple interconnected small scale water storages within an E-hub district.

The second technology focusses on Thermochemical heat storage (TCS). The properties and performances of TCS are studied in relation to the E-hub heat storage system requirements. Two varieties of TCS are included, 'open sorption' and 'closed sorption'.

Chapter 2 describes the basic heat storage system requirements as part of an E-hub and the selection of the heat storage R&D paths.

Chapter 3 describes the development and tests on collective virtual energy storage by partner VITO.

Chapter 4 describes the development and test of TCS using an open sorption concept (ECN) and Chapter 5 for TCS using a closed sorption system concept (TNO).

The technology chapters have their own introduction and discussion and conclusion sections focused on its specific technology development. Chapter 6 has the general discussion and conclusions regarding the applicability and merits of the different heat storage technologies as part of an E-hub district.

## 2. Heat storage system requirements and research approach

### 2.1. Introduction

In a district with collective renewable energy production and a district heating network, the integration of short and long term thermal energy storage is important to match supply and demand for heat. For the E-hub district energy concept a variety of solutions for thermal energy storage can be applied, and no single solution is applicable throughout all districts. Districts can have very different energy supply and demand patterns, arising from different climatic regions, different building construction characteristics, variations in types of districts and the occupation level etcetera. This leads to a variety of requirements when it comes to the energy supply, energy demand and the need for energy storage systems.

For thermal energy storage this means that at the current stage of development of the E-hub concept there is not a single set of thermal storage system requirements, that defines the storage capacity, thermal power of heat supply and demand, the temperature levels for charging and discharging, the duration of the storage and how many charge and discharge cycles are needed.

The research approach chosen for thermal energy storage in this work package is to study innovative concepts and technologies that can offer the heat storage function within an E-hub. Through development, testing and modelling of the new heat storage technologies the general performance characteristics are characterized. These characteristics will then be used in the E-hub system simulation environment or tool to study their applicability and its potential benefit and added value for the district energy system, and the increase of the share of renewable energy.

The selected innovative heat storage concept is to use individual hot water storage vessels present in a district as a Virtual Collective Storage system. The selected storage technology is thermochemical heat storage. Both are described in more detail in the following sections.

### 2.2. Distributed heat storage

To create flexibility and therefore the ability to match the demand of heat to the supply, there is a need for thermal storage in district heating grids, as already stressed in the previous chapter. Several forms of thermal storage exist, however the far most commonly applied type of heat storage exists of sensible energy storage in water storage tanks.

In district heating grids, central water tanks are often installed next to the heat production units like CHP's. These large storage tanks are applied a long time already. However, in most district heating grids these tanks are used as hydraulic separation between the production unit and heating grid or to reduce shifting behaviour of the production unit.

In more recent generations of district heating systems, this central storage tanks are used for peak shaving purposes: Verda and Colella [1] show that the integration of a 3000 m<sup>3</sup> central water storage tank is able to reduce the peak load in the morning from 600 MW to about 500 MW making it not necessary to use the back-up boilers. As a result the fraction of the total annual heat demand of the district that is delivered by the central CHP increases from 85% without TES to 94% using an optimally sized TES. The investment cost of the TES is estimated at 2400 €/m<sup>3</sup>. Labidi et al [2] demonstrate annual energy cost savings of 48.3 k€ by optimizing the energy production of a multi-energy heater by adding a central water storage tank. These savings mainly result from the increase of the heat production from wood, reducing the gas consumption. The 200 m<sup>3</sup> water storage tank showed a pay-back time of 2 years and an economic gain of 1.1M€ over 25 years. Pagliarini and Rainieri [3] quantified the impact of a stratified water storage tank on the energy use of the CHP unit of a University campus. They conclude that a water storage tank of 1500m<sup>3</sup> is able to significantly improve the transient behaviour of the CHP unit, resulting in a pay-back period of 4.4 to 3.5 years for an investment cost of 311 to 460 k€.

Only in the latest generations of district heating grids, the storage tanks are actively used to decouple the moment of heat production from the moment of consumption, and therefore control the moment

when the production unit is switched on. Nevertheless, when the district heating grid is supplied by a CHP (which is the case for about ¾ of the grids), this can have a large benefit. The electricity produced simultaneously with the heat production can be sold on the spot markets. Since the increased variance in the price of electricity, for the profitability of the CHP plant it is important to produce electrical power when the price is high. In this way, the CHP indirectly contributes to the balance of the electricity grid. In [4] the simulation results are shown for the optimal control of a CHP with a thermal storage. For different situations the cost savings are calculated. Compared to the case whereby the CHP is following the heat demand, the cost saving due to active control amounts to 17% for example.

In all these applications, the water storage tanks are large central tanks. Nevertheless, in most district heating grids, even without these storage tanks a lot of thermal mass is available: the buildings connected represent a lot of thermal mass, and sometimes (mainly for comfort reasons) distributed water buffers are installed in the buildings to supply domestic hot water. Still, this thermal mass is not actively used yet.

In the work described in chapter 3, it is investigated how these forms of storage can replace the common central storage concepts. Both distributed water buffers and the thermal mass of buildings are assessed in this work. To demonstrate the practical applicability of the concept, a test setup was also built and tested for the distributed buffers.

In the second part of chapter 3, a method is developed to minimise the number of temperature sensors in distributed water storage tanks. Indeed, when using these tanks actively, the state of charge of the storage tanks must be known precisely and without measures, a lot of sensors are needed for this. By reducing the number of sensors by means of the methods described in that chapter, the investment cost of the installation can be limited.

### 2.3. Thermochemical heat storage

In Europe, the bulk of the solar radiation is received in the summer months while radiation is relatively low during the winter months. The ability to effectively store solar thermal energy for a period of months provides an opportunity to substantially increase the use of solar energy. Although seasonal storage is already successful (UTES, Underground Thermal Energy Storage), to date these demonstration projects appear to have limited application in retrofitting the existing building stock. Other, more compact solutions are needed to address the challenges of increasing solar energy use in the built environment.

The basic principle for compact thermal storage based on sorption technology is simple: a suitable chemical compound is heated to the point where the compound dissociates into two (or more) other compounds. When these compounds are recombined, they re-form the original compound and discharge heat in the process. (see Figure 2-1) The individual compounds can be stored at ambient temperatures for indefinite periods, without any of the thermal energy being lost: thermochemical energy storage. In real applications, evidently there are losses from tanks, pipes and heat exchangers.

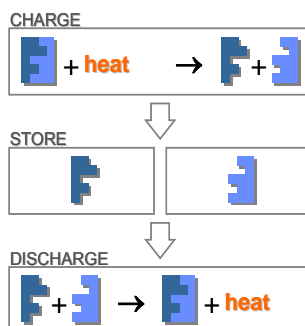


Figure 2-1 Operational concept of Thermochemical heat storage.



The principle of thermochemical heat storage (TCS) indeed seems simple. However, many technical challenges are still present and commercialization is still a point in the future. The solution would have to be appropriately scaled to integrate easily into the existing heating systems of our buildings and to meet a number of other market requirements. Below, an overview is given on the current status on thermochemical storage using closed sorption, and on the improvements needed for successful application.

Sorption processes can be divided in **adsorption** or **absorption**. In adsorption, the physical process of water or another compound adhering to a surface takes place. In absorption, the active compound is changed by the sorption of one compound, and forms a different compound. The former takes place in e.g. silicagel or zeolites showing modest energy densities, while the latter can be seen in e.g. salt hydrates showing much higher energy densities.

A practical thermochemical storage material has to meet the requirements of the desired application, i.e. be reliable, safe, non-toxic, long lasting, inexpensive, and able to be recycled. It is clear from literature that for both silicagel/zeolite and for salt hydrates the main contribution to the heat of sorption is the condensation enthalpy of the working fluid. For applications of long-term or seasonal storage, in general water is used as a reactant, being cheap, safe, easy to use, and with good and useful properties.

When considering the gaseous working fluid (or reactant) such as water vapour, it is convenient to distinguish between open and closed systems. In open systems, the working fluid is then released to the ambient. In closed systems, the working fluid is separately stored.

In addition to chemical parameters there are thermo-physical parameters that determine reaction performance. For example, in the discharge phase, temperature and power of delivered heat is strongly dependent on the rate of water supplied. In atmospheric systems, the water vapour content of the supplied air is relatively low due to lower ambient temperatures. Additional heat sources are required to enhance the vaporization like borehole heat-exchangers, solar thermal assistance, or others. The advantage of open systems is that in principle they can reach higher energy densities than closed systems. However, when considering the use of auxiliary energy and the limited availability of water vapour in winter conditions, a closed sorption system may offer benefits over an open system. In this case, heat exchangers and reactor will become more important as these elements determine the power of charging/discharging and the efficiency of the storage.

While the open thermochemical systems have the advantage of being more suited for practical use without heavy vacuum equipment, the disadvantage of having to provide a forced airflow through the system requiring 'parasitic' electrical energy exists. A closed vacuum system has the advantages of higher power densities and fast charging and discharging of the store, while its obvious disadvantage is that a vacuum has to be maintained.

At ECN materials characterizations and the first lab-scale prototype systems were developed to study and test the open sorption TCS concept. The water vapour adsorption and desorption behaviour of the materials were studied, to proof the concept and to define the operational constraints and materials stability issues. Another important aspect was the analysis of the output temperatures that can be reached in the discharge mode. This has to reach 60°C in order to fulfil the requirements for legionella prevention in hot water storages. A 1<sup>st</sup> stage prototype open sorption heat storage system was built and tests were performed on it in the framework of the E-hub project. The lessons learned from this were applied to design, built and test a 2<sup>nd</sup> prototype. The work performed on the open sorption concept is described in chapter 4.

At TNO, a zeolite-based bench-scale test set-up for thermochemical storage was constructed some years ago. With this set-up, heat and mass transfer characteristics could be obtained and influenced and a general feel for the particular process at hand was obtained. It proved the working principle for thermochemical storage, and gave insight into heat and mass transfer (both found to be limited). Power in/output measurements were conducted, and based on this it was concluded that system improvements were needed.

In order to reach higher temperature lifts of the delivered heat, another reactor had to be designed, based on different adsorber/desorber heat exchangers and with a different evaporator process. Furthermore, more elaborate sensing needed to be installed for detailed experimentation. The work on this improved reactor set-up was carried out in the E-hub project, and is described in Chapter 5.

### 3. Assessment of the performance of distributed heat storage in smart district heating networks

#### 3.1. Introduction

In today's European district heating grids, about three quarter of the total heat supply is supplied by combined heat and power plants (CHP) [5]. The electricity produced simultaneously with the heat production can be sold on the spot markets. Since the increased variance in the price of electricity, for the profitability of the CHP plant it is important to produce electrical power when the price is high. In this way, the CHP indirectly contributes to the balance of the electricity grid: when a lot of intermittent renewable power is available the remaining power demand and correspondingly the price will be low, stimulating the CHPs to switch off. In the same way, scarcity of renewable energy will invoke the CHPs to switch on.

Of course, the demand of thermal power will never be fully synchronised to the demand of electricity. Therefore, thermal energy storage is required when controlling the CHP electricity driven. In appendix A.1. Characterization of thermal storage techniques' an overview is given of different storage techniques which can be applied in district heating grids. In section 3.2, a quantitative comparison is made for a number of storage configurations in a district heating grid. Total energy consumption, and the costs and revenues are determined for the selected storage technologies.

When switching on the CHP when the electricity price is high instead of when heat is needed, the control framework must be modified. To optimise the performance of such a controller, it is important to know the state of charge of the buffers in the grid. As a consequence, to quantify the state of charge precisely, the number of temperature sensors in the buffers should be very large. However, it will be too expensive to install a large amount of temperature sensors in these tanks. Therefore, in section 0 techniques were developed to accurately determine the temperature profile in a buffer tank, with a minimum of sensors.

#### 3.2. Assessment of the performance of distributed heat storage in smart district heating networks

##### Goal of the research

In district heating grids heated by CHPs, the thermal storage consists of one large water storage tank placed next to the CHP. This is the most obvious solution, but other options can be thought of as well. In this chapter, we want to assess the performance of decentralised storage vessels placed in every building. After all, already nowadays a lot of single household buildings in district heating grids already have a storage tank installed to cover the peak load of production of domestic hot water. Nevertheless, the flexibility of these distributed storage tanks is not used yet.

The performance of the distributed buffers is compared to the performance of the central buffer and a configuration without buffers. Therefore, a hardware-in-the-loop simulation model was developed for a fictive district heating grid in a neighbourhood with 100 connected buildings. The district heating grid is heated by a CHP and gas boiler. We quantify the profit of switching district heating CHPs at appropriate moments (high spot market price) and compare the performance of the different storage possibilities. To achieve this, a representative winter week was simulated for a reference case and the different storage cases. The following tests are performed:

1. As a reference case, first the CHP is heat-driven controlled, i.e. no thermal storage is present and the CHP always produces the actual heat demand of the heat district grid. In this case, electricity is a surplus product sold at any price.
2. The first storage configuration is a configuration whereby next to the CHP a central storage tank is installed. The CHP is electricity driven, so the operation of the CHP is optimized to the price of electricity. The central buffer is used to store or deliver heat when the demand of heat differs from the supply of heat by the CHP. The big advantage of this configuration is that there is no intervention in the local control system in the connected buildings. This means that, when a

building needs heat at a certain time, the valve of the district heating opens until no heat is needed anymore. As a result, no communication is needed between the CHP control software and the individual buildings.

3. In the second storage configuration, instead of central storage the thermal storage is distributed under the individual buildings. When it is interesting to enable the CHP, the control system will open the valves of the buildings with the highest actual heat demand, i.e. the building with the emptiest buffer. Since in this configuration communication is needed between the individual buildings and central control system anyway, also the thermal mass of the building can be activated. This is established by increasing the indoor temperature of the building within certain limits. In this configuration, the total volume of all buffers is the same as the central buffer in the first storage configuration but the thermal mass of the building could possibly increase the storage capacity compared to the first configuration.
4. The last storage configuration is included to quantify the potential of the activation of building mass only. This configuration is similar to the second one, only the distributed buffers are omitted. If the performance is reasonable, it is not profitable to invest in these buffers.

### **The studied district heating network during one week**

As already mentioned, a simulation model was developed to compare the different storage options. For the configurations without buffers or with the central buffer, this is a pure simulation. For the configuration with distributed buffers, a hardware-in-the-loop simulation was built. Indeed, a lab test setup representing the buffers from 4 houses was built in the lab. The other 96 buffers were simulated in the network model. The objective of using these real buffers is twofold:

- Firstly, they are used to validate the buffer models.
- Secondly, the lab setup makes it possible to assess the problems resulting from the difference between theoretical simulation and practical implementation. The lab setup should therefore be seen as a first step in the actual implementation of the active control algorithm in real life district heating grids.

A schematic representation of the district heating network studied in this work is shown in Figure 3-1. The CHP provides heat to 100 buildings, located in 4 streets. The network consists of twin pipes with a total length of 2.1 km and pipe diameters ranging from DN25 to DN100. With these diameters, the pressure losses in the pipes are limited to 200 Pa/m.

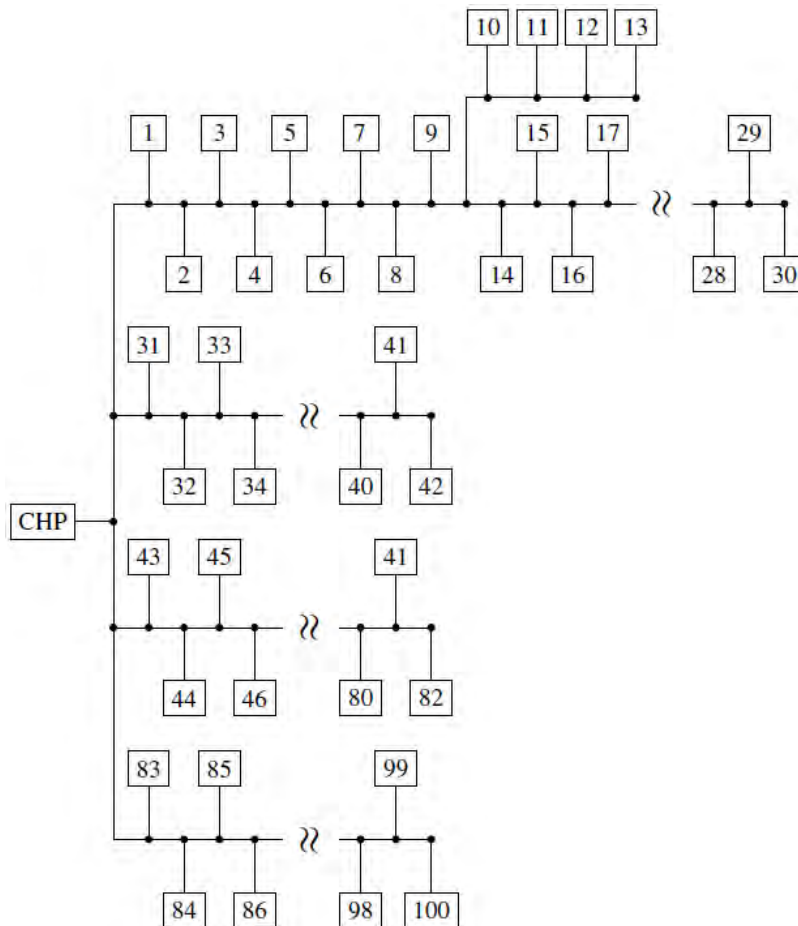


Figure 3-1: Schematic representation of the district heating grid

For every simulation, the same representative winter week was used. This week was chosen as the week in which the mean outside temperature was the closest to the mean temperature during the whole heating season in Belgium. A typical meteorological year (TMY) profile is used as weather data profile. The mean outside temperature during the heating season in Belgium (1 October to 30 April) is  $6.1^{\circ}\text{C}$ . The week used in the simulation is the week with the smallest difference to this mean temperature. This is week 46 (12 to 18 November) with a mean ambient temperature of  $6.2^{\circ}\text{C}$ .

## Numerical models

### The district heating pipe model

#### Flow calculation

To calculate the flow rates and pressures in the network, a method developed by Valdimarsson [6] is used. On the analogy of electrical circuits the Kirchoff laws are applied, whereby voltage is replaced by pressure and flow rate by current. However, a complication is that in hydraulic circuits the relation between flow rate and pressure is not linear, like the relation between voltage and current in electrical circuits (Ohm's law), but quadratic.

#### Temperature calculation

To calculate the temperature evolution in a pipe, the node model developed by Benonysson [7] was implemented. This quasi-dynamic model relies on the fact that pressure and flow in district heating grids change orders of magnitudes faster than the temperature of the water in the pipes. This makes it possible to calculate flows and pressures in the grid in a static way which means that, at the beginning of every time step, the pressures and flows are calculated and that during the time step these values are assumed to remain constant. The temperature change during the time step is then estimated by solving the formula:

$$\frac{\partial}{\partial t}(m c_{pw} T_w) + \frac{\partial}{\partial x}(\dot{m} c_{pw} T_w) + hA(T_w - T_g) = 0 \quad \text{Equation 3-1}$$

with  $m$  the mass of the water,  $c_{pw}$  the thermal capacity of the fluid,  $T_w$  the temperature of the fluid,  $\dot{m}$  the mass flow rate in the pipe,  $h$  the heat transfer coefficient between the pipe and the ground,  $A$  the outside area of the pipe and  $T_g$  the temperature of the ground.

In the node model, the equation is not solved explicitly, another approach is followed. In this model, at every time step the number of time steps  $n$  it takes for water to travel through the pipe is defined. The outlet temperature of the pipe is then matched to be inlet temperature of  $n$  time steps before. Afterwards a correction is performed on this calculated outlet temperature, to take into account the heat capacity of the pipe wall and heat losses to the environment. In practice, this method goes through the following steps, as summarized in [8].

## The building model

Every building in the network is represented by a lumped capacitance model. In these models the thermal problem is translated to an electric analogon, whereby a temperature is transformed to a voltage and thermal power to an electrical current. The building properties are described as a combination of resistances ( $R$ ) and capacitances ( $C$ ). By solving the Kirchoff equations, the evolution of the temperatures in the buildings are calculated. The buildings in the studied network all have the same circuit, shown in Figure 3-2, but the values of the parameters differ for every house.

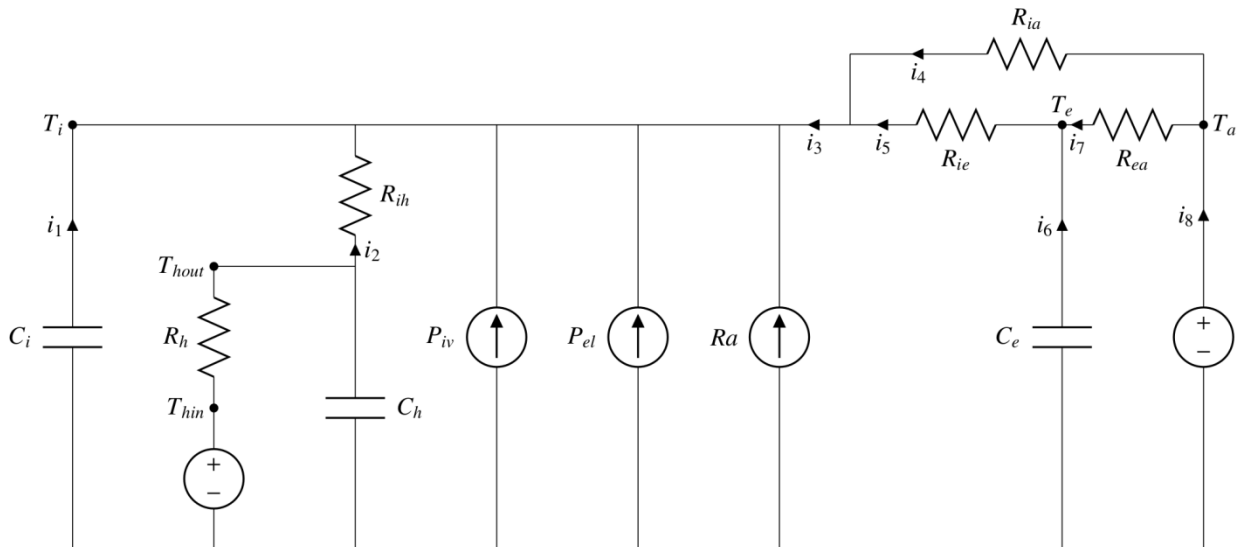


Figure 3-2: RC-circuit of the building model

A lot of variants are available in literature. This model was chosen because it takes into account both solar irradiation, and infiltration/ ventilation. Besides that this variant model does not model the power provided by the heating circuit as an imposed input value, like most of the models do. Instead the heating circuit inlet temperature ( $T_{hin}$ ) and the flow rate (included in  $R_h$ ) is used as input. The outlet temperature, and thereby the heating power, is a result from the interaction with the building and is calculated by the model. In this way, this variant was judged to represent the reality best.

In Table 3-1 an overview is given of the meaning of the different parameters, inputs and outputs of the model as well as the units used in the simulations. In annex A.1. Characterization of thermal storage techniques, the determination of the parameter values is discussed.

Table 3-1: *parameters, inputs and outputs of the RC-circuit of the building*

symbol	description	unit
parameters		
$R_h$	thermal resistance radiator	$^{\circ}C/kW$
$R_{ih}$	thermal resistance radiator to inside	$^{\circ}C/kW$
$R_{ie}$	thermal resistance inside to envelope	$^{\circ}C/kW$
$R_{ea}$	thermal resistance envelope to ambient	$^{\circ}C/kW$
$R_{ia}$	thermal resistance inside to ambient	$^{\circ}C/kW$
$C_i$	thermal capacitance inside	$kWh/^{\circ}C$
$C_h$	thermal capacitance radiator	$kWh/^{\circ}C$
$C_e$	thermal capacitance envelope	$kWh/^{\circ}C$
$H$	boolean indicating if heating is on	-
inputs		
$T_{hin}$	heating system inlet temperature	$^{\circ}C$
$T_a$	ambient temperature	$^{\circ}C$
$P_{iv}$	power of air infiltration	$kW$
$P_{el}$	electrical power building	$kW$
$Ra$	power of solar irradiation	$kW$
outputs		
$T_i$	building inside temperature	$^{\circ}C$
$T_e$	building envelope temperature	$^{\circ}C$
$T_{hout}$	heating system return temperature	$^{\circ}C$

## The central buffer model

All buffers in the simulations are modelled by means of a multinode model. This is a one-dimensional model whereby the buffer vessel is represented as number of stacked volume segments. Each segment is fully-mixed, meaning that the whole segment has the same temperature. A mathematical description of the model is described in [9, 10]. In the simulation described in this paper, the buffer has 50 layers. In the configuration with a central storage buffer, there are no storage vessels installed in the houses. In this case, the coupling between the building and the district heating network is achieved by means of a commonly used indirect substation set as shown in Figure 3-3.

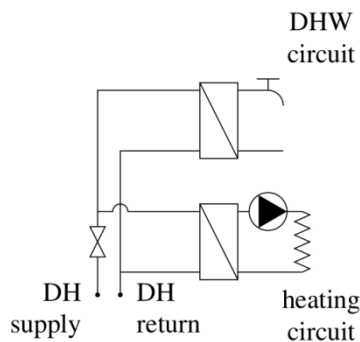


Figure 3-3: *Substations in configurations without local buffers*

## The distributed buffers model

In the configuration with the distributed buffers, three types of buffers are considered. The first type is an open buffer type, as shown in Figure 3-4 (a). This is the simplest type of buffer, with no separation between the primary and secondary flow of the buffer. In this buffer, heat is stored for building heating

as well as domestic hot water production. Two heat exchangers are provided to separate the district heating water from the building's heating circuit and the domestic hot water. The buffers in the simulation have a volume of 500 l.

The second type is a buffer with an immersed coil heat exchanger, as presented in Figure 3-4 (b). This type of buffer is commonly used in solar thermal installations, where the coil heat exchanger realizes a physical barrier between the heat transfer fluid and the domestic hot water. A buffer volume of 200 l is used in the simulations.

The last type of buffer as a tank-in-tank buffer Figure 3-4(c), whereby the water from inner tank is heated by the fluid in the other tank. The tank wall between the inner and outer tank acts as a heat exchanger in this case. In the model, the inner tank has a volume 164 l while the outer tank's volume is 39 l. In these cases, heat for space heating is not stored, so the demand of heat needs to be fulfilled directly by the district heating grid.

Like in the configuration with a central buffer vessel, also a multinode model is implemented. In this configuration, each local buffer has 15 layers.

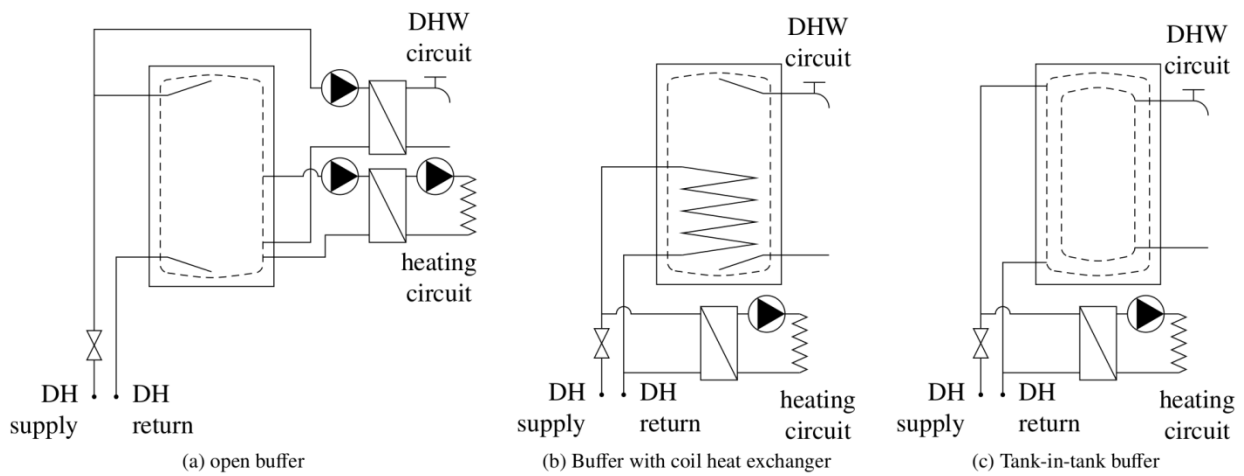


Figure 3-4: Buffer types used in the simulation

## The CHP and boiler model

The heat to the network is provided by a gas fired CHP, with a gas boiler as backup. These components are represented by means of quasi-static black-box models. The equations for the CHP are:

$$\begin{cases} P_{el} = P_{el \max} f_m, & f_{m \min} \leq f_m \leq 1 \\ P_{heat} = A_{heat}(T_{in}) f_m + B_{heat}(T_{in}) \\ P_{gas} = \alpha_{gas} f_m^2 + \beta_{gas} f_m + \gamma_{gas} \\ A_{heat}(T_{in}) = \alpha_{heat} T_{in}^3 + \beta_{heat} T_{in}^2 + \gamma_{heat} T_{in} + \delta_{heat} \\ B_{heat}(T_{in}) = \varepsilon_{heat} T_{in}^2 + \zeta_{heat} T_{in} + \eta_{heat} \end{cases} \quad \text{Equation 3-2}$$

where  $P_{el}$  and  $P_{heat}$  are the electrical and thermal power produced by the CHP,  $P_{gas}$  is the input power consumption.  $P_{el \max}$  is the maximum electrical power of the CHP (parameter),  $f_m$  the modulation factor of the CHP which is limited between  $f_{m \min}$ , the lower modulation limit and 1.  $\alpha_{gas}$  to  $\gamma_{gas}$  and  $\alpha_{heat}$  to  $\eta_{heat}$  are parameters, fitted to partial load curves supplied by a CHP-supplier. Apart from the calculation of these equations, a minimum on and off time ( $\Delta t_{on \min}$  and  $\Delta t_{off \min}$ ) is added to the



model. This means that, once the CHP is active, the CHP must stay on during a certain time. In the same way, once the CHP shuts down it stays off during a certain period. The parameters used in the simulation are shown in Table 3-2.

Table 3-2: values of the CHP parameters

parameter	value	unit
$P_{el\ max}$	600	$kW$
$f_{m\ min}$	0.4	—
$\Delta t_{off\ min}$	15	$min$
$\Delta t_{on\ min}$	15	$min$
$\alpha_{gas}$	31.250	$kW$
$\beta_{gas}$	1310.75	$kW$
$\gamma_{gas}$	181.35	$kW$
$\alpha_{heat}$	$3.1537 \cdot 10^{-5}$	$kW/(^{\circ}C)^3$
$\beta_{heat}$	$-7.4162 \cdot 10^{-3}$	$kW/(^{\circ}C)^2$
$\gamma_{heat}$	-0.3258	$kW/^{\circ}C$
$\delta_{heat}$	704.09	$kW$
$\varepsilon_{heat}$	$6.0633 \cdot 10^{-4}$	$kW/(^{\circ}C)^2$
$\zeta_{heat}$	-0.1848	$kW/^{\circ}C$
$\eta_{heat}$	160.01	$kW$

Similarly, also for the gas boiler a quasi-static model was developed:

$$\left\{ \begin{array}{l} P_{gas} = P_{gas\ nom} f_m, \quad f_{m\ min} \leq f_m \\ P_{out} = eff \cdot P_{gas} \\ eff = A(P_{gas}) * T_{in}^3 + B(P_{gas}) * T_{in}^2 + C(P_{gas}) * T_{in} + D(P_{gas}) \\ A(P_{gas}) = \alpha P_{gas}^2 + \beta P_{gas} + \gamma \\ B(P_{gas}) = \delta P_{gas}^2 + \varepsilon P_{gas} + \zeta \\ C(P_{gas}) = \eta P_{gas}^2 + \theta P_{gas} + \iota \\ D(P_{gas}) = \kappa P_{gas}^2 + \mu P_{gas} + \nu \end{array} \right. \quad \text{Equation 3-3}$$

where  $P_{heat}$  is the heat output,  $P_{gas\ nom}$  the nominal gas input,  $P_{gas}$  the gas input  $\alpha$  to  $\nu$  are parameters again, fitted to supplier data.  $f_{m\ min}$  is the lower modulation limit. In Table 3-3 an overview is given of the parameters used.

Table 3-3: values of the gas boiler parameters

parameter	value	unit
$P_{gas\ nom}$	1100	$kW$
$f_{m\ min}$	0.1	—
$\alpha$	$-7.758\ 10^{-13}$	$(^{\circ}C^3\ kW^2)^{-1}$
$\beta$	$-1.119\ 10^{-10}$	$(^{\circ}C^3\ kW)^{-1}$
$\gamma$	$3.295\ 10^{-6}$	$(^{\circ}C^3)^{-1}$
$\delta$	$1.195\ 10^{-10}$	$(^{\circ}C^2\ kW^2)^{-1}$
$\varepsilon$	$2.911\ 10^{-8}$	$(^{\circ}C^2\ kW)^{-1}$
$\zeta$	$-4.665\ 10^{-4}$	$(^{\circ}C^2)^{-1}$
$\eta$	$-6.067\ 10^{-9}$	$(^{\circ}C\ kW^2)^{-1}$
$\theta$	$-1.558\ 10^{-6}$	$(^{\circ}C\ kW)^{-1}$
$\iota$	$1.800\ 10^{-2}$	$(^{\circ}C)^{-1}$
$\kappa$	$1.121\ 10^{-7}$	$(kW^2)^{-1}$
$\mu$	$-1.503\ 10^{-5}$	$(kW)^{-1}$
$\nu$	$7.675\ 10^{-1}$	—

## The lab setup of the distributed buffers

As mentioned above, of the 100 distributed buffers used in the simulation, 4 are physically present in the lab. The 4 real buffers are the buffers of buildings 10 to 13 in Figure 3-1.

In Figure 3-5 a schematic representation is shown of the lab test setup. The two buffers on the left only provide domestic hot water. The two on the right also supply hot water for space heating.

The first domestic hot water buffer is a ACV SmartLine cylinder, which is a tank-in-tank system. In this concept, an inner tank (water storage) is heated by an outer tank, in which the outer tank is coupled to the lab heating grid. This system is able to heat a large amount of water in a small amount of time, due to the large heat exchanging surface of the inner tank. The cylinder has a total storage capacity of 203 l (an inner tank of 164 l and an outer tank of 39 l) and is thermally insulated by a 50mm thick layer of high density polyurethane, which should limit the static heat loss to 0.35°C/hour (at 85°C).

The second domestic hot water buffer is a 'Viessmann Vitocell 300-V (EVI)'. This buffer consists of a stainless steel storage tank with a capacity of 200 l. The cylinder is thermally insulated with highly effective polyurethane foam. Heat is provided to the cylinder by an internal coil heat exchanger, which enables indirect heating of the water. The coil is located at the lower half of the cylinder.

The other buffers also supply heat for space heating. These systems do not include an internal heat exchanger for indirect heating, instead, they are charged by the influx of hot water. Two installations are included in the lab setup: a 'Vaillant AllStor 500' and a 'TiSun PS500'. On the side of heat production the buffers are directly connected to the central lab heating grid. However, on the side of delivery they are indirectly connected to the DHW and space heating systems by two heat exchangers. The hot water supply of the central heating grid branches out to the first heat exchanger, which is coupled to the DHW delivery system (it also allows for the top layers of the buffer to connect with the heat exchanger). This enables instantaneous DHW heating. The output flow of the heat exchanger is led to the bottom of the buffer vessel. The second heat exchanger connects the buffer to the heating delivery system. It uses hot water drained from the middle of the vessel, and it returns the output flow to the bottom of the vessel. The Vaillant buffer has a storage capacity of 500 litres and has a 70mm thick layer of thermal insulation surrounding its stainless steel vessel. The TiSun buffer also has 500 litres of storage capacity, and is thermally insulated by 100mm of polyester fibre fleece insulation.

The heat inputs of the 4 buffers are connected a hot water pipe (1), representing the supply pipe of the district heating grid. The water from the buffers is returned to another pipe (2), representing the return pipe of the grid. Pipe (4) is a cold water pipe, at a temperature around 15°C. The mixing valves

MV1 and MV2 control the power exchange by heat exchanger HX3 and HX4 by mixing this cold water with return water from the heat exchangers. The returning water of pipe 4 is injected in pipe 3. Pipe 5 contains city water and is heated to the required domestic hot water temperature. In this way, pipes 1 and 2 can be seen as the district heating grid and pipe 5 is the city water connection of the building. Pipes 3 and 4 do not represent physical infrastructure of the buildings or the district heating network but is lab infrastructure to emulate the building's heating demand.

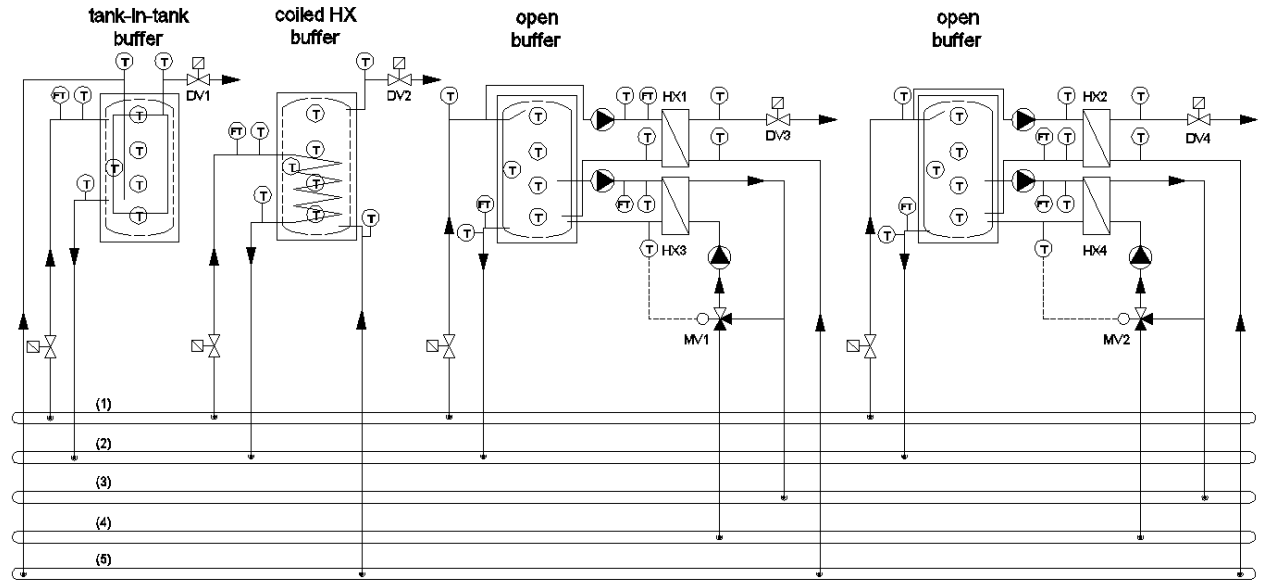


Figure 3-5: Schematic representation of the test setup of the four buffers in the lab of VITO

In the simulation model at every time step the inlet temperature to the buildings 10 to 13 in Figure 3-1 is calculated. This temperature is transferred to the lab controller which controls this temperature to the demanded set temperature. The measured return temperatures from the buildings are then transferred to the simulation model to calculate the return temperature to the CHP. The lab controller also adjusts the heating power in heat exchangers HX3 and HX4 to the calculated value in the model, and opens the domestic hot water demand valves DV1 to DV4 at the right moments.

In total, the test setup contains 44 temperature sensors (indicated with 'T' at the figure) and 8 flow meters ('FT'). The temperature sensors are PT100-type sensors with four-wire connection and an accuracy class of 1/10 DIN, resulting in a tolerance of  $\pm 0.04\%$  on the measurement value. The flow meters are electro-magnetic sensors with a tolerance of  $\pm 0.2\%$  on the measurement. A photo of the test setup is shown below, Figure 3-6.



Figure 3-6: Photo of the test setup of the four buffers in the lab of VITO

## The control algorithms

### Reference case

#### *The local building control system*

In the reference case no storage is applied. All buildings use a common thermostat control system to maintain the indoor temperature settings. This means that, when the building indoor temperature drops below a set point, the valve from the district heating grid is opened and heat is supplied to the building until the indoor temperature rises above another set point. The heating circuit supply set point temperature is determined by means of a heating curve. This set point is maintained by adjusting the flow rate of the district heating water with the district heating valve. When there is a domestic hot water demand, the district heating valve is fully opened. When both a heating demand and domestic hot water demand exist, the district heating water flow rate is divided over the two circuits.

#### *The CHP and gas boiler control system*

The set temperature of the district heating grid supply temperature is determined by a heating curve, using the mean outside temperature during the past 24 hours as an input. The CHP is then modulated to this set temperature. If the set temperature cannot be reached by the CHP, the gas boiler is enabled as well. Also if the desired power of the CHP is below the lower modulation limit of the installation, the CHP shuts down and the gas boiler is used to supply the necessary heat.

### Active control cases

To start with, we would like to mention the main challenges that were tackled in order to get an efficient control framework.

- A. The CHP will interact with an external electricity market. Here the price changes with time. The CHP should be switched on when the prices are high. However, if the heat demand of the district is low at that moment, this will result in an increase in the temperature of the district heating water. This temperature increase will then invoke extra heat losses, and should therefore be avoided. Contrary, if the houses would open their district heating valve at high electricity prices, it would take a while before the CHP responds to this due to the fact that the low temperature return water takes a while to reach the CHP. The price opportunity might then have been passed.  
The controller will therefore have to be hybrid, in the sense that the electric power consumption/production has to be in line with the external energy prices. However the temperature in the district heating cannot become too high to prevent losses.
- B. Taking into account a full model of the district network and the houses seems unpractical and unrealistic, since a lot of measurements and information are required for this and the local control actions are often binary.
- C. Even if a full model would be present, an appropriate solver is highly complex due to the fact that the problem is intrinsically a mixed integer non-linear problem. A stable and practical solver for such problems is highly impractical and the maintenance of such a framework requires a lot of expert knowledge.

A detailed description of the control systems is added in 0, however in a general sense the framework consists of 3 steps:

1. A model predictive control (MPC) module schedules the optimal production profile for the next 15 minutes, based on the electricity price and the prediction of the heat demand of the buildings.
2. A market-based multi-agent system (MAS) distributes the produced heat to the different buildings (in the configuration without buffers or with distributed buffers) or to the central buffer (in the configuration of a central buffer).
3. Since there is a difference between the predication of heat demand and the actual heat demand, a PI-controller makes sure that the demanded power consumption is always reached.



## Results and discussion

### Operational behaviour of the district heating network components

As discussed in the introduction, the aim of the active control algorithm is to maximise the revenue of the network operator.

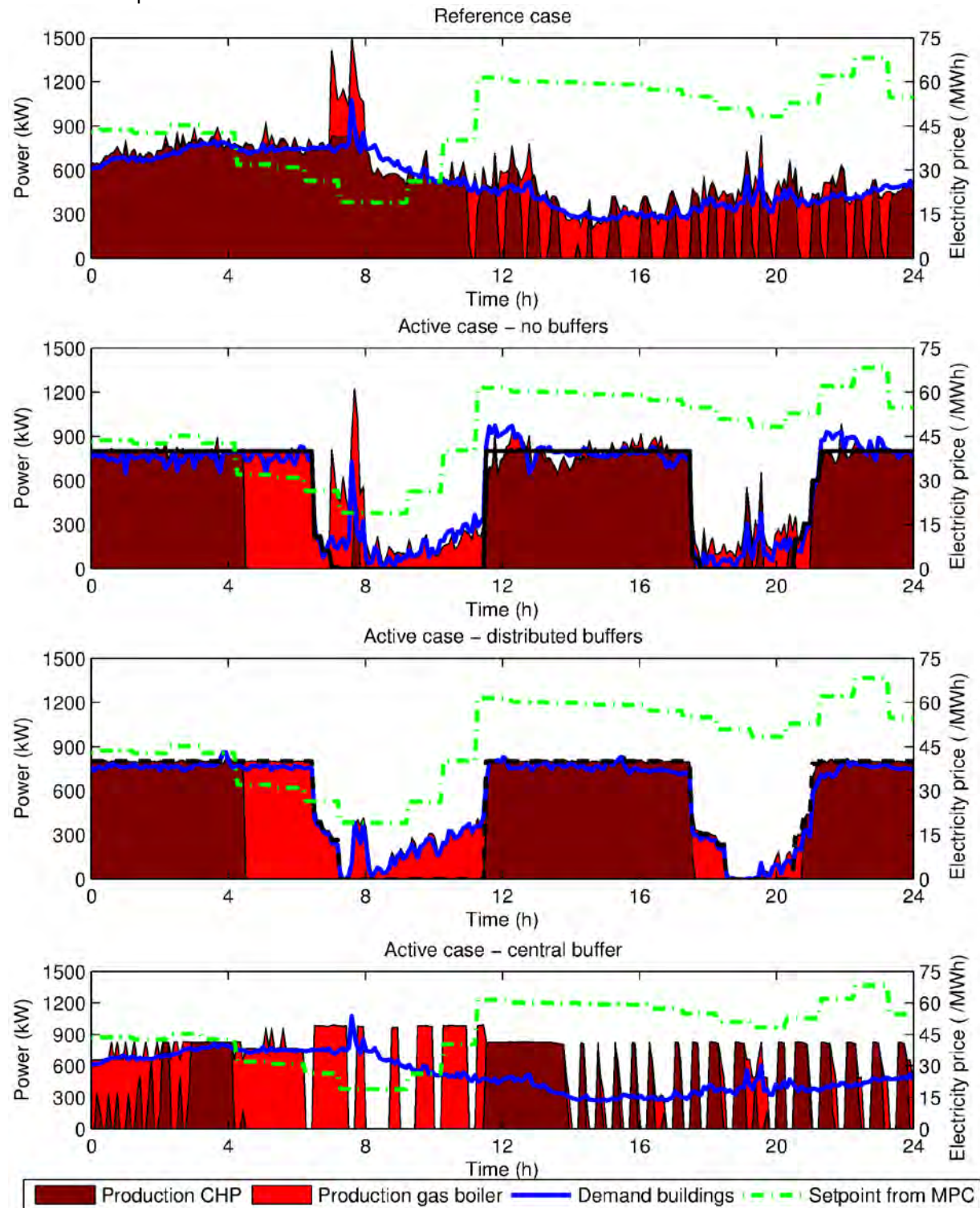


Figure 3-7: Behaviour of the different components of the DHN during one day

Figure 3-7 shows the behaviour in the DHN during one day (day 5). In the top figure the reference situation is shown. It is clear that the production and demand of heat (left axis) is independent of the price of electricity (right axis). There is a small deviation between heat production and heat demand

because of heat losses in the grid and because of the time delay in the grid. If the power demand is above the lower modulation limit of the CHP (about 400 kW), the CHP is switched on. If the power demand is below this limit, the CHP is switched off and the gas boiler takes over. This explains why e.g. between 11h and 23h the production is mostly fulfilled by the gas boiler. The graph also depicts (around 7h30) that, when the heat demand is higher than the maximum power of the CHP, the gas boiler supports the CHP.

The figures below show the same day for the active control cases. In these cases there is a much higher correlation between the heat production and high electricity prices (before 7h, between 11h30 and 18h30 and after 20h30). As explained higher, the controller framework consists of two different layers. Firstly, a MPC controller plans the optimal power production during the next time frame. The result of this planning is the black line in the figure. Secondly, the MAS and PI controller distributes the thermal power to the most appropriate buildings. As can be seen, this controller performs properly, since the power production (the filled red area) corresponds very well to the planning. There are some deviations e.g. for the active case without buffers between 7h30 and 11h30, where according to the planning the production should be 0. The reason for this is that when there is a domestic hot water demand, the district heating valve must be opened for comfort reasons, and therefore heat must be produced inevitably.

Once the optimal power production during the time step is known, the choice must be made of supplying the heat by the CHP or by the gas boiler. Since the CHP is selling its electricity to the spot market, the control algorithm will try to switch on the CHP when the electricity price is the highest. At other moments, when the electricity price is low, it could be more advantageous to switch on the gas boiler instead of the CHP. This can also be seen in the figure. In the active control case without buffers, before 5h, about 800 kW of heat must be produced. At that time the electricity price is high and therefore the demand is fulfilled by the CHP. However after 5h the electricity price decreases and the heat is produced by the gas boiler. This phenomenon can be observed a number of times.

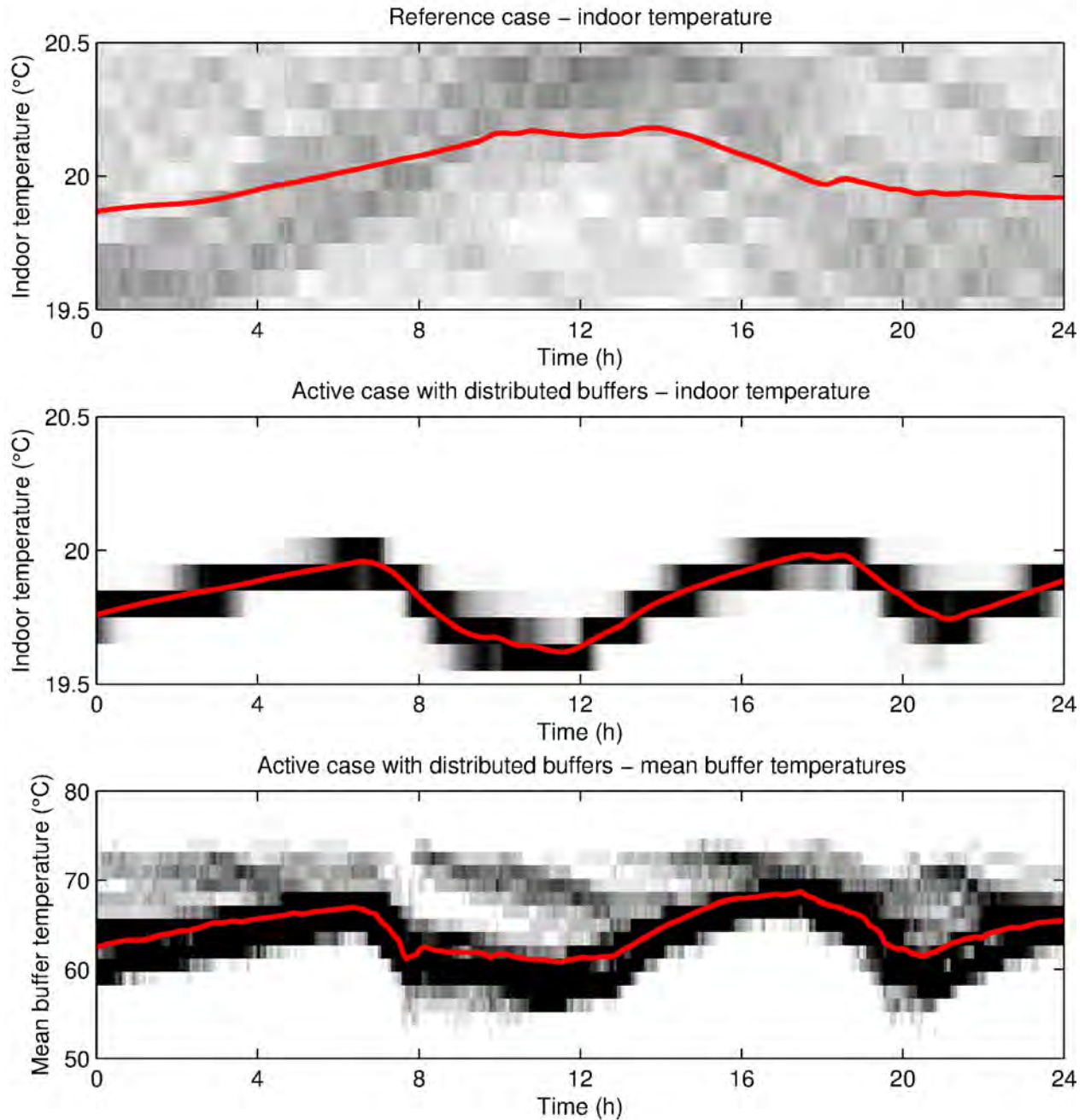


Figure 3-8: Evolution of the building indoor temperatures and the mean buffer temperatures during one day

Figure 3-8 gives an insight on how the heat demand profile is manipulated by the control framework. The top figure shows the mean indoor temperature of all the 100 buildings (red line) and the distribution of this indoor temperature (shading). Comparing the indoor temperature of the reference case to this of the active case (figure below), one can notice that the indoor temperature distribution for the active case is much more concentrated. This is because the MAS controller always distributes the heat available to the house with the highest heat demand. As a consequence, the building with the lowest temperature is always dragged to the rest of the buildings. In the bottom figure, the mean temperature in the distributed buffers is shown. A comparable evolution as for the indoor temperature can be noticed. As can be seen from this picture, when the control framework decides to heat a building, the building structure as well as the buffers are heated.



## Energy consumption and production

In Table 3-4 and Figure 3-9 the total energy consumption and production is shown for the different configurations.

Table 3-4: *Energy consumption and production for the different cases*

	Energy consumed by the buildings (kWh)		Energy produced (kWh)					
			Total		CHP		Gas boiler	
no buffers, regular control (reference)	70649		79447		58714		20651	
no buffers, active control	73562	(+4.1%)	79600	(+0.2%)	52100	(-11.3%)	27985	(+35.5%)
distributed buffers, active control	73594	(+4.2%)	80965	(+1.9%)	59177	(+0.8%)	21900	(+6.0%)
central buffer, active control	70577	(-0.1%)	78741	(-0.9%)	43750	(-25.6%)	35804	(+73.4%)

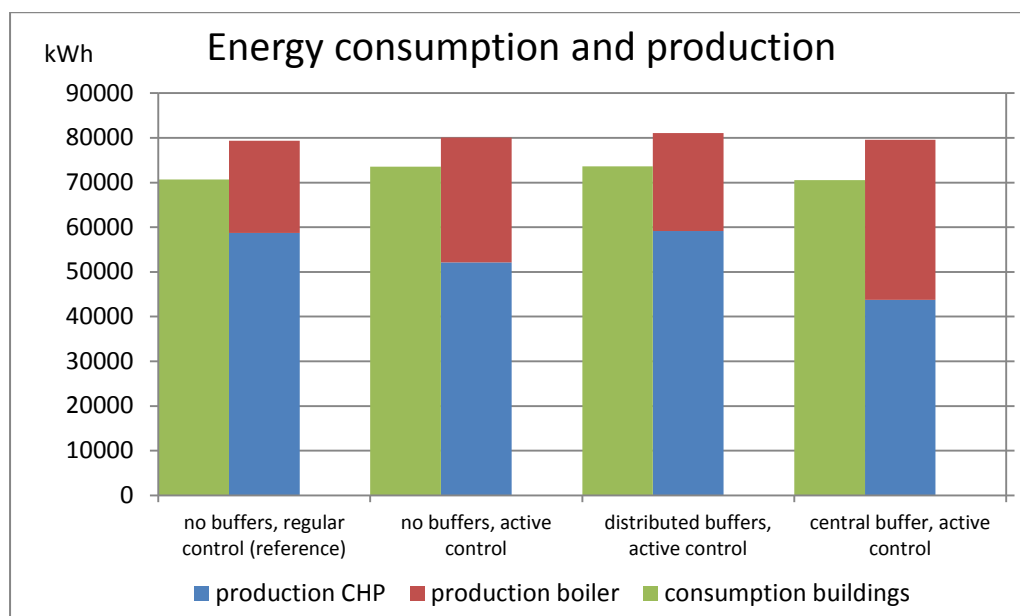


Figure 3-9: *Energy consumption and production for the different cases*

With respect to the energy demand of the buildings, the Table above shows that the consumption of the central buffer is the same as for the reference case. This is logical, since in both cases the control strategy of the individual buildings is the same. For the other active cases, the energy demand of the buildings is higher than that of the reference control case. The difference is the result of the different control strategy in the two cases. In the reference case, the number of times that the district heating valve is opened, is minimized: only when the indoor temperature drops below the lower limit (19.5°C) the valve is opened until the indoor temperature reaches the upper limit (20.5°C). This valve is opened a lot more in the active cases, resulting in higher thermal start-up losses. For the configuration with the distributed buffers the higher consumption is also resulting from the heat loss of the distributed buffers. The total heat loss of these buffers amounts to 606 kWh during the tested week.

Having a look at the production of energy, i.e. the energy which is delivered to the district heating grid, compared to the reference case, the efficiency of the district heating grid is somewhat higher for the active control case with distributed buffers and the active case without buffers (90.9% and 92.4% versus 88.9%). This means that the heat losses in these cases would be a bit lower. This is explained by the variation of the power demand and power supply in the grid. In the reference case, whenever

one of the buildings need heat, the district heating valve is opened. This means that often the total heat demand of the grid is low. In the active control cases however, the algorithm aims to switch off the power demand of the buildings until the electricity price is high. Once the price is high enough the CHP should switch on, implying that the energy demand of the buildings should be higher than the lower modulation limit of the CHP (of about 400 kW). Therefore, less moderate heat demands occur in the active cases: the heat demand is either high or very low, as can be seen in the histograms in Figure 3-10.

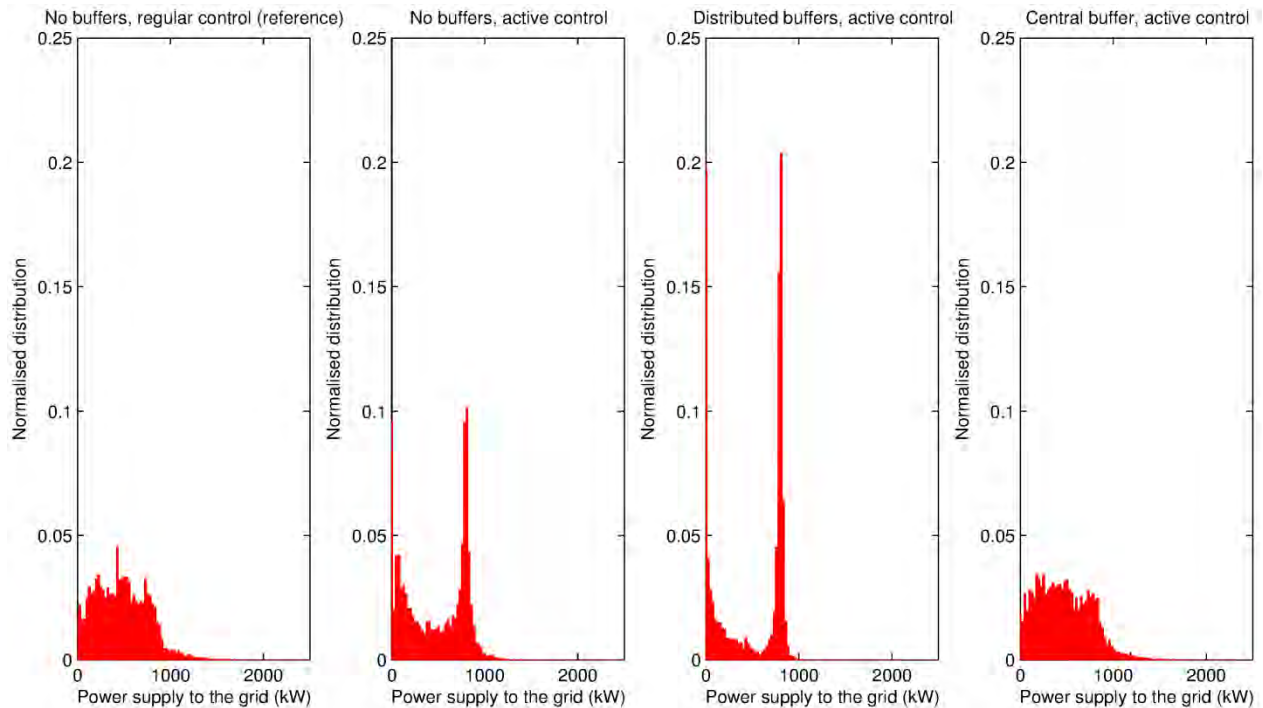


Figure 3-10: *Distribution of the power supply to the grid for the different storage configurations*

Higher powers correspond to higher flow rates and velocities, and shorter travelling times for the water through the pipes. In the network model, the pipe outlet temperature drop due to heat loss is modelled as an exponential descending function of the travelling time (Equation 3-8). The on average shorter travelling times for the active cases lead to lower temperature losses and in the end lower heat losses.

## Costs and revenues

In this final analysis the costs and revenues of the different configurations are compared. The costs consist of the gas costs of the CHP and the gas boiler and the pumping costs. The revenues are resulting from the sale of heat to the customers and electricity to the spot market. The parameters used in this analysis are: a natural gas price of 39.9 €/MWh which is the mean natural gas price for small industrial customers in Belgium in the first semester of 2013 [13]. The heat is sold at a price of 54.5 €/MWh, i.e. the natural gas price of residential customers in Belgium in the first semester of 2013 [13].

In Figure 3-11 the operational profit, i.e. the difference of the total revenue minus the total costs, is shown for the different configurations. As can be seen, the active control is able to significantly increase this profit due to the higher revenue from the electricity production of the CHP.

This analysis also indicates that the active case with distributed buffers performs best. The case without distributed buffers performs slightly worse. The case with the central buffer gives less good results, however the difference with the reference case still is significant. This is a bit surprising, since one would expect higher flexibility for the configuration with a central buffer, as also stated in Nuytten [71]. That work nevertheless only calculated the flexibility of the system, not how that flexibility is utilised. Moreover, a large difference between the central buffer configuration and the other active configurations is that in these last configurations also the building mass of the houses is activated.

The total thermal capacity of the buildings in the simulation amounts to 4165 kWh for the permitted temperature variation of 1°C. The thermal mass of both the central buffer and the distributed buffers is 39.5 kWh/k. Since the district heating network has a design regime of 80/40°C, this results in a maximum buffer capacity of the buffers of 1580 kWh which is a lot less than the thermal mass of the buildings. Activating the building mass is therefore shown to be very interesting. For the same reason, the difference in profit between the active case without buffers and the case with distributed buffers is limited.

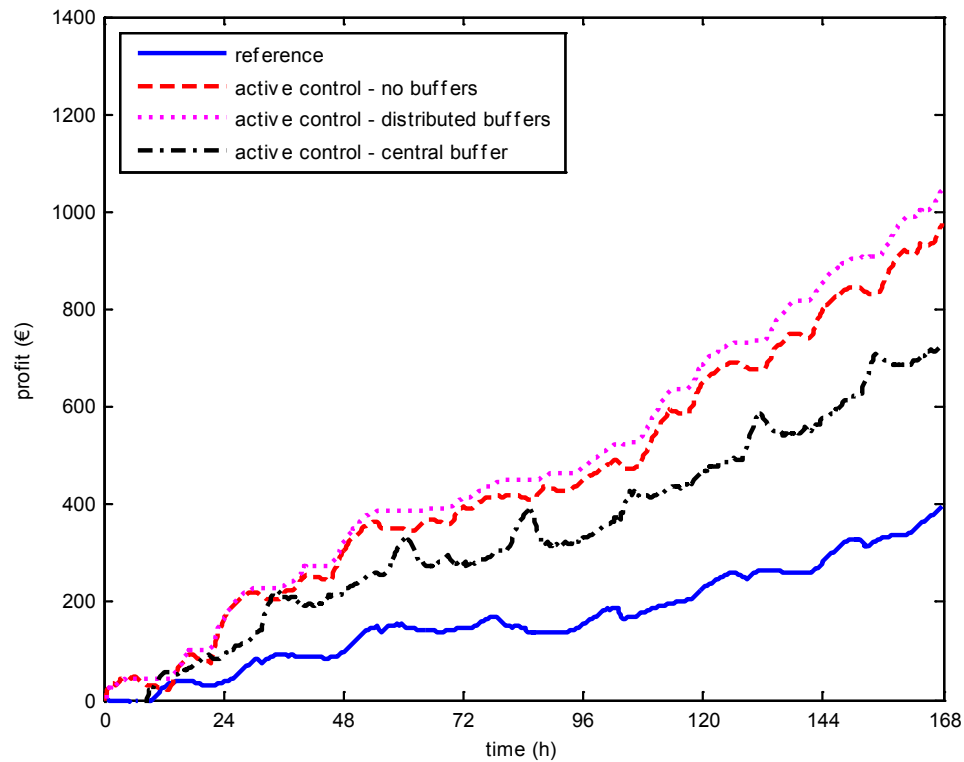


Figure 3-11: Operational profit for the different buffer configurations during the tested week

## Conclusions

In this chapter a number of storage configurations for district heating grids are compared to each other. To achieve this, a (hardware-in-the-loop) simulation model was built. The flexibility resulting from the storage vessels is used to actively control a CHP, which in this way can produce electricity at times of high electricity prices.

The simulation results indicate that the developed control framework perform well, i.e. that the business case – maximisation of the profit – is achieved.

The profit resulting from the different storage configurations are compared to each other. The results show that active control of the CHP is able to increase the profit of the CHP significantly. The configuration with distributed buffers performs best, however only slightly better than the active configuration without buffers. This finding indicates that active control of the thermal mass of the building is very promising.

The results for the central buffer case are a little worse, but still a lot better than in the reference case. The reasons for this worse behaviour is that the thermal mass of the buildings, which is activated by the active case without buffers and the active case with distributed buffers, is a lot higher than that of the buffers, resulting in much more flexibility and as a result higher yields.

### 3.3. Characterization of thermal storage buffers

#### Introduction

In the previous section it is indicated that active control of district heating grids can be beneficial. To optimise the performance of such advanced controllers as demonstrated in the previous section, it is very important to know the state of charge of the different buffers.

Nevertheless different approaches can be thought of when developing these intelligent controllers, mostly - and also in the controllers used in section 3.2 - these controllers look ahead to schedule their activities. Often, models are used for this forecasting activity [16]. And this leads to a number of problems when implementing this in practice. First of all, a huge number of buffer tanks are available in industry, all with different characteristics (dimensions, type and thickness of insulation, heating principles...). It is therefore not possible or feasible to use a dedicated model for every different buffer. For that reason, a generic grey-box buffer model is proposed in this section. Besides the requirement that such a model must be flexible, it is also important that the model is simple to avoid long calculation times for the controller. Obviously, like every model this model uses a number of parameters. Of course, if such controllers are enrolled on large scale, we cannot expect from technicians to parameterize each system installed over and over again. Therefore, to determine these parameters for a random buffer, also identification procedure is introduced.

Another important difficulty for the implementation of an intelligent controller is that for optimal performance, the state of charge for the buffers must be precisely known and that the models used by the intelligent controller must be calibrated. The state of charge of a buffer is determined by the temperature profile of the buffer. This means that, the more temperature sensors are installed in a buffer, the better the temperature profile is known and the better the state of charge can be determined. However, when equipping a district heating grid with a number of thermal storage tanks, it will be very expensive to install a large number of sensors. Therefore, in this section methods are also presented to assess the state of the buffers, when only few or no sensors are present in the buffers.

The structure of the section is as follows. First, the grey-box buffer model is proposed. Then, the identification procedure for the parameters is explained and the simulation results of these models are compared to experimental results. Finally, the state estimation methods whereby the number of sensors is minimized, are explained.

#### Generic grey-box heat buffer model

The model is a one-dimensional model, consisting of  $N$  vertical layers, a cold water input and a hot water output. The cold water input is assumed to be at the bottom of the vessel and the output on the top. If hot water is injected, it is modelled as heating of these layers. Additionally, there is the possibility of adding an internal heat exchanger to the vessel, providing heat to several layers according to the heat exchanger geometry. The temperature of the layers in the model can change according to:

- Heat exchange between neighbouring layers, or between a layer and its surroundings (heat loss to the outside environment);
- Convection, due to hot water being tapped off at the top of the buffer;
- Heating of specific layers in the buffer by an internal heat exchanger;
- Mixing.

The latter can occur when temperature inversion has occurred and a colder layer is on top of a warmer layer. In this case the denser colder layer will descend and the warmer layer will rise. In this process some heat will be exchanged between the layers. The overall evolution equation is:

$$\frac{dT}{dt} = \underbrace{A(T - T_{\text{external}})}_{\text{heat exchange}} + \underbrace{m(BT + C)}_{\text{draining}} + \underbrace{Du}_{\text{heating}} + \underbrace{E\Delta T}_{\text{mixing}} \quad \text{Equation 3-4}$$

The explanation on the structure and the physics of the matrices can be found in Annex D.

## Estimation of buffer parameters

### Markov-Chain-Monte-Carlo (MCMC)

To start with, a multiple shooting technique was developed for estimation of the parameters with good results. However, later it was decided to switch to a Markov-Chain-Monte-Carlo method. This method has some advantages in comparison to multiple shooting, since MCMC can better deal with these characteristics of the model:

1. It is nonlinear in the parameters. Equation 3-4 is linear in the parameters, but this linearity vanishes when the equation is integrated in time.
2. It is nonlinear in the temperatures; especially Equation 0-8 causes nonlinear relations.
3. The constraints are all linear in the parameters.
4. Non-differentiable with respect to the parameters. Again Equation 0-8 causes the problem.

MCMC methods also give some additional advantages:

1. it is easy to implement and the risk of introducing bugs is rather small;
2. it only needs to integrate the model forward, so no derivatives are needed;
3. Constraints on the parameter space can easily be incorporated;
4. It finally provides not only the most likely parameter values, but the entire parameter distribution.

These advantages makes it possible to automate the identification process of the parameters, which definitely is needed when enrolling the controllers on large scale.

### Identification procedure

As a type of MCMC algorithm, more specifically a Metropolis-Hasting sampling algorithm is applied. Alternative algorithms which will probably perform fine as well are genetic algorithms or cross entropy methods. The Metropolis-Hasting sampling algorithm works as follows:

1. Initialize the parameter set randomly,  $\theta_0 = (\alpha_0, \beta_0, \gamma_0, \delta_0, \varepsilon_0)$  and the initial cost function to  $C_0 = \infty$ ;
2. Check if all constraints are met. If not, redo (1);
3. Run the model forward;
4. Calculate the least squares cost function  $C(\theta)$  for the modelled temperature values in each layer by comparing them with the measurements;
5. Calculate the Hastings ratio

$$r = \min(1, C(\theta)/C_0(\theta_0)) \quad \text{Equation 3-5}$$

6. Accept the parameter values with a probability  $r$ , i.e. draw a sample from a uniform distribution between zero and one. If this sample is smaller than  $r$ , overwrite  $\theta_0 = \theta$  and  $C(\theta) = C_0(\theta_0)$ .
7. Perturb the parameter values with a random number, drawn from a Gaussian distribution. These distributions have zero mean and its standard deviation is tuned so that the acceptance rate is about 30%.
8. Repeat steps (2) to (7) for a predefined number of steps.

The random number used in 5 allows the algorithm to select worse solutions. This avoids that the algorithm converges immediately to the closest local minimum in the cost function surface. Some practical aspects in the implementation are:

- Initial values for the parameters are unknown. These are randomly chosen within the constraints and a burn-in period of 30.000 iterations was run to find good initial values. After about 5000 iterations, good parameter values are often found.

- In this burn-in run, after every hundred iterations, the parameter set was reset to the best values found so far. This avoids that the algorithm would spend too much time searching in regions with high cost function.
- For the final estimation of the parameter distributions, the most probable value was chosen as initial value and resetting the parameters was no longer performed. The standard deviation of the parameter perturbation was set to  $\sigma_{\theta} = \theta_0$ , which apparently results in an acceptance rate of roughly 30 - 50%.

### ***Application of MCMC to identify the parameters of the buffers in the lab***

In this section the results for the identification of the four buffer types are discussed. Firstly, the results of the parameter estimations are discussed and next the most probable model is compared with the measurements and the relation between the grey-box model and the physical structure of the buffer is explained. Finally, the shortcomings of the generic grey-box model and possible improvements are discussed.

#### ***The lab tests***

The test setup in the lab of VITO was already discussed before. In Figure 3-5 a schematic overview of the test setup is shown. The setup consists of four buffers. The two buffers on the left only supply domestic hot water. In the next of this section they will be indicated as 'domestic hot water cylinder' or 'DHW'. The buffers which also provide heat for space heating will be called 'hot water storage buffer' or 'HWSB'.

A series of tests has been carried out to gain knowledge on the charge, discharge and static heat loss behaviour of the vessels. Monitoring results include: the water temperatures at different heights in the vessel, heat input originating from the central lab heating grid, supply and return temperatures as well as flowrate on the side of delivery. DHW is drawn from the vessels by the opening of an automated valve. The power requested by the space heating is controlled by adjusting the supply temperature to the heat exchanger on the side of delivery, by means of a mixing valve in the lab's thermal grid.

Each vessel has been monitored in a separate charge-discharge test. The test-sequence consists of a series of actions and conditions, which are executed in the time-span of approximately 5 to 10 hours. This is illustrated by the routine for the DHW cylinders:

1. Fully charge the vessel to 70°C
2. Draw water from the vessel for DHW supply, until the outgoing temperature drops below 30°C.
3. Start charging until the middle internal temperature sensor indicates a temperature >50°C.
4. Draw water from the vessel for DHW supply, until the outgoing temperature drops below 50°C.
5. Start charging until the middle internal temperature sensor indicates a temperature >60°C.
6. Draw water from the vessel for DHW supply, until the outgoing temperature drops below 50°C.
7. No actions for 1 hour. Static heat loss to the environment.
8. Draw water from the vessel for DHW supply, until the outgoing temperature drops below 40°C.
9. Start charging until the middle internal temperature sensor indicates a temperature >65°C.
10. No remaining actions. Static heat loss to the environment.

The results of these tests are used to fit the parameters of the buffer model.

#### ***Identification of the parameters***

The parameter estimation process is further described in 0. The most likely parameter values are given in Table 3-5 for the different boilers.

Table 3-5: *most likely parameter values. Parameter values which are significantly different from zero are shown in bold.*

	DHWC 1	DHWC 2	HWSB 1	HWSB 2
Heat loss (1/s)	<b>-2.03e-06</b>	-4.29e-06	-1.60e-06	-9.25e-05
Heat exchange (1/s)	3.05e-06	5.63e-06	5.10e-03	1.36e-03
Heat convection (1/L)	3.57e-02	<b>4.94e-02</b>	7.60e-01	1.01e02
Mixing (1/s)	2.64e-11	5.44e-12	1.10e-06	5.91e-08
Heating layer 1 (Ks/J)	<b>1.11e-06</b>	<b>1.22e-06</b>	3.18e-08	<b>2.09e-05</b>
Heating layer 2 (Ks/J)	<b>1.33e-06</b>	<b>1.21e-06</b>	2.80e-08	<b>2.07e-05</b>
Heating layer 3 (Ks/J)	<b>1.31e-06</b>	<b>1.10e-06</b>	3.17e-08	<b>2.07e-05</b>
Heating layer 4 (Ks/J)	<b>1.14e-06</b>	<b>9.89e-07</b>	<b>1.63e-06</b>	<b>2.43e-05</b>
Heating layer 5 (Ks/J)	<b>8.95e-07</b>	-	-	-

When applying the values from this table to the model, it is interesting to have a look at the difference between the simulation and the measurements. Note here that only the initial conditions are provided to the model. All other temperatures inside the buffers are reconstructed by fitting the entire model on the data. This is shown in Figure 3-12.

For DHWC1, overall the model can capture most features present in the data. However, some model errors will always remain present. In the first experiment (DHWC 1, Figure 3-12), the temperatures of the layers continue to rise, even if heating is already stopped. This can easily be explained. The inner part of the inner tank is still warmer than the outer tank. It takes a while for this heat to reach the outer tank. Such dynamics are not modelled and cause the most striking model errors in the first experiment. We cannot expect that this simple model is able to describe all variations in these experiments.

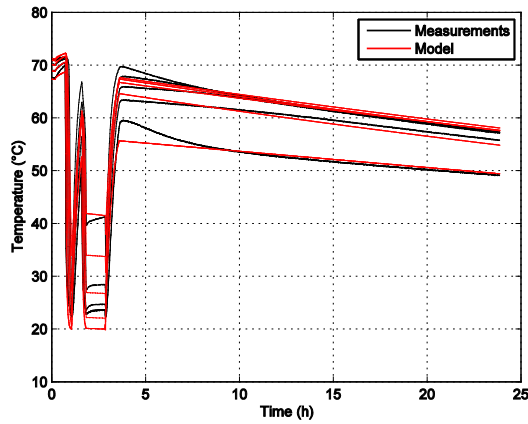
Also for DHWC2 the simulation results and the measurements coincide pretty well, with the difference that the modelled temperatures diverse faster. One could possibly argue that this could be remedied by a higher heat exchange parameter, but the match on the data during the rest period (from hour 2 to 5) would become worse. We can conclude that the MCMC algorithm has balanced the errors made during the charge and discharge periods with the errors made during the rest of the test cycle. Also between hour 3 and 4 there is some difference between simulation and measurements. This is just after a lot of hot water is drained and cold water is injected from below. This process cannot be captured completely by the model and a too large temperature difference must be allowed to match the data during this period.

For the HWSB's, as is explained in 0, it was not possible to define the parameters sharply. Nonetheless, the comparison between the measurements and the optimized model is still very good, as Errors are not significantly larger than in the experiments with distinct parameter values. The most visible difference in the first HWSB is the temperature rise above 70°C, as can be seen in Figure 3-12, during the heating period at hour 10. The model is told that a certain amount of heat is injected, without any temperature bounds. In reality, hot water with a temperature of about 70°C is injected in the top layer. Evidently, the top layer can in reality not rise above this 70°C.

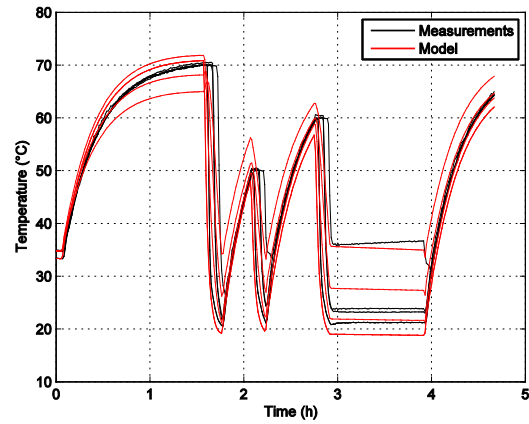
An important effect, not shown here, is that during rest periods, colder water sinks to the bottom layers and pushes the lighter warmer water up (buoyance effect). As a result the buffer becomes stratified after a while. This effect is not incorporated in this model and can thus not be described either. One possible solution is to make the heat loss parameter  $\alpha$  layer-dependent. We have tried this solution, but without success. A larger number of model parameters increase the accuracy of the

model, but at the same time the speed decreases. In balance, the loss in speed is larger than the gain in accuracy. For that reasons, we continue with the model presented here.

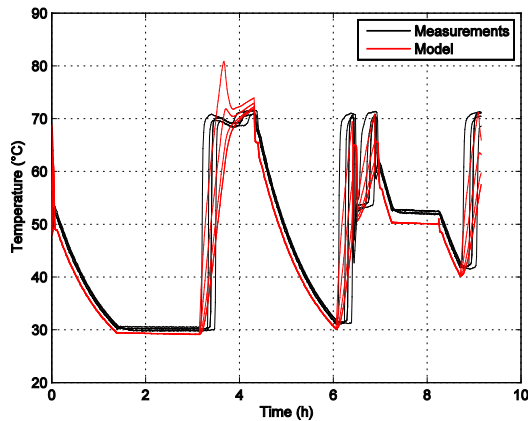
DHWC1



DHWC2



HWSB1



HWSB2

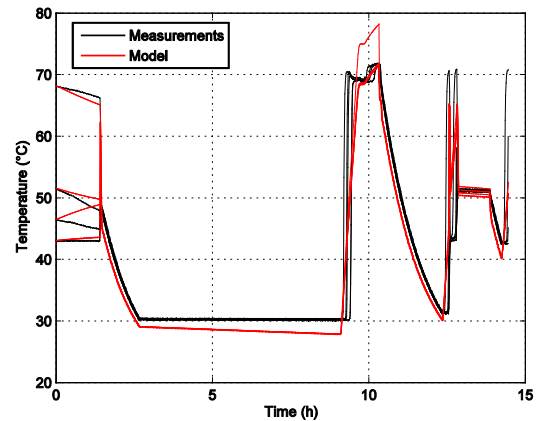


Figure 3-12: *measured and simulated temperatures inside the different buffers*

## Minimization of the number of sensors in the buffer

The ambition is to minimize the number of sensors in the buffers. Therefore, first a procedure based on a Kalman filter is presented to estimate the temperature in the buffer at positions where no sensors are present. If this is possible, a number of sensors can be eliminated.

In the next part, the optimal location for the remaining sensors is determined. Indeed, when installing the sensors in the buffer, not every location is equally 'valuable' to estimate the temperature profile in the buffer.

Finally, it is tried to estimate the temperature profile in the buffers, when no sensors at all are present.

## A Kalman filter for state estimation

When only a few temperature sensors are present, the state is only known in the layers where these sensors are present. A Kalman filter can then be used to estimate the state of the other layers [17]. The procedure is further explained in Annex F.



### Application of the Kalman filter shooting to a simple example

A model with 20 layers is used. All layers are initially 50°C. At time step 1 hot water is tapped, at steps 25 and 26 heat is added to layer one. Each layer is initialized at a random temperature between 0°C and 100 °C. A sensor is placed in layers 1, 5, 10 and 20. The true temperatures are shown in Figure 3-13. The estimated temperatures are shown in Figure 3-14. In this example the temperatures are reasonably well estimated after about 10 updates. In conclusion, the Kalman filter is able to reconstruct the temperatures in each layer after a few minutes.

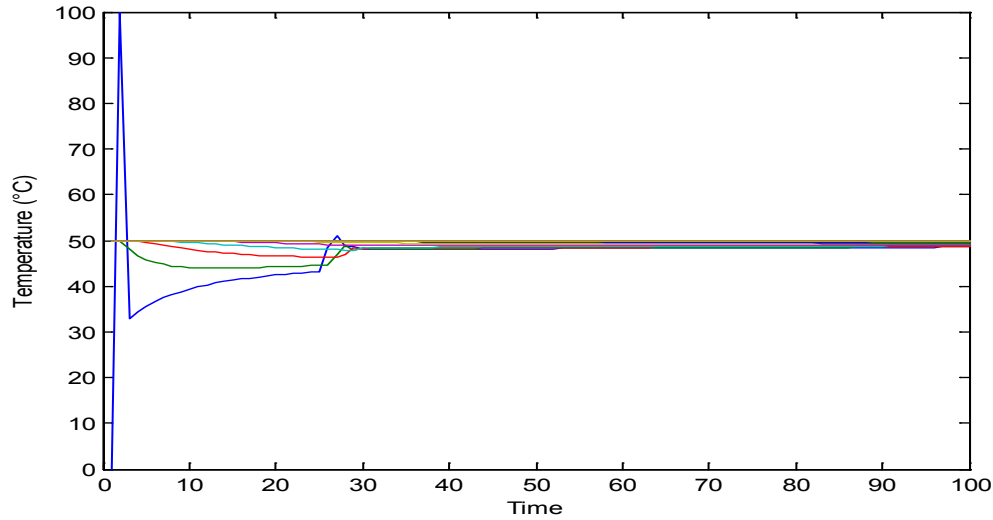


Figure 3-13: *The true temperatures of the 20 layers.*

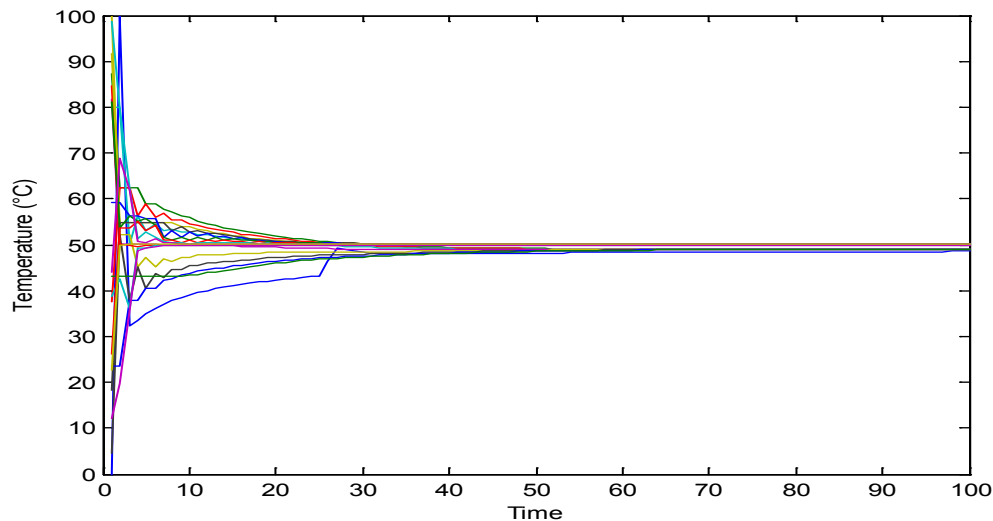


Figure 3-14: *The estimated temperatures of the 20 layers by the Kalman filter*

### Identifying the optimal sensor position

In this section, the optimal position of two temperature sensors will be identified. So the objective is to place these sensors such that the mismatch between the estimated temperature of each layer and the true temperature is as low as possible.

In a first experiment, ten temperature layers are used and the system is integrated over 50 minutes. The results are shown in Figure 3-15. The optimal position, i.e. the combination with the smallest least squares error, is at layers (6,10).

Figure 3-16 shows the true temperature profiles. Figure 3-17 shows the reconstructed temperatures if the sensors are placed at none optimal positions and Figure 3-18 shows the reconstructed temperature profiles if sensors are placed at optimal positions. It is clear that the position of the sensors has a large impact on the ability to reconstruct temperatures.

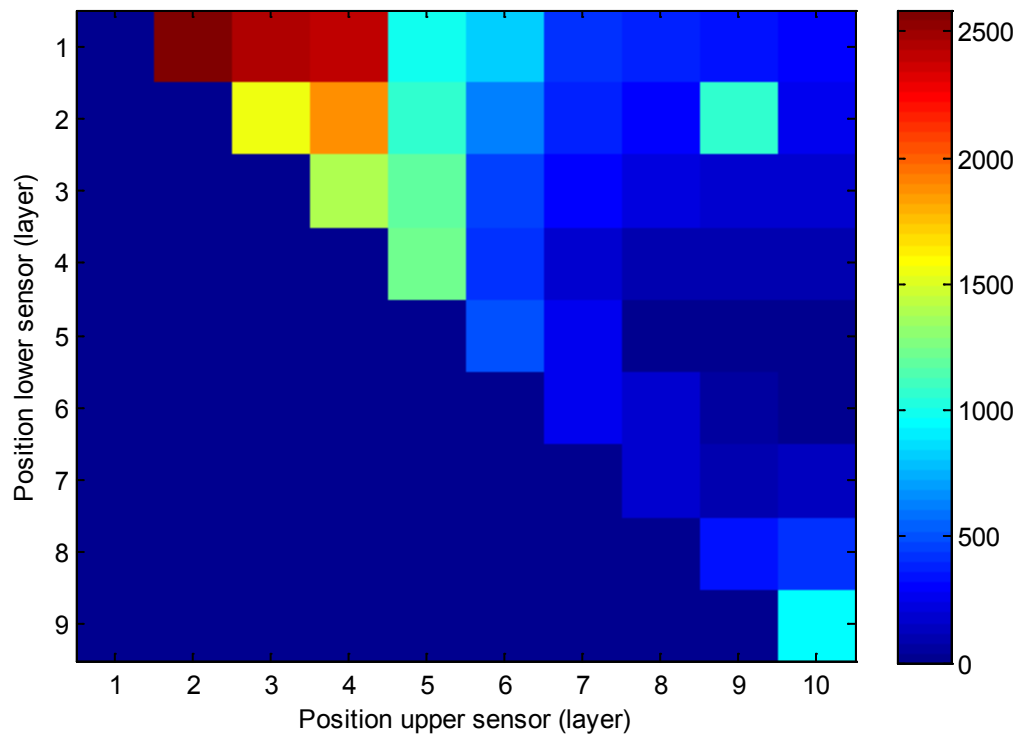


Figure 3-15: the least squares difference between the real and estimated temperature after 50'.

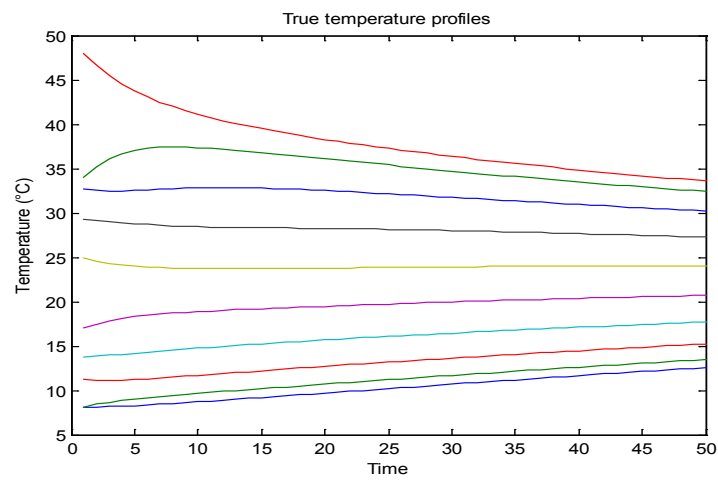


Figure 3-16: true temperature profile.

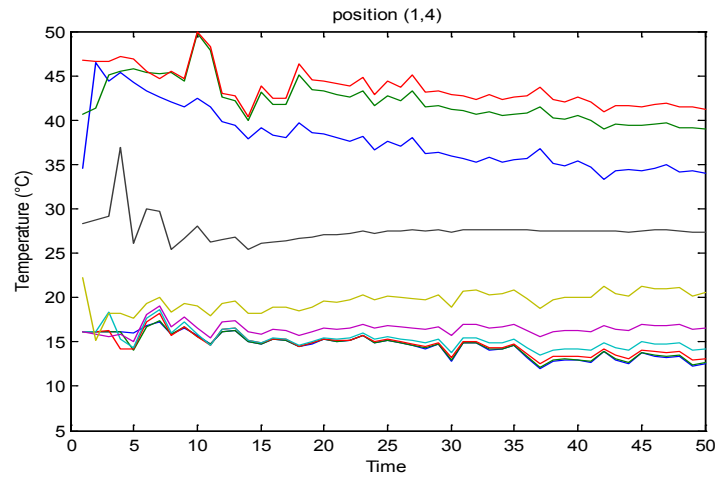


Figure 3-17: temperature profile, when the sensors are placed at position (1,8).

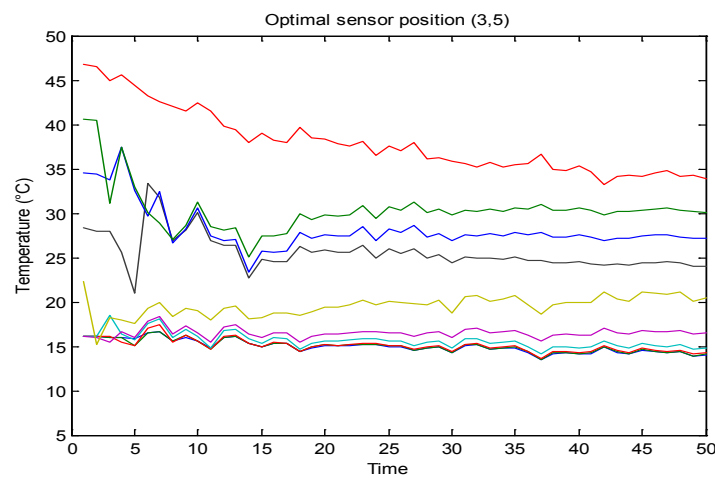


Figure 3-18: temperature profile, when the sensors are place at the optimal position (6,10).

## State estimation without any sensors

The aim of this research is to estimate the state of charge of a buffer tank when no internal heat sensors are present. Inlet and outlet temperatures can be measured, together with the flow rate and heating of the buffer tank. The temperature inside the buffer tank is discretized, and a temperature is associated to each layer.

For some types of buffer tanks, the strategy explained below is redundant. If the buffer tank is heated by means of a coiled heat exchanger e.g., the temperatures can be measured directly by the following procedure. Firstly, stop the flow of the heating circuit, so that the water inside the spiral can reach an equilibrium temperature. Next, restart the flow and measure the temperature of the water coming out of the spiral. This is a direct measurement of the temperature profile in the buffer tank. If such strategies are not possible, the outlet temperature of the buffer tank can be estimated. This estimation is discussed in this report.

The problem considered is twofold:

- The state space parameters (temperature of each layer) are unknown;
- The model parameters (conduction, convection, etc.) are unknown;

Both sets of parameters can be estimated with a Kalman filter. The main novelty of this implementation is that the Kalman filter is extended so that it can cope with constraints.

The constraint Kalman filter is a simple adaptation of the unconstrained one, where in each time step an additional step is performed: if one of the constraints is violated

$$\hat{x} = \arg \min_x (x - \tilde{x})^T W (x - \tilde{x})$$

Equation 3-6

Subject to

$$Dx \leq d$$

$$D_{eq}x = d_{eq}$$

With  $\hat{x}$  the constraint state space parameters,  $\tilde{x}$  the unconstrained state space parameters,

$W = P^{-1}$  a weighing matrix, usually equal to the inverse of the state space covariance matrix and  $(D, d, D_{eq}, d_{eq})$  matrices defining the equality and inequality constraints. Constraints are given in Equation 3-3. Equation 3-18 is a quadratic optimization problem, which can be solved by e.g. cvx.

First the good news. The method is pretty good in predicting the outlet temperature, as can be seen in Figure 3-19. In the first hours large deviations occurs from time to time, but after a while the covariance on the model parameters shrink and the mode becomes more certain, adapts less and follow the observations more closely.

Figure 3-20 and Figure 3-21 show how well the method is able to reconstruct the layers where sensors are placed. Note that these sensor data are not used in the Kalman filter. Overall, the filter is quite well able to reconstruct the internal temperature layers, but when the temperature changes quickly severe errors can occur. Whether this is due to ill model parameters or the numerical impossibility to reconstruct the interior of the buffer tank without any data is still unclear. Maybe a measurement series with more and faster temperature variations could clarify this. On the other hand, the histograms of the errors made at the three sensors and at the outlet are reasonable, as is shown in Figure 3-22. Standard deviations are respectively 6.3, 5.3, 3.43 and 1.0, which result in a precision of about 10% for the interior of the buffer tank.

To conclude, one can say that the method works pretty well, especially in predicting the outlet temperature and reasonably well in predicting the layer temperatures in the buffer tank, which can be used to estimate the State-of-Charge.

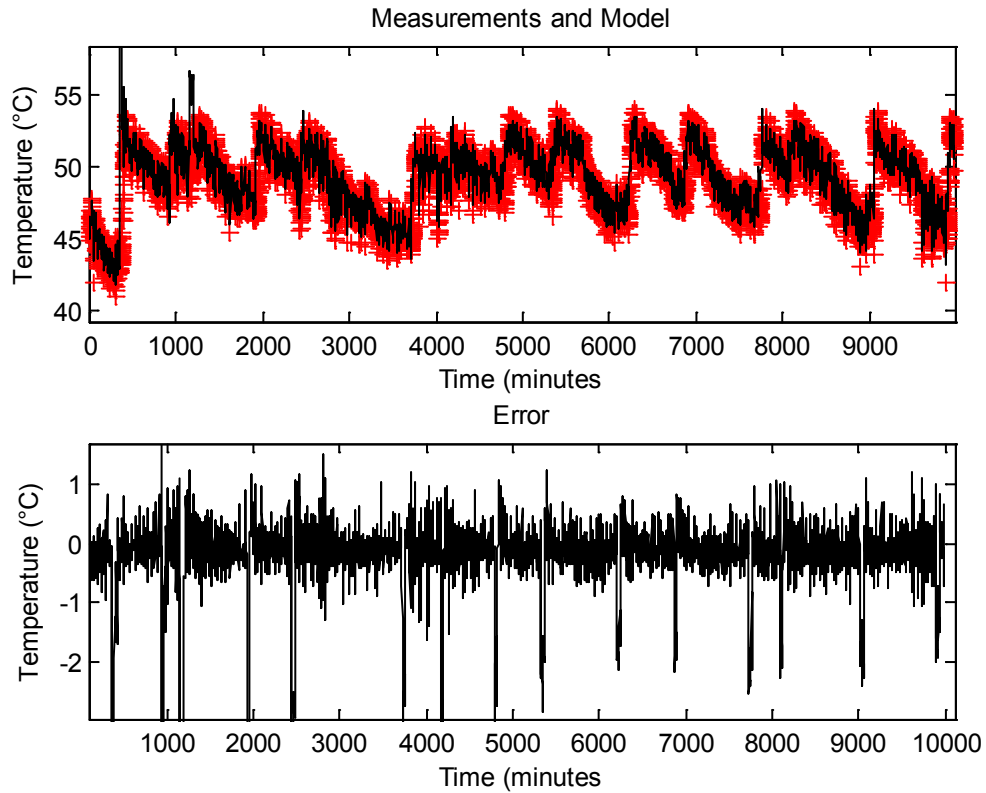


Figure 3-19: *Top: the measured outlet temperature in red and the predicted temperature in black. Bottom: the error between both.*

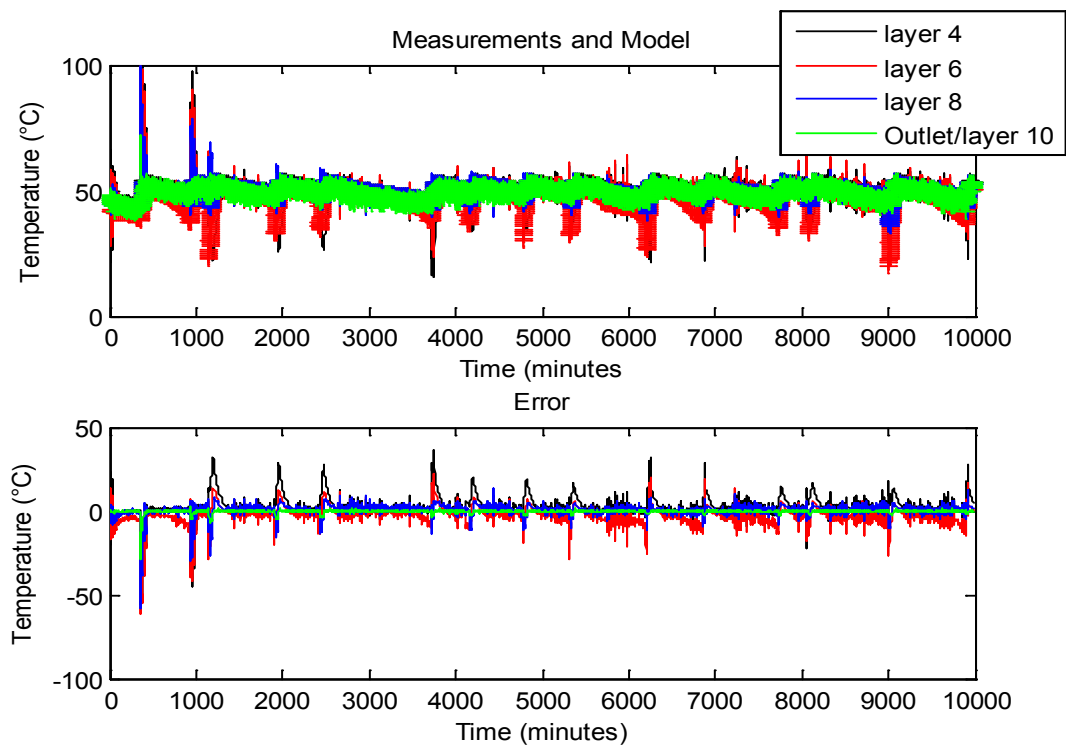


Figure 3-20: *Top: the estimated temperature of the three measured layers and their measured values. Note that these measured temperatures are not used in the Kalman filter. Bottom: the error between both.*

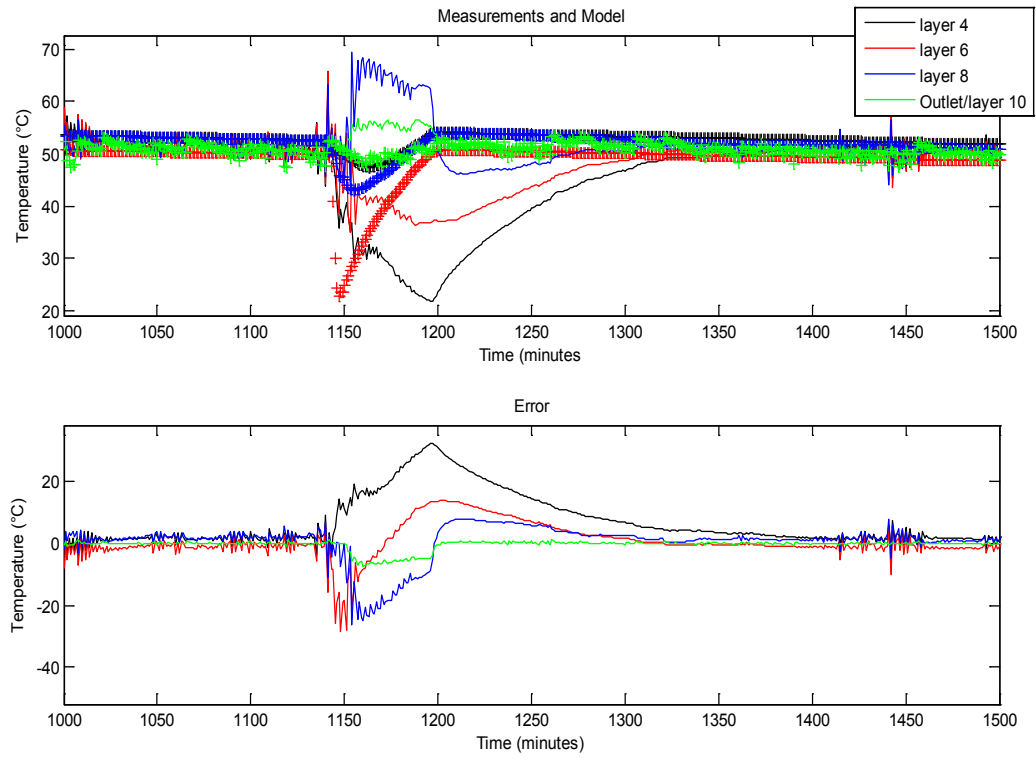


Figure 3-21: *details from Figure 3-20.*

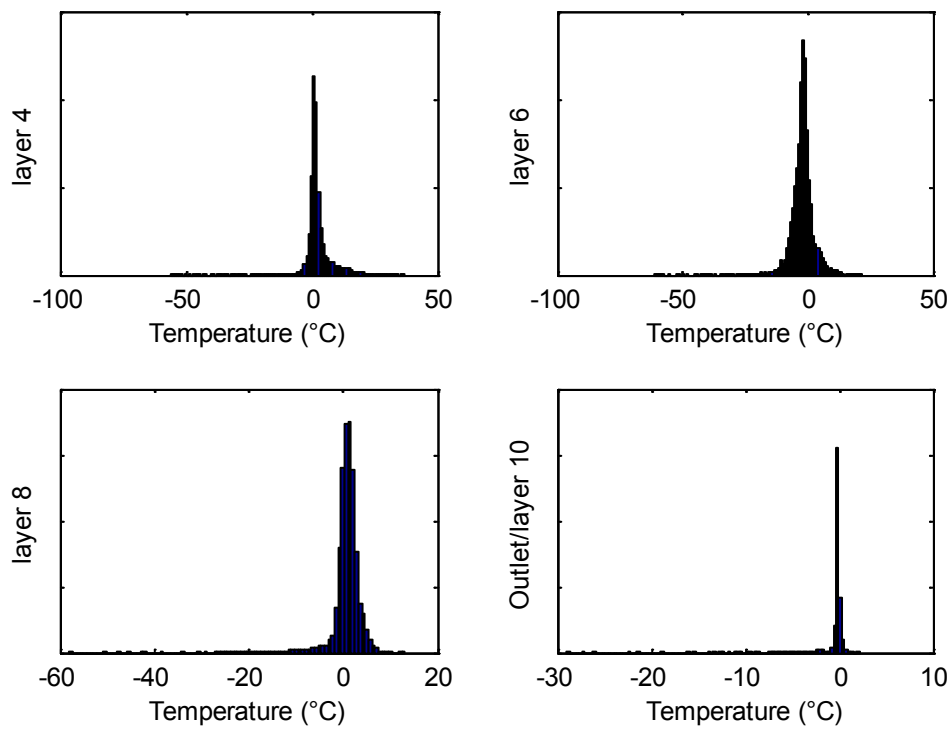


Figure 3-22: *histograms of the error between measured and reconstructed temperatures.*

## Conclusion

In this chapter a simple grey box model is proposed together with an identification procedure based on measurements taken on four different hot water vessels in a laboratory setup. The aim is to have a fully automated characterization for hot water storage systems. The model consists of four processes, i.e. heat losses and heat exchange between the water layers, heat convection when the system is drained, mixing and heating. Some of these processes were not active in some experiments and the procedure was able to identify this correctly.

The method to estimate the temperature profile in the buffer tanks when the number of sensors is minimized also shows good results. However, it was shown that the position of the sensors is important to get good results with only a few sensors.

An extension of this method to a situation without a single temperature sensor in the buffer gives good results with respect to the predication of the outlet temperature of the buffer. The estimation of the temperature profile in the buffers give good results during a very large period of the tests. Only when the temperature changes rapidly, the method is not able to reconstruct the temperature profile accurately.

## 4. Thermochemical heat storage using open sorption

### 4.1. Introduction

Thermochemical heat storage (TCS) has the potential to provide a very compact way to store thermal energy. Volume reductions of a factor of 10 compared to sensible water storage can theoretically be achieved and the energy can be stored with low thermal losses during long storage periods. To overcome seasonal mismatch of summertime solar heat supply and wintertime heat demand for buildings, the heat is stored using reversible physical or chemical sorption reactions. Especially the solid-gas based reactions provide an attractive option for long term storage.

The basic concept of TCS is shown in the scheme below

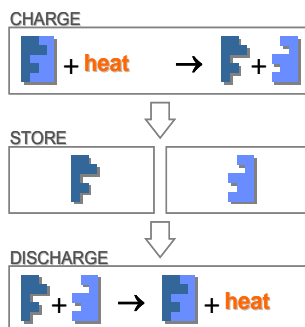


Figure 4-1 *concept of the Thermochemical Heat Storage technology.*

The present work is focused on the development of an open sorption TCS concept. In this concept a solid material (the sorbent) is used in combination with water vapour (the sorbate), as the reacting media. When the solid material is heated, the water vapour is removed from the solid and the sorption heat is then stored. In periods of heat demand, water vapour is again absorbed by the solid and the heat of sorption is then released.

During charging the sorbent is heated by hot air passing through the sorbent bed, and the water vapour is carried away in the air flow. In discharge mode, humid air is passed through the sorbent bed and the water vapour is then absorbed in the sorbent. The heat of absorption is released and this results in heating up the air flow through the sorbent bed (see Figure 4-2). As a result, open sorption TCS systems have a direct connection with ambient conditions as the amount of water vapour in the air depends on ambient conditions.

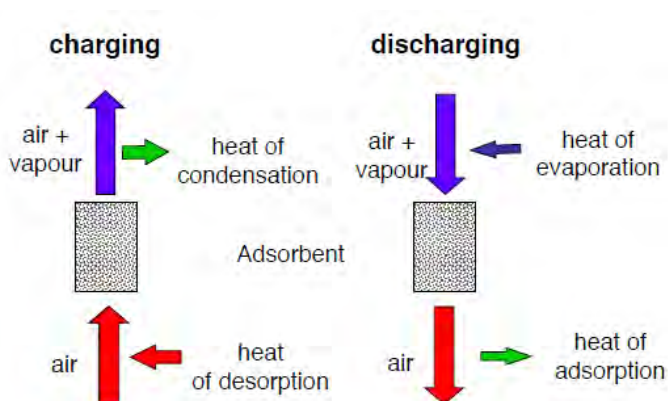


Figure 4-2 *Schematic of the charge and discharge operation modes of the open sorption system concept*



The performance of the TCS system is to a large extent determined by the temperature and humidity levels of the air, which is passed through the sorbent bed.

To assess the technical feasibility and potential added value of long term heat storage in the framework of the Energy Hub concept, knowledge is required about the performance characteristics under typical operating conditions of the open sorption thermochemical reactions. This forms the goal of the research work described in this chapter:

***Determine the performance characteristics under typical operating conditions of an open sorption TCS system***

Achieving this goal will allow a better evaluation of the technical feasibility of TCS systems as a thermal storage option within an Energy Hub, and allows an analysis of the contribution of a TCS system to enlarging the share of renewable energy within an energy district. (part of WP4, overall system modelling)

An experimental approach is chosen to acquire knowledge on the performance characteristics of the TCS system, supported by TCS system modelling. A prototype development of an open sorption system concept is undertaken on the relevant scale to enable model validation.

The starting point of the work is the definition of TCS system requirements and system configuration. This is followed by the selection of the suitable thermochemical materials. The prototype development was undertaken in two stages. A 1<sup>st</sup> stage bench-scale prototype was built and tested to learn the basic operational characteristics as well as the critical aspects of the open sorption TCS concept. The results from this work were taken as input for the further development and testing of the 2<sup>nd</sup> stage prototype that is built on a larger scale and supported by the development of a dynamic system model.

## 4.2. System design and construction

A strong driver in the development of compact long term heat storage solutions is its potential application as decentralized seasonal solar heat storage system for low-energy single family houses. The abundant heat from a solar collector system in summertime needs to be stored in a compact manner for a period of several months for use in wintertime by using a TCS system. With this application in mind, the global system specifications for an open sorption storage system are derived for the operating temperatures, thermal power levels, storage capacity and efficiency.

Table 4-1: Design values for a domestic seasonal heat storage system

property	Value
Charge temperature solar collector vacuum tube	130°C
Discharge temperature	60°C
Air humidity level	12 mbar H <sub>2</sub> O pressure
Charging power	3 kW
Discharging power	1.5 kW
Storage capacity	6 GJ (delivered) 1700 kWh
Thermal storage efficiency	60%
Auxiliary electric energy	<5% of thermal energy

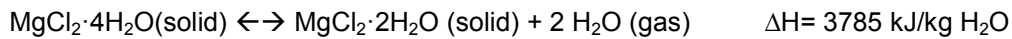
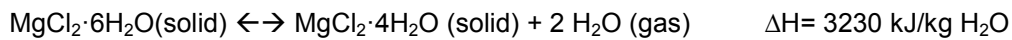
The values given in Table 4-1 are considered to be the target values to reach in the seasonal heat storage application for a single family house. The prototypes are developed based on 'derived' specifications. The focus of the first prototype development is on attaining stable operation within the required temperature levels in a small-scale TCS system.

### Open sorption heat storage Prototype 1

The open sorption heat storage system concept was initially tested by a first stage prototype [24](Figure 4-3 and Figure 4-4). This prototype of 20 dm<sup>3</sup> storage reactor volume contained 9 kg of MgCl<sub>2</sub>·6H<sub>2</sub>O as thermochemical heat storage material.

The selection of  $\text{MgCl}_2\text{-H}_2\text{O}$  as thermochemical reacting system was based on its high theoretical storage density, ( $2 \text{ GJ/m}^3$ ), reaction temperatures that match with those of solar heat supply ( $130^\circ\text{C}$ ) and domestic heat demand ( $60^\circ\text{C}$ ) and its low price ( $<1\text{€/kg}$ )

The equilibrium storage reactions and associated reaction heat used in the setup is



The effective heat storage density of  $\text{MgCl}_2\cdot 6\text{H}_2\text{O}$  amounts to  $2 \text{ GJ/m}^3$  taking the density of the salt hydrate to be  $1.6 \text{ kg/dm}^3$ .

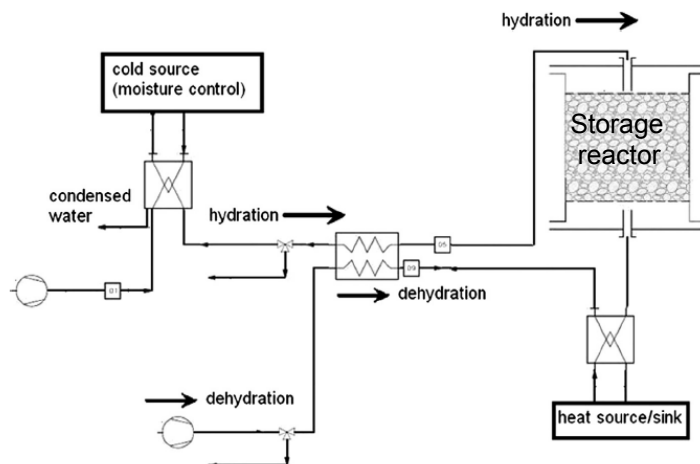


Figure 4-3: flow diagram of the 1<sup>st</sup> stage prototype TC-storage reactor with a low temperature heat source to evaporate/condense the water and a high temperature heat source/sink



Figure 4-4: Picture of prototype 1 test setup

Key results obtained in the testing of this system were:

- Thermal storage density of the reactor  $0.5 \text{ GJ/m}^3$
- The heat storage capacity of the prototype system was  $10 \text{ MJ}$  ( $3 \text{ kWh}$ )
- Temperature of heat delivery  $>60^\circ\text{C}$ .
- Charging temperature of  $130^\circ\text{C}$  was sufficient
- Charge and discharge duration  $> 24$  hours
- Peak thermal powers of  $150 \text{ W}$

Important observations on testing prototype 1 were:

- heat losses during the charging and discharging stages are significant and strongly reduce the overall heat storage efficiency

- design for low parasitic power for fans and auxiliaries is mandatory to maintain low electric to thermal energy ratio
- Questions were raised about the chemical stability of  $\text{MgCl}_2\text{-H}_2\text{O}$  system under typical seasonal heat storage conditions

These observations were taken into account in the design and development of the 2<sup>nd</sup> stage prototype system.

## Open sorption heat storage Prototype 2

### Selection of heat storage material

The chemical stability of the selected  $\text{MgCl}_2\text{-H}_2\text{O}$  sorption heat storage system raised questions during testing in prototype 1. Traces of corrosive gas were observed during one of the regeneration tests of the system. To study the long term stability of the salt-hydrate system, analytical experiments (thermal analysis, thermogravimetry and XRD analysis) were conducted under simulated operating conditions for charging and discharging of the salt-hydrate.

The long term stability of the  $\text{MgCl}_2\text{-H}_2\text{O}$  reacting system is not sufficient for the intended application. An irreversible decomposition reaction occurs during the dehydration, leading to formation of traces of HCl gas and gradually reducing the storage capacity of the salt in time. Lowering the charging temperatures from 130 to 110°C did not prevent the decomposition. The amount of heat involved in the storage reaction decreases by ~5% each cycle. The irreversible reaction in the  $\text{MgCl}_2\text{-H}_2\text{O}$  system is:



The HCl gas is transported by the air flow out of the system. It is toxic and corrosive and reacts with metal parts in the system. This decomposition is an irreversible process, which permanently changes the material properties. This makes the system performance decrease over time. A solution to suppress this irreversible reaction is to be found, before to use this material in a large scale long term heat storage system. This is currently being researched by a PhD student in the framework of the Dutch ADEM program.

This led to the conclusion that  $\text{MgCl}_2 \cdot 6\text{H}_2\text{O}$  was not applicable for prototype 2. To bypass the material stability issue, zeolite 13X was selected as a stable replacement material, in order to allow further system development. Zeolite type 13X is well known as a stable adsorption material applicable in both drying and heat storage applications [25, 26 27, 28]. Its thermal properties and sorption properties have been studied sufficiently to allow the use of zeolite 13X as a replacement of the salt in prototype 2.

The differences of 13X in comparison to  $\text{MgCl}_2\text{-H}_2\text{O}$  system are:

- high chemical and mechanical stability
- lower heat storage density (at least a factor of 2 lower than the practical value of salt)
- gradual change in water uptake during heating and cooling, whereas salt has stepwise changes
- higher optimal regeneration temperature (200°C instead of 130°C)
- higher cost

The zeolite is used in this work as a 'dummy' sorption material. It allows us to study the characteristics of the open sorption system concept in detail, while avoiding the long term stability and potential corrosion problems. It also allows us to verify the sorption storage system model, as described in 4.3. Once a stable salt-hydrate is obtained, the zeolite can be replaced by the salt.

### Process design

The basic requirements for Prototype 2 system are given below:

- Storage capacity: 15 kWh, 50 MJ
- Thermal power: 0.5-1 kW
- Temperature range for charge – discharge: 200 – 60°C
- Air humidity level: 12 mbar  $\text{H}_2\text{O}$  pressure

- Modular storage system concept: flexible for changes in capacity and power requirements for various applications

Starting from these values, a static system model was first made to calculate the thermal requirements for separate components of the system. Important aspect of the open sorption concept is the calculation of air flow rates, being an important design parameter of the heat exchangers. The air handling needs to be equipped with a humidity control system, to allow performance tests of the heat storage system at well controlled water vapour pressures.

The process flow diagram is shown in Figure 4-5. Key components are 4 heat exchangers (designated with E), 2 reactors (R) filled with zeolite, heating and cooling devices (X), and a fan (B). Zeolite temperatures, air temperature, air and liquid flow rates, air humidity, air pressure and pressure drop, are measured at various locations in the system.

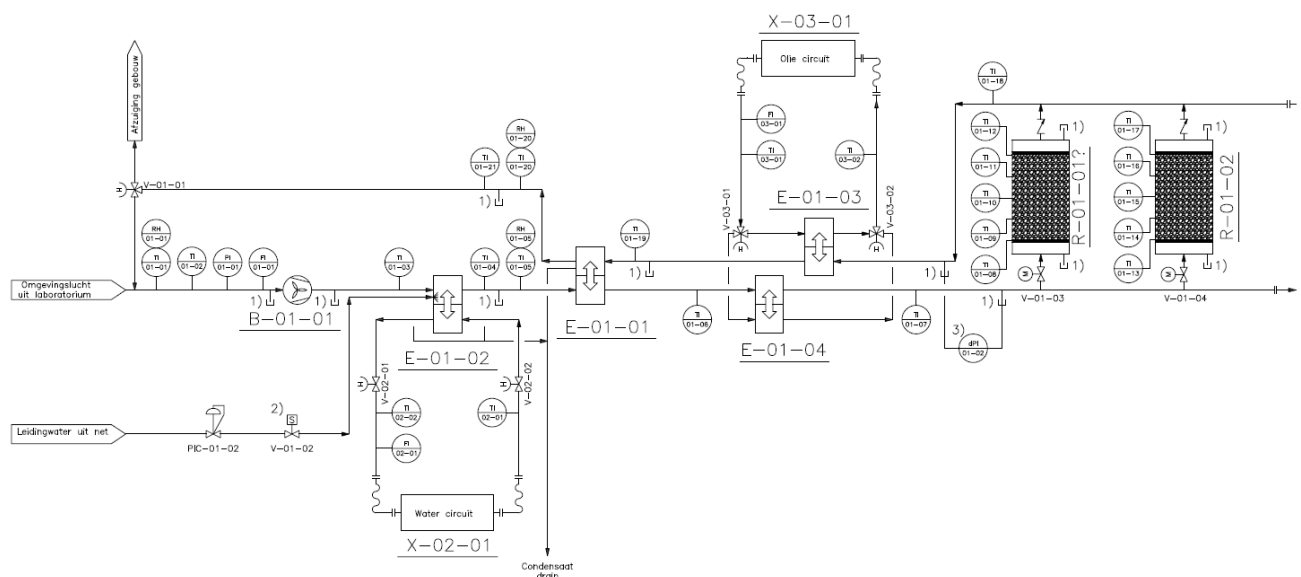


Figure 4-5: *Process and Instrumentation Diagram (P&ID) for the open sorption storage test system.*

Key components to obtain good overall thermal efficiency of the sorption system are the air-to-air heat recovery unit (E-01-01) as well as the thermal insulating material used in the construction.

### System design

On the basis of the P&ID, all components were specified and purchased or custom built in the workshop at ECN. The prototype system was designed with the aim to reach a compact unit. All air heat exchange operations were placed together in the air handling part of the system, (right part in Figure 4-6) the zeolite storage reactors were put together in the second part (left side of Figure 4-6). The air channels were constructed from 100 mm thick thermal insulating material, with the aim to reach low thermal leakages.

The two storage reactors can be operated separately by opening and closing the valve in the bottom section of each reactor.

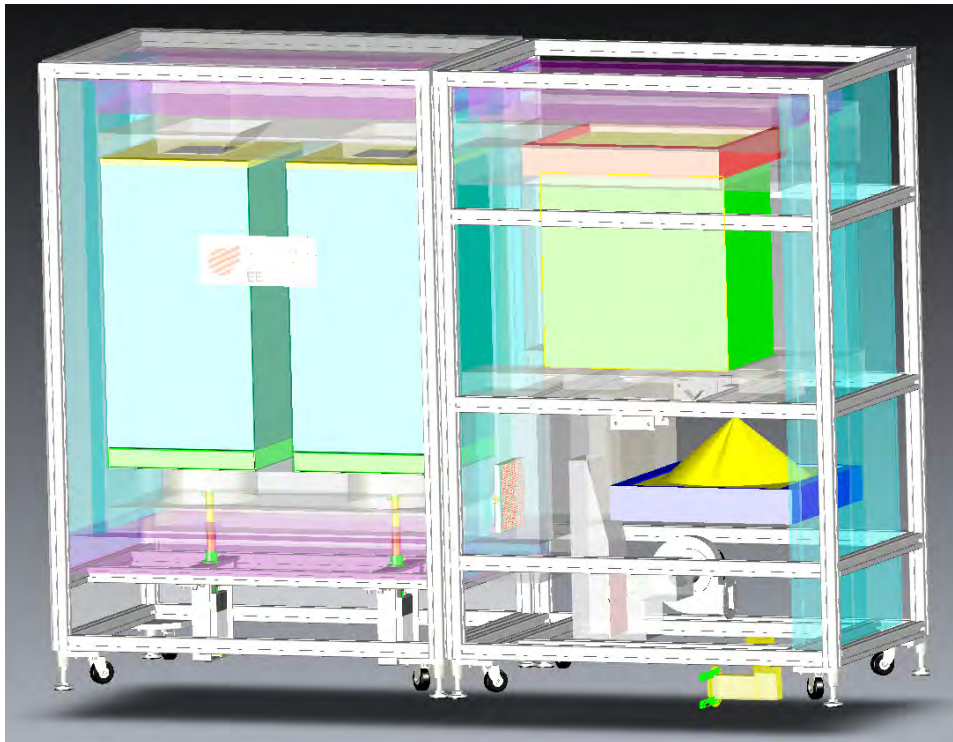


Figure 4-6: design drawing of the zeolite heat storage system: left part are the storage reactors, right part is the air handling unit

### Measurement and control

All measurement devices of the test rig are connected to an automated data acquisition system. A graphical user interface (Figure 4-7) is used to enable the control of the system and to monitor its actual status.

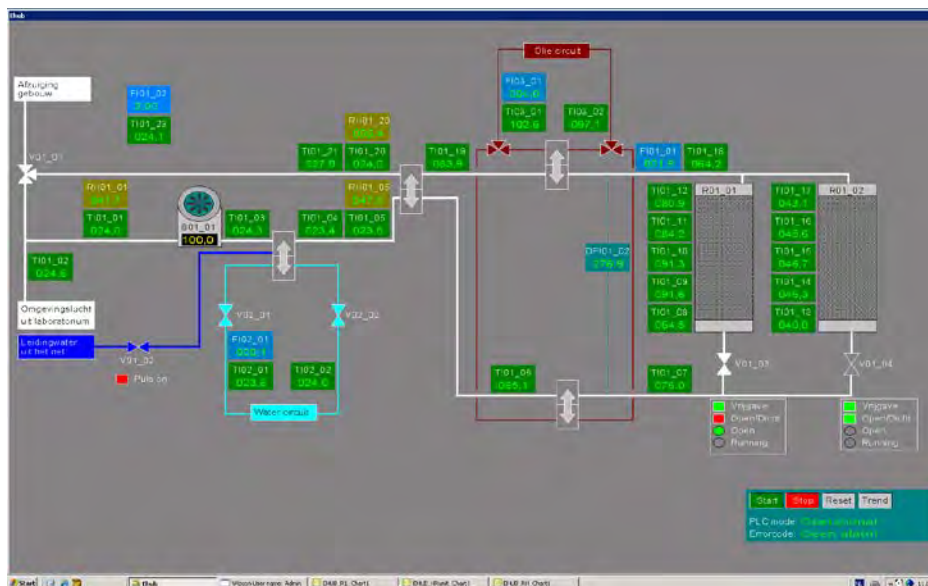


Figure 4-7 Graphical User Interface for control and monitoring of the heat storage system

Measurement devices consist of PT-100 temperature sensors, flow measurement devices for water and oil, air velocity sensors and air humidity sensors, and air pressure measurement devices. The heat input to the system for charging is delivered by a thermostatic bath as external heat source using oil as heat transfer fluid. A second thermostatic bath is applied to provide temperature control in the humidification section of the air flow. The thermostatic baths also have a cooling modus in order to be used during discharge of the system.



### Construction

The assembly of the components of the heat storage system was done in ECN's workshop. The pictures below (Figure 4-8) give an impression of the construction stages. Figure 4-9 shows the prototype in its final state installed in the laboratory.



Figure 4-8 pictures of the prototype under construction in the workshop. The upper pictures show the zeolite storage reactors under construction, the pictures below show the air handling unit.



Figure 4-9 the heat storage prototype in its final state installed in the laboratory.

Key characteristics of the storage system are:

Property	value
Storage container volume, dimensions	112dm <sup>3</sup> , 70x40x40 cm (h x w x d)
Number of storage containers	2
Sorption material	Zeolite 13X binderless, Chemiewerk Bad Koestritz,
Shape	beads of 2.5-3.5 mm
Weight	150 kg (total, 2 containers)
Air flow rate	Max 80 m <sup>3</sup> /hr
Maximum heat input:	200°C, 2 kW



### 4.3. Numerical models

The mathematical description of a sorption heat storage system has a dynamic character. A heat storage system often has changing conditions and does not have a 'steady state' operation mode. Within ECN a generic sorption system model was developed. This generic model is programmed in Matlab and is used as starting point for the development of the sorption heat storage system simulation model. The model allows us to simulate the behaviour of solid sorption reactors and heat exchangers.

#### Sorbent reactor model

For the calculation of the sorbent reactor, it uses three calculation layers that are connected in a 2 dimensional grid, schematically shown here below, figure 4-10. The first layer represents the flowing humid air through the bed. The second layer represents the sorbent material, zeolite 13X, and the third layer represents the thermal insulation. The flowing air has an extra top row in the grid to describe the initial conditions for the air entering the zeolite bed.

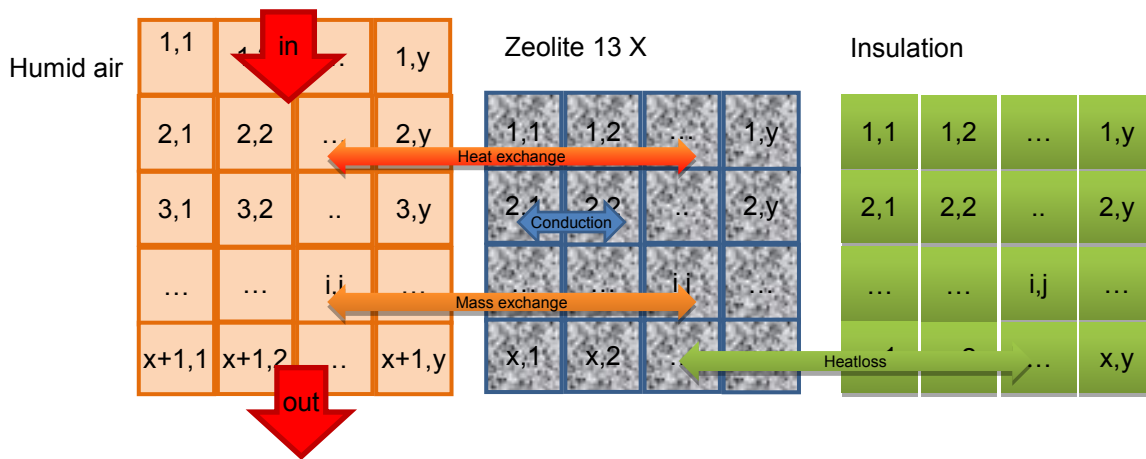


Figure 4-10 Graphical representation of the calculation grid and the heat and mass transfer processes of the sorbent reactor.

The heat transfer between the air and the solid sorbent bed is defined as:

$$P_{UA,i,j} = HT\ rate / dx (T_{sorb,i,j} - T_{air,i,j}) \quad \text{Equation 4-1}$$

The heat fluxes in the sorbent bed occur in horizontal direction by means of conduction.

$$P_{UA,i,j \rightarrow j+1} = k / dx (T_{sorb,i,j+1} - T_{sorb,i,j}) \quad \text{Equation 4-2}$$

In vertical direction the heat flux takes place by convection of the air flow:

$$P_{heatflow,air,t} = ms_{tert} (h_{air,in,t} - h_{air,out,t}) \quad \text{Equation 4-3}$$

In which  $h$  is the enthalpy of humid air.

Heat loss occurs as a result of a temperature difference between the sorbent bed and the insulating material and by temperature difference between the insulation material and the surroundings.

The mass transfer of the water vapour (the sorbate) takes place between the stationary zeolite bed and the flowing humid air. The driving force for mass transfer of the water vapour between the zeolite and the air is the difference in equilibrium water vapour pressure of the zeolite and the water vapour

pressure of the air. The amount of water vapour transport inside a segment is calculated by the local pressure difference multiplied by a transport constant and the sorbent constant mass within a segment ( $\text{kg}_{\text{sorbate}}/\text{kg}_{\text{sorbent}} \cdot \text{s} / \text{Pa} = \text{s} / \text{Pa}$ )

The sorption equilibrium properties for the zeolite 13X-  $\text{H}_2\text{O}$  system are taken from [29]:

$$p_{eq} = p_0 e^{\left(\frac{A-B}{T}\right)} \text{ with } A = a_0 + a_1w + a_2w^2 + a_3w^3 \text{ and } B = b_0 + b_1w + b_2w^2 + b_3w^3 \quad \text{Equation 4-4}$$

And depicted in Figure 4-11

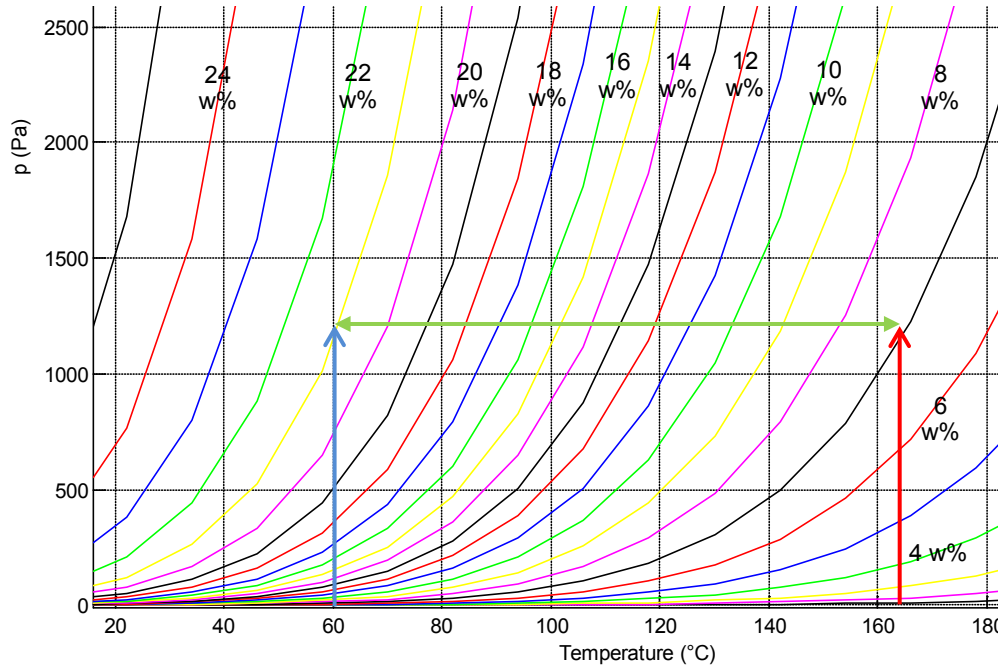


Figure 4-11 *Isosteric chart for Zeolite 13X -  $\text{H}_2\text{O}$ . The arrows within the plot show the water loading of 21 w% at a temperature of 60°C and a partial vapour pressure of 1200 Pa till 7.5 w% for a regenerating temperature of 165°C. w% indicates the amount of water (grams) adsorbed by the weight of zeolite*

The sorption enthalpy per unit mass of sorbate follows from:

$$dH = \frac{b_0 + b_1w + b_2w^2 + b_3w^3}{R} \quad \text{Equation 4-5}$$

The total heat of sorption follows from the product of the sorbate mass and the sorption enthalpy.

The partial vapour pressure for water is taken from [30]:

$$p_w = p_{ws}RH \quad \text{Equation 4-6}$$

Where the saturation pressure of water vapour equals (Temperature range from 0 - 200°C): [30]

$$\ln(p_{ws}) = \frac{c_8}{T} + c_9 + c_{10}T + c_{11}T^2 + c_{12}T^3 + c_{13}\ln(T) \quad \text{Equation 4-7}$$

And depicted in Figure 4-12

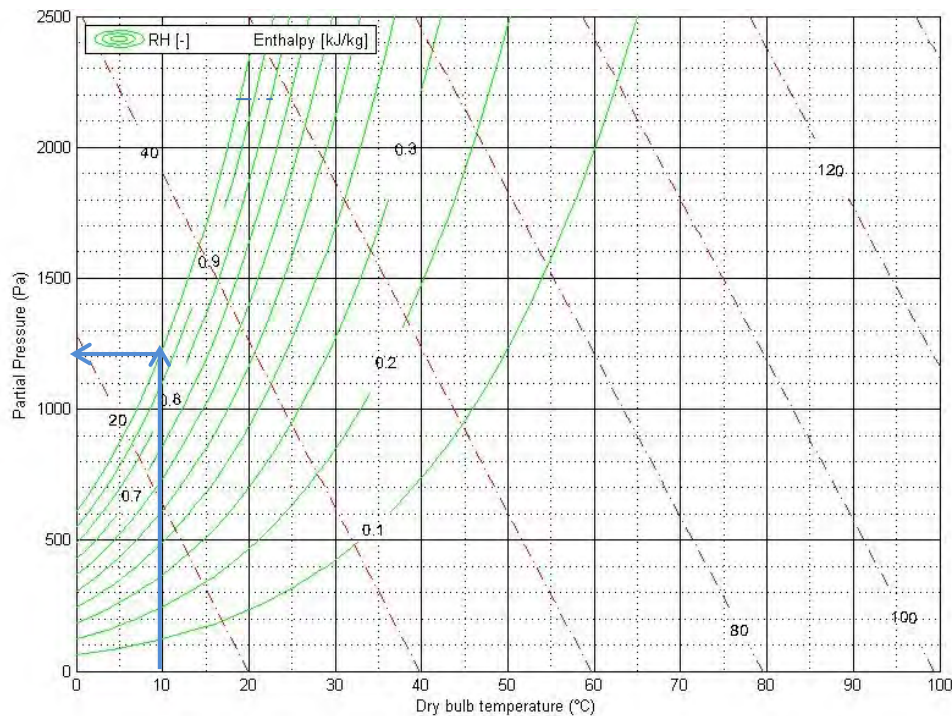


Figure 4-12 Mollier diagram for humid air. Completely humidified (saturated) air of 10°C has a water vapour pressure of 1200 Pa (blue arrows).

In each timestep, a new temperature for the sorbent, the air and the insulating layer is being calculated, based on the energy balance. The mass balance is used to calculate the distribution of the water vapour between the air and the sorbent. The model uses a variable timestep. Stability criteria (boundaries) are defined and the timestep is automatically enlarged as long as the results remain within the boundaries and the maximum timestep has not yet been reached. When the calculation becomes unstable the timestep is reduced again. This allows to have overall shorter calculation times.

## Heat exchanger model

Besides the zeolite sorption reactors the prototype has heat exchangers for water-to-air for air-to-air and two oil-to-air heat exchangers. The cross flow heat exchangers are calculated in a primary and secondary grid, for the primary and secondary fluid. The calculation of the heat exchange performance is comparable to the reactor calculation, but doesn't include any mass transfer between the fluids.

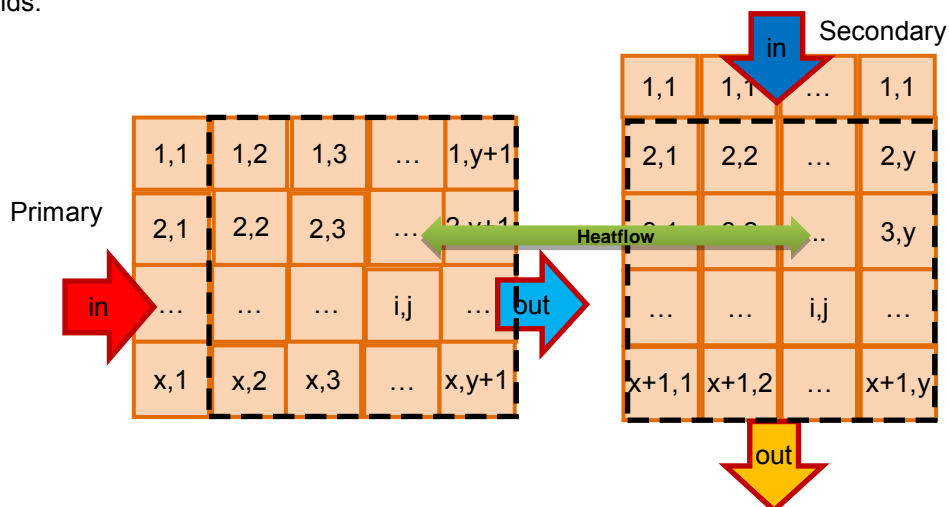


Figure 4-13 Graphical representation of the dynamic heat exchanger performance calculation.

#### 4.4. Experiments and results

The TCS prototype system was installed in the lab (August 2013) and connected to the thermostatic baths and PLC controller to provide temperature and humidity control of the air in the system and to provide heat input and output to the system.

Functional checks of the separate components in the system were performed followed by first exploratory measurement of charging and discharging of the system.

An important observation in the first measurement was the leakage of air from inside to outside of the system as well as some internal air leakages (shortcuts) between air inlet channels and outlet channels of the system. A large effort had to be made to locate the air leakage spots and to make the necessary repairs to reduce the amount of leakage. Air leakages obstruct the correct measurement of the heat and mass balances on the system.

The air tightness of the system was sufficiently improved in several steps to carry out basic performance measurements.

#### TCS performance measurements

Figure 4-14 shows a scheme of the air flow directions (indicated by the arrows) through the system and the locations of the measurement devices.

The zeolite storages both have 5 temperature sensors at different heights of the bed. Airflow velocity, temperatures and relative humidity are measured at several points inside the air channels. The thermal powers transferred by the heat exchangers are determined both at the primary and at the secondary side of the exchanger. The water uptake by the zeolite cannot be measured directly. It is calculated based on the zeolite temperature, the actual water vapour pressure, and the known sorption equilibrium properties.

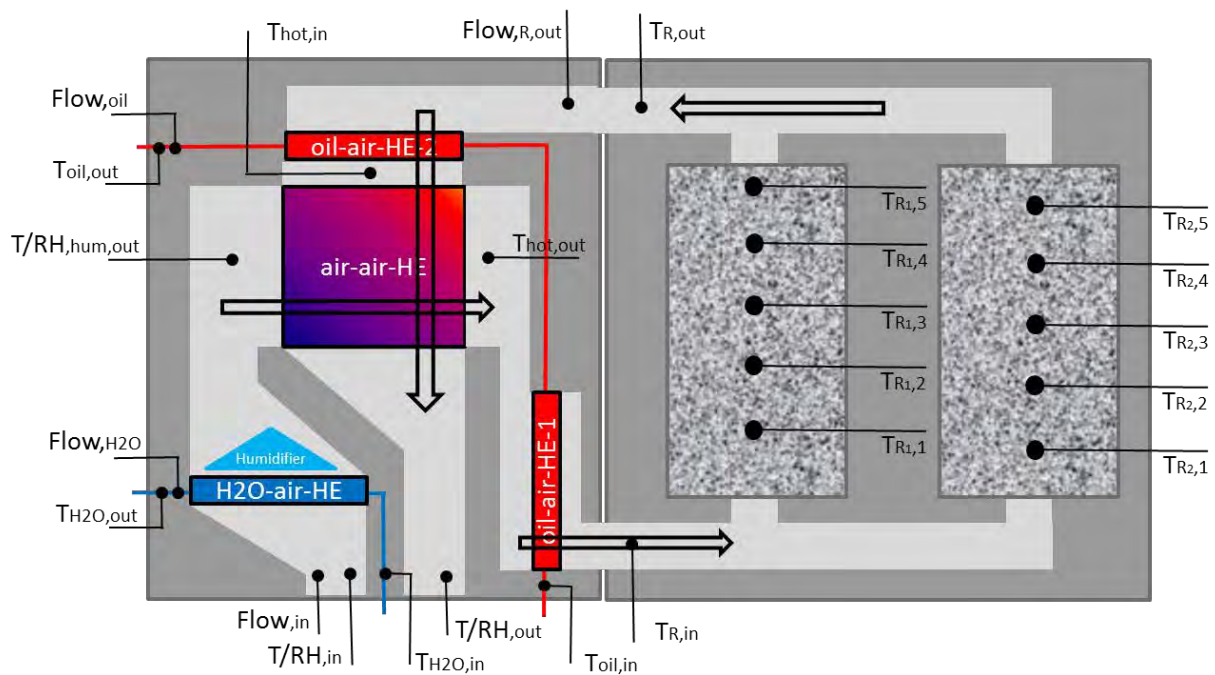


Figure 4-14 Overview of the air flow directions through the TCS prototype system and the various measurements devices and their locations within the storage prototype system.

The zeolite storage reactors were discharged by prolonged contact with ambient air before the first charge-discharge cycle measurement. The adsorption of humidity from the air continued until an equilibrium was reached at room temperature and the zeolite then holds about 24 w% of water.

The temperature program for a charge-discharge cycle for reactor 1 and 2 is schematically shown in Figure 4-15. The TCS system is charged during 4 days (2 days per reactor). Charging occurs by heating the inlet air to the reactors to 180°C, using the oil-air HE-1. The reactors are then allowed to cool down over 5 days to reach ambient temperatures. To discharge the heat storage, the air flow to the zeolite bed is humidified to 12 mbar of water vapour. This water vapour pressure is derived from humidification of air at 10°C, representing the use of a borehole as winter heat source. The zeolite adsorbs the water vapour and the heat of adsorption is released. The zeolite and the air flow heat up and the hot air leaving the zeolite bed can transfer its excess heat to the oil-air HE-2 in the system. The air flow applied during all measurements was kept at 80 m<sup>3</sup>/hr.

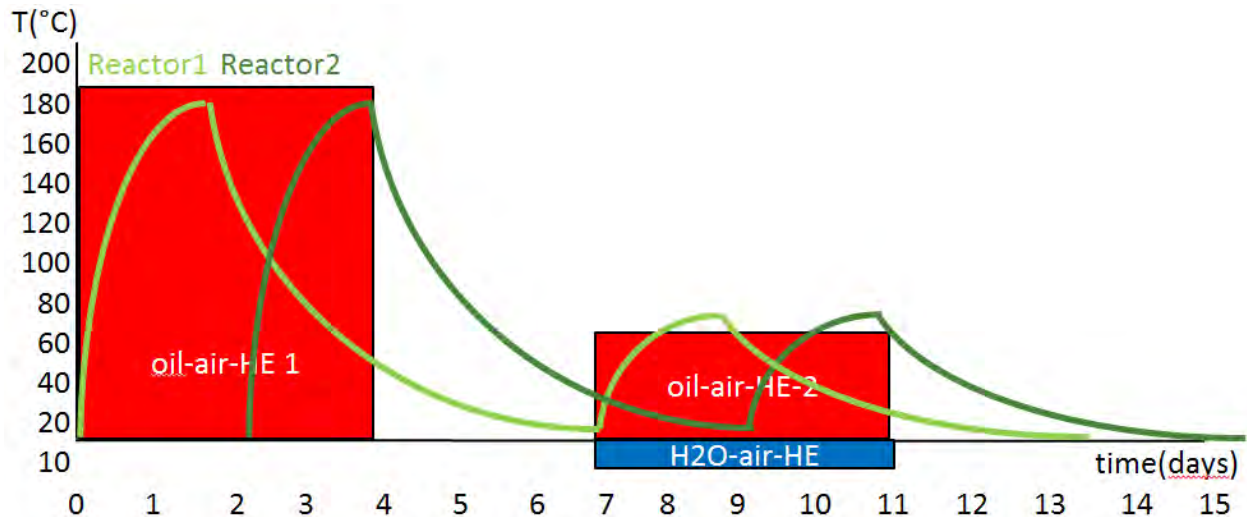


Figure 4-15 Simplified temperature profiles for the zeolite reactors during the charge and discharge measurement. The green lines indicate the evolution of the reactor temperatures.

#### Charging of the zeolite reactor

The temperature change in the zeolite reactor during the charging phase is shown in Figure 4-16.

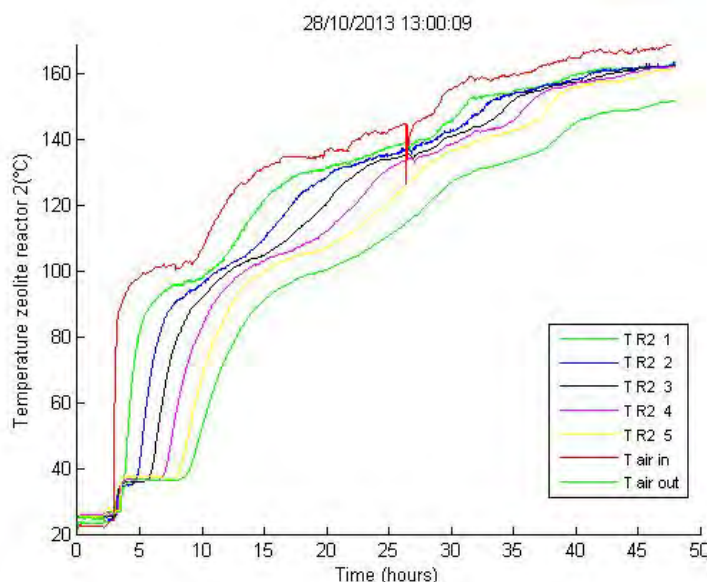


Figure 4-16 Temperature over time of the air and the zeolite bed of reactor 2 during charge process

The temperature of the zeolite follows the air supply temperature (brown top line in the figure above) with a delay. The temperature in the bed rises from bottom to top and follows the air supply direction. The temperature gradient in the bed can be seen as a moving reaction zone of desorption. The



stepwise increase of the air supply temperature is caused by the thermal power limitations in the oil to air heat exchanger. It takes about two days to fully charge a single reactor.

The thermal powers transferred during the charge process are shown in Figure 4-17. The total power supplied to the reactor by the air flow is on average around 800 W (purple line). Part of the energy is used to desorb the water from the zeolite (sorption heat, green line) and another part is used to increase the temperature of the zeolite (sensible heat, black line). During the first 15 hours of charging these sources of heat form the larger fractions. After 15 hours the system reaches average temperatures of more than 100°C and the contribution of heat losses to ambient are becoming predominant (blue line).

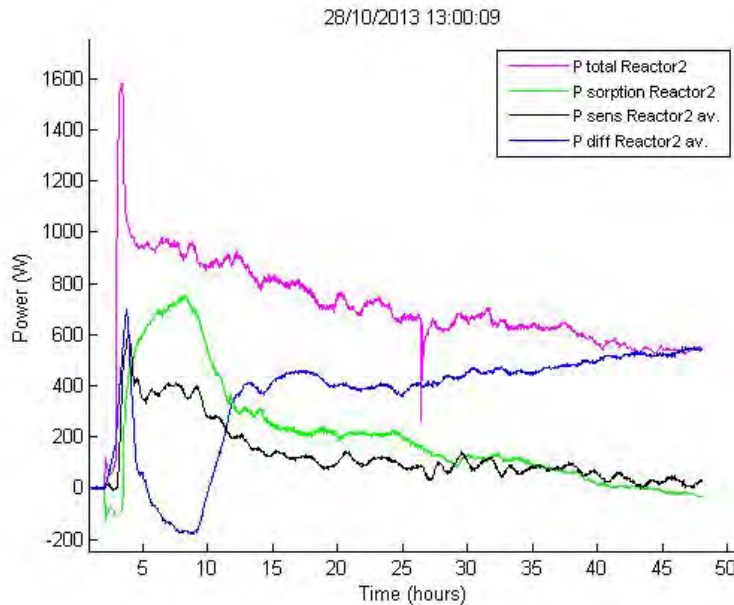


Figure 4-17 Thermal power transferred during charging of zeolite reactor 2

The heat storage capacity derived from the measurements as function of the charging temperature is shown in Figure 4-18. The storage capacity is derived from multiplying the thermal powers for sensible heat and sorption heat by the time.

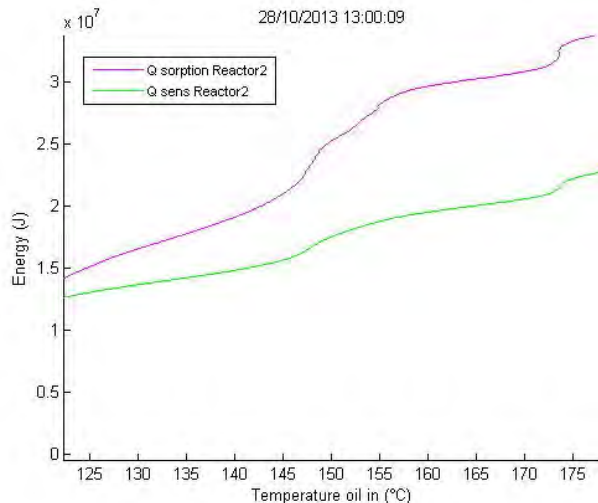


Figure 4-18 Storage capacity of zeolite reactor 2 as a function of the charging temperature

The storage capacity increases with temperature because both desorption and temperature rise contribute to it. The ratio of sorption heat over sensible heat increases with increasing temperature to 3:2 at 170°C.

The storage capacity for sorption heat is around 35 MJ for a single reactor. It also holds up to 20 MJ of sensible heat when heated to 175°C. The sensible heat as well as sorption heat can be recovered. The sensible heat was lost on purpose in the test program in order to proof that the sorption heat can be recovered after fully cooling down the zeolite to ambient temperature. For short term storage the recovery of the sensible heat is possible and this will improve the storage efficiency.

### Discharging of the zeolite reactor

Figure 4-19 below shows the change of temperature of the air and the zeolite bed during the discharge phase.

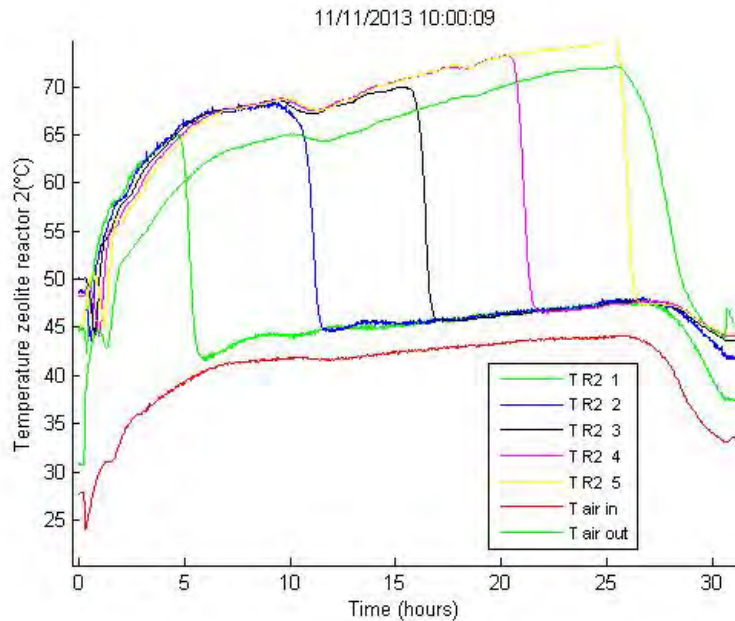


Figure 4-19 *Temperature over time of the air and the zeolite bed of reactor 2 during the discharge process*

When cool and humidified air (12 mbar water vapour pressure) is blown through the dried zeolite reactor the water is adsorbed. The air-to-air heat recovery unit makes the inlet air to the bed rise slowly to 40°C. The heat of sorption is released and over time the zeolite and the air both increase in temperature up to 70°C. After 25 hours of discharge the zeolite has reached its equilibrium sorption capacity and heat release stops rapidly. It is clearly seen from the steep temperature front through the bed (figure above), that the adsorption process shows a distinct reaction zone inside the bed that gradually shifts from bottom to the top.



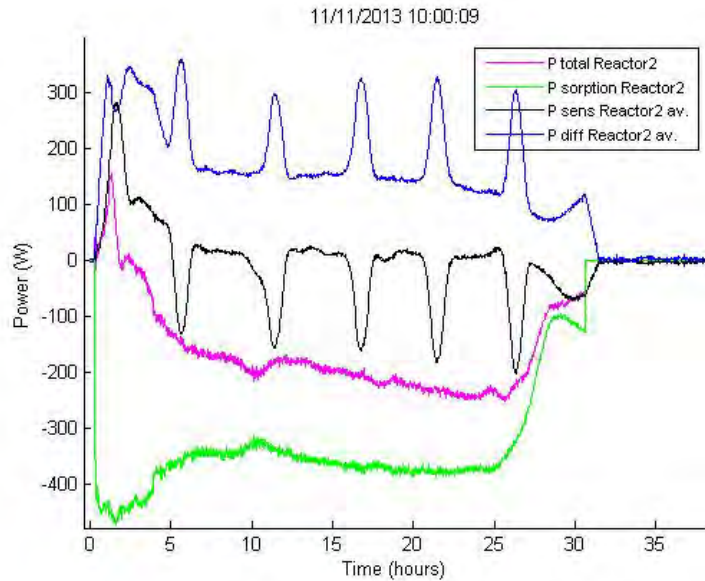


Figure 4-20 Thermal power transferred during discharging of zeolite reactor 2

The thermal powers obtained in the discharge process are shown in Figure 4-20. The maximum power of adsorption is just above 400 W and remains fairly constant over the discharge period (green line). The net power transferred to the air (purple line) is initially much lower because almost all of the sorption heat is used as sensible heat for increasing the zeolite bed temperature. After 5 hours the net power transferred to the air stabilizes around 200 W for 20 hours.

The spikes in the calculated thermal power for sensible heat (black line) are artefacts due to the coarse (5 segments) discretization of the temperature measurement of the zeolite reactor. When the temperature of one segment suddenly changes it is assumed that this is true for the whole segment of 20 cm bed height. The calculated heat losses (Pdiff, blue line) are resulting from the power balance and also show these spikes.

#### Thermal storage efficiency analysis

The storage cycle efficiency for reactor 2 was analysed based on the measurement described in the foregoing sections. The result is shown below in Figure 4-21.

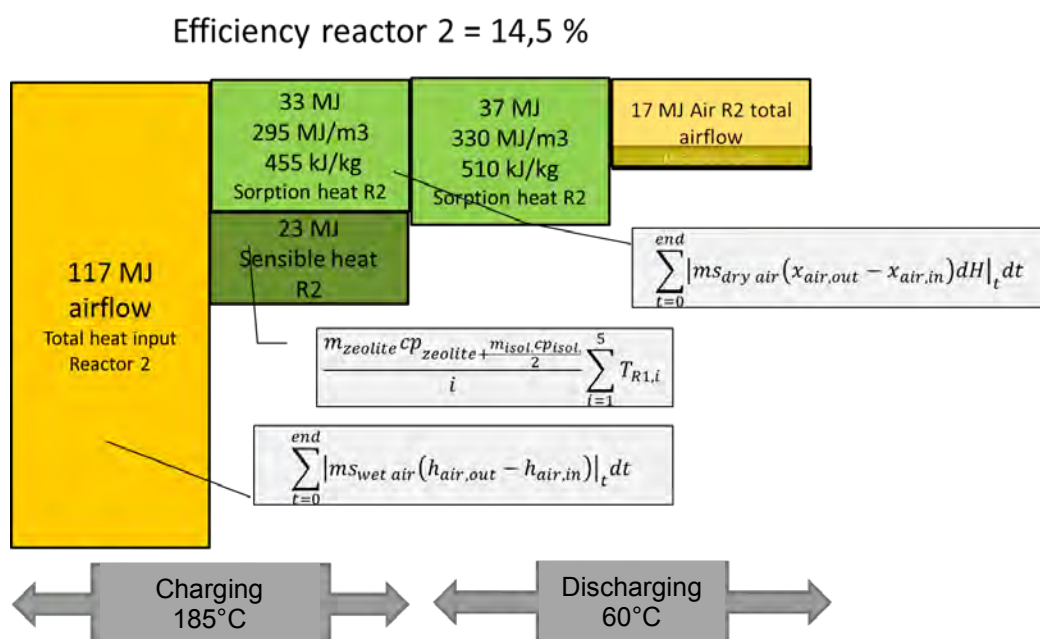


Figure 4-21 Calculated overall storage cycle efficiency for reactor 2.

Figure 4-21 shows the change in energy content from left to right. Left is the amount of heat supplied by the hot airflow to the reactor. The next bar shows the amount of heat that is stored in the zeolite, both sorption heat and sensible heat. In the discharge mode only the sorption heat is regained, and of this amount, a part is being transferred to the air flow passing through the bed.

The net result of the storage thermal efficiency is only 15% for the current measurement. The loss factors included in the analysis are thermal losses due to convection and due to air leakages. Especially in the charging phase these losses are significant due to the high temperatures of 180°C applied during that stage. Further improvement of the thermal insulation and air tightness of the system will certainly improve the overall efficiency. Another factor is the duration of the charging, because in the end stage of the charging the heat losses are much larger than the amount of heat energy stored in the reactor. Better timing of the process can further improve the efficiency.

The difference between the sorption heat in the charge phase (33 MJ) and the sorption heat in discharge (37 MJ) is caused by the difference between the initial state of the zeolite and the final state. In the final state it has adsorbed more water vapour than it had at the start of the charging stage.

Another aspect of efficiency holds for the sensible heat that is charged to the system and is completely lost later on, when the system has cooled to ambient temperature. In the case of zeolite the ratio of sensible heat over sorption heat is less favourable than for salt hydrates. But in all cases, an improvement can be obtained when also the sensible part can be kept in the storage and be used during discharge.

In a fully optimised system without air leakages and without convective heat losses during the charging and discharging, only the sensible heat loss of the zeolite itself should be taken into account as a loss factor in long term storage. For this situation an efficiency of 60% could be obtained.

#### **Auxiliary electric power consumption**

The overall energy balance of the open sorption storage concept includes also the use of auxiliary electric power for the forced airflow through the heat exchangers and the sorbent reactors. In the design of the system attention was paid to use low air flow velocities have low overall low air pressure drop. The electric power needed for the fan to circulate the air through the air handling system and the zeolite beds was 50 W.

From energetic design considerations of a heat storage system, the ratio of thermal power over electric power should be around 20 (auxiliary electric power / thermal power < 5%). This means that with a 50W fan the thermal power should reach an average of 1 kW. The current prototype has a thermal to electric ratio of less than 10 during the initial period of charge and discharge and even less than 4 towards the end of the charge process. This thermal to electric ratio needs further improvement and should be carefully addressed in the development of next stage open sorption heat storage systems.

## 4.5. Model validation

This paragraph looks into the comparison of the measurements of the TCS system and model calculations. The measurements performed in the period of 11-18 November 2013 were selected for the comparison. The sequence of discharge-charge conditions for both reactors is shown in Figure 4-22. The measurement starts with the discharge of reactor 2 during 30 hours, followed by the discharge of reactor 1 for 40 hours. Reactor 1 is then first charged again for 50 hours, followed by reactor 2. The model calculations are performed for both reactors. The results for reactor 1 are used in this section.

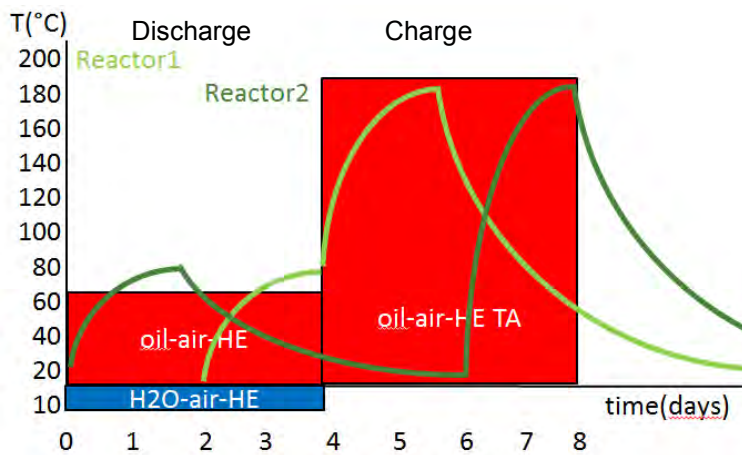


Figure 4-22 Schematic overview of the discharge-charge cycle used in the model validation

The model uses a set of measurement values as input conditions for the simulation: (see Figure 4-14)

- Air flow entering the system: Temperature ( $T_{in}$ ), Relative humidity ( $RH_{in}$ ) and flow rate of the incoming air.
- Temperature of the water inlet to the water to air heat exchanger ( $T_{H_2O,in}$ ).
- Temperature of the oil inlet to the oil to air heat exchanger ( $T_{oil,in}$ ).
- Position of the valves at the bottom of the reactors.

The model takes into account the heat loss that occurs from the reactors to the ambient. The efficiency of the air-to-air heat recovery unit (air-air-HE) is also taken into consideration in the model. The thermal losses occurring in the air-handling part of the system are not included nor the heat losses that occur due to air leakages.

Figure 4-23 shows the comparison between model and experiment of the temperatures inside the reactor. At the start of the discharge, the temperature of the whole bed increases rapidly to a level of 70-80°C. The heat of adsorption released in the lower sections of the bed is distributed through the bed by the air flow. Once the lower zeolite section stops adsorbing, the temperature in that section drops quickly (2), to the level of the temperature of the incoming air. The adsorption of humidity follows a sharp reaction zone. The simulation also shows this effect, but less pronounced (1), due to the discretization of the sorbent reactor in only five segments. The model shows the average of a single reactor segment, whereas the experiment shows the temperature at a single very small thermocouple location.

In the charging part of the analysis, a comparable observation of the temperatures can be made. The simulation shows a more gradual temperature change, compared to the experiment, which is steeper and stepped. The final temperature reached in the experiment is 20°C lower than in the model (3). This is caused by the air leakage in the system.

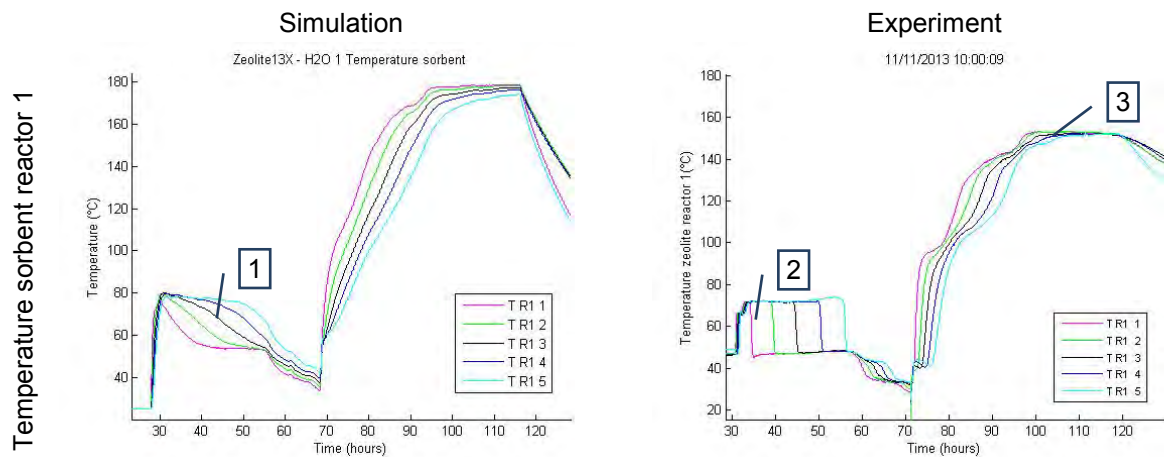


Figure 4-23 Comparison of temperature profile of reactor1 in simulation (left) and experiment (right)

The thermal powers due to the sorption process (sorption power) in the reactor during an experiment are calculated based on the difference in humidity of the air flow entering and exiting the reactor. The amount of water vapour adsorbed or desorbed is multiplied by the enthalpy of sorption. The total thermal power from the reactor is obtained from the difference in enthalpy of the air (temperature and humidity) between inlet and the outlet of the reactor.

Figure 4-24 shows the thermal powers of the sorption process to and from the reactor for the simulation and for the experiment. The simulation shows that the sorption power at the start of the discharge is first used to increase the temperature of the zeolite in the reactor (1) and no net effective thermal power is taken from the reactor. The higher initial temperature of the reactor in the experiment compared to the model makes this effect less pronounced (2). When the reactor has reached its equilibrium temperature, the heat of adsorption (3) is being transferred to the air resulting in a net heat release (4). The sorption heat in the experiment is higher than in the simulation (5), which could be caused by small errors in the humidity measurements.

The thermal powers in charge mode are higher than in discharge mode. The thermal power sent to the reactor is significantly higher than the desorption power. In the regeneration phase when temperatures increase to 180°C the heat loss to ambient becomes larger and this is clearly seen in the model and the experiment (6 and 7). Despite the thermal insulation, still a relevant part of the thermal power sent to the system is lost. The air leakage in the experiment causes an even bigger loss, not included in the model.

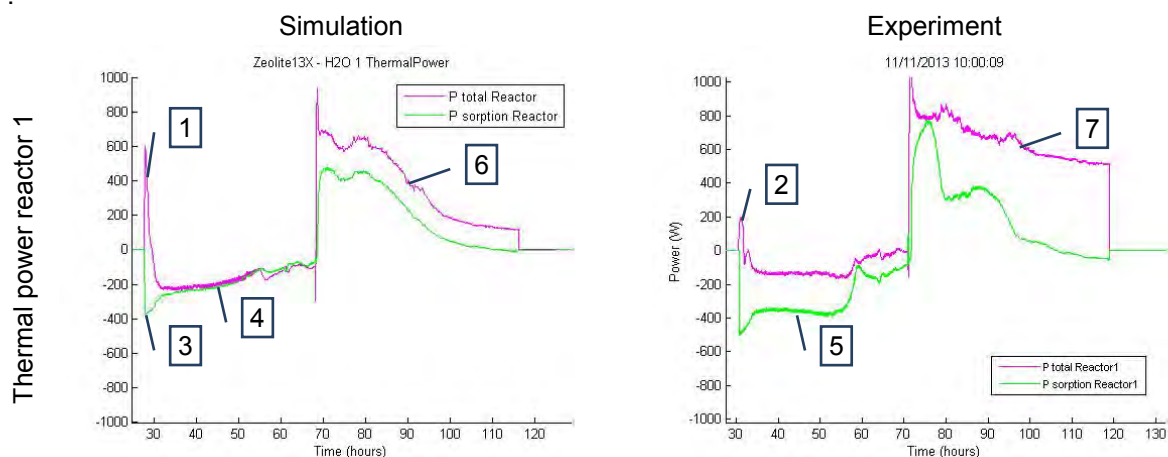


Figure 4-24 Comparison of thermal power levels between simulation and experiment. Purple line: total power, green line sorption power.

The water uptake by the zeolite cannot be measured directly. It is calculated based on the zeolite temperature, the actual water vapour pressure, and the known sorption equilibrium properties.

Starting from the known initial water uptake in the zeolite and applying the water mass balance over the system, the actual overall uptake of the reactor is obtained. The simulation allows to calculate the local water uptake in different segments of the reactor(1). The average water uptake in the simulation (dotted line) corresponds quite well to the experiment (2)

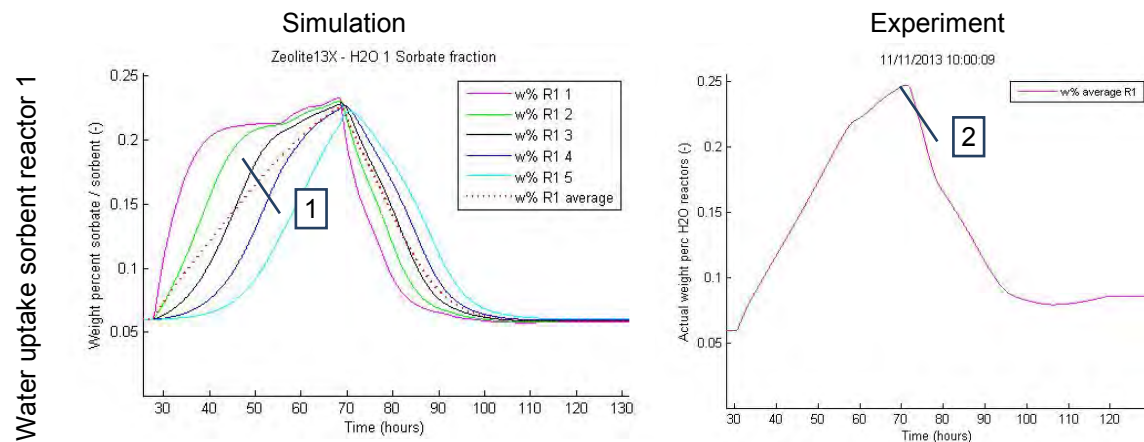


Figure 4-25 comparison of water uptake of the storage reactor during charge and discharge process in simulation and experiment

### Thermal storage efficiency

The energy balance of the storage reactors is also evaluated using the simulation model. A charge and discharge cycle is performed in the simulation, in which in total 66 MJ of heat is stored in the two reactors. To get this amount in the reactors, almost double the amount of heat is needed as input. The high temperatures needed (180°C) to charge the system lead to significant heat losses. This is both heat loss for sensible heat as well as heat loss to the environment by conduction, see Figure 4-26. This last factor will decrease when the system is scaled-up to higher storage capacities. The amount of sorption heat used in the process depends on the initial conditions of the bed and the humidity levels of the air used in the process.

The heat stored as sorption heat is for an amount of 70% being released again to the air in the discharge of the storage system. The heat storage efficiency of the storage reactor obtained in this simulation is 35%. The difference between the two reactors is caused by the difference in charging-discharging conditions. Especially the duration of charging and discharging influences the overall efficiency. The overall system efficiency will be lower due to some additional losses in the heat recovery unit and the other heat exchangers.

The thermal storage efficiency in the experiments was analysed (see also Figure 4-21) for several full charge-discharge cycles. The efficiency of a storage reactor was found to be around 15%, much lower than in the model. The main cause for the lower efficiency is the leakage of hot air from the system, predominantly in the charging phase.



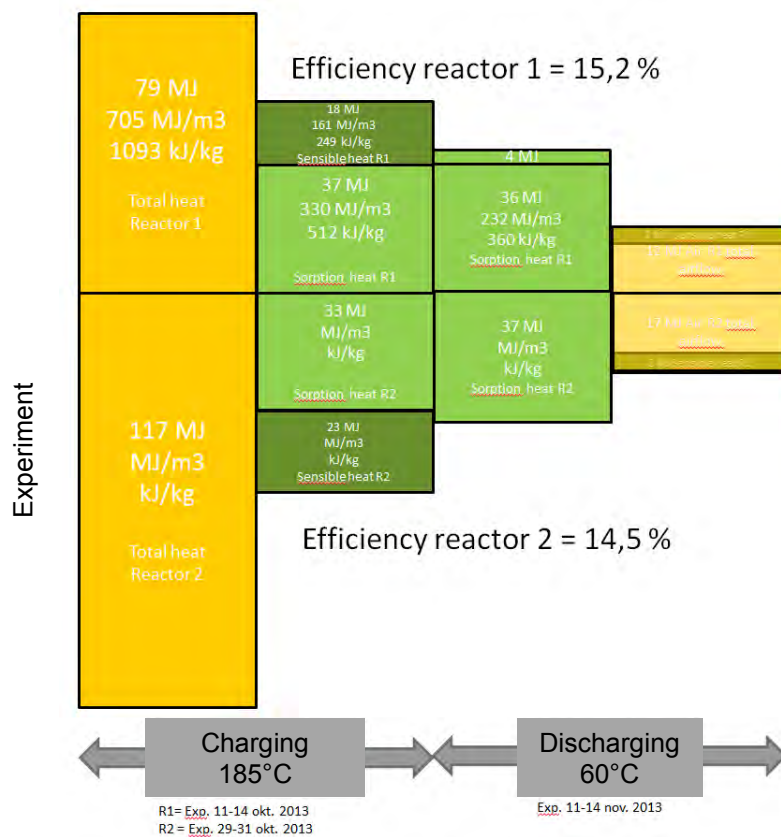
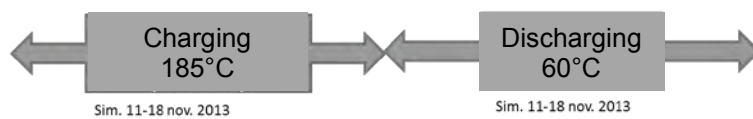
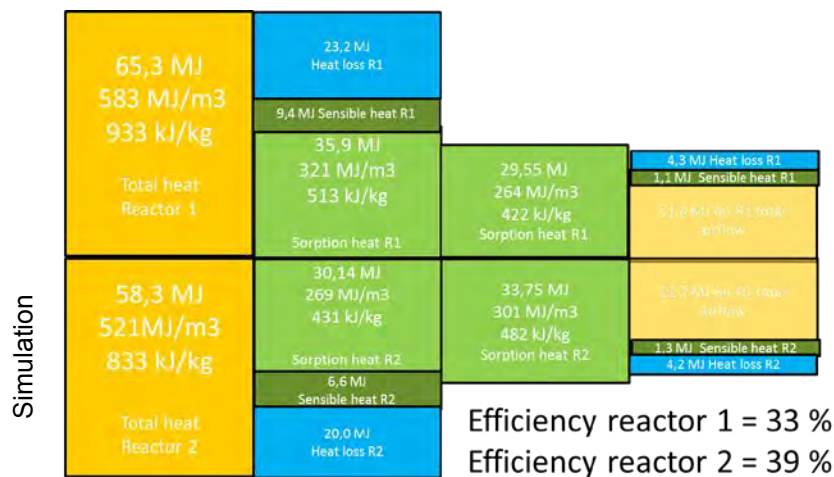


Figure 4-26 Analysis of the energy balance of the storage reactors by simulation and experimental

## 4.6. Discussion and conclusions

The development, test and analysis of the results of the open sorption TCS prototype have provided valuable knowledge on the operational characteristics of the heat storage concept.

The test result on the open sorption system concept has shown that it is possible to use this technology for storing heat and use this heat at a later stage. This storage period can be several months, making it suitable for seasonal heat storage of summer excess heat for use in winter periods.

The temperature levels achieved in discharging of the open sorption system are sufficient for domestic hot water supply at 60°C and can also be applied for room heating. Both for the zeolite materials in prototype 2 as for the salt in prototype 1 the outlet temperature of 60°C was reached when ambient air conditioned to 10°C and 12 mbar H<sub>2</sub>O pressure (saturation at 10°C) was used as input for the heat storage system.

Zeolite proved to be a mechanically and chemically stable material under the conditions used for charging at 180°C, and discharging to provide 60°C. MgCl<sub>2</sub>-H<sub>2</sub>O however needs additional R&D efforts on the materials level to increase its chemical stability under the applied conditions for seasonal solar heat storage.

The good stability of the zeolite and its well-known sorption behaviour allowed us to continue with prototype system development. Lessons learned in this development are directly transferable to open sorption heat storage concepts using other sorption materials, such as salt hydrates, that can attain higher heat storage densities and higher system efficiencies.

An attractive aspect of the modular open sorption storage concept is the simplicity of the storage reactor design. It can be a basic vessel or container with an internal structure to assure that the air flow is evenly distributed through the bed of sorbent material and an air valve to control the air flow through the storage module. The modular storage concept allows flexibility in the storage specifications because of the decoupling of the storage capacity and the thermal power requirements. The storage capacity is determined by the size and number of modules, the thermal power is determined by the size of the air handling system.

The drawback of simplified storage reactor design is the higher complexity needed in the heat transfer operations between the air flow and the external heat transfer media. This requires careful design of the heat exchangers, to find a compromise between heat transfer efficiency, air side pressure drop and air velocity, volume and price level of the heat exchangers and the auxiliary power needed for fans and pumps to drive the heat transfer processes.

The thermal cycle efficiency of the current heat storage system was found to be in the range of 15%. So of 100 Joule of heat energy supplied to the system in charge mode, only 15 Joule are recovered in discharge mode. Much of the heat is lost in the charging process where high temperature of 180°C was supplied and losses by conduction and air leakages are high. Optimization of the charging process (timing and temperatures) and necessary improvement in the air tightness will lead to substantial increase of the efficiency. The thermal efficiency limit of the zeolite system in a seasonal heat storage application is limited by the ratio of sensible heat to sorption heat. The amount of sensible heat needed for the zeolite and its direct surrounding structures to reach their maximum temperature on charging will be lost, when the system is left to cool down again to ambient. Therefore the ratio of sensible heat over sorption heat should be minimal, and for this the use of a salt hydrate is favourable over zeolites. The use of a heat recovery procedure when using multiple storage modules, in order to exchange the sensible heat from one module to the next, will further increase the thermal efficiency, but also increase the complexity.

A system simulation model was developed that calculates the dynamic processes within a sorption heat storage reactor. The simulation results showed a good correspondence to the results obtained in the experiments. The changes over time of the temperature levels in the reactor, the thermal power transferred by the air and the water uptake levels calculated by the model resembled well the observations in the experiment. The strongest deviations were found in the overall thermal powers and the storage efficiency. These differences were primarily caused by the air leakage in the experimental setup, which were not taken into consideration in the model.



The open sorption TCS simulation tool can be a valuable product in support of the design of future TCS systems for different applications.

An important aspect regarding the overall energy balance of the open sorption storage concept is the use of auxiliary electric power for the forced airflow through the heat exchangers and the sorbent reactors. In the second prototype, attention was paid to use low air flow velocities in the system and to design for low air pressure drop. Nevertheless the electric power needed for the fan was about 50 W, continuous. From energetic design considerations, the thermal power should reach about 20 times the electric power, (auxiliary electric power / thermal power < 5%) (1 kW) otherwise the benefits of a heat storage system become minimised in comparison to a state of the art electric heat pump system. The current prototype has a thermal to electric ratio of less than 10 during the initial period of charge and discharge and even less than 4 towards the end of the charge process. So further improvement is required in this area.

#### Open sorption storage as part of an E-hub

When considering an open sorption TCS system as a thermal storage component within the E-hub concept, it is important to consider its dynamic behaviour. From the current prototype, fairly slow dynamics are found for the storage system. This is caused by the relatively low thermal power that can be exchanged with the air. To achieve faster dynamics of charging and discharging, so shorter periods of peak charging and peak discharging, the air handling unit needs to be enlarged. No intrinsic limitation in the thermal power transfer is present in the zeolite system itself, only the speed at which hot air is passed through the bed or moist air is supplied to the bed. In designing an E-hub concept that includes an open sorption TCS, information on the charging and discharging thermal powers and on the anticipated storage capacity need to be known, in order for the TCS system to be designed accordingly. Combinations of TCS storage with sensible heat storage will allow to deal with the different dynamics of short term and seasonal heat storage.

Switching rapidly between charge and discharge at first deploys the sensible heat stored in the TCS system. To be effective as a long term heat storage system, the sorption part needs to be used as much as possible, otherwise a more basic sensible heat storage can be applied. The open sorption TCS system concept using modular storage containers provides a flexible solution when more frequent switching between charging and discharging occurs. Instead of using the whole bulk of storage material to a very limited amount, in a modular system only a small part of the bulk is used to its full potential, leaving the rest of the storage material unchanged.

#### **In conclusion**

The test results on the prototype of the open sorption TCS technology have shown that it provides a solution for long term thermal energy storage. It can provide thermal energy at temperature levels useful in the domestic applications.

To bring the system to the next stage of development it is required to put R&D effort in

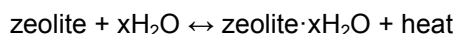
- Obtaining stable sorption materials with higher energy storage density
- Improving the system thermal storage efficiency, by improving air tightness and reducing thermal losses
- Increasing the ratio of thermal power over auxiliary electric power

The open sorption TCS system concept, based on modular storage containers and a separate air handling unit has the flexibility to match the TCS system design to the local long term heat storage requirements: storage capacity, charge-discharge powers and timing. Sizing of the individual storage modules, the number of modules to be applied, and the sizing of the thermal power in the air handling unit gives this flexibility. The TCS simulation model gives a good prediction of the current system performance and can be a useful tool for analysis of improvement options and for the future design of open sorption heat storage systems for different applications.

## 5. ThermoChemical heat storage using closed sorption

### 5.1. Introduction

Thermochemical heat storage is a promising technology to solve the mismatch between seasonal heat supply and demand as a typical problem for temperate climate zones, and storing the energy is based on reversible thermochemical reactions such as:



where  $x$  denotes the number of water molecules absorbed and the water is generally in the form of water vapour.

Heat can be stored in thermochemical materials (TCM's) for prolonged periods without heat losses. In addition TCMs allow much higher energy densities, for instance up to 3.2 GJ/m<sup>3</sup> using Na<sub>2</sub>S, which can lead to more compact systems.

For long term storage especially the solid-gas based reactions are interesting because of their high thermal storage density. Such reactions release heat by ad-/absorption which can be used as input for space heating (SH) and domestic hot water (DHW) applications. The TCS system can be charged by desorption using excess solar energy. Usually, water is used as a sorbate. Because of negligible heat losses during prolonged storage, thermochemical systems have a significant advantage over existing long term thermal energy storage (TES) technologies such as sensible heat storage in aquifer (ATES), boreholes (BTES), caverns (CTES), pits and water tanks or latent heat storage (LHTES) using phase change materials (PCM).

On the other hand, TCS systems also have to sufficiently fulfil heat transfer characteristics in terms of heating power and temperature lift for space heating and/or domestic hot water applications. In this chapter we will show the results of a 3 kWh thermochemical heat storage system based on a closed sorption system that has been optimized with respect to the previous bench-scale set-up to reach higher temperature differences and a higher storage capacity.

### Approach and overview

Over the past years, TNO has concentrated on vacuum-operated thermochemical storage systems. These systems use water vapour only as the reactant gas, as opposed to open (atmospheric) systems that use moist air. While the latter have the advantage of being more suited for practical use without heavy vacuum equipment, the disadvantage of having to provide a forced airflow through the system requiring 'parasitic' electrical energy exists. A closed vacuum system has the advantages of higher power densities and fast charging and discharging of the store, while its obvious disadvantage is that a vacuum has to be maintained.

As has been mentioned above, vacuum solid sorption systems with zeolites are used as test-systems for easy reactor development. Stage 1, the building and testing of a desk-top vacuum zeolite reactor set-up has been conducted before. This system, shown in Figure 5-1, showed fast mass and heat transfer but energy density (~0.25 GJ/m<sup>3</sup>) and temperature level of the water leaving the reactor needed improvement. In the current report, the development and testing of its successor, a 3 kWh vacuum reactor, is discussed, improving significantly on  $\Delta T$  and capacity.

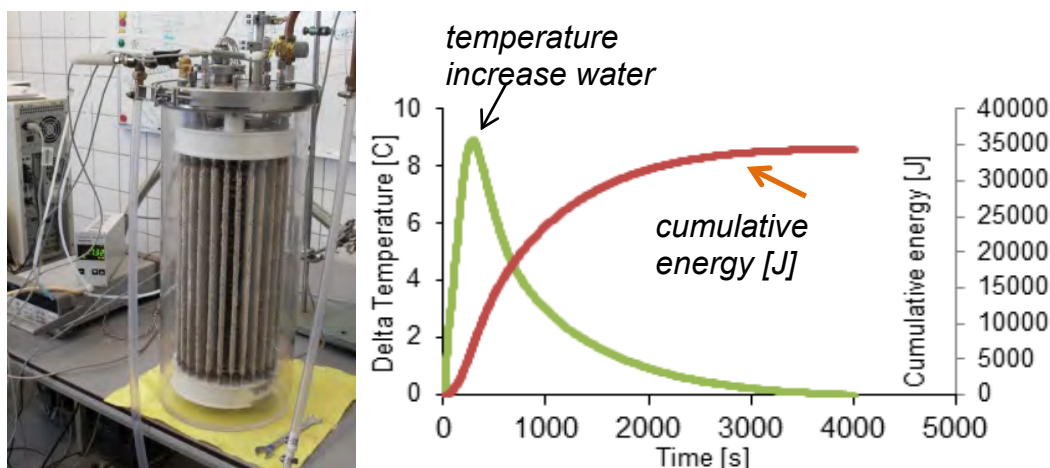


Figure 5-1 Example of a previous version of a vacuum fixed-bed reactor set-up developed at TNO, and some major results.

This novel 3 kWh reactor has a similar setup as the previous reactor, having active material present in the length (height) of the reactor, while the evaporator resides in a separate volume and is connected by tubes. Based on previous experiments, the active material was introduced in the fin-and-tube heat exchangers with glue holding the particles together. The distribution of active material in the heat exchangers differed from former designs, having some bulk-material present while maintaining a high surface to volume ratio. This way, both high in/output power and a large storage density could be obtained.

After introduction of the active material, vacuum pump, valves, sensors for temperature and pressure, as well as water inlet/outlet for both heat exchangers were installed. Measurements were carried out by setting the initial temperatures of the heat exchangers to a fixed value for the particular measurement, application of the vacuum, and then opening the valves for the water admission into the system. Results of the measurements are given in chapter 5.4.

## 5.2. System design and construction

### Specifications

The specifications and additional requirements on the basis of which the 3 kWh reactor was designed and constructed were reported before. A brief summary is given below (Table 5-1 and further). A full summary of the previous design document is given in Annex G.

In the design it is considered that the reactor meet requirements that are similar to those in the built environment. For the design of the storage systems, it is assumed that charging of thermal energy occurs in summer in North Western Europe and that the system is used for space heating during winter. Accordingly, the main constraints are given by

- Solar heat charging by solar collectors, operating at a temperature between 90 and 135°C. Most residential buildings with solar systems make use of non-concentrated, solar thermal liquid collectors such as flat plate or evacuated tube collectors collecting heat for SH and DHW. Typical operating temperature spans for flat plate collectors are about 20-80°C and for evacuated tube collectors at 50-120°C. Stagnation temperatures can reach values up to 200°C;
- Evaporation heat is delivered by a ground water heat source operating at 10°C in winter time;
- Condensation of water vapour during desorption occurs at 30°C (summer);
- The system should deliver heat for space heating (low temperature heating) at a temperature of 40°C. Thermal storage for domestic hot water has not been taken into account.

Below the most relevant requirements have been summarized (Table 5-1). Additional requirements that were deemed important were: as low temperature differences as feasible; normal flow conditions at water side (flow vs. pressure drop); space for pump inside; maximum size of vessel; maximum weight of vessel; 40mm KF flange for measurements and pump connection; water level sensor; temperature sensors.

Table 5-1. *Design specifications used for the 3 kWh reactor set-up.*

Property	Value
Heat storage capacity	3 kWh
Power output reactor	800 W
Temperature evaporator	10 °C
Temperature condenser	30 °C
Water temperature space heating	40 °C
Hydration temperature	45 °C
Source temperature dehydration 1	90 °C
Dehydration temperature 1	85 °C
HX temperature loss	5 °C
Maximum pressure loss liquid water	0.2 bar
Maximum pressure loss in vapour transport	1 mbar
Closed system, vacuum, fixed bed	

### E-hub reactor PID

Below, a brief overview of the TNO E-hub reactor design and construction are given.

The system overall outline is given in Figure 5-2. The reactor can be seen on the bottom left, containing adsorber/desorber heat exchangers and the active material. The condenser/evaporator can be seen on the top right. The whole system is fitted with sensors and valves and connected to a monitoring computer. Reactor and components were placed on a movable unit, fixed within an aluminium frame. An overview of the sensors in the adsorber/desorber unit and in the evaporator/condenser unit is given in Annex G.

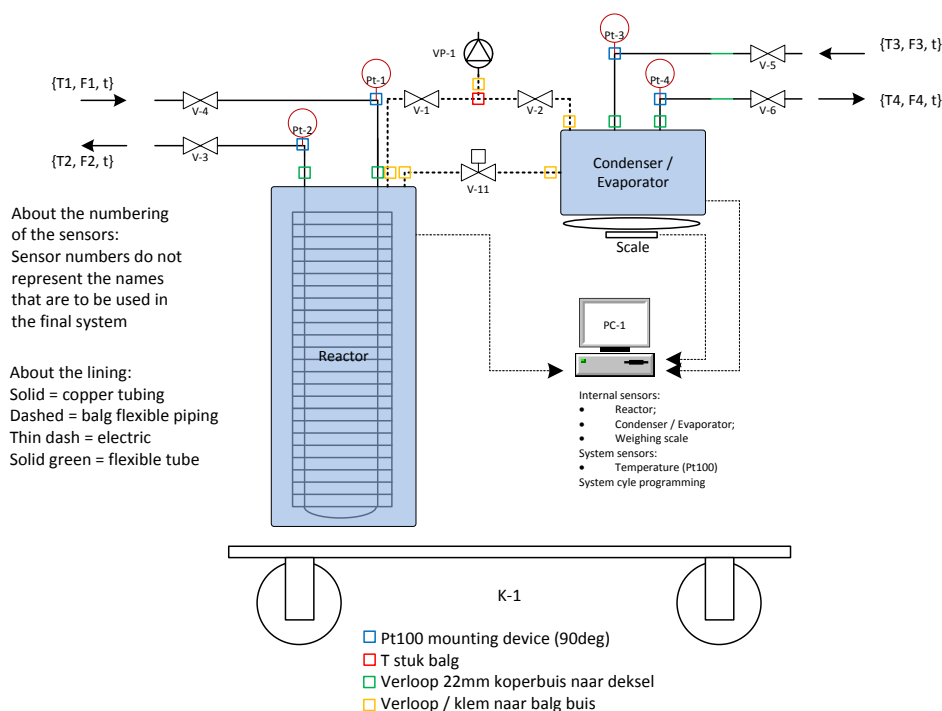


Figure 5-2. E-hub measuring system overall out-line.

As has been described above, a test rig was constructed containing the heat storage module, consisting of one adsorber/desorber unit and one evaporator/condenser unit. As heat sources were chosen a 12 kW electrical heater feeding the desorption process and individual, thermostatic water baths for evaporation, condensation and adsorption.

In order to obtain accurate test results in terms of power and energy content calculations, Pt100 of type IEC 751 class A (variance < 0.1 K between 0°C and 100°C) and electromagnetic flow meters of type Promag H (manufactured by Endress + Hauser) for low flow rates up to 4700 dm<sup>3</sup>/min (including temperature compensation for proper density values) were used in all water circuits. In order to gain insight in heat transfer values and water vapour flow behaviour to and from the adsorber/desorber unit, thermocouples of type T class 1 (variance < 0.5 K between -40°C and 350°C) were placed at the outer surface of the heat exchanger, at the outer surface of the zeolite bed and in the centre of the heat exchanger (centre of zeolite bed).

## Design considerations adsorber/desorber

The sorption pair zeolite 5A – water was chosen for its hydrothermal and mechanical stability as well as safety precautions and minimization of corrosion of heat exchanger components. Calculations, concerning 3 kWh of heat release during hydration, led to a mass of 41 kg zeolite (hydrated) that were needed. Zeolite of type 5A, manufactured by Sigma Aldrich (composition: 0.80 CaO: 0.20 Na<sub>2</sub>O: 1 Al<sub>2</sub>O<sub>3</sub>: 2.0 ± 0.1 SiO<sub>2</sub>: x H<sub>2</sub>O), in the form of spheres (diameter 2 – 3mm) was implemented as a packed bed into finned heat exchangers. Placed in a cylindrical vessel of stainless steel, 8 heat exchanger blocks with sizes of 1000x300x33mm (height x width x depth) were arranged in such a way that the water flow can be heated in parallel by the adsorption process. Further design specifications resulted in a deliverable hydration heating power of 800 W. A graphical representation of the reactor is given in Figure 5-3.



Figure 5-3. Adsorber/desorber finned-plate heat exchangers; (left) 8 adsorber/desorber units containing a total of 41 kg of zeolite spheres during design phase, fitted in a cylindrical vessel; (middle) 8 units during building, before mounting in the vessel; (right) detail.

## Design considerations evaporator/condenser

The evaporator/condenser unit needs to be coupled to a low temperature heat source. The options for this heat source are a ground source, energy roof or dry cooler. In the latter cases these are directly coupled to the outdoor air. When condensing this can be advantageous in winter because the air temperature is generally lower than the ground temperature in moderate climates. In summer the ground is cooler which is of advantage then. For condensing, the requirement is that the source temperature is below that of the environment of the storage location (otherwise the condensate will form on the wall of the vessel). For the evaporator, the situation is the other way around; a higher temperature will allow faster evaporation. Unfortunately, for seasonal storage, this situation is in contradiction with its functional use. Evaporation will occur in winter in order to generate heat, and dehydration of the TCS material will occur in summer. In applications for short term storages the situation is less clear and probably access to both forms of heat source will deliver the highest output. But this will come at a cost. In Dutch climates the ground and air have a yearly average temperature level around 10°C.

The governing factors in the design are actually the allowed temperature differences over the evaporator wall and along the evaporator. Preferably, as small temperature differences as practical feasible are necessary to keep the generated water vapour as close as possible to the input temperature.

For the evaporator principle there are several options: pool boiling, laminar film and capillary action, although the latter can be considered a special form of laminar film. Capillary action is the most interesting option because it avoids the use of a pump to circulate the water in the evaporator. Capillary action depends on the surface geometry in relation to the surface tension. When the geometry is sufficiently small the surface tension of the water will cause it to creep against gravity, creating an all wetted surface. Such desired surface geometry has to be created. In heat pipe technology this is generally created by either using grooved surfaces, open sintered coatings or cladding with gauze. Other options are a cladding with paper or use of thin wires. Tests showed the capillary action to be able to reach 50 cm heights in paper.

The size of the required surface area can be calculated from the required power output. The best option for a compact solution is a series of parallel plates with a header construction.

For evaporation and condensation a single unit was thus developed. It consists of a combination of a copper fin connected on one side to a copper spiral and a capillary working material on the other side (Figure 5-4), so that the heat exchanger can serve both processes, of evaporation and condensation. The unit contains a heat exchange surface of 1.4 m<sup>2</sup>, resulting from 20 spirals with a diameter of 0.3m, delivering a theoretical power peak of 3000 W. The evaporator was designed such that, during the adsorption, that the water vapour is not limiting the total adsorption system power (800 W).



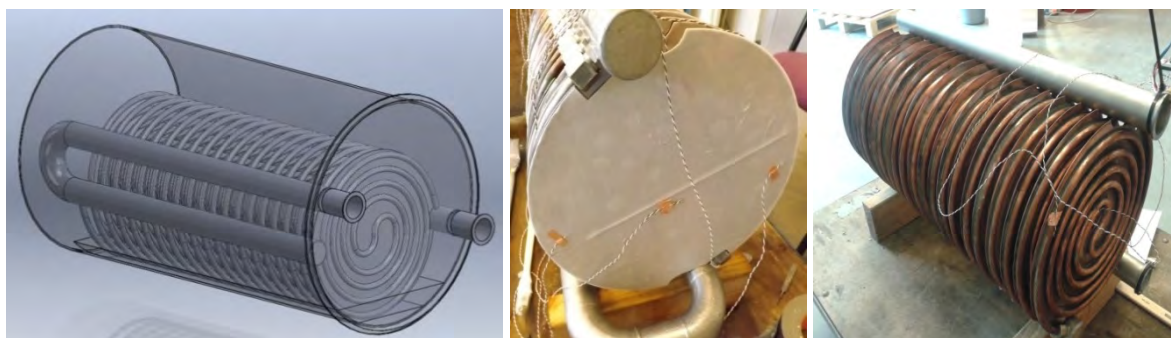


Figure 5-4. *Evaporator/condenser unit; (left) during the design phase, mounted in a cylindrical vessel; (middle) during building phase, capillary side for evaporation; (right) copper tubing on the reversed side for condensation.*

### Other aspects

Due to the absolute pressure difference of around 1 bar the reactor and the evaporator/condenser vessels need to be cylindrical with a lid for easy access during mounting to avoid extreme wall thickness.

Based on the above, the full system was ordered and built. The final system as was used for measurements and evaluation is depicted in Figure 5-5.



Figure 5-5. *The fully built E-hub laboratory fixed-bed zeolite vacuum thermochemical storage set-up, including water baths and monitoring equipment.*



### 5.3. Numerical models

#### Introduction

Here we give a brief summary of the TCS (ThermoChemical heat Storage) model developed for the current project E-hub. A more extensive version of the model containing all relevant physics and model data, and including the developed matlab code, is available as a separate document. The parameters used for the modelling exercise are given in Annex G. The TCS model describes a major part of the system for the storage of a certain amount of heat. The overall system is sketched in Figure 5-6. Heat is stored by drying a stock of TCM (ThermoChemical Material), in our case zeolite 5A, by heating up the adsorber/desorber to a certain relatively high temperature, e.g. by 90°C water from a solar collector during summer. Long-term storage of heat is achieved by keeping the adsorber dry. In colder times, heat is released by sorption of water vapour, which is produced by the evaporator. In the current paragraph, we describe the modelling of the sorption process. In paragraph 5.6 we make a comparison between the model and a sorption experiment (validation).

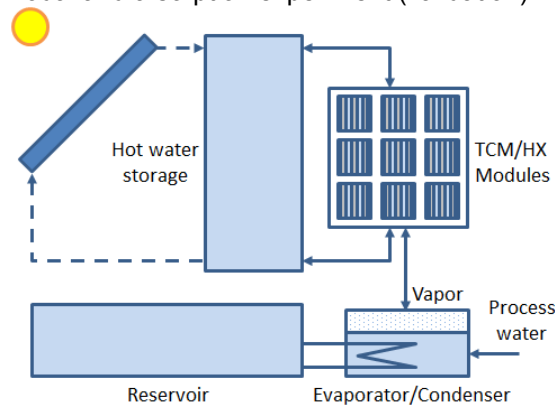


Figure 5-6. Possible system for TCM heat storage.

#### Modelling a TCS system

In this section we give a brief discussion of the physical processes involved and how they are modelled. The model describes a liquid water evaporator providing water vapour for sorption in the Zeolite 5A (Z5A) stock contained by the reactor as sketched in Figure 5-7. Heat is supplied to the evaporator by a flow of liquid water from a reservoir and heat is extracted from the reactor also by a flow of liquid water that is led to hot water storage.

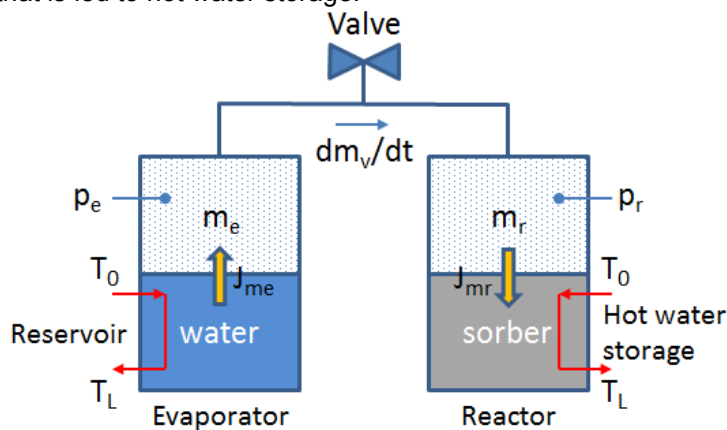


Figure 5-7. System for TCM heat storage with the evaporator (left) and reactor (right).

For the evaporator, the following physical models are used:

- The equilibrium vapour pressure in the evaporator and the evaporation heat of water are computed with the Antoine equation and its derivative;
- The dynamic pressure drop at evaporation is computed with the Langmuir equation;

- The consumed evaporation power is determined from the mass flow rate;
- Temperature changes of the evaporator are computed from the power balance, involving evaporation power, heat exchanger (HX) power and heat losses to the ambient environment;
- The HX with the reservoir is modelled by considering the liquid water at uniform temperature and in the stationary state. This yields a decaying exponential function of temperature difference (between liquid water and evaporator) with the HX length.

For the valve, the following physical models are used:

- Vapour flow is modelled by the De Saint Venant equation, giving the mass flow rate as a function of the pressure drop. The flow is considered adiabatic and largely in the choked flow regime, limited by the speed of sound of the downstream area;
- The temperature drop during expansion is determined from the Poisson equation, linking pressure and temperature for an adiabatic process.

For the reactor, the following physical models are used:

- Heating up vapour to reactor temperature is computed;
- The equilibrium vapour pressure of Z5A is computed from inverting the Toth equation and the sorption heat from the derivative of that function;
- The dynamic pressure drop at evaporation is computed with the Langmuir equation;
- The dynamic pressure drop for vapour transport in Z5A is modelled by diffusion with a diffusion constant  $D = 8.8 \cdot 10^{-8} \text{ m}^2/\text{s}$ . This value is determined from an analysis the relaxation time of the vapour pressure in Z5A. It is interesting to note that this value for D corresponds to Knudsen transport with a mean free path of 4 Å, which corresponds remarkably well with the cavity size of 5 Å in Z5A;
- The output sorption power is determined from the liquid water mass flow rate;
- Temperature changes of the reactor are computed from the power balance, involving sorption power, heating up water vapour, HX power and heat losses to the ambient environment;
- The HX to the output is modelled by considering the liquid water at uniform temperature and in the stationary state. This yields a decaying exponential function of temperature difference (between liquid water and reactor) with the HX length.

The model assumes a quasi-stationary situation where the water vapour mass flow rate of the evaporator, valve and reactor are all equal. This is necessary for the De Saint Venant equation and also for the exponential function by which the HXs are modelled. This is a limitation. For instance, it is not possible to model the start-up situation after opening the valve during which the initial pressure difference between evaporator and condenser is equalized.

## Iterative solution

Figure 5-8 shows the time loop for simulating sorption mode of the reactor. The given flow diagram comprises the following simulation steps:

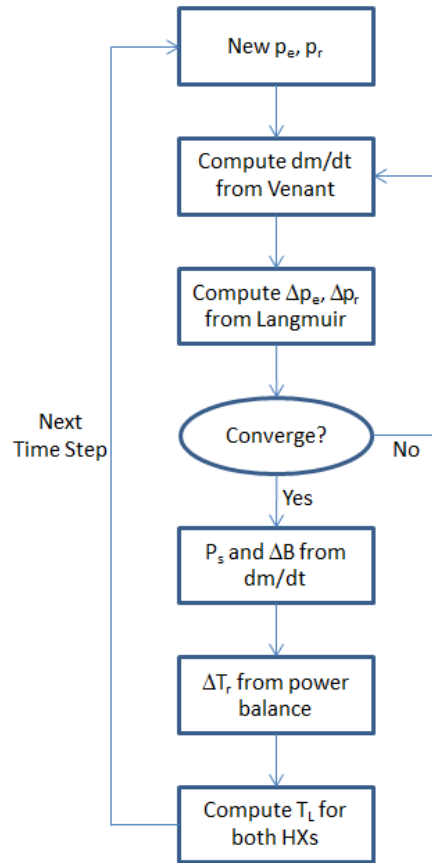


Figure 5-8 Flow diagram of simulation time loop.

- From the current  $T_e$ , compute the equilibrium vapour pressure  $p_{weq}$  for water and from the current  $T_r$  and water loading  $B$  in the sorber, compute  $p_{seq}$ ;
- First assume  $p_e = p_{weq}$  and  $p_r = p_{seq}$  and compute initial  $dm/dt$  during a finite time step  $\Delta t$ ;
- From this  $dm/dt$  determine Langmuir pressure drops  $(p_{weq} - p_e)$  and  $(p_r - p_{seq})$  over the interfaces giving new values of  $p_e$  and  $p_r$ , giving new  $dm/dt$ , and so on, iterate to solution for this  $\Delta t$ ;
- From the equilibrium  $dm/dt$ , compute sorption power  $P_s$  for this  $\Delta t$ ;
- From  $P_s$  and power balance compute reactor heating  $\dot{Q}_d$  in time step  $\Delta t$ ;
- With the new  $T_r$ , compute new output temperature  $T_L$  for both the HX with the hot water storage and the low temperature reservoir for this  $\Delta t$ ;
- From the equilibrium  $dm/dt$ , compute change in TCM water loading  $\Delta B$  in time step  $\Delta t$ ;
- From new  $B$  and new  $T_r$  compute new  $p_{seq}$ ;
- Next time step with latest values of  $p_e$  and  $p_r$ .

## Modelling results

Figure 5-9 and Figure 5-10 show the results of a sorption mode simulation. The following may be observed from the Figures:

- After opening the valve, there is an equalization of pressures between evaporator and reactor in about 300s, illustrated by Figure 5-9 (left);
- During the first 200s, the water vapour mass flow is limited by choked flow, where the flow speed of entering the reactor is limited by the speed of sound, illustrated by Figure 5-9 (middle);

- The initial reactor power peaks near 14kW, and in the beginning most of the power is used for heating up the reactor. When the reactor reaches maximum temperature, most of the sorption power is transferred to the HX fluid, illustrated by Figure 5-9 (right) and Figure 5-10 (left);
- The rapid change in reactor temperature, the increasing equilibrium vapour pressure and the increasing 'beladung'  $B$  or water content of the Zeolite from 0.17 to 0.21g H<sub>2</sub>O/g Z5A are illustrated by Figure 5-10 (middle & right).

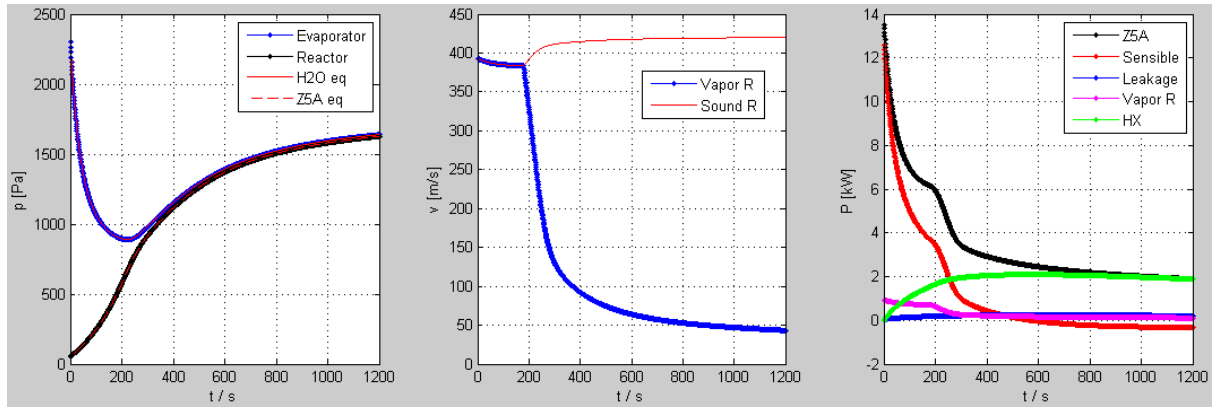


Figure 5-9. Operation pressures (left) of adsorber and evaporator, flow speed of water vapour into the reactor (middle), and generated/transferred powers in different reactor components (right).

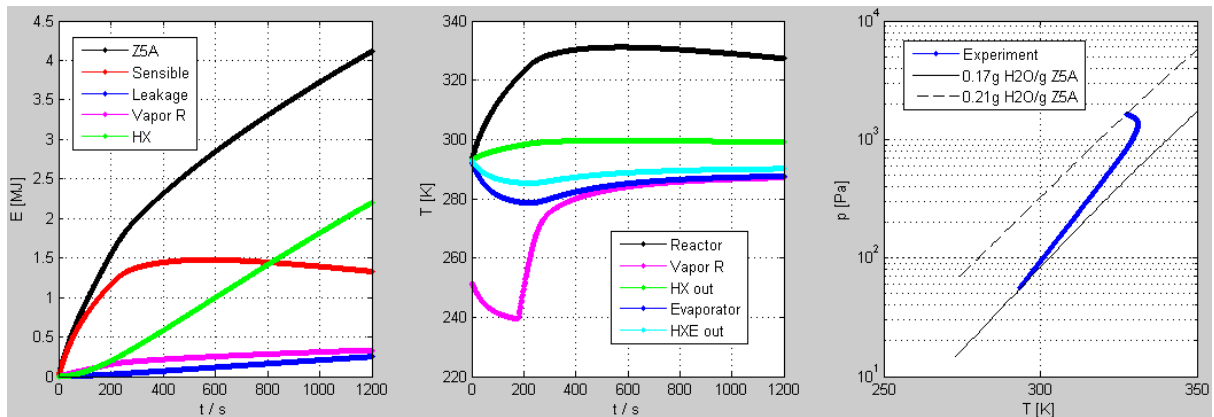


Figure 5-10. Cumulative energy absorbed in different reactor components (left), temperature in different reactor components (middle), and Z5A temperature vs. pressure from initial to final water loading (right).

## 5.4. Experiments and results

The E-hub reactor is built in stages. During this process, a number of initial tests were performed. If any component did not perform as expected, it was studied (and modified) before further compilation of the system. A detailed representation of tests performed can be found in Annex G: Supporting information for design, modeling, construction and testing of the closed sorption TCS system.

After the initial tests, a number of experiments were carried out at different condenser and evaporator temperatures in order to characterize the system behaviour under different operating conditions. In between the experiments the system was left to stay under vacuum.

After the characterisation experiments, a number of additional experiments were performed to obtain parameters such as heat losses to the environment and to study some unexpected phenomena that occurred during the characterisation experiments.

### Characterisation experiments

Table 5-2, summarizes the characterisation experiments that were carried out. A complete list of all experiments including operational parameters and results is provided in Annex G.

Table 5-2. Overview of experiments carried out, and the major conditions applied.

Experiment	remarks	T desorption	T condenser	T adsorption	T evaporator	Time duration experiment
[#]		[Celsius]	[Celsius]	[Celsius]	[Celsius]	
1		90.0	10.0	20.3	18.1	4 hours
2		80.0	12.0	21.5	19.4	4 hours
3		95.0	12.0	24.7	14.8	4 hours
4		80.0	12.0	21.3	12.3	4 hours
5		91.0	11.0	21.4	7.8	4 hours
6	air in heat exchanger	91.0	11.0	21.6	14.9	4 hours
7		91.0	11.0	21.3	14.8	4 hours
8		97.0	11.0	21.9	14.8	4 hours
9		97.0	20.0	20.7	14.8	4 hours
10		102.0	20.0	22.0	14.8	4 hours
11		100.9	13.6	30.0	15.3	13 hours
12		101.4	12.6	29.9	15.3	13 hours
13		112.6	6.3	20.6	15.2	13 hours
14		94.5	14.9	20.8	15.3	13 hours
15		89.6	13.6	20.7	15.3	13 hours
16		91.3	17.3	21.1	15.2	13 hours
17	vapour valve partly open	90.0	14.5	20.9	15.4	13 hours
18		111.5	7.0	20.7	15.2	13 hours
19		102.4	6.9	20.6	15.4	13 hours
20		103.5	12.9	20.9	15.4	13 hours
21		103.3	20.7	21.0	15.3	13 hours
22		96.1	11.1	20.9	15.3	13 hours
23		103.7	19.9	20.4	8.4	13 hours
24	higher flow adsorber	103.6	20.5	29.5	15.3	13 hours
25		103.6	20.5	20.8	15.3	13 hours

26	focus on pressure drop	104.1	16.3	20.8	49.6	13 hours
27		103.6	23.1	30.1	20.2	13 hours
28	experiment focus on pressure drop between adsorber and evaporator / 30 s open valve					
29	experiment focus on pressure drop between adsorber and evaporator / 5 min open valve					
30	change vapour valve setting	104.4	20.6	20.1	20.2	4 hours
31	higher flow adsorber	104.8	18.6	20.2	20.3	13 hours
32	/ higher flow adsorber	104.6	20.7	19.6	20.3	4 hours

In the next chapter, a typical experiment is analysed in detail with a stepwise description of the parameter studied.

### Typical experiment

Prior to an adsorption experiment the zeolite was dehydrated at 103°C (desorption) and 20°C condensation for about 2.5 hours and afterwards cooled down to the used adsorption and evaporation temperature conditions (20 and 15°C, respectively). This process is to mimic the drying process using solar heat during summer. A graphical representation is given in Figure 5-11 and Figure 5-12.

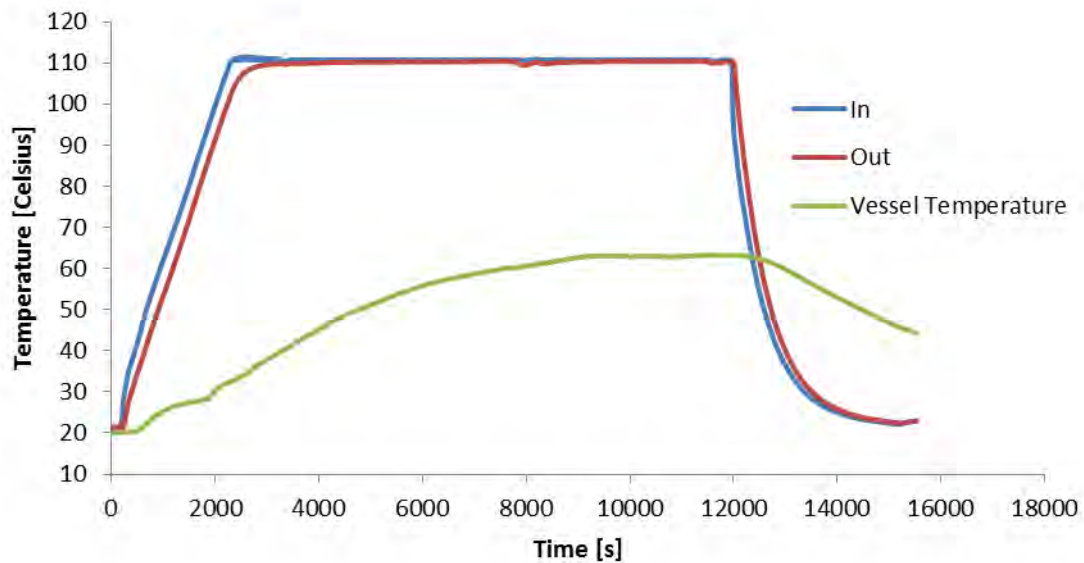


Figure 5-11. Desorber heat exchanger and vessel temperatures in a typical experiment.

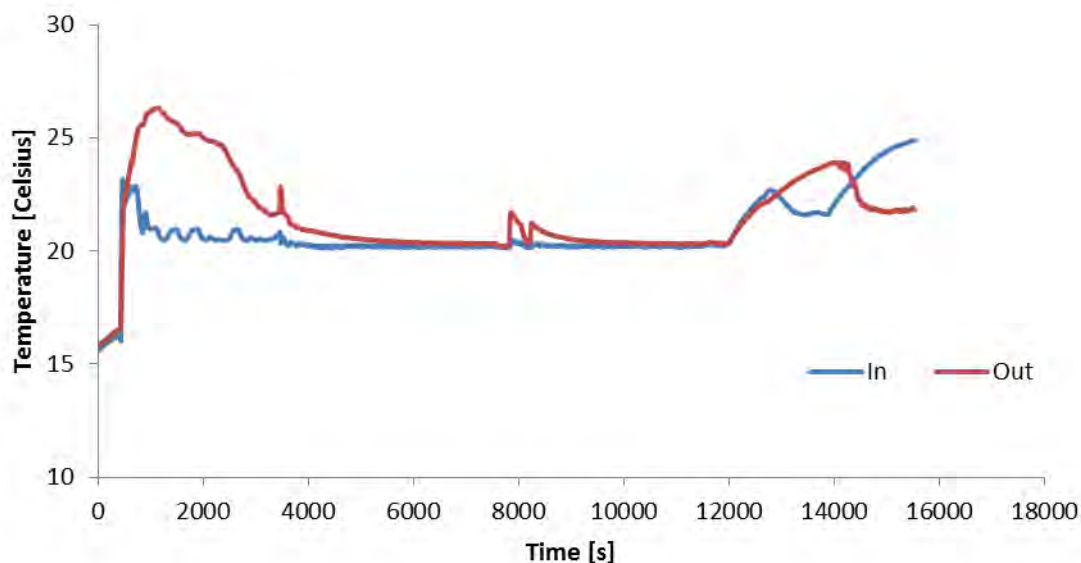


Figure 5-12. *Condenser heat exchanger temperatures in a typical experiment.*

When desorption starts (Figure 5-11 and Figure 5-12), hot water is led through the desorber heat exchanger (Figure 5-11). The heat is taken up by the zeolite material and water is evaporated from it. It takes a small amount of time before the zeolite reaches the inlet temperature, and therefore at the beginning of desorption the outlet desorber temperature is somewhat lower than the incoming temperature. Furthermore, it can be seen from the desorption experiment that it takes a while for the condenser outgoing temperature to reach the set temperature after initiating the desorption (Figure 5-12).

In this period of time, the storage vessel also slowly heats up (see also Figure 5-11). This effect occurs because of radiation of the hot desorber heat exchangers towards the vessel wall. After sufficient time, the desorption of the zeolite material is complete and the reactor can be considered to be dry (at the given measurement conditions, in this case desorption at 103°C and condensation at 20°C). Now, the reactor can be cooled down to ambient before an adsorption measurement starts.



In the typical adsorption experiment (Figure 5-13 and Figure 5-14), after an initial time to allow the system to reach equilibrium (approximately 3000 s in Figure 5-13), the zeolite temperature increases gradually and peaks after 1500 s (25 minutes). Figure 5-13 shows that the maximum temperature lift - the difference between outlet and inlet of water circuit temperatures - during hydration (adsorption) is 31.2 K. Over a period of 1 hour and 18 minutes the adsorber delivers water with a temperature lift over 20 K. In this period, the average temperature lift was 25.5 K. Looking at a deliverable, average temperature span of 20 K over the adsorber heat exchanger (which was one of the design parameters), a time frame of 2 hours and 42 minutes can be noticed.

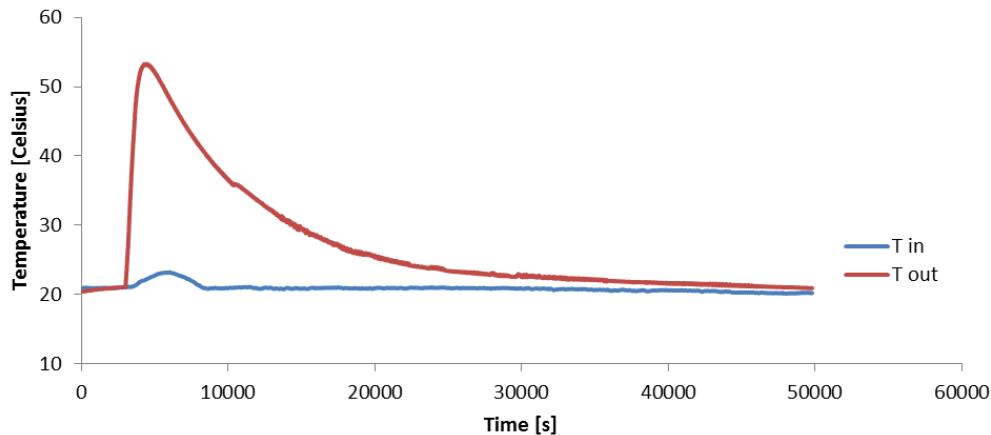


Figure 5-13. Adsorber in/out flow temperatures in a typical experiment.

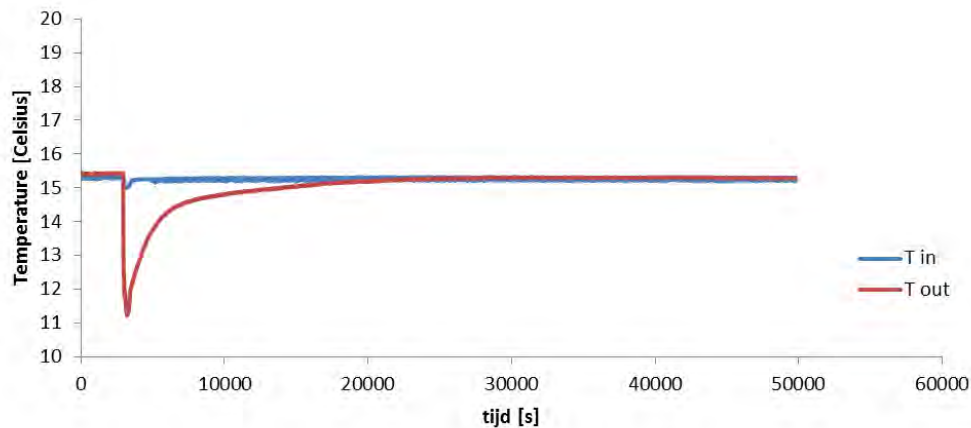


Figure 5-14. Evaporator in/out flow temperatures in a typical experiment.

In Figure 5-13, a temperature change of 2.5 K for the adsorption inlet temperature can be seen. This artefact temperature increase has to do with the fact that the thermostatic water bath, used as heat sink, could not fully dissipate the peak power delivered by the adsorption process. In future measurement set-ups this is remedied by pre-cooling the outlet water stream from the adsorber before entering the water bath. The evaporator shows similar behaviour (Figure 5-14); heating power is insufficient to keep initial evaporation temperatures at 15°C, but eventually (after about 20000 s) equilibrium is reached and the evaporator can deliver the necessary temperature to the evaporating water in a steady state.

In the next chapters, the following aspects of this experiment will be analysed in more detail:

1. power density and energy density
2. heat transfer
3. water vapour flow in the adsorber
4. evaporation power

## Analysis of power density and energy density

The power and cumulative heat released by the adsorber were derived from temperature and flow measurements of the adsorber water circuit in. For the typical experiment, this is illustrated in Figure 5-15.

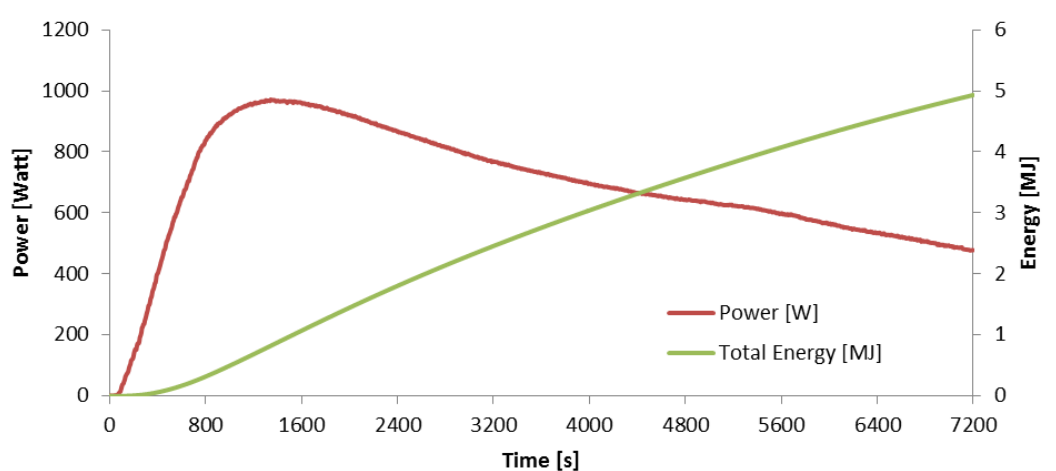


Figure 5-15. Output heating power and total energy output for a typical experiment.

Figure 5-15 shows that a maximum adsorption power released of 970 W was realized at the particular conditions of this experiment (103°C for desorption, 20°C for condensation, 20°C for adsorption and 15°C for evaporation). Thus, 41 kg of zeolite yield a maximum specific power of 24 W/kg. When related to the period of 1 hour and 14 minutes during which an average temperature lift higher than 20°K was obtained, an average heating power of 800 W was found (equal to the design specification). This corresponds to an average specific power of 20 W/kg.

After 2 h (7200 s) an amount of heat equal to 4.9 MJ (1.4 kWh) was transferred to the water circuit. At this time, the temperature difference between inlet and outlet in the water circuit had dropped to 15.4°K. After 50000 s (about 14 hours) the total heat extracted from the adsorption process is 9.3 MJ (2.6 kWh). This corresponds to 226 J/g zeolite 5A. At that time, the temperature lift in the water circuit had dropped to less than 0.5 K.

Taking the 41 kg zeolite and a materials density of 750 kg/m<sup>3</sup>, a material energy density of 0.17 GJ/m<sup>3</sup> zeolite can be calculated from the maximum useful energy retrieved. As the zeolite makes up only about 27% (by volume) of the current total reactor system, overall energy density in this particular experiment was 0.045 GJ/m<sup>3</sup>.

## Analysis of heat transfer coefficient

An important parameter determining the performance of a TCM reactor is the heat transfer between the zeolite spheres, through the heat exchanger, to the water in the water circuit. This parameter was measured during the adsorption process using thermocouples to measure the zeolite temperatures. Along with inlet and outlet water circuit temperatures a mean temperature integral could be calculated. Thus, assuming quasi-stationary heat adsorbed by the zeolite, a heat transfer coefficient of 28±3 W/(m<sup>2</sup>K) was found. This agrees well with a theoretical value of 30 W/(m<sup>2</sup>K).

## Analysis of water vapour flow in the adsorber

The reactor is designed such that water vapour entering the reactor vessel is distributed evenly over the vessel volume allowing uniform absorption by the zeolite and resulting in a uniform temperature increase of the zeolite in the reactor vessel.

However, if the water vapour cannot reach specific parts of the absorber, these parts will show lower or no temperature increase during the experiment. This was analysed by looking at the temperature sensors located on different parts of the heat exchangers.

In Figure 5-16, three different spots, distributed over the height of the heat exchanger, at the outer surface, were chosen. As the water vapour inlet is at the top of the adsorber vessel, the homogeneous temperature increase in this figure shows that the water vapour is evenly adsorbed over the reactor, indicating that there is no substantial pressure drop of water vapour along the zeolite bed or between the heat exchanger blocks. The same approach of looking at the temperature slope was taken for the pressure drop through the zeolite bed. The measured temperatures at “zeolite 50cm surface” and “zeolite 50cm centre” do not show any difference, showing that there is no significant restriction of water vapour transport through the zeolite bed. For clarity, also the adsorber heat exchanger inlet and outlet temperatures are shown in Figure 5-16 (bottom lines). It can be seen that there is a delay of about 70 seconds between the temperature increase in the zeolite material and the temperature increase of the water at the heat exchanger outlet.

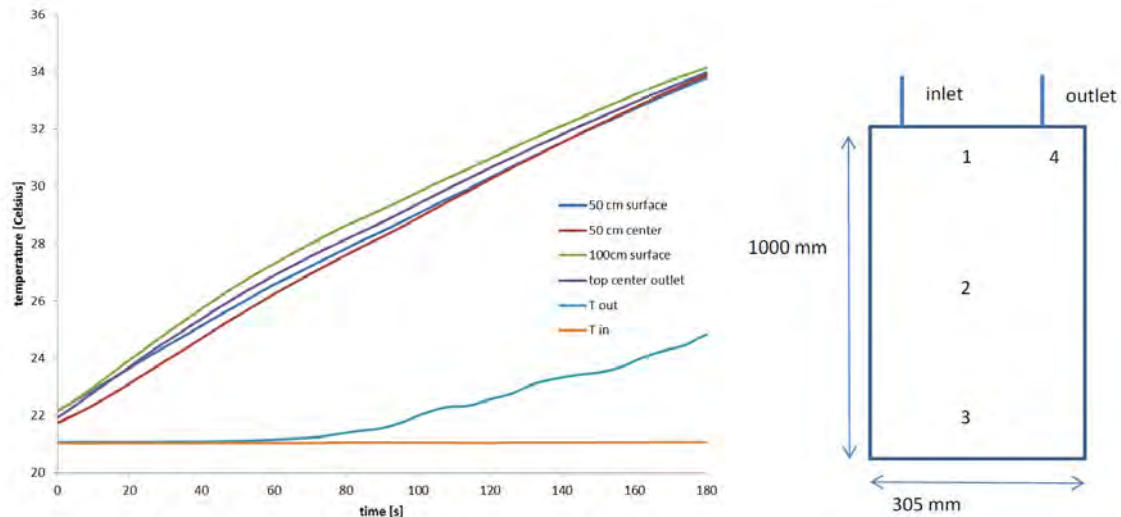


Figure 5-16. Zeolite temperatures at different positions and adsorber in/out flow temperatures in a typical experiment. The temperatures have been measured at different locations on the heat exchanger, as noted schematically as (1) 50 cm surface, (2) 50 cm centre, (3) 100 cm surface and (4) top centre outlet.

## Analysis of evaporation power

The power provided by the evaporator is calculated from the liquid water mass flow and the temperature difference between outlet and inlet. Provided the water in the evaporator is not cooled down, the evaporation power is a measure of the amount of water evaporated. The maximum evaporation power thus calculated in this particular experiment is 2300 W.

The maximum power for evaporation can easily be increased by increasing the flow rates in the water circuit. This way, evaporation pressures of up to 2900 W were achieved in other experiments, thereby reaching the design specification.

In practical applications, a general assumption is that heat for the evaporation of water is delivered by a low-temperature heat source (typically at 10°C) under equilibrium conditions. However, in this experiment, the temperature in the evaporator heat exchanger drops rapidly in the first seconds after the start of the experiment (red line in Figure 5-17). This is due cooling of the water within the evaporator because of high evaporation powers that are required to sustain the initial adsorption of water vapour in the adsorber.

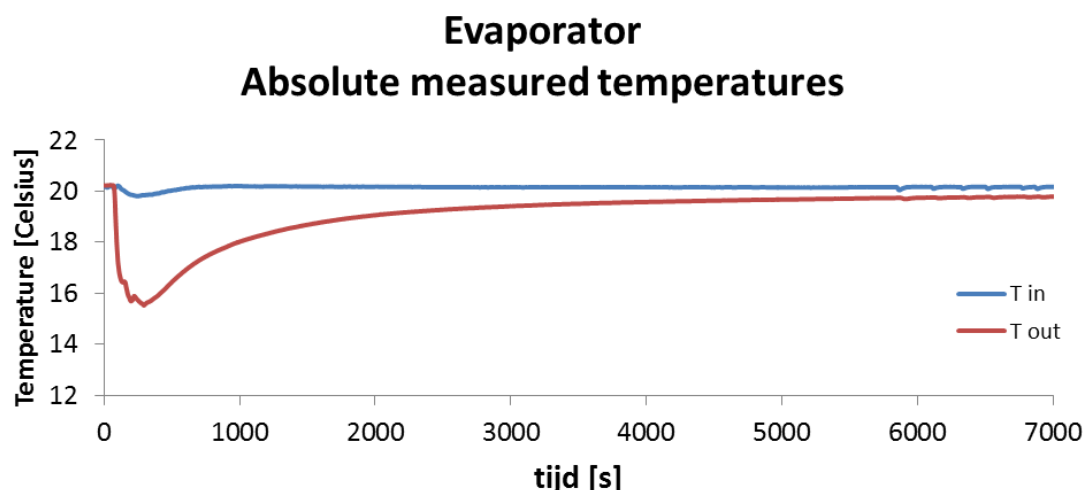


Figure 5-17 *Evaporator inlet and outlet temperatures for a typical experiment*

Temporarily, the contribution from the heat capacity of the water to the evaporation power appears to be much higher than heat from the low temperature heat source (powers in the order of 20 kW have been found).

### Effect of different desorption/condensation temperatures on heat storage capacity

As mentioned previously, the thermochemical heat storage module was designed to be charged (desorbed) using solar heat at temperatures between 80°C and 120°C and condensation temperatures between 20°C and 30°C.

Due to higher equilibrium water vapour pressures, higher desorption temperatures in the desorption stage yield dryer zeolite and therefore higher intrinsic heat storage capacity. In addition, due to lower equilibrium water vapour pressures at lower condensation temperatures in the desorption stage, also dryer Zeolite and higher heat storage capacities are obtained. Of these two parameters, the desorption temperature was thought to be the most determining parameter. Therefore, the energy content of the module under various experimental conditions was plotted vs. this parameter in Figure 5-18. In this figure, condensation temperature and desorption temperature during regeneration were varied while adsorption and evaporation temperature were held constant at 20°C and 15°C respectively.

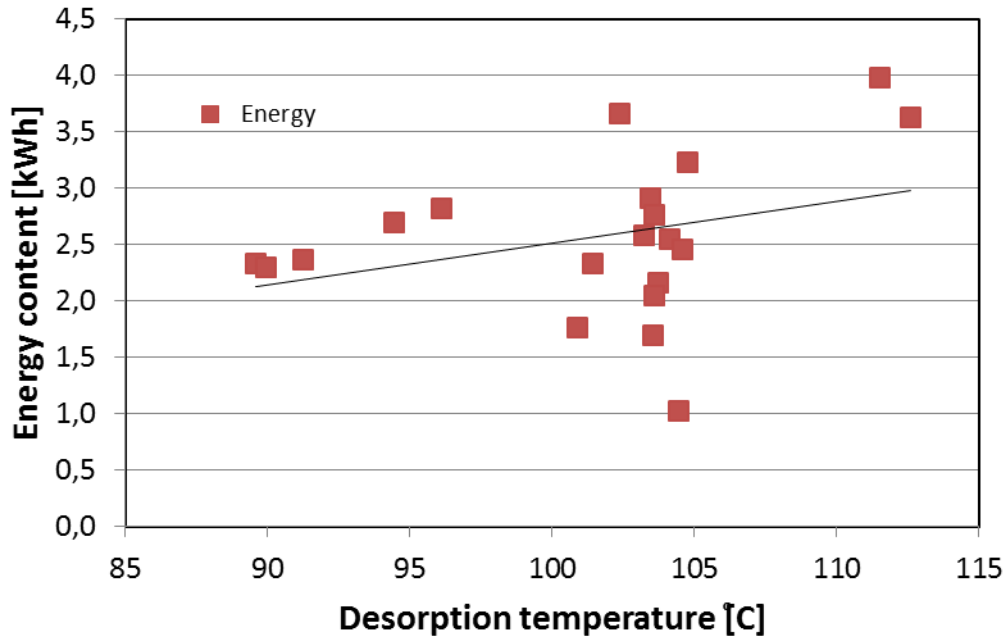


Figure 5-18. *Energy content measured as function of the desorption temperature.*

What can be clearly seen in Figure 5-18 is that –on the average– that the energy content increases with an increasing desorption temperature. It also shows that at desorption temperatures over 110°C, the design specification of 3 kWh was reached.

Note that at desorption temperatures around 100°C, the energy content varies significantly. This is due to the fact that the other experimental conditions varied, in particular condensation temperature during desorption.

Of interest is the comparison of experimental results with theoretical values. This was done by reading the hydration and dehydration states from Clausius-Clapeyron curves <sup>1</sup> at the temperatures for desorption, condensation, adsorption and evaporation that were applied in each experiment. The results are shown in Figure 5-19 below. The red line denotes where experimental results are equal to theoretical values.

<sup>1</sup> Here we used data extracted from the measurements performed by Wang et al. [Wang *et al.*, “Adsorption Equilibrium of Carbon Dioxide and Water Vapour on Zeolites 5A and 13X and Silica Gel” *J. Chem. Eng. Data* 2009; 54: 2839-2844]. The curves yield an average adsorption enthalpy of 54.5 kJ/mol water on zeolite, which is approximately 20% higher than the evaporation enthalpy of water with (44 kJ/mol). This results in a theoretical value of 3 MJ/kg of adsorption enthalpy per kg of water.

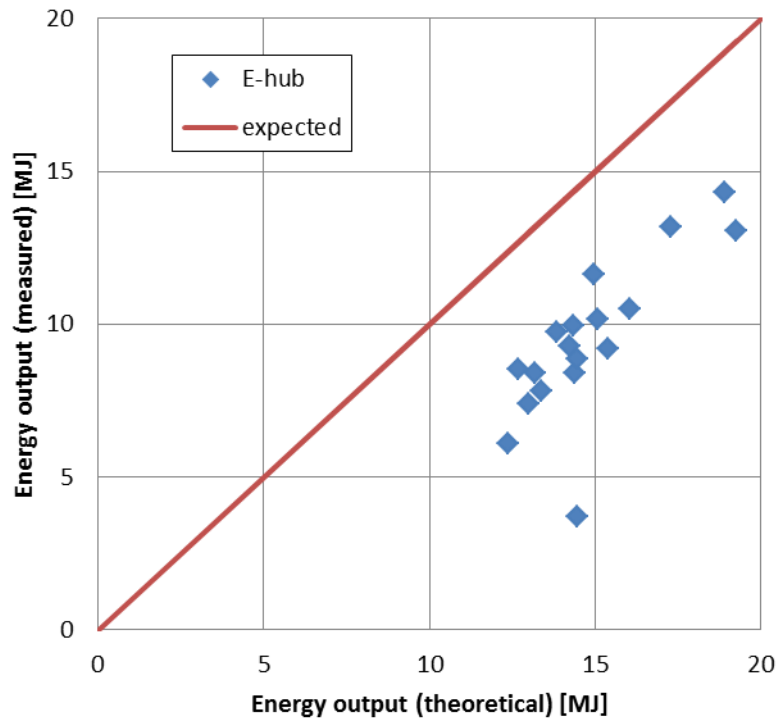


Figure 5-19. Comparison of theoretical energy output and experimentally measured energy output.

As can be seen in Figure 5-19, the experimentally determined values for the energy content are lower than the theoretical values. On average, the experimental values are approx. 5 MJ lower than the theoretical values. Possible explanations for this deviation may be related to:

1. Deviation in theoretical loading state because of different zeolite properties from different suppliers. In our experiments we have used zeolite 5A supplied by Sigma Aldrich, while the zeolite for which the Clausius-Clapeyron diagrams were recorded by Wang et al. was delivered by Grace.
2. Heat losses during adsorption, not yet taken into account.
3. Incomplete energy collection due to finite measurement time.

The discrepancy between measured and theoretical energy output is currently under investigation.

## Effect of different adsorption/evaporation temperatures on heat storage capacity

Further experiments were carried out to investigate the effect of adsorption and evaporation temperatures on heat storage capacity. This is of importance for practical applications because the evaporation temperature is determined by the low temperature heat source and the adsorption temperature is determined by the desired level of heat output. For instance, the production of DHW at 60°C, requires a higher adsorption temperature than the production of heat for space heating (typically 35°C for low temperature heating systems)

The evaporation temperature was varied within the range of 5 – 15°C and the adsorption temperature was varied between 20 and 30°C. In these experiments, the desorption and condensation temperatures were held constant at 103°C and 20°C respectively.

Decreasing the evaporation temperature from 15°C to 5°C decreased the energy content from 9.3 MJ down to 7.8 MJ which is 16% lower. Increasing the adsorption temperature from 20°C to 30°C decreases the energy content from 9.3 MJ down to 7.4 MJ which is 20% lower (*Figure 5-20*).

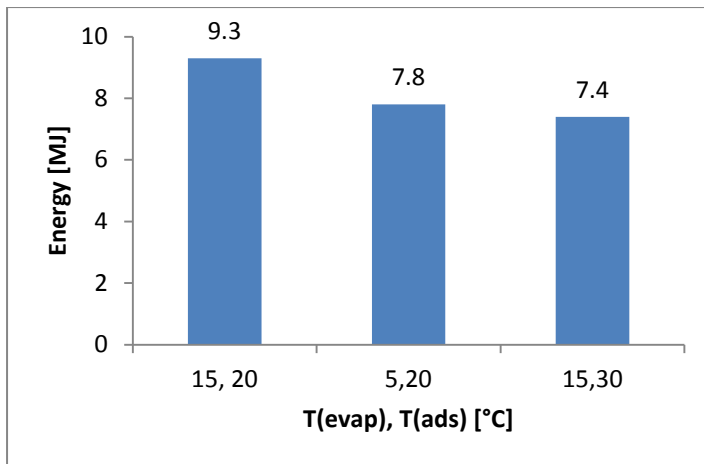


Figure 5-20. Energy content as function of evaporation and adsorption temperature.

## Heat losses to the environment

An additional experiment was carried out to calculate the heat losses from the reactor vessel to the environment during adsorption and desorption. In this experiment, water at 40°C was continuously transported through the reactor for 2 days with ambient temperatures varying between 21.5 and 23.3°C.

The difference of inlet and outlet water circuit temperature is a measure of the heat released inside the storage module which - assuming quasi-stationary conditions – equals heat losses of the module to the environment.

Taking the geometry of the reactor vessel into account yielded an average heat resistance of 5.8 K/W.

The cycle efficiency of several experiments was analysed. In a typical measurement, a total desorption energy of 26.7 MJ was supplied to the reactor, whereas the delivered energy upon absorption amounted to 10.1 MJ. This results in a cycle efficiency of 38%. For the other experiments, under various experimental conditions, the cycle efficiency was determined as well, and is found to be in the range of 30-35%. Here it is noted, that we did not focus our attention on the optimization of the cycling efficiency.

## Pressure equilibration after opening of the valve (300 seconds experiment)

Initially, an enigma was the pressure difference that was measured between the absorber vessel and the evaporator vessel in the first stage of experiments. As both vessels are connected by a short (length 0.5m) and rather wide pipe (diameter 4 cm), the pressures were assumed to be equal or near equal.

In order to better understand the pressure differences in the first stage of the experiment, a particular test focused on the first 300 seconds using high resolution pressure meters. Below, a representation is given of the circumstances during the test (Figure 5-21).



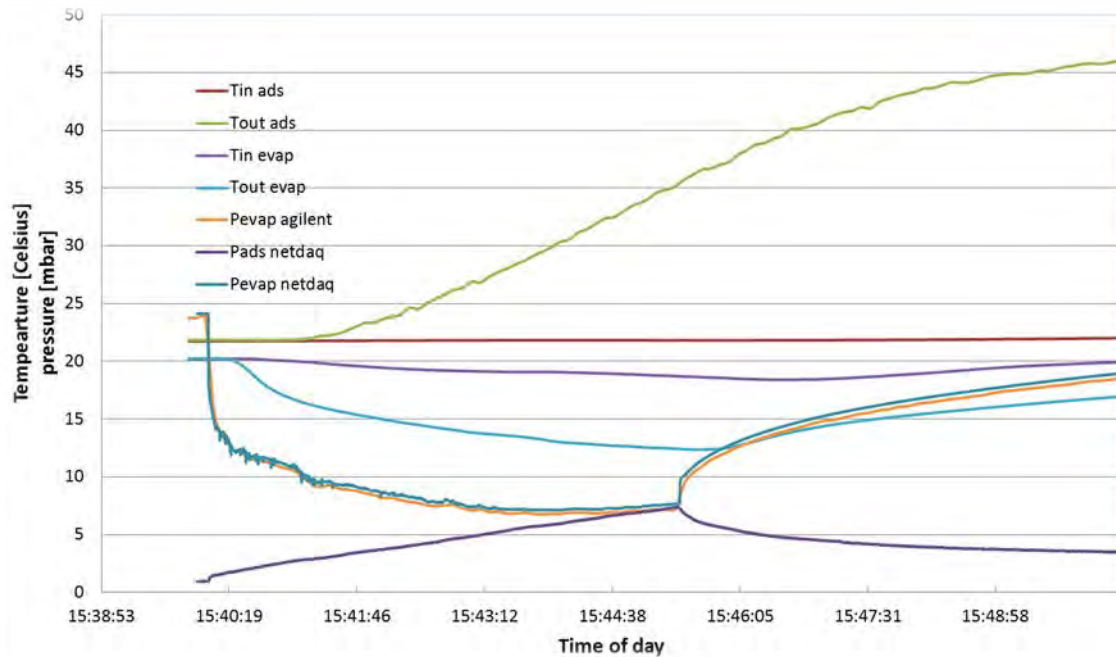


Figure 5-21. *Temperatures and pressures in evaporator and adsorber vessels during the 300 seconds experiment.*

In this experiment, at  $t=15:40$ , the valve connecting the evaporator and adsorber is opened, and after 300 seconds ( $t=15:45$ ) the valve is closed again. It was expected that pressures would even out instantly after opening the valve, but this appears not to be the case.

In the left half of Figure 5-21, it can be seen that there is a quick initial evaporator pressure drop of  $\sim 8$  mbar (orange and turquoise lines – 2 different sensors) due to the redistribution of the available water vapour over the two vessels.

The adsorption pressure (purple line) starts at very low values ( $\sim 1$  mbar) because the zeolite is very dry and readily absorbs any water vapour in the vessel. The pressure gradually rises in time due to water vapour being adhered onto the zeolite material.

However, a pressure difference remains between the evaporation vessel and the adsorption vessel which decreases only slowly, to the point where they are more or less equal at  $t=15:45$ . Calculations show that this pressure difference is caused by very high gas speeds at which water vapour is being transported through the tubing from the evaporator to the adsorber. In fact, calculations show that the speed of gas ( $\sim 400$  m/s) exceeds the speed of sound, giving rise to a regime of so-called 'choked flow'. This yields evaporation flow rates of 4 g/s on average, or 1.2 kg over the full 300 seconds yielding a total of  $\sim 1$  kWh of heat released. This corresponds to an average power delivered in the first 5 minutes of 12 kW. This is rather high, and close to the value of 15 kW generally used in DHW systems.

At a certain point in time (in the graph around  $t=15:45$ ), pressure levels are almost similar and the driving force for the gas transport is therefore much smaller. At this point, for the sake of the experiment, the valve is closed again so that the two vessels are again separated.

In the adsorption vessel, the water vapour pressure (purple line) slowly decreases again. Apparently, any remaining water vapour is being adsorbed by the - still rather - dry zeolite. The time constant of this process ( $\tau_{\text{grains}}$ ) is around 75 seconds, giving a measure for the diffusion time of the water vapour in the zeolite grains.

In the evaporation vessel (orange and turquoise lines) the pressure rises again due to the restored functionality of the vaporiser heat exchanger when no more water vapour is being carried away to the absorption vessel. In addition, a rapid initial restore (2 mbar), towards equilibrium pressure ( $\sim 20$  mbar), can be seen comparable to when the valve was opened. A possible explanation is that a pressure drop exists between the water interface and the pressure sensor, e.g. between the disks of the evaporator.

## Comparison with design specifications

Table 5-3 compares the results of our experiments to the design specifications. It clearly shows that all design specifications were reached.

Table 5-3. *Design specifications reached for the 3 kWh reactor set-up.*

Property	Design Value	Experimental Value	Value Reached
Heat storage capacity	3 kWh	3.6 kWh	☑
Power output reactor	800 W	1570 W max 1040 W over 1.8 hours 640 W over 4.4 hours	☑
Temperature evaporator	10 °C	Variable 5-15 °C	☑
Temperature condenser	30 °C	Variable 5-30°C	☑
Water temperature lift for space heating	20 °C	Peak 50,6 °C 36°C over 1.8 hours 20°C over 4.4 hours	☑
Desorption temperature	90 °C	Variable 70-110°C	☑
HX temperature loss	5 °C		☑
Maximum pressure loss liquid water	0.2 bar		☑
Maximum pressure loss vapour transport	1 mbar	< 1mbar	☑
Closed system, vacuum, fixed bed	☑		☑

\*Experimental values are achieved at  $T_{des} = 112^{\circ}\text{C}$ ,  $T_{cond} = 5.2^{\circ}\text{C}$ ,  $T_{evap} = 15.5^{\circ}\text{C}$  and  $T_{ads} = 20.6^{\circ}\text{C}$ .

## 5.5. Model validation

Below, a model comparison with the 300s adsorption experiment is made. Figure 5-22, Figure 5-23, Figure 5-24 and Figure 5-25 show a comparison of simulations and experimental data. The following may be observed from the figures:

- The pressures in reactor and evaporator have roughly the same trend in simulation and experiment, illustrated by Figure 5-22.
- The HX output temperature starts increasing later, but then increases more rapidly than predicted from the simulation, illustrated by the red symbols/line in Figure 5-25.
- Power and accumulated energy are determined from the HX output temperatures. We see that the total delivered energy roughly corresponds to the prediction, illustrated by the blue symbols/line in Figure 5-24.

The mismatch between HX output temperatures between experiments and simulations may be due to the stationary modelling of the HX. This assumes a uniform reactor temperature and therefore a constant value during the flow of a fluid element through the entire reactor. This approximation is allowed if the HX throughput time  $L/v = 67\text{s}$  is small compared to reactor temperature changes. However, the relatively large reactor temperature changes of Figure 5-25 (black line) suggest that this may not be the case and that modelling of the HX in  $N$  sections of length  $L/N = v\Delta t$  may lead to better agreement between experiments and simulations.

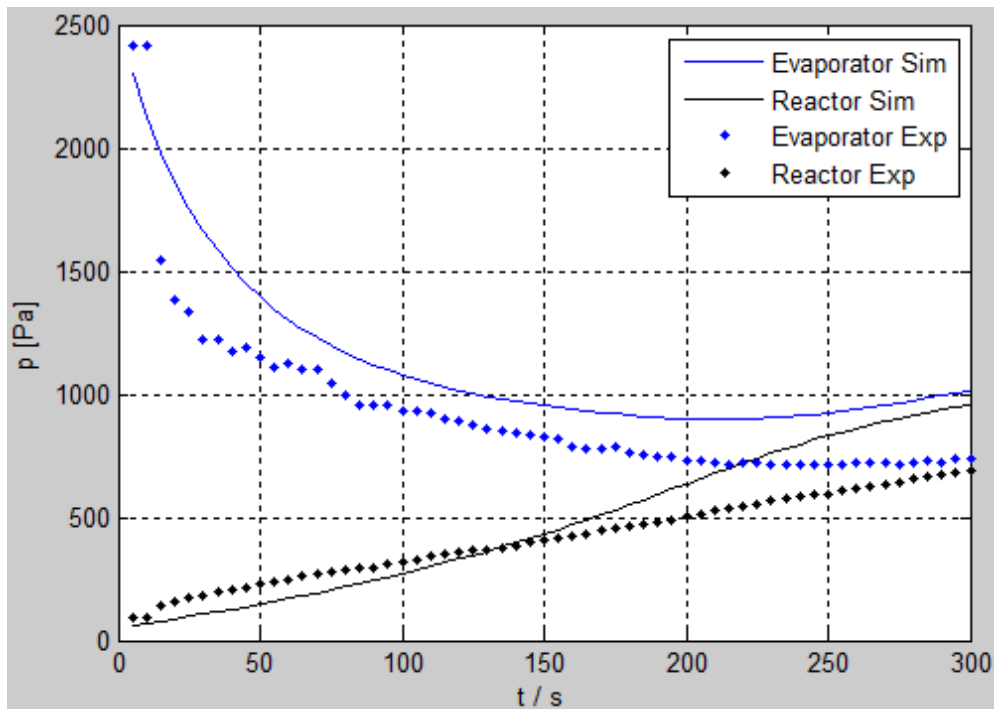


Figure 5-22. Pressures as a function of time. Symbols represent measured data, lines represent model calculations.

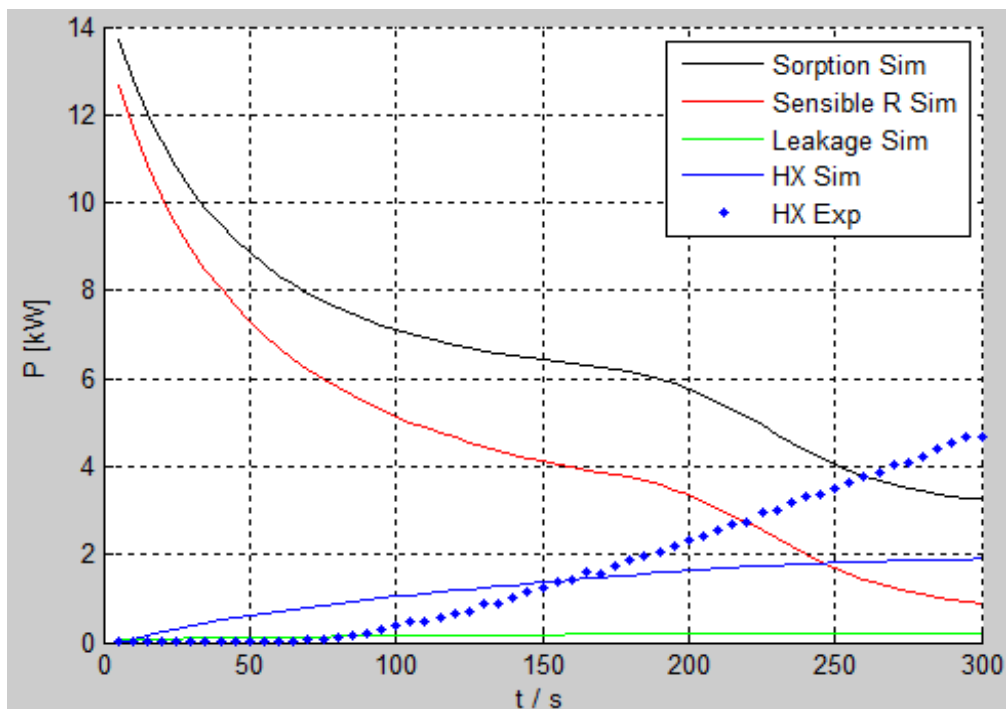


Figure 5-23. Powers as a function of time. Symbols represent measured data, lines represent model calculations.

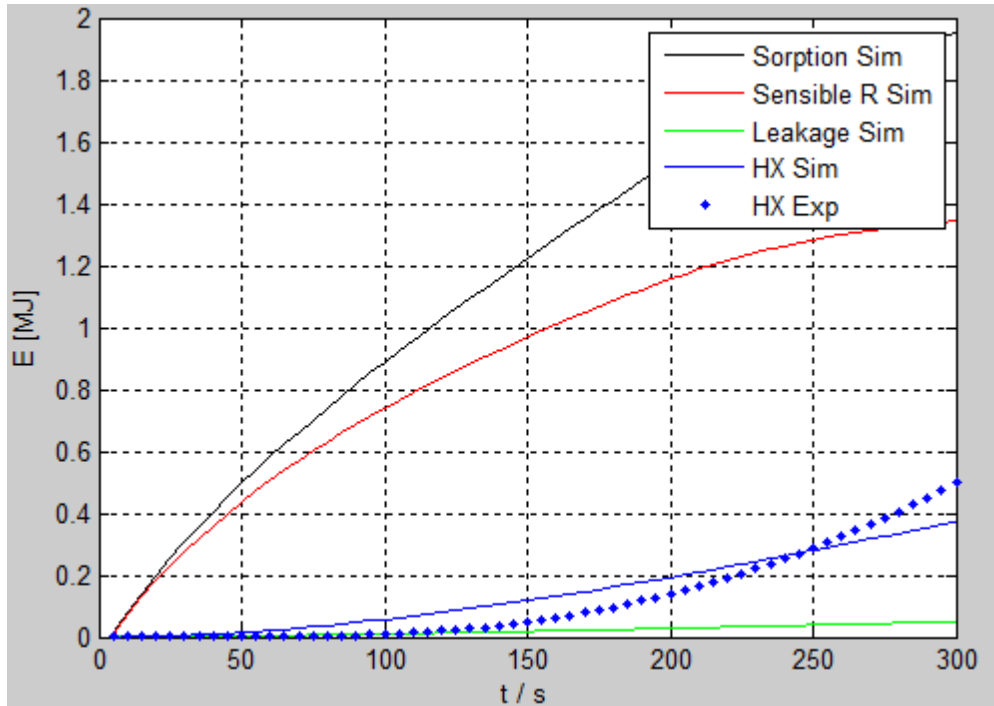


Figure 5-24. Cumulative energy as a function of time. Symbols represent measured data, lines represent model calculations.

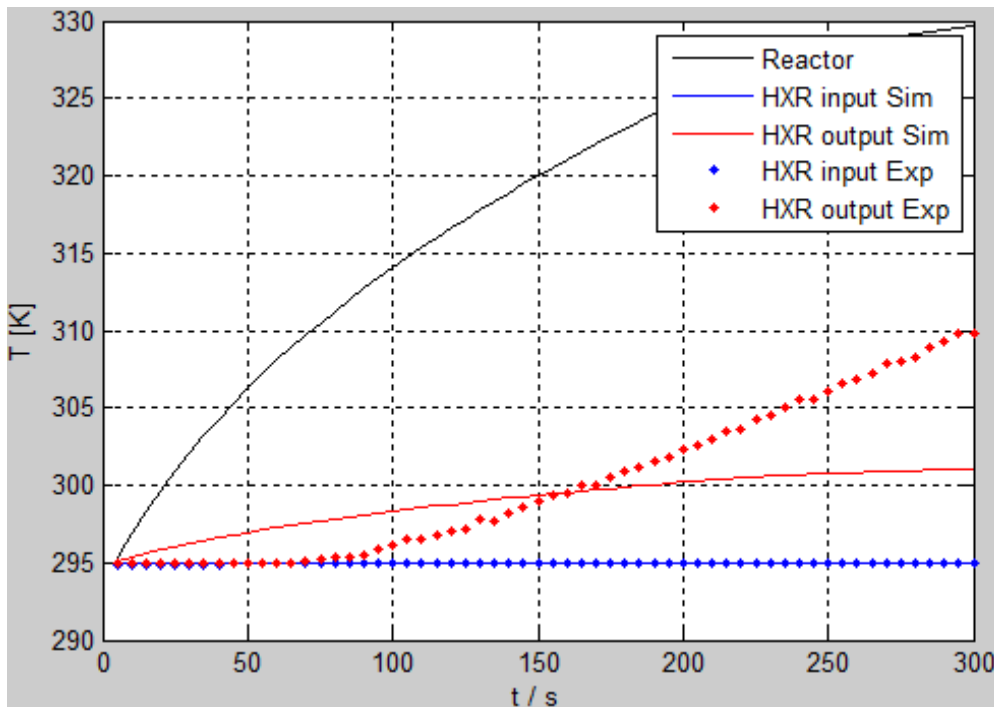


Figure 5-25. Temperatures as a function of time. Symbols represent measured data, lines represent model calculations.

Note that the simulation parameters are first guesses from physical considerations and not yet fitted to the experiments. The list of simulation parameters that may be fitted can be found in Annex G. In future modelling studies, these physical parameters will be fitted to experiments to actually gain insight in the parameters, and in the right way of optimizing particular experimental set-ups.

## Suggestions for future work

The above suggests the following model improvements:

- Adjusting TCM model parameters to the experiments, manually or by a fitting tool (e.g. Simulated Annealing). Note that with the initial parameter guesses, the correspondence between simulation and experiments is already rather good.
- Modelling HX of the reactor in a number of segments (typically 20) to better model the heating of a fluid element passing through the reactor. It is expected that this will decrease the difference between the experimentally observed and the numerically calculated outlet temperature of the water circuit.
- Modelling TCM grains of radius  $r$  in shells instead of a single diffusion layer of thickness  $r/4$ . Thus we can distinguish inner and outside water loading on particles ("*beladung*") and better model vapour transport in the TCM.
- Similarly to sorption, iterative modelling and experiments for desorption.

## 5.6. Design of 15 kWh reactor

On the basis of the experience gained during the experiments and modelling described above, a funded design direction for larger thermal storages based on the current set-up has been made. It was agreed that the 'up-scaled and optimized version' of the thermochemical storage developed in the E-hub project would be able to store roughly 15 kWh. The current design therefore aims to reach this storage capacity, while maintaining the operational characteristics based on the performance on the 3 kWh reactor design, as described in the previous sections. A full description of the 15 kWh design based on the current knowledge is given below.

### Demands and principles

Some general principles should be applied in order for the design to be practical, usable, and useful as 15 kWh thermal energy storage for dwelling applications. These principles were taken into account:

- Vessel height maximum 2m to allow installation in dwellings
- Capable of containing 175 kg zeolite (according to the current performance the equivalent zeolite quantity for a 15 kWh set-up)
- Higher packing density in the cylindrical volume, so more compact.

With these principles, the design criteria for the 3 kWh reactor presented in detail in the current report should still be met, i.e. 800W power output and an obtainable temperature difference of over 20K for space heating purposes.

Furthermore, the adsorber heat exchanger demands for the 15 kWh reactor design are as follows (comparable to the 3 kWh design):

- Large surface area for powder/crystal loading
- Short heat pathway between zeolite and water circuit
- Low material use for vessels and tubing
- Modular
- Compact filling of the vessel;

In addition to the above, the updated and scaled-up 15 kWh design should come close to the current design in order for the current experimental and theoretical findings to be useful.

### Solution possibilities

Based on the above principles and demands, the solutions for up-scaling should be found in the following system characteristics:

- Ratio adsorber fin surface area vs. pipe diameter should be kept as is;
- Adsorber pipe fitting should be optimized to better fit the vessel.

With the same surface area vs. pipe diameter (i.e. the same heat exchanger geometry), the results obtained in the described experiments are expected to be largely valid in a larger 15 kWh set-up. Also

the heat response, power and temperature output characteristics will generally comply with obtained results of the 3 kWh reactor. In addition to the characteristics that will be kept similar, the usable volume contained by active material and adsorber heat exchanger can be optimized by slightly changing the heat exchanger size, and by placing these heat exchangers differently in the available volume. An example of an optimized set-up based on the rectangular heat exchangers is given in Figure 5-26.

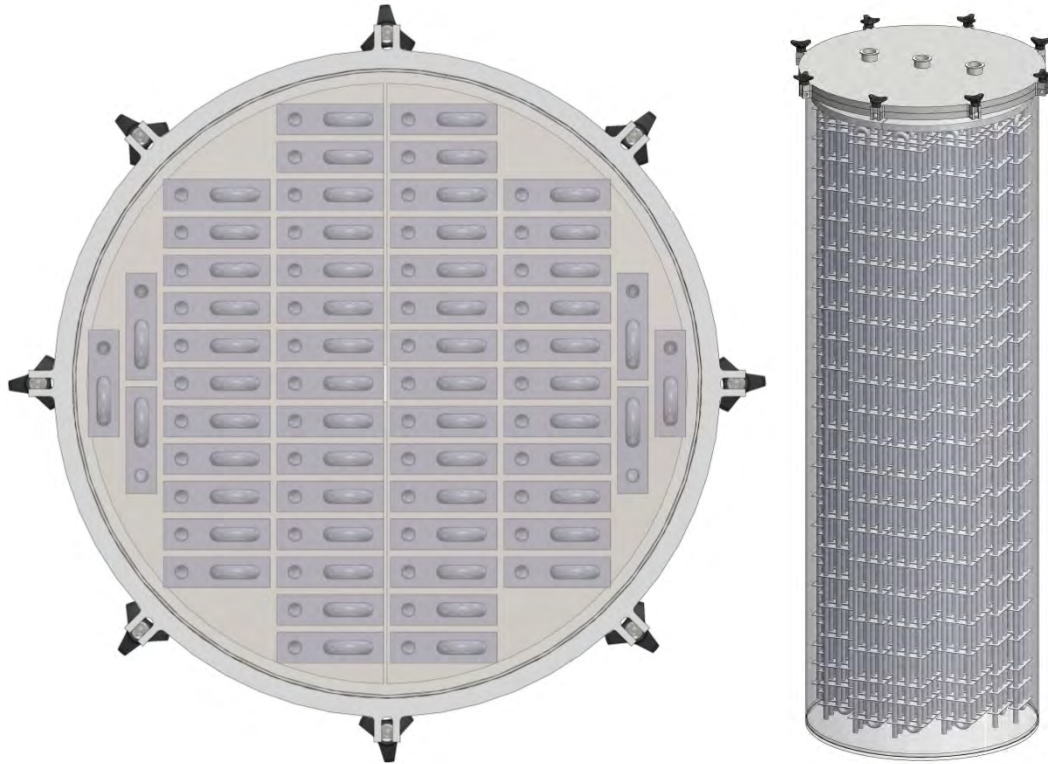


Figure 5-26. *Optimized use of vessel volume by optimized lay-out of rectangular adsorber heat exchangers, bottom view of storage vessel (left) and 3D-view (right).*

The optimized set-up as given above yields more compact thermal storage set-up due to better use of the available volume. The given heat exchanger set-up yields 16 kWh heat storage capacity for the given 174 pipes of 1.8m length, put in a vessel of  $\varnothing 676 \times 2025 \text{ mm}$ .

Optimizing vessel volume coverage by the heat exchangers will be more easy if the heat exchangers are no longer rectangular, but of circular form. An example of an optimized heat exchanger arrangement that fits even better in the available reactor volume, is given in Figure 5-27. The optimized set-up as given yields and even more compact thermal storage set-up due to even better use of the available volume. The given heat exchanger set-up with circular fin-and-tube heat exchanger pipes yields 16.4 kWh heat storage capacity for the given 164 pipes of 1.8m length, put in a slimmer vessel of  $\varnothing 616 \times 2060 \text{ mm}$ . Still, it has been taken into account that enough empty space will be available for the water vapour flow to reach the active material. Clearly, a major improvement can be realized in either of these ways.





Figure 5-27. *Optimized use of vessel volume by optimized lay-out of circular adsorber heat exchangers, bottom view of storage vessel (left) and 3D-view (right).*

Besides a better arrangement of the adsorber/desorber heat exchangers in the available reactor volume, also a slightly different way of feeding the heat exchange liquid through the reactor can be imagined. A header pipe for distribution of the heat exchange liquid was already part of the 3 kWh reactor. In a larger 15 kWh reactor this header pipe might be slightly changed to optimize heat flows in/out of the reactor and therefore to meet the demands more easily. This was already incorporated in the designs discussed above.

A comparison to scale of the new ~15 kWh adsorber/desorber reactor designs with the current set-up of the 3 kWh reactor is given in Figure 5-28 below. It can clearly be seen that a slight increase of size combined with the more-efficient lay-out of the slightly changed heat exchangers yields an enormous amount of additional storage density. The most-optimized reactor would be the one having circular heat exchangers, capable of storing 16.4 kWh with similar operation characteristics to the current set-up (Figure 5-28 right). In principle, it could be produced from the current results directly.



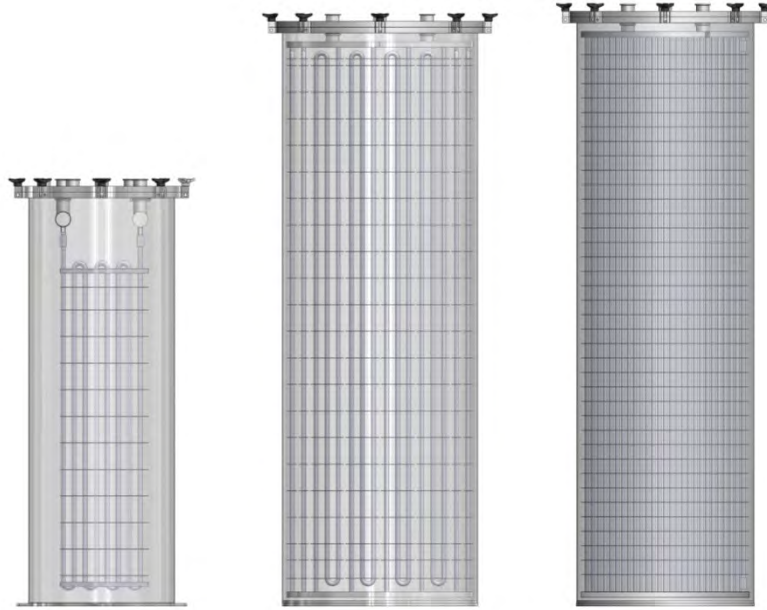


Figure 5-28. Comparison of the 3 reactor designs to scale; current 3 kWh reactor (left), 16 kWh reactor with rectangular heat exchangers (middle) and 16.4 kWh reactor with circular heat exchangers (right).

## Further optimisation

Further optimization can be reached by changing the total set-up even further, thereby using the available cylindrical reactor volume even better. Areas for further improvement are:

- Optimize header/vapour distributor;
- Optimize constructability;
- Optimize vessel and heat exchanger material use;
- Optimize packing of the active material;
- Optimize connections.

When this has been established, it is estimated that a similar-sized vessel can hold a total of about 22 kWh, without changing charging and discharging characteristics too much.

For further cost optimization and reduction of the total mass, the vessel construction should be redesigned.

Using a vessel design with ribbons, the vessel wall thickness can be reduced. Also, materials other than steel can be applied in the vessel, realizing a light-weight and more cost-effective vessel design. However, these further improvements desire further in-depth studies not within the scope of the current project.

## Suggestions for future work

The above suggests the following experiment and model improvements:

- Adjusting TCM model parameters to the experiments, manually or by a fitting tool (e.g. Simulated Annealing). Note that with the initial parameter guesses, the correspondence between simulation and experiments is already rather good;
- A number of model improvements discussed in the previous chapter;
- Use the numerical model to improved design of evaporator, reactor and operation, including HX dimensions, flow speeds, valve dimensions etc. For instance, it seems that power output is mainly limited by (1) choked flow (2) vapour transport in the TCM grains (3) power supply from the reservoir to the evaporator;

- Reconsider power output requirements: how much output power is actually required for a module with a given storage capacity? Is the demonstrated power output of the current E-hub reactor with a storage capacity of about only 3kWh already satisfactory?
- Also reconsider total system setup and operation, e.g. with on-demand heat delivery or with full (de)sorption of modules using a hot water storage.

## 6. Discussion and Conclusions

The previous chapters 3, 4 and 5 described in detail the development, test and analysis of the performances of different concepts for thermal energy storages technologies. The key aspects for these technologies as part of an E-hub system are highlighted in this chapter.

### **Distributed thermal energy storage**

In chapter 3 a comparison is made between different storage concepts for district heating systems. The business case is a situation whereby the district heating grid is heated by a CHP. The electricity produced simultaneously is sold to the spot market. By using the flexibility of the thermal storage in the grid, the operation of the CHP can be transferred to the most appropriate moments (i.e. when the electricity price is high). For every storage concept, the profit is determined. The studied concepts are a common central buffer concept, a concept whereby the thermal mass of the building is used as a heat storage buffer and a concept where the thermal mass of the building in combination with distribution water tanks is used. The profit for these active storage cases are compared to a reference case with normal heat-driven control and no storage available in the grid.

To be able to use the thermal storage efficiently, also an active control framework needed to be developed. The simulation results indicate that the developed control framework perform well, i.e. that the business case – maximization of the profit – is achieved for every case.

The comparison of the profit resulting from the different storage configurations showed that active control of the CHP is able to increase the profit of the CHP significantly. The configuration with storage in distributed buffers and building mass performs best. However this is only slightly better than the active configuration with storage in the building mass only. The results for the central buffer case are a little worse, but still a lot better than in the reference case. The reasons for this worse behaviour is that the thermal mass of the building, which is activated by the first two configurations, is higher than that of the buffers, resulting in much more flexibility and, as a result, higher yields.

The result of this work therefore indicates that active control of district heating grids is very promising with respect to the maximization of the profit of a district heating network supplied by a CHP. It can also be concluded that active storage in the thermal mass of buildings is very promising.

The second part of the work in chapter 3 describes a method to minimize the number of temperature sensors in distributed water storage tanks. Therefore first a simple grey box model for the buffer is proposed, as well as an identification procedure for the model parameters. Validation of this model showed that the procedure was able to identify this correctly. The method to estimate the temperature profile in the buffers when the number of sensors is minimized also shows good results. However, it was shown that the position of the sensors is important to get good results with only a few sensors.

### **Thermochemical heat storage**

At ECN, test results on the open sorption TCS, showed that the concept is capable of working under the designed conditions for long term heat storage. It allows us to store heat for a long period of time and to provide heat at a temperature of 60°C, as needed for domestic hot water and room heating purposes.

However, chemical stability problems of the  $\text{MgCl}_2\text{-H}_2\text{O}$  system prevented its use in the 2<sup>nd</sup> prototype test rig. Zeolite 13X, a stable material as replacement, allowed us to further study the technical aspects of the open sorption concept.

The modular open sorption storage concept has a simple storage reactor design and has the intrinsic flexibility to match both storage capacity and the thermal power requirements. However, the optimization of the design of the air heat exchangers needs careful attention as well as the reduction of heat losses in the air-handling system. The thermal efficiency of the current heat storage system was only 15%. Various causes of heat loss by radiation, convection and by air leakage should be addressed in future prototype systems, in order to reach efficiencies of more than 40%.

A system simulation model was developed that calculates the dynamic processes within a sorption heat storage reactor. The simulations results showed a good agreement with the results obtained in

the experiments. The open sorption TCS simulation model is a valuable tool in support of the design of future TCS systems for different applications.

When considering an open sorption TCS system as a thermal storage component within an Energy hub district it is important to consider slow dynamics. Combinations of TCS storage with sensible heat storage will allow to deal with the different dynamics of short term and long term seasonal heat storage and to provide peak thermal power demands.

To bring the open sorption storage concept to the next stage of development it is required to focus R&D effort on

- Obtaining stable sorption materials with higher energy storage density
- Improving the system thermal storage efficiency, by improving air tightness and reducing thermal losses
- Increasing the ratio of thermal power over auxiliary electric power

At TNO, test results with the 3 kWh reactor showed that design criteria were met experimentally. A temperature lift of 20 – 50 K, a heating power range of 700 – 1600 W and a maximum energy content of 14.3 MJ (4 kWh) were realized. In addition, storage materials (zeolite 5A) properties proved to be constant throughout the measurements performed.

The numerical model developed shows good agreement with the experimental results, even if the simulation parameters were first guesses and not tuned to the experiments. It shows that the main processes of evaporation, mass transport and absorption are well understood and that the model can guide the development of future and larger systems. Further improvements in the modelling can be made, e.g, by modelling the heat exchanger in partitioned sections, and by including the diffusion of water vapour into the zeolite grains in more detail.

A 15 kWh module was designed based on the experience gained with the 3 kWh module. Basically it is a geometrically optimized and slightly enlarged version of it, capable of containing 16.4 kWh under the operation conditions applied to the 3 kWh reactor.

The storage density obtained with zeolite in the 3 kWh reactor is approx. 0.3 GJ/m<sup>3</sup> under the operation conditions applied, assuming the use of solar collectors in the charging process. The system energy density is somewhat lower at 0.08 GJ/m<sup>3</sup>. In the design of the 15 kWh reactor, system energy density was increased to 0.13 GJ/m<sup>3</sup> due to an optimized system lay-out.

However, for practical applications it is necessary to achieve even higher storage densities, in the order of 1 GJ/m<sup>3</sup>. This can be realized by using salt hydrates as storage medium. Future work therefore includes active material enhancement.

## 7. References

- [1] V. Verda and F. Colella, "Primary energy savings through thermal storage in district heating networks," *Energy*, vol. 36, no. 7, pp. 4278–4286, 2011.
- [2] M. Labidi, J. Eynard, O. Faugeron, and S. Grieu, "Optimal design of thermal storage tanks for multi-energy district boilers," in *4th Inverse Problems, Design and Optimization Symposium*, 2013.
- [3] Pagliarini, G. & Rainieri, S., 2010. Modeling of a thermal energy storage system coupled with combined heat and power generation for the heating requirements of a University Campus. *Applied Thermal Engineering*, 30(10), pp.1255–1261.
- [4] Brujic D, Ristic M, Thoma K. Optimal Operation of Distributed CHP Systems for Participation in Electricity Spot Markets. In: *Proceedings of Eurocon 2007, The International Conference on Computer as a Tool*. Warsaw, Poland. ISBN 142440813X; 2007, p. 1463–9. doi:10.1109/EURCON.2007.4400624.
- [5] DHC+ Technology Platform. 2009. "District Heating & Cooling - A Vision Towards 2020 - 2030 - 2050." Brussels: DHC+ Technology Platform.
- [6] Valdimarsson, P. 1993 "Modelling of Geothermal District Heating Systems." PhD thesis, University of Iceland
- [7] Benonysson, Atli. 1991. "Dynamic Modelling and Operational Optimization of District Heating Systems." PhD thesis, Technical University of Denmark (DTU).
- [8] Pálsson, Halldór, Helge V. Larsen, Benny Bøhm, Hans F. Ravn, and JiJun Zhou. 1999. "Equivalent Models of District Heating Systems." 1323. Technical University of Denmark (DTU), RISØ National Laboratory.
- [9] Kleinbach, E M, W A Beckman, and S A Klein. 1993. "Performance Study of One-dimensional Models for Stratified Thermal Storage Tanks." *Solar Energy* 50 (2) (February): 155–166.
- [10] Newton, Brian J. 1995. "Modeling of Solar Storage Tanks." PhD thesis, University of Wisconsin-Madison.
- [11] E. F. Camacho and C. Bordons. 2004. "Model Predictive Control"
- [12] S. Boyd, L. Vandenberghe, and A. El Gamal. 2001. "Design of robust global power and ground networks." In *Proc. of 2001 International Symposium on Physical Design*, 60-65, Sonoma, USA
- [13] "Eurostat." 2013. [http://epp.eurostat.ec.europa.eu/portal/page/portal/statistics/search/\\_database](http://epp.eurostat.ec.europa.eu/portal/page/portal/statistics/search/_database).
- [14] K. Kok, Z. Derzsi, J. Gordijn, M. Hommelberg, C. Warmer, R. Kamphuis, H. Akkermans, Agent-based Electricity Balancing with Distributed Energy Resources, A Multiperspectice Case Study, *Proceedings of the 41st Hawaii International Conference on System Sciences*, 2008.
- [15] E. Peeters, R. Belhomme, C. Battle, F. Bouffard, S. Karkkainen, D. Six, M. Hommelberg, ADDRESS: Scenarios an dArchitecture for Active Demand Development in the Smart Grids of the Future. 20th International Conference on Electricity Distribution, CIRED, 2009.
- [16] K. Vanthournout, R. D'hulst, D. Geysen, G. Jacobs, A Smart Domestic Hot Water Buffer, *IEEE transactions on Smart Grid* 3(4) (2012) 2121-2127.
- [17] B.R.O Anderson, J.B. Moore, *Optimal Filtering*, Dover Publications, New York, 1979.
- [18] R. Pintelon, J. Schoukens, *System Identification a Frequency Domain Approach*, IEEE Press, New York, 2001.

- [19] L. Ljung, System Identification, Wiley Encyclopedia of Electrical and Electronics Engineering, John Wiley & Sons, Hoboken, 1999.
- [20] E.T. Jaynes, Probability Theory The Logic of Science, Cambridge, Cambridge, 2011.
- [21] R. Fletcher, Practical Methods of Optimization, John Wiley & Sons, Hoboken, 1987.
- [22] S. Boyd, L. Vandenberghe, Convex Optimization, Cambridge press, Cambridge, 2011.
- [23] B.D.O. Anderson, J.B. Moore, Optimal Filtering, Dover Publications, New York, 1979.
- [24] H.A. Zondag, B. Kikkert, S.F. Smeding, R. de Boer, M. Bakker, Prototype thermochemical heat storage with open reactor system, Applied Energy 109 (2013) 360–365
- [25] A. Hauer, Evaluation of adsorbent materials for heat pump and thermal energy storage applications in open systems Adsorption (2007) 13: 399–405
- [26] A. Hauer, S. Hiebler, M. Reuss, Waermespeicher, BINE fachbuch 2013 chapter 5.3
- [27] P. Gantenbein, S. Brunold, F. Flückiger, U. Frei Sorbtion materials for application in solar heat energy storage, <http://solarenergy.ch/fileadmin/daten/publ/sorption01.pdf>, accessed 03.01.2014
- [28] G. Santori, A. Frazzica, A. Freni, M. Galieni, L. Bonaccorsi, F. Polonara, G. Restuccia , Optimization and testing on an adsorption dishwasher, Energy 50 (2013) 170 176
- [29] G. Cacciola and G. Restuccia, Reversible adsorption heat pump: a thermodynamic model , Int. J. Refrigeration, Vol 18, No. 2, pp 100 106, 1995
- [30] ASHRAE Handbook , fundamentals 1997

## 8. Annexes

### Annex A: Literature review: distributed thermal storage for application in district heating networks

Thermal storage is suggested as one of the key features in tackling the mismatch between the intermittent heat demand in buildings and the availability of renewable energy sources in a conversion towards a zero-energy or zero-carbon environment. In this context, storage has been acknowledged as one of the key components in the development of energy-efficient district heating systems. In the common case where a central combined heat and power (CHP) plant is responsible for the heat production in a district heating systems, the use of thermal storage shows many benefits:

- Reduction of the use of peak generation units for the heat production
- Reduction of part-load operation in summer periods
- Possibility to match CHP operation with electricity price profiles

Moreover, the use of storage facilitates an energy efficient integration of renewable energy sources by decoupling the energy demand and the production in district heating systems.

Whereas most existing examples of district heating networks make use of large-scale centralized storage units close to the central production units [35-43]. Recent developments in district heating systems are focussed also on the integration of distributed renewable energy sources, such as solar heating. As such, not only the heat demand, but also the heat production has a strong stochastic nature, increasing the need for storage. Gadd and Werner [44] estimated demand fluctuations using time series analysis for Swedish district heating systems. They find a relative seasonal load variation 17% to 28% of the annual average heat demand. Daily load variations of 2.5% to 6% of the annual average heat demand are found, demonstrating that both long-term as short-term storage are essential for balancing between demand and supply. The variations in the demand and supply profiles, and thus the need for storage are therefore categorized in 3 groups:

- Long-term, seasonal storage is designed to overcome the seasonal variation of the heat demand as function of the outdoor climate. Moreover the solar heating potential is higher in summer than winter increasing the need for seasonal storage.
- Short-term is designed for time scales of hours up to half a day, corresponding to the daily variation of the heat demand of buildings. Peak demand periods typically occur in the morning, when recovering from night set-back and in the afternoon, when occupants return from work. The integration of renewable energy sources increases the need for short term storage due to their stochastic nature.
- Medium-term storage is not often discussed in the context of district heating systems as it is not required in the traditional framework but mostly results from the use of renewable energy sources like solar heating. Thereby mid-term storage is used to bridge periods of 1 day to 1 week where solar irradiation is low or overproduction in the electricity network exists due to high wind generation, reducing the profitability of CHP units.

Compared to traditional central powered district heating systems, the integration of renewable energy sources, such as solar heating systems, influences the topology of the network as they often consist of local decentralized production units. Therefore, the integration of distributed thermal storage systems may become more important in the near future. In this context, this chapter gives an overview of the state-of-the-art in distributed thermal storage technologies. Thereby the emphasis is on sensible storage for heating applications.

Firstly, a review is given of the main thermal storage technologies on a system level. Secondly, the active use of the building fabric is analysed as a potential contribution to existing storage technologies. For both structural and non-structural storage an overview of the state-of-the-art technologies is given and the main advantages and disadvantages are discussed. Finally, potential interactions between both means of thermal storage are identified.



## A.1. Characterization of thermal storage techniques

In general three strategies for thermal storage exist:

- Sensible thermal storage
- Latent thermal storage
- Thermochemical thermal storage

Thereby sensible storage is considered as simplest and most widespread technology. The amount of sensible heat that is stored within a material is described by Equation 0-1.

$$Q_{storage} = (m\rho c)\Delta T \quad \text{Equation 0-1}$$

Due to the high volumetric heat capacity and low cost of water compared to other storage media, water is widely used as storage medium for space heating and cooling as well as for domestic hot water storage. In contrast, concrete, melted salts or metals have been applied in high temperature storage ( $>100^{\circ}\text{C}$ ) applications such as solar power or industrial applications [45]. For most construction materials the specific heat capacity  $c$  [ $\text{J}/(\text{kg}\cdot\text{K})$ ] lies within the narrow band of 800-1100  $\text{J}/(\text{kg}\cdot\text{K})$ . Therefore the sensible storage capacity is mainly defined by the amount of heavy construction materials and components that is accessible for thermal storage, e.g. concrete floors, masonry walls...

Moreover the formula points out that sensible thermal storage demands for a change in temperature ( $\Delta T$ ) of the storage materials. In case of sensible storage using the building fabric this change in temperature may influence the thermal environment of the building occupants and is therefore limited by thermal comfort boundaries. It is evident that as the available temperature difference for sensible storage decreases large volumes are required. In order to overcome this problem and increase the storage density, latent TES systems and thermo-chemical storage systems are being developed. These two strategies provide a high storage density and are characterized by a constant temperature at which the storage process occurs. Figure 0-1 compares the required storage volume that is required to cover the annual demand of a Passive house [46]. Assuming a temperature range for sensible storage of 20 K, the energy density of latent TES units is found to be 3 to 5 times higher. Colella et al. [47] however demonstrate that the difference in energy density become less pronounced as the temperature difference available for storage increases. In the context of district heating systems the benefits of using LTES are most important for storage on the building level where the temperature difference is small compared to the primary district heating network.

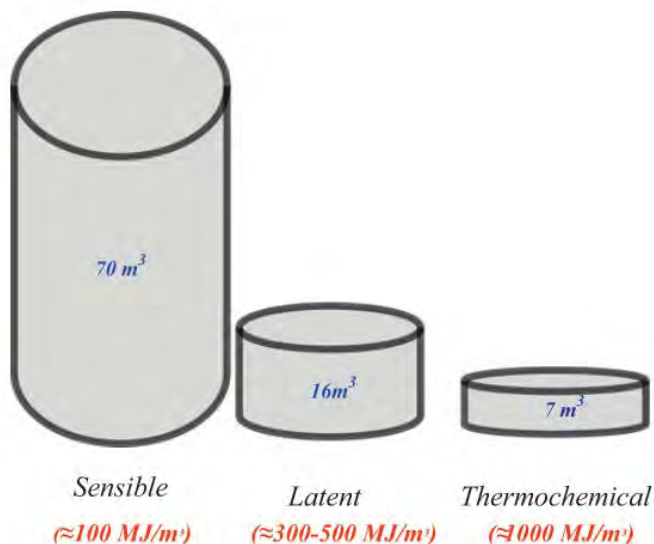


Figure 0-1: Comparison of the required volume to cover the annual storage need of an energy efficient passive house (6480 MJ) [46].

In latent TES applications, the phase change temperature of the storage medium is chosen within the application range for the storage system. As such the latent heat that is absorbed or released during the phase change process contributes to the storage capacity. Thermochemical storage systems make use of reversible thermochemical processes to store energy. Heat is thereby absorbed in an endothermic reaction, breaking or reforming the molecular bonds of the storage medium. This heat can be recuperated in the exothermic, reverse reaction. An extensive literature overview of latent and thermochemical TES systems is given in respectively [46,48-50]. Within the context of this work, the main focus is on sensible thermal storage.

## A.2. Non-structural thermal storage

Non-structural distributed thermal energy storage (TES) systems are defined as TES units that are part of the heating or cooling system of buildings. In the context of district heating systems they are located between the heat exchanger with the district heating system and the heat emission system. The following paragraphs give an overview of the main technologies that are currently available and discuss main benefits and drawback of non-structural storage.

### State-of-the-art technologies

The most common and mature technology for distributed TES on the building system level is sensible TES using water as a storage medium. Water storage tanks are widely used in space heating and domestic hot water applications, to overcome intermittent demand and increase the efficiency of heat production systems. Nevertheless, the energy and exergy efficiencies of these systems is often not satisfactory [51]. The main reason for exergy destruction results from the mixing of the hot supply water with the storage medium typically at a lower temperature. Therefore state-of-the-art technologies are focussed on thermally stratified storage tanks that try to avoid mixing by exploiting the density difference of hot and cold water as shown in Figure 0-2. The use of stratified storage tanks shows potential energy savings up to 20% [52].

Numerical and experimental studies show that the quality of the thermocline and thus the stratification effect is affected by size and shape of the tank (height to diameter ratio), location and geometry of inlets and outlets, temperature and flow rates during charging and discharging and many strategies have been implemented to improve stratification [52-54]. Also adequate insulation of the storage tank is required to avoid the destruction of the thermocline and guarantee a high storage efficiency [54].

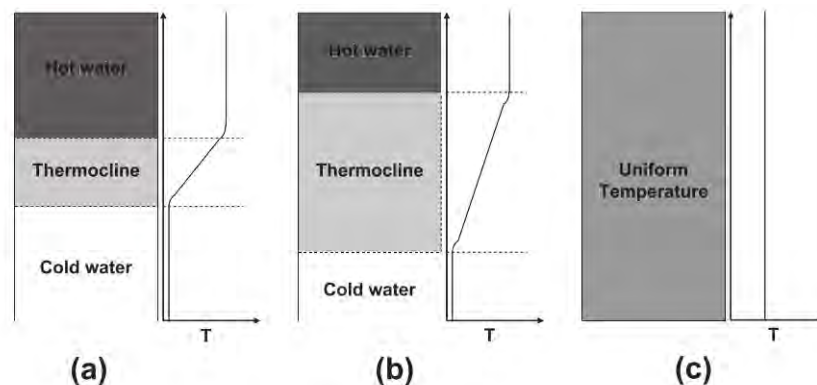


Figure 0-2 Different levels of stratification within a storage tank: (a) highly stratified; (b) moderately stratified; (c) fully mixed [55]

Whereas detailed 2D and 3D simulations, e.g. using computational fluid dynamics, have been established for the development and optimization of stratified storage tanks, a key challenge lies in the development of simplified models. The simplified models should be able to accurately simulate the efficiency and dynamic effects of stratified storage tanks in a computational efficient way, making them suitable for control implementation and building energy simulations. A survey of various types of

storage tanks as well as an overview of simulation models for stratified storage tanks is given in Han et al. [52].

Apart from the simulation of the thermodynamic behaviour of storage tanks, knowledge about the time-varying temperature profile in the storage tank is required if an advanced demand-side management control is to optimize the use of the TES unit. Kreuzinger et al. demonstrate a state estimation procedure to reconstruct the temperature profile based on temperature measurements [56].

Alternatives for sensible thermal storage stratified hot water tanks are mainly focussed on long-term storage [57], such as aquifer [58, 59] or rock-bed and ground storage [60,57]. These technologies are generally characterized by a low energy densities but high volumes, making them more interesting for centralized storage applications where economy of scale plays an important role.

## Benefits and drawbacks

In this paragraph the benefits and drawbacks of non-structural TES for district heating are discussed based on a literature review of the application of distributed non-structural TES. Verda and Colella [61] show that the integration of a 3000 m<sup>3</sup> central water storage tank is able to reduce the peak load in the morning from 600 MW to about 500 MW making it not necessary to use the back-up boilers. As a result the fraction of the total annual heat demand of the district that is delivered by the central CHP increases from 85% without TES to 94% using an optimally sized TES. The investment cost of the TES is estimated at 2400 €/m<sup>3</sup>. Labidi et al. [62] demonstrate annual energy cost savings of 48.3 k€ by optimizing the energy production of a multi-energy heater by adding a central water storage tank. These savings mainly result from the increase of the heat production from wood, reducing the gas consumption. The 200 m<sup>3</sup> water storage tank showed a pay-back time of 2 years and an economic gain of 1.1M€ over 25 years. Pagliarini and Rainieri [63] quantified the impact of a stratified water storage tank on the energy use of the CHP unit of a University campus. They conclude that a water storage tank of 1500m<sup>3</sup> is able to significantly improve the transient behaviour of the CHP unit, resulting in a pay-back period of 4.4 to 3.5 years for an investment cost of 311 to 460 k€.

Nevertheless, application of distributed storage in district heating systems are not common in literature. They are mentioned though as a solution to deploy district heating in areas with low heat densities [64]. The motivation then is that these storage vessels can decrease the peak loads to be transported over the heating network. Therefore the distribution pipes can be dimensioned smaller and consequently the investment costs decrease. As a result, even in areas with low heat densities, district heating can become profitable. Moreover, the use of distributed storage increases the flexibility for modifications to the district heating network, due to a spread out of the investment cost. More important, distributed storage facilities may already be available on a building level when a district heating system is deployed in an existing neighbourhood. As such, the use of these distributed storage facilities may reduce the investment cost significantly.

The use of water storage tanks in residential heating systems has mainly been investigated in the context of peak load reductions and efficiency gains in the heat production system under intermittent heating or cooling conditions.

Already in 1979, Packer et al. [65] demonstrated the potential peak load reductions and energy savings by integration of thermal storage in a residential heat-pump system. The storage tank is used for both space heating and cooling in respectively heating and cooling season. Although a clear reduction in the operational cost was shown, the authors point out the significant investment cost of the TES unit. As such, the storage unit was not economically interesting at that time. Haeseldonckx et al. [66] show the positive effect of thermal storage on the efficiency and lifetime of residential CHP facilities. Including short-term storage increases the operation time and reduces the on/off cycling frequency of a CHP unit significantly, resulting in a reduction of the overall CO<sub>2</sub> emissions.

Recently, due to the increasing importance of renewable energy sources the potential of demand-side management and grid balancing using thermal storage units has been investigated. De Coninck et al. [67] show how demand side management using a domestic hot water tank with very simple rule-based controls is able to reduce PV inverter shut down significantly.

Vanhoudt et al. [68] indicate that addition of thermal storage to a residential heat pump installation can increase the self-consumption of energy produced by photovoltaic power panels.

Arteconi et al. [69] demonstrate that a demand-side management control using a water storage tanks is able to shift the heat demand between 16:00 and 19:00 to off-peak hours (Figure 0-3).

Kiviluoma [70] demonstrates that thermal storage can enhance the operation of electric boilers and CHP units to balance variability in wind production. Thereby the cost optimal share of wind power increased from 35% to 47%.

Whereas these applications focus on the use of storage in electrical Smart Grids, it can be argued that the potential benefits and drawbacks of storage facilities in district heating

systems are comparable with the smart grids scenario. This is especially true, in district heating systems where distributed heat production and solar heating technologies are taken into account.

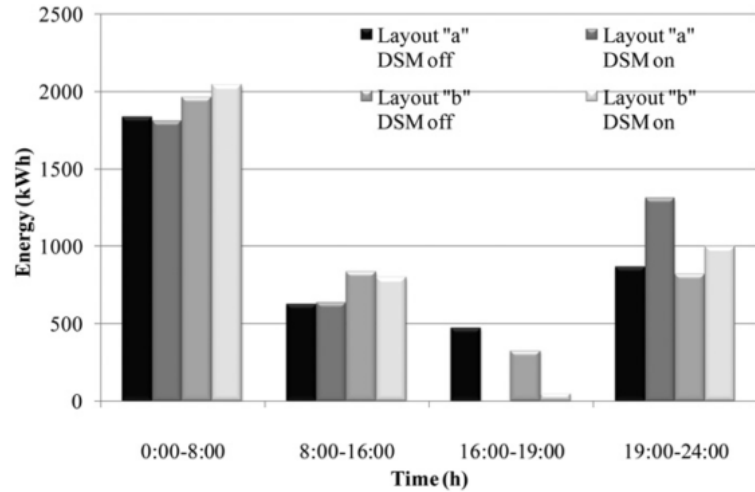


Figure 0-3 Energy consumption for two heating systems with demand-side management using TES enabled ("DSM on") or disabled ("DSM off") [69]

The major drawback of the application of distributed energy storage is discussed by Nuytten et al. [71]. They calculated the flexibility of a CHP with TES in a district heating system, comparing the behaviour of a central located storage near the production unit and distributed small-scale storage at the building level. Thereby the flexibility of the distributed small-scale storage was found to be small, due to a "weakest link" effect. This effect resulted from the fact that the CHP needed to be activated whenever one of the distributed storage vessels is empty, disregarded the state of charge of the other units, demonstrating the need for communication and more advanced control strategies.

Moreover, literature points out that thermal storage comes at a high investment cost [72]. The investment cost of an insulated storage tank varies between 1000-1500 euro/m<sup>3</sup>. The additional cost for the control system is estimated on 1600 euro [73]. In case of LTES, the cost for the PCM is estimated at 1.5 euro/kg or 150 euro/MJ. It is evident that an important cost reduction could be obtained by including the available storage capacity from existing storage units or the structural storage capacity into account in the development of new district heating systems.

### A.3. Structural thermal storage

In addition to the integration of storage devices, the building fabric may be actively or passively used as a short term storage capacity. Although the integration of PCM in building materials is investigated as a possible way of enhance the thermal storage capacity of building components [74-76], structural thermal storage applications mainly rely on sensible thermal storage. The amount of thermal energy that can be stored thereby function of the thermal properties of the building and the heating system as well as the temperature fluctuations that are acceptable for activating the structural TES without jeopardizing thermal comfort.

For typical concrete building structures the thermal storage capacity per square meter of floor area is in the order of magnitude of 12-24 Wh/(°C.m<sup>2</sup>) [77]. For a medium-sized office building [78] with a floor area of 2000 m<sup>2</sup> and a typical comfort range of 2°C, i.e. comfort category 1 defined by EN 15251 [79], the available storage capacity ranges between 120-240 kWh. Within this limited comfort range the structural storage capacity of this office is comparable to a water storage tank of 5000-10000 l, assuming a 20°C temperature range in the storage tank.

Thermal effusivity ( $e$ ) is found to be the main parameter that defines the thermal storage capacity of a building material. Thermal effusivity of a material is defined as the square root of the product of the specific heat capacity  $c$  [J/(kg.K)], the density  $\rho$  [kg/m<sup>3</sup>] and the thermal conductivity  $\lambda$  [W/(m.K)]:

$$e = \sqrt{\rho c \lambda}$$

Equation 0-2

Since the specific heat capacity for common construction materials is within the narrow range of 840-1100 J/(kg.K), heavy construction materials with high thermal conductivity will contribute significantly to the structural storage capacity.

Nevertheless, the availability of thermal mass is not only function of the material properties at the interior surfaces [80]. Also the geometry of the building, the distribution of the thermal mass and the interaction between the heating or cooling systems and the thermal mass play a role in the potential of structural thermal storage [81-85]. Moreover, the thermal performance of the building envelope is expected to influence the potential of structural storage. Since the activation of the thermal mass demands for temperature fluctuations, the use of structural storage results in increased transmission and ventilation losses [86]. As such, the efficiency of the structural storage is higher for well insulated buildings. Nevertheless, the amount of heat that can be stored efficiently for demand-side management reduces with increasing insulation level, since it is not possible to recuperate the heat that is not used for space heating [87].

Evidently, thermal comfort plays an important role in the potential of structural storage as it imposes limits to the allowable temperature fluctuations when the building is occupied. In literature, two general approaches are found to take into account the thermal comfort limits into DSM control strategies. A first approach introduces thermal comfort into the cost function that is optimized to calculate the temperature setpoints [88,89]. As such the cost for deviations from the comfort temperature should be defined and evaluated against the energy cost for heating. Specifying the cost for comfort violations is proven difficult due to the subjective nature of thermal comfort sensation [90]. Therefore the second approach uses thermal comfort criteria to impose boundary conditions to the optimization problem. The level of allowed temperature fluctuations is then based on thermal comfort standards. Commonly thermal comfort criteria are specified in steady state using the PMV-PPD method introduced by Fanger [91] and employed in the ISO 7730 standard [92]. However, Humphreys and Nicol [93] show that due to the flexibility of users in residential buildings, steady state comfort models are no longer valid. Over the last decades the use of adaptive thermal comfort criteria has been suggested in residential buildings to account for the wide range of possibilities to adapt to the thermal environment [94,95]. However, it could be argued that the use of optimal control strategies limits the freedom of the users and thus violates the requirements for adaptive comfort criteria.

## **State-of-the-art technologies**

Passive thermal storage corresponds to the buffer effect of the thermal mass that is available on temperature changes and intermittent gains, such as penetration of solar gains through windows or internal gains from occupants and appliances. As such, passive use of the structural storage capacity may reduce the need for cooling and improve thermal comfort.

Alternatively, active use of the structural storage capacity is a strong growing research topic in the context of demand-side management. By taking into account for example time-of-use energy prices or the intermittent characteristics of renewable electricity production, intelligent control strategies are able to activate the thermal mass embedded in buildings as an active structural storage capacity for demand-side management.

## **Passive use of building mass**

The use of the building mass is well known in moderate climates as a passive means of regulating the indoor temperature. By adapting the architecture to integrate massive construction components, it is possible to benefit from the time lag and damping effects of the thermal mass in order to reduce indoor temperature swings and cooling loads and increase the penetration of passive solar gains [96]. Thereby both numerical and experimental research indicate that an optimal combination and configuration of massive construction materials and thermal insulation in the building envelop reduces the energy use for cooling significantly, especially for locations with large diurnal temperature swings [80,97]. Zhu et al. [98] demonstrate how the thermal mass in heavy buildings is able to store the heat from solar gains and high outdoor temperatures throughout the day and release it at night, resulting in more stable indoor comfort conditions and a significant reduction of the peak cooling load.

The benefits of passive thermal storage are largest for climates with a high daily variation in the ambient temperature.

## Active use of building mass

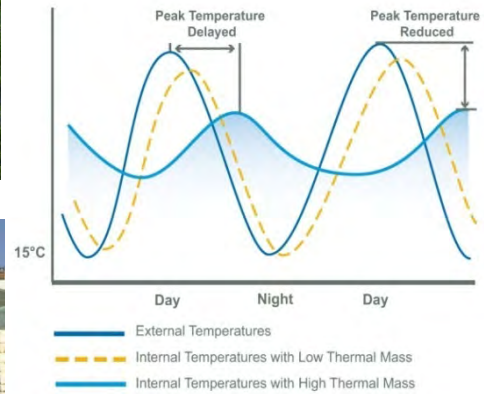
Whereas the passive use of building mass is able to reduce the peak cooling loads, the influence on the overall energy use is limited by the ability to use the free cooling potential at night to regenerate the storage capacity for the next day. Therefore, a lot of work is done on active thermal storage taking into account the interaction between the building mass and the thermal systems. In general, two technologies are suggested to active the structural storage capacity, i.e. (i) the use of ventilation air and (ii) thermally activated building systems.



(a) Low thermal mass



(b) High thermal mass



(c) Temperature profiles

Figure 0-4 Comparison of passive thermal response of light-weight building (a) and heavy-weight building (b)

## Night ventilation

With night ventilation, the cool outside air is used to cool the surfaces of the interior building fabric, regenerating the thermal storage capacity that is charged by internal or solar gains throughout the day. It is proven that the use of night ventilation may reduce the energy use for cooling in office buildings significantly given the diurnal temperature variations are sufficient to provide the cooling load and the building exists of a heavy-weight construction that is easily accessible for the ventilation air [85,99-101]. As shown in Figure 0-5, the free cooling potential for night ventilation strongly depends on the climatic conditions, since the cooling potential decreases with increasing outdoor temperature.

Both natural and mechanical ventilations systems can be used. Thereby the pressure differences and air flow rates obtained by buoyancy-driven or wind-driven natural ventilation are often small and hard to predict. Mechanical ventilation provides a better control on the air flow rate. However, since night ventilation demands for increased air change rates, the use of mechanical ventilation requires high ventilator power and increases the electricity use. In both cases, the accessibility of the thermal mass has a high impact on the efficiency of the system.

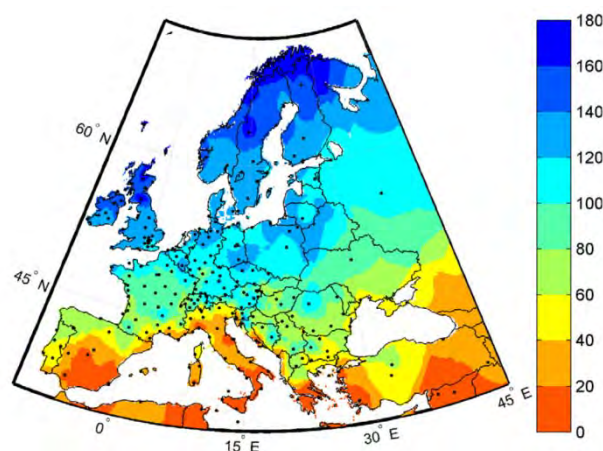


Figure 0-5 Mean climatic cooling potential (Kh/night) in July based on Meteonorm data [102]



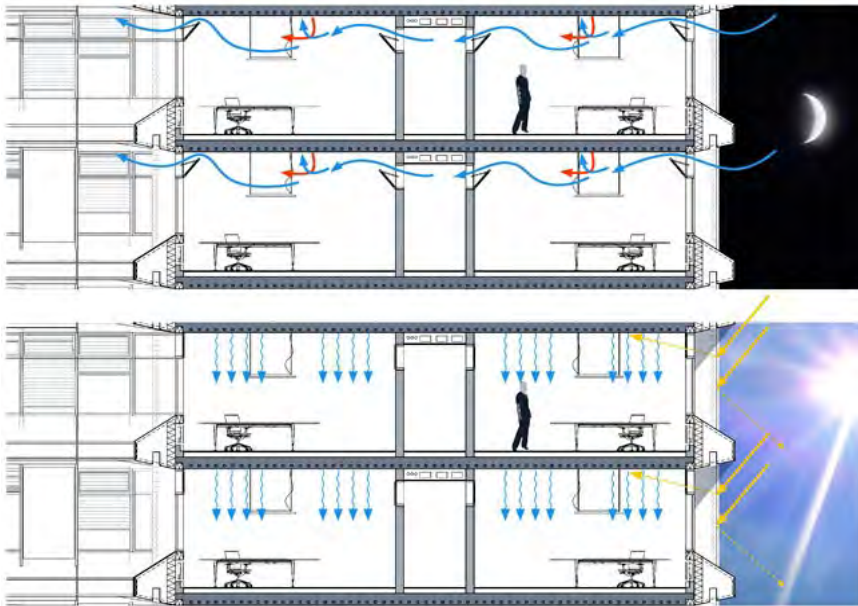


Figure 0-6 Concept of night ventilation in office buildings. (source: <http://www.designyougo.com/projects/fp-0028en.html>)

### ***Thermally activated building systems***

Thermally activated building systems (TABS) are used for heating and cooling in buildings. By integrating pipes into the building fabric, mostly concrete floors and ceilings, the emission system of the heating and cooling system is embedded into the thermal mass of the building which allows to use the thermal buffer of the construction components.

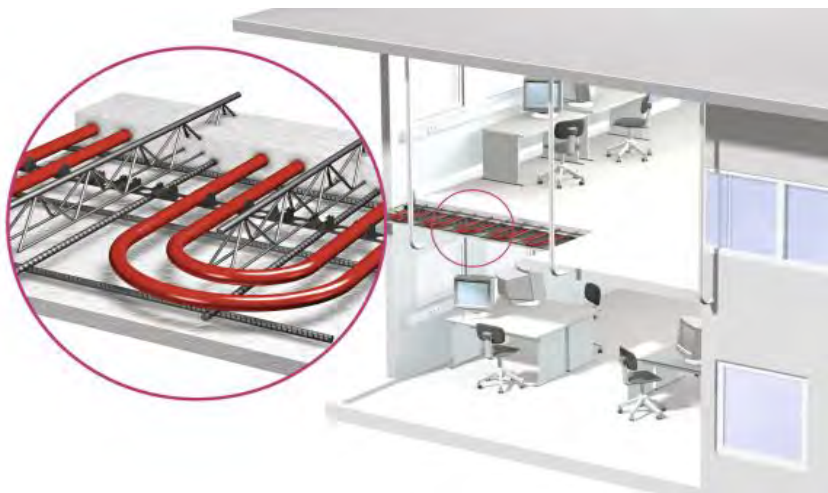


Figure 0-7 Example of TABS in office building (source: <http://www.specifile.co.za/product-highlights/article.php?q=2012-03-28-rehau-promotes-energy-efficient-building-solutions>)

The benefits of TABS are twofold. Firstly, TABS provide cooling at high temperatures (typically 18°C) and heating at low temperatures (typically 25-35°C). As such high efficiencies of the heat production unit can be achieved, resulting in potential energy savings for heating and cooling up to 70% [103,104]. In addition to these energy savings, the storage capacity of TABS allow to deliver the heating and cooling at low power, reducing the required HVAC capacity. By taking into account the



storage capacity of TABS reductions up to 50% of the installed cooling capacity in office buildings are shown, reducing the investment cost for HVAC significantly [82].

Secondly, TABS can rely on the storage capacity of the building mass to reduce the peak heating and cooling demand and shift the energy demand for heating or cooling in time. On the one hand this enables to use the free cooling potential at night or a higher utilization of the passive solar gains during the heating season. On the other hand, TABS have shown a high potential for demand-side management based on e.g. time of use energy prices. As shown in Figure 0-8, intelligent control strategies can be used to optimize the use of thermal storage in buildings by taking into account the thermal characteristics of the building and time-of-use energy prices provided by smart meters [105,106].

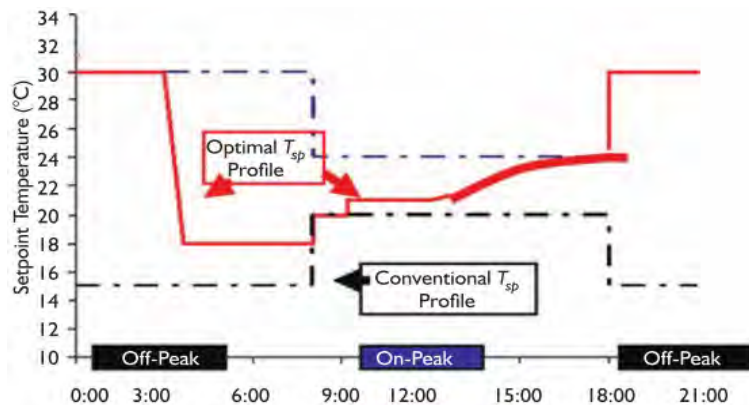


Figure 0-8 Optimal control set-point temperature for off-peak precooling using building thermal mass [86]

## Major benefits and drawback

### Environmental impact

The benefits of using the building mass for thermal storage result from the increased flexibility to shift the energy demand for heating and cooling in time and reduce the peak heating and cooling power. An active and intelligent use of the building mass allows for a better match with the passive gains [88,107] and free cooling potential [107]. Model predictive control in a passive solar commercial building, taking into account the structural storage capacity, resulted in 20% energy savings during mid-season and an increase of thermal comfort with 18% [88]. The energy savings are obtained by a higher penetration of passive solar gains due to the active use of the storage capacity.

Moreover the use of structural thermal storage enables demand-side management opportunities to increase the flexibility of a building in a Smart grid or district heating system. As such a wider penetration of renewable energy sources may be achieved by reducing the mismatch between the energy demand for heating and cooling and the decentralized electricity production. Using the thermal mass as an active storage up to 96% of peak electricity demand of a heat pump system may be shifted to off-peak hours, reducing the impact on the electricity network and increasing the match with local PV-production.

Finally, as shown in Figure 0-9 control strategies that take into account the storage capacity of buildings may use this flexibility to increase of the total primary efficiency of the heating systems [108,109]. As such, a strong reduction of the primary energy use for heating and cooling in the building sector may be achieved.

The potential benefits and efficiency of the activation of the building mass strongly depend on the control strategy. Research shows that traditional control strategies are not able to make use of the storage potential and flexibility that is available in the building mass [110]. Due to the slow dynamics, the use of thermal mass with traditional control often even has a negative impact on the thermal comfort and the total energy use [111-113]. To overcome the problems with controllability, predictive control strategies prove to be able to increase the control efficiency and optimize the use of the storage capacity by taking into account the predicted heating or cooling demand of the building [114,115,88,106,109].

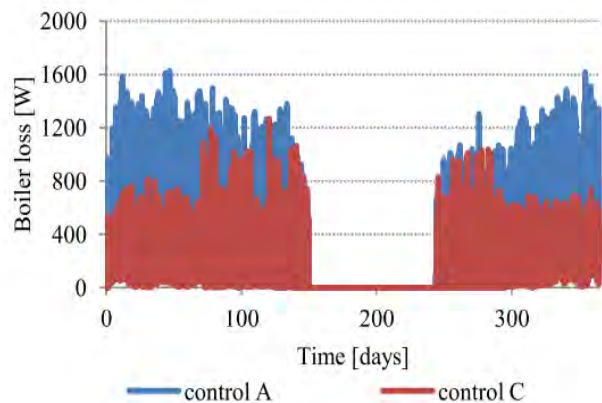


Figure 0-9 *Boiler losses in a residential building for a reference thermostatic control (control A) and a rule-based predictive control that takes into account the thermal mass of the dwelling (control C). A clear reduction of the boiler loss is shown increasing the system efficiency [109].*

In the case of inefficient control, studies on the active use of the building mass demonstrate that activating the thermal mass of buildings results in strongly increased thermal losses by transmission and ventilation, since activating the thermal mass changes the indoor temperature, increasing the temperature difference between the indoor and outdoor environment. Inefficient use of the energy stored within the building mass may therefore increase the total heating and cooling demand of a building [116,117].

In order to obtain an overall reduction in the primary energy use, these storage losses need to be balanced by increased efficiency at production and distribution level [118].

## Economic impact

### Potential

Simulation-based and experimental results show that a model predictive control strategy (MPC) that takes into account both the structural storage capacity of the building and the active thermal storage capacity may result in energy cost savings of 26% up to 40% [77, 119] while maintaining or even improving thermal comfort. These savings mostly result from the free cooling potential (e.g. through night ventilation) [120], a higher contribution of solar and internal gains for passive heating [88] and especially the price differences between peak to off-peak periods in time of use pricing scenarios.

Moreover it has to be emphasized that the investment costs for the activation of the building mass are limited. Based on information from large Belgian engineering companies the additional cost of installing TABS instead of a traditional HVAC-system in office buildings, can be estimated on 18 €/m<sup>2</sup>. Figure 0-11 shows that for medium-size office buildings TABS with a ground coupled heat pump system for heating and cooling are cost-optimal solutions for energy efficient office buildings, i.e. for operating primary energy use below 35 kWh/m<sup>2</sup>a. Nevertheless, in most office and tertiary buildings as well as in massive residential buildings an important storage capacity is already available. In order to activate this building mass, investments are needed in control systems and modifications to HVAC systems, e.g. automated valves, additional sensors.

### Risks and challenges

Both simulations and experimental studies indicate that, although potential energy savings are shown for the use of structural thermal storage, the economic benefits strongly depend on time of use energy tariffs and the use of free cooling potential and passive gains [80,121].

Figure 0-10 shows the energy cost savings obtained by model predictive control using the thermal mass of a three-story office building with a total floor area of 1728 m<sup>2</sup> under three different time of use tariffs. Total energy cost savings vary from 17.9% for the strong incentive time of use tariffs in the heavy-weight building to 0% with weak price incentives and a light-weight building [116].

Table 0-1 shows how energy cost savings obtained by optimal control using only the thermal mass of an office building (zero storage cases) decrease significantly as the outdoor humidity increases. Thereby the outdoor humidity is a measure for the free-cooling potential [120]. For the heavy-weight buildings energy cost savings up to 40% can be achieved using only the thermal mass of the building. As the free-cooling potential decreases, cost savings are negligible. Nevertheless, the authors emphasise that due to the small investment cost of implementing optimal control, assuming most large office buildings are equipped with a control systems, even small cost savings of less than 5% may be profitable.

Table 0-1 Comparison of optimal control of structural thermal storage with weak, normal and strong time of use price incentives [116].

Effect of TOU rate		Heavy mass			Medium mass			Light mass		
		Strong	Normal	Weak	Strong	Normal	Weak	Strong	Normal	Weak
Base case	Chiller elec. (\$)	226	249	249	229	253	269	230	254	270
	Cooling elec. (\$)	309	341	382	313	345	367	313	346	368
	Total cost (\$)	816	908	978	819	912	983	820	913	984
Opt case	Chiller elec. (\$)	76	124	262	85	134	268	87	138	269
	Cooling elec. (\$)	173	278	361	183	289	367	187	295	368
	Total cost (\$)	678	824	976	685	832	983	692	836	984
Savings	Chiller saving	-66.3%	-50.3%	5.0%	-63.1%	-47.0%	-0.4%	-62.0%	-45.6%	-0.1%
	Cooling saving	-44.0%	-18.5%	-0.4%	-41.5%	-16.3%	-0.1%	-40.3%	-14.9%	-0.1%
	Total saving	-16.9%	-9.3%	-0.2%	-16.4%	-8.9%	0.0%	-15.6%	-8.5%	0.0%

Finally, the influence of user behaviour and acceptability will strongly influence the overall potential of building mass activation. Since sensible thermal storage has an impact on the indoor temperature it directly effects the thermal comfort of the occupants. Although studies prove an improved thermal comfort by using predictive control, the flexibility and freedom of users might be influenced.

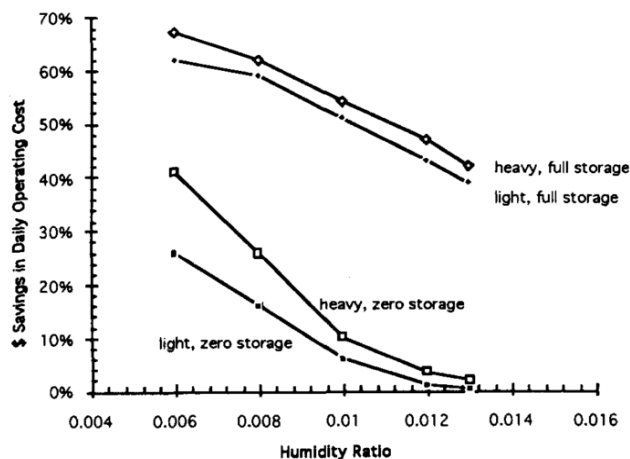


Figure 0-10 Influence of the outdoor humidity on the energy cost savings for optimal control of an office building. A strong decrease in savings is shown due to the decreasing free-cooling potential for increasing humidity [120].

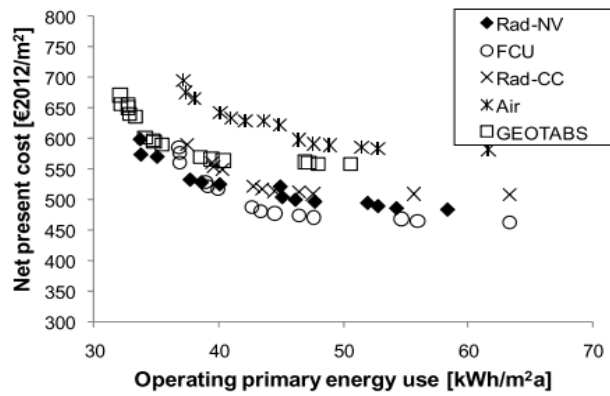


Figure 0-11 Pareto optimal building design variants. In all cases the insulation level, airtightness and glazing area is modified, as well as the heating system. A radiator heating and night ventilation systems (Rad-NV), a fan coil unit (FCU), radiators with chilled ceiling (Rad-cc), an all air system (Air) and a TABS system with a geothermal heat pump (GEOTABS) have been investigated.

## A.4 Bibliography

- [31] V. Verda and F. Colella, "Primary energy savings through thermal storage in district heating networks," *Energy*, vol. 36, no. 7, pp. 4278–4286, 2011.
- [32] M. Labidi, J. Eynard, O. Faugeron, and S. Grieu, "Optimal design of thermal storage tanks for multi-energy district boilers," in *4th Inverse Problems, Design and Optimization Symposium*, 2013.
- [33] Pagliarini, G. & Rainieri, S., 2010. Modeling of a thermal energy storage system coupled with combined heat and power generation for the heating requirements of a University Campus. *Applied Thermal Engineering*, 30(10), pp.1255–1261.
- [34] Brujic D, Ristic M, Thoma K. Optimal Operation of Distributed CHP Systems for Participation in Electricity Spot Markets. In: *Proceedings of Eurocon 2007, The International Conference on Computer as a Tool*. Warsaw, Poland. ISBN 142440813X; 2007, p. 1463–9. doi:10.1109/EURCON.2007.4400624.
- [35] Labidi, M., Eynard, J. & Faugeron, O., 2013. OPTIMAL DESIGN OF THERMAL STORAGE TANKS FOR MULTI-ENERGY DISTRICT BOILERS.
- [36] Eynard, J., Grieu, S. & Polit, M., 2012. Predictive control and thermal energy storage for optimizing a multi-energy district boiler. *Journal of Process Control*, 22(7), pp.1246–1255.
- [37] Verda, V. & Colella, F., 2011. Primary energy savings through thermal storage in district heating networks. *Energy*, 36(7), pp.4278–4286.
- [38] Wigbels, M., Bohm, B. & Sipilae, K., 2002. Dynamic heat storage optimisation and demand side management,
- [39] Brujic, D., Ristic, M. & Thoma, K., 2007. Optimal Operation of Distributed CHP Systems for Participation in Electricity Spot Markets. In *Proceedings of Eurocon 2007, The International Conference on Computer as a Tool*. Warsaw, Poland, pp. 1463–1469.
- [40] Christidis, A. et al., 2012. The contribution of heat storage to the profitable operation of combined heat and power plants in liberalized electricity markets. *Energy*, 41(1), pp.75–82.
- [41] Gebremedhin, A. & Zinko, H., Seasonal heat storage in district heating systems. , pp.1–8.
- [42] Mostafavi Tehrani, S.S. et al., 2013. Hourly energy analysis and feasibility study of employing a thermocline TES system for an integrated CHP and DH network. *Energy Conversion and Management*, 68, pp.281–292.
- [43] Novo, A. V. et al., 2010. Review of seasonal heat storage in large basins: Water tanks and gravel–water pits. *Applied Energy*, 87(2), pp.390–397.
- [44] Gadd, H. & Werner, S., 2013. Daily heat load variations in Swedish district heating systems. *Applied Energy*, 106, pp.47–55.
- [45] S. M. Hasnain, "Review on sustainable thermal energy storage technologies, part I: Heat storage materials and techniques," *Energy Convers. Manag.*, 39(11), pp. 1127–1138, 1998.
- [46] Tatsidjoudoug, P., Le Pierrès, N. & Luo, L., 2013. A review of potential materials for thermal energy storage in building applications. *Renewable and Sustainable Energy Reviews*, 18, pp.327–349.
- [47] Colella, F., Sciacovelli, A. & Verda, V., 2012. Numerical analysis of a medium scale latent energy storage unit for district heating systems. *Energy*, 45(1), pp.397–406.
- [48] Baetens, R., Petter, B. & Gustavsen, A., 2012. Phase change materials for building applications : A state-of-the-art review. *Most*, 42(2010), pp.1361–1368.

- [49] Chan, C.W. & Russel, N., 2011. Thermal Energy Storage Technologies,
- [50] Parameshwaran, R. et al., 2012. Sustainable thermal energy storage technologies for buildings: A review. *Renewable and Sustainable Energy Reviews*, 16(5), pp.2394–2433.  
Parys, W., 2013. Cost Optimization of cellular office buildings based on building energy simulation (phd thesis). KU Leuven.
- [51] Rosen, M.A. & Dincer, I., 2003. Exergy methods for assessing and comparing thermal storage systems. *International Journal of Energy Research*, 27(4), pp.415–430.
- [52] Han, Y.M., Wang, R.Z. & Dai, Y.J., 2009. Thermal stratification within the water tank. *Renewable and Sustainable Energy Reviews*, 13(5), pp.1014–1026.
- [53] Alizadeh, S., 1999. An experimental and numerical study of thermal stratification in a horizontal cylindrical solar storage tank. *Solar Energy*, 66(6), pp.409–421.
- [54] Nelson, J.E.B., Balakrishnan, A.R. & Murthy, S.S., 1999. Parametric studies on thermally stratified chilled water storage systems. , 19, pp.89–115.
- [55] Arteconi, a., Hewitt, N.J. & Polonara, F., 2012. State of the art of thermal storage for demand-side management. *Applied Energy*, 93, pp.371–389.
- [56] Basecq, V. et al., 2013. Short-term storage systems of thermal energy for buildings: a review. *Advances in Building Energy Research*, 7(1), pp.66–119.  
Braun, J.E., 2003. Load Control Using Building Thermal Mass. *Journal of Solar Energy Engineering*, 125(3), pp.292–301.
- [57] Pinel, P. et al., 2011. A review of available methods for seasonal storage of solar thermal energy in residential applications. *Renewable and Sustainable Energy Reviews*, 15(7), pp.3341–3359.
- [58] D. Vanhoudt, J. Desmedt, J. Van Bael, N. Robeyn, and H. Hoes, “An aquifer thermal storage system in a Belgian hospital: Long-term experimental evaluation of energy and cost savings,” *Energy Build.*, vol. 43, no. 12, pp. 3657–3665, Dec. 2011.
- [59] Paksoy, H., Snijders, A. & Stiles, L., 2009. State-of-the-art review of aquifer thermal energy storage systems for heating and cooling buildings. *Proceedings of Effstock*, pp.1–9.
- [60] Dincer, I., 2002. Thermal energy storage systems as a key technology in energy conservation. *International Journal of Energy Research*, 26(7), pp.567–588.
- [61] V. Verda and F. Colella, “Primary energy savings through thermal storage in district heating networks,” *Energy*, vol. 36, no. 7, pp. 4278–4286, 2011.
- [62] M. Labidi, J. Eynard, O. Faugeron, and S. Grieu, “Optimal design of thermal storage tanks for multi-energy district boilers,” in *4th Inverse Problems, Design and Optimization Symposium*, 2013.
- [63] Pagliarini, G. & Rainieri, S., 2010. Modeling of a thermal energy storage system coupled with combined heat and power generation for the heating requirements of a University Campus. *Applied Thermal Engineering*, 30(10), pp.1255–1261.
- [64] Zinko, Heimo, Benny Bøhm, Halldor Kristjansson, Ulrika Ottosson, Miika Rämä, and Kari Sipilä. 2008. “District Heating Distribution in Areas with Low Heat Demand Density.” International Energy Agency.
- [65] Packer, M. & Glicksman, L., 1979. An assessment of thermal energy storage in conjunction with heat pumps for residential heating and cooling. *Energy*, 4, pp.393–399.

- [66] Haeseldonckx, D. et al., 2007. The impact of thermal storage on the operational behaviour of residential CHP facilities and the overall CO<sub>2</sub> emissions. *Renewable & Sustainable Energy Reviews*, 11(6), pp.1227–1243.
- [67] De Coninck, R. et al., 2013. Rule-based demand-side management of domestic hot water production with heat pumps in zero energy neighbourhoods. *Journal of Building Performance Simulation*, pp.1–18.
- [68] Vanhoudt, D. et al., 2014. An actively controlled residential heat pump: Potential on peak shaving and maximization of self-consumption of renewable energy. *Renewable Energy*, 63(3), pp.531–543
- [69] Arteconi, a., Hewitt, N.J. & Polonara, F., 2013. Domestic demand-side management (DSM): Role of heat pumps and thermal energy storage (TES) systems. *Applied Thermal Engineering*, 51(1-2), pp.155–165.
- [70] Kiviluoma, J., 2013. Managing wind power variability and uncertainty through increased power system flexibility (phd thesis).
- [71] Nuytten, T. et al., 2013. Flexibility of a combined heat and power system with thermal energy storage for district heating. *Applied Energy*, 104, pp.583–591.
- [72] Rezaie, B., 2013. Assessing District Energy Systems Performance Integrated with Multiple Thermal Energy Storages.
- [73] Johansson, C., Martin, V. & He, B., 2006. Distributed high capacity cold storage in district cooling systems. In *Ecostock*, 1th international conference on thermal energy storage. Stockton,USA.
- [74] W. a. Qureshi, N.-K. C. Nair, and M. M. Farid, "Impact of energy storage in buildings on electricity demand side management," *Energy Convers. Manag.*, vol. 52, no. 5, pp. 2110–2120, May 2011.
- [75] N. Soares, J. J. Costa, a. R. Gaspar, and P. Santos, "Review of passive PCM latent heat thermal energy storage systems towards buildings' energy efficiency," *Energy Build.*, vol. 59, pp. 82–103, Apr. 2013.
- [76] M. Medrano, L. F. Cabeza, C. Castello, R. Leppers, and O. Zubillaga, "Use of microencapsulated PCM in concrete walls for energy savings," *Energy Build.*, vol. 39, pp. 113–119, 2007.
- [77] Braun, J.E., 2003. Load Control Using Building Thermal Mass. *Journal of Solar Energy Engineering*, 125(3), pp.292–301.
- [78] Parys, W., 2013. Cost Optimization of cellular office buildings based on building energy simulation (phd thesis). KU Leuven.
- [79] EN15251, 2007. Indoor Environmental Input Parameters for Design and Assessment of Energy Performance of Buildings – Addressing Indoor air Quality, Thermal Environment, Lighting and Acoustics.
- [80] Balaras, C.A., 1996. The role of thermal mass on the cooling load of buildings. An overview of computational methods. *Energy and Buildings*, 24(1), pp.1–10.
- [81] Holford, J.M. & Woods, A.W., 2007. On the thermal buffering of naturally ventilated buildings through internal thermal mass. *Journal of Fluid Mechanics*, 580, pp.3–29.
- [82] Rijksen, D.O., Wisse, C.J. & van Schijndel, A.W.M., 2010. Reducing peak requirements for cooling by using thermally activated building systems. *Energy and Buildings*, 42(3), pp.298–304.
- [83] Corgnati, S.P. & Kindinis, A., 2007. Thermal mass activation by hollow core slab coupled with night ventilation to reduce summer cooling loads. *Building and Environment*, 42(9), pp.3285–3297.



- [84] Russell, M., & Surendran, P., 2001. Influence of active heat sinks on fabric thermal storage in building mass. *Applied energy*, 70(1), pp.17–33.
- [85] Wang, Z., Yi, L. & Gao, F., 2009. Night ventilation control strategies in office buildings. *Solar Energy*, 83(10), pp.1902–1913.
- [86] Roth, K., Dieckmann, J. & Brodrick, J., 2009. Using Off-Peak Precooling. *ASHRAE Journal*, (March), pp.80–83.
- [87] Reynders, G., Nuytten, T. & Saelens, D., 2013. Potential of structural thermal mass for demand-side management in dwellings. *Building and Environment*, 64, pp.187–199.
- [88] Kummert, M., André, P. & Nicolas, J., 2001. Optimal heating control in a passive solar commercial building. *Solar Energy*, 69, pp.103–116.
- [89] Castilla, M. et al., 2011. A comparison of thermal comfort predictive control strategies. *Energy and Buildings*, 43(10), pp.2737–2746.
- [90] Mozer, M., Vidmar, L. & Dodier, R., 1997. The neurothermostat: Predictive optimal control of residential heating systems. In *Advances in Neural Information Processing System 9*. Cambridge, MA: MIT Press.
- [91] Fanger, P., 1970. *Thermal comfort: analysis and applications in environmental Engineering.*, United States: McGraw-Hill Book Company.
- [92] ISO 7730, 2005. Ergonomics of the thermal environment – Analytical determination and interpretation of thermal comfort using the PMV and PPD indices and local thermal comfort criteria.
- [93] Nicol, J.F. & Humphreys, M.A., 2002. Adaptive thermal comfort and sustainable thermal standards for buildings. *Energy and Buildings*, 34, pp.563–572.
- [94] Peeters, L. et al., 2008. Control of heating systems in residential buildings: Current practice. *Energy and Buildings*, 40(8), pp.1446–1455.
- [95] De Dear, R. & Brager, G., 1998. Towards an adaptive model of thermal comfort and preference. *ASHRAE Transactions*, 104(1), pp.145–167.
- [96] Al-Sanea, S. a., Zedan, M.F. & Al-Hussain, S.N., 2012. Effect of thermal mass on performance of insulated building walls and the concept of energy savings potential. *Applied Energy*, 89(1), pp.430–442.
- [97] Ogoli, D.M., 2003. Predicting indoor temperatures in closed buildings with high thermal mass. *Energy and Buildings*, 35(9), pp.851–862.
- [98] Zhu, L. et al., 2009. Detailed energy saving performance analyses on thermal mass walls demonstrated in a zero energy house. *Energy and Buildings*, 41, pp.303–310.
- [99] Kolokotroni, M. & Aronis, A., 1999. Cooling-energy reduction in air-conditioned offices by using night ventilation. , 63, pp.241–253.
- [100] La Roche, P. & Milne, M., 2004. Effects of window size and thermal mass on building comfort using an intelligent ventilation controller. *Solar Energy*, 77(4), pp.421–434.
- [101] Geros, V. et al., 1999. Experimental evaluation of night ventilation phenomena. *Energy and Buildings*, 29(2), pp.141–154.
- [102] Artmann, N., Manz, H. & Heiselberg, P., 2007. Climatic potential for passive cooling of buildings by night-time ventilation in Europe. *Applied Energy*, 84(2), pp.187–201.

- [103] Armstrong, P.R. et al., 2009. Efficient Low-Lift Cooling with Radiant Distribution, Thermal Storage, and Variable-Speed Chiller Controls—Part II: Annual Use and Energy Savings. *HVAC&R Research*, 15(2), pp.402–432.
- [104] Gayeski, N.T., 2010. Predictive Pre-Cooling Control for Low Lift Radiant Cooling using Building Thermal Mass by. , (2002).
- [105] Qureshi, W. a., Nair, N.-K.C. & Farid, M.M., 2011. Impact of energy storage in buildings on electricity demand side management. *Energy Conversion and Management*, 52(5), pp.2110–2120.
- [106] Oldewurtel, F. et al., 2012. Use of model predictive control and weather forecasts for energy efficient building climate control. *Energy and Buildings*, 45, pp.15–27.
- [107] Yang, L. & Li, Y., 2008. Cooling load reduction by using thermal mass and night ventilation. *Energy and Buildings*, 40(11), pp.2052–2058.
- [108] Oldewurtel, F. & Gyalistras, D., 2010. Increasing energy efficiency in building climate control using weather forecasts and model predictive control. 10th REHVA World ....
- [109] Reynders, G., Baetens, R. & Saelens, D., 2012. Using thermal mass to counter decreasing overall heating system efficiencies in low-energy dwellings. In 5th International Building Physics Conference. Kyoto.
- [110] Sun, Y. et al., 2013. Peak load shifting control using different cold thermal energy storage facilities in commercial buildings: A review. *Energy Conversion and Management*, 71, pp.101–114.
- [111] Saelens, D., Parys, W. & Baetens, R., 2011. Energy and comfort performance of thermally activated building systems including occupant behavior. *Building and Environment*, 46(4), pp.835–848.
- [112] Sourbron, M. et al., 2009. Efficiently produced heat and cold is squandered by inappropriate control strategies: A case study. *Energy and Buildings*, 41(10), pp.1091–1098.
- [113] Gwerder, M. et al., 2008. Control of thermally-activated building systems (TABS). *Applied Energy*, 85(7), pp.565–581.
- [114] Chen, K., Jiao, Y. & Lee, E.S., 2006. Fuzzy adaptive networks in thermal comfort. *Applied Mathematics Letters*, 19(5), pp.420–426.
- [115] Chen, T.Y., 2002. Application of adaptive predictive control to a floor heating system with a large thermal lag. , 34, pp.45–51.
- [116] Zhou, G., Krarti, M. & Henze, G.P., 2005. Parametric Analysis of Active and Passive Building Thermal Storage Utilization. *Journal of Solar Energy Engineering*, 127(1), p.37.
- [117] Cho, S.. & Zaheer-uddin, M., 2003. Predictive control of intermittently operated radiant floor heating systems. *Energy Conversion and Management*, 44(8), pp.1333–1342.
- [118] Reynders, G., Nuytten, T. & Saelens, D., 2013. Potential of structural thermal mass for demand-side management in dwellings. *Building and Environment*, 64, pp.187–199.
- [119] Henze, G.P., Felsmann, C. & Knabe, G., 2004. Evaluation of optimal control for active and passive building thermal storage. *International Journal of Thermal Sciences*, 43(2), pp.173–183.
- [120] Kintner-Meyer, M. & Emery, A.F., 1995. Optimal control of an HVAC system using cold storage and building thermal capacitance. *Energy and Buildings*, 23(1), pp.19–31.
- [121] Henze, G., Le, T. & Florita, A., 2007. Sensitivity analysis of optimal building thermal mass control. *Journal of solar energy*, 129(November), pp.473–485.

## Annex B: Determination of the values of the building model parameters

The 100 buildings used in the simulation are all derived from one standard building, in detail described in [122]. This building is a detached house with a living area of 103 m<sup>2</sup> and a protected volume of 452 m<sup>3</sup>. The building has a K-value of 40, which is the legal norm in Flanders since 2012. For this building  $C_i$  is 20.13 kWh/K, and  $C_e$  is 21.23 kWh/K. The building is heated by means of radiators which have a low thermal mass, resulting in a thermal capacitance  $C_h$  of 0.17 kWh/K.

Air infiltration losses are modelled by as a power  $P_{iv}$  and resistance  $R_{ia}$ . The power loss  $P$  due to infiltration can be calculated by the formula:

$$\begin{aligned} P &= -\dot{m} c_p \Delta t \\ &= -\rho \dot{V} c_p \Delta t \end{aligned} \quad \text{Equation 0-1}$$

where  $\dot{m}$  is the mass flow rate of the air flow due to infiltration,  $\dot{V}$  the volume flow rate,  $c_p$  and  $\rho$  the heat capacity and density of air and  $\Delta t$  the temperature difference between inside and outside.  $\dot{V}$  was determined by the formula [123]:

$$\dot{V} = A_L \sqrt{C_S \Delta t + C_W U^2} \quad \text{Equation 0-2}$$

where  $A_L$  is the effective air leakage area,  $C_S$  is the stack coefficient and  $C_W$  the wind coefficient and  $U$  the wind speed. Linearisation of this formula leads to:

$$P = \frac{\Delta T}{R_{ia}} + A_{P_{iv}} \cdot U + B_{P_{iv}} \quad \text{Equation 0-3}$$

With

$$\begin{aligned} R_{ia} &= -[A_L \rho c_p \frac{C_S + 2C_S \Delta t_0 + 2C_W U_0^2}{2\sqrt{C_S \Delta t_0 + C_W U_0^2}}]^{-1} \\ A_{P_{iv}} &= -A_L \rho c_p \frac{C_W U_0 \Delta T_0}{\sqrt{C_S \Delta t_0 + C_W U_0^2}} \\ B_{P_{iv}} &= A_L \rho c_p \frac{C_S + 2C_W U_0^2 \Delta T_0}{2\sqrt{C_S \Delta t_0 + C_W U_0^2}} \end{aligned} \quad \text{Equation 0-4}$$

Finally  $P_{iv}$  is defined as  $P_{iv} \equiv A_{P_{iv}} \cdot U + B_{P_{iv}}$ . In the simulation, the following values are used for the coefficients:  $C_S = 4.35 \cdot 10^{-4}$ ,  $C_W = 1.61 \cdot 10^{-4}$ ,  $A_L = 621 \cdot 10^{-4} \text{ m}^2$ ,  $\Delta T_0 = 12.5^\circ \text{C}$  and  $U_0 = 3.5 \text{ m/s}$ .

Calculated according EN 12831 [124], the reference building has maximum static power demand of 9.8 kW at an internal temperature of 20°C and an ambient temperature of -8°C, and excluding ventilation and infiltration losses ( $R_{ia} = 0$ ), electrical power ( $P_{el} = 0$ ) and solar irradiation ( $R_a = 0$ ). From the scheme in [fig:RC], one then can deduct  $R_{ie} + R_{ea} = (20^\circ \text{C} - (-8)^\circ \text{C}) / (9.8 \text{ kW}) = 2.87^\circ \text{C/kW}$ . For the reference building  $R_{ie} = 1^\circ \text{C/kW}$ .

Once all the values for the coefficients are known, the design power for the heating system can be determined. Therefore to the maximum static power demand of 9.8 kW the infiltration losses are added, as well as a reheat term to allow fast reheat of the building. This reheat term was chosen at 22 W/m<sup>2</sup> of heated floor area. In this way, the heating system design load for the standard building is 16.0 kW. The design temperature regime for the heating system is 70°C – 30°C, therefore  $R_h$  can be calculated as  $R_h = (70 - 30) / 16.0^\circ \text{C/kW} = 2.49^\circ \text{C/kW}$ . In the same way,  $R_{ih}$  can be defined as  $R_{ih} = (30 - 20) / 16.0^\circ \text{C/kW} = 0.62^\circ \text{C/kW}$ .

The values above are determined for the standard building. Since in the simulation 100 buildings are used it is relevant to introduce statistical spread in the building parameters. Therefore, for the different buildings the parameters  $C_i$ ,  $C_e$ ,  $C_h$ ,  $C_W$ ,  $C_S$ ,  $R_{ie}$  and  $R_{ea}$  are normally distributed around the value of the standard building with a standard deviation of 20% of the mean value. An overview of the resulting values used in the simulations is shown in Table 0-1.

Table 0-1: *values of the RC-circuit parameters of the building*

parameter	Mean	min	max
$R_h$	2.4825	1.5881	3.6914
$R_{ih}$	0.6206	0.3970	0.9229
$R_{ie}$	1.0035	0.5332	1.7233
$R_{ea}$	2.0057	0.9350	5.0462
$R_{ia}$	12.3195	4.6360	25.5365
$C_i$	20.2141	10.0500	30.9041
$C_h$	0.1621	0.0936	0.2301
$C_e$	21.2738	12.4910	30.5981

## References

[122] Verbeek, Griet. 2007. "Optimisation of Extremely Low Energy Residential Buildings." PhD thesis, KULeuven.

[123] American Society of Heating Refrigeration and Air-Conditioning Engineers. 2009. 2009 *ASHRAE Handbook - Fundamentals*.

[124] European Committee for Standardisation. 2003. "EN 12831 Heating Systems in Buildings - Method for Calculation of the Design Heat Load."

## Annex C: Description of the active control framework

### Configuration without buffers or with decentralised buffers

In the framework proposed in this work we tackled the problems as described in The control algorithms. This control framework used is represented in Figure 0-1. We have a central controller defining the optimal power for the entire district (left side). This controller uses a meta-model of the district and the houses, and defines control actions based upon market information and technical and comfort constraints. The control action resulting from the central controller has to be realised in the actual network with a limited temperature increase to reduce losses (right side). The control actions available are the valves in the different houses, i.e. setting the local heating on/off.

Setting the local heating on/off, results in a mass flow through the local heat exchangers, the local mass flow defined is chosen in the local thermostat controller. As such the idea is to activate as many local thermostats as is required to obtain the power at the generation point selected by the central controller.

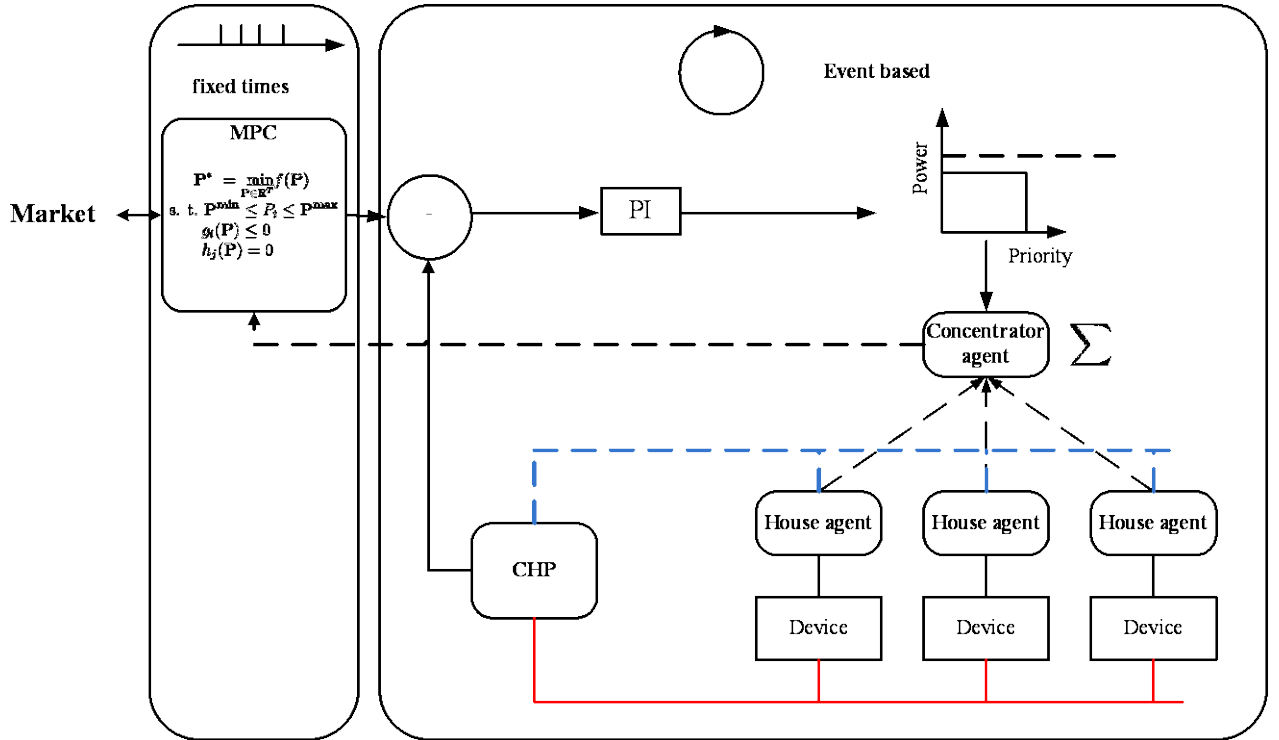


Figure 0-1: Illustration of the controller concept used for optimal control of district heating

### Central Optimization

The central controller is here defined as an MPC controller, i.e. a model predictive controller [11]. It is beyond the scope of this document to describe all details of MPC. Basically an MPC controller defines an optimal set point for the next time slot  $t$  by performing an optimization as defined below with an horizon  $T$ .

$$\begin{aligned}
 P^* &= \arg \min_{P \in R^T} P^T \lambda \\
 \text{s. t.} \\
 T_{A,t} &\leq T_{max} \\
 T_{A,t} &\geq T_{min} \\
 T_{A,t+1} &= \alpha_A(T_{B,t} - T_{A,t}) + \beta_A(T_{O,t} - T_{A,t}) + \gamma_A P_t + Q_t \\
 T_{B,t+1} &= \alpha_B(T_{A,t} - T_{B,t}) + \beta_B(T_{O,t} - T_{B,t}) + \gamma_B P_t + Q_t \\
 \forall t \in \mathbf{T},
 \end{aligned}$$

Equation 0-1

The problem is defined as a linear optimization problem. A linear meta-model of the entire district is governed by the equations is the constraint set  $(T_A, T_B)$ . This model together with predictions of temperature and external distortions is used to define the *optimal* control actions. The  $T_A$  term corresponds to the average temperature of all households as measured by the thermostats. This data is assumed to be available from the thermostats.  $T_o$  Corresponds to the outside temperature,  $Q$  to the external disturbances, e.g. solar irradiance. The temperature  $T_B$  corresponds to a ‘virtual’ mass temperature of the building to include the slow dynamics of the building. Since this is not measured (and cannot be) directly, a state estimation technique is used in the simulations. The linear program is solved with a standard interior point solver [12].

### Agent based dispatch model

Once the optimal heat production is known, this heat needs to be distributed to the different buildings. To this end we use a market-based multi-agent system, similar as in [15]. Basically every agent  $n$  (corresponding to a building) is represented on a virtual market by adding a bid-function  ${}^nb(p_r)$  which indicates the power it will consume (according to ON/OFF) versus a priority  $p_r$ , which indicates the willingness to consume energy.

Also, a required power  $u_D$  is defined by a central controller. A clearing priority  $p_r^*$  is defined which will be sent to the different households. The building for which  ${}^nb(p_r^*) > 0$ , will start consuming energy from the district heating (internally a heating curve is used to define the setpoint).

$$p_r^* = \arg \min_{p_r} \left| \sum_{n=1}^N {}^nb(p_r) - u_D \right|,$$

Equation 0-2

For a building, the priority is defined as:

$$p_r = 1 - SoC = \frac{T_{max} - T}{T_{max} - T_{min}}$$

Equation 0-3

With  $T$  the temperature as measured by the thermostat,  $T_{max}$  and  $T_{min}$  the comfort thresholds. As such an effective State of Charge (SoC) is used. In Figure 0-2, one can see an illustration of the clearing process. The aggregated bid-function of the entire cluster is given as is the bid function corresponding to  $u_D$  (dashed line).

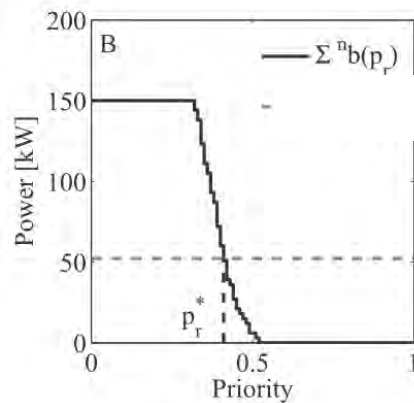


Figure 0-2: Illustration of the bidding process, indicated by the full line is the aggregated bid function of the entire cluster and the bid-function corresponding to control action defined by the central controller, indicated by the dashed line.

In the scenario where local storage is present in the buildings the storage system is also represented by a bid function, using the same definition as above, however with different values for  $T_{max}$  and  $T_{min}$ .

An important feature implemented in the controller (see also Figure 0-1) is a PI(D) controller, which goal is to obtain the power  $P^*$  defined by the central controller described below. It is the output of the PI (we omitted the D action here) controller that represents  $u_D$ . The advantage of using a PI controller is that it solves (to a large extent) some of the problems defined above, i.e. the thermal controllers in

the houses are switched on until the control value  $P^*$  is met. As a consequence the power value  $P^*$  is met without any changes in the supply temperature, which would have resulted in extra losses.

Equally important about the PI controller is that the bid-functions no longer have to be expressed in terms of (thermal) power, but can be expressed in terms of flowrate, which is more practical from an engineering perspective.

At the beginning of every time step, the network supply temperature  $T_{set}$  is defined by means of a heating curve and the mean outside temperature during the last 24 hours. When a number of houses switch their heating system on, this results in a mass flow and temperature drop (between the supply and return side). This power required to keep the inlet temperature at the set temperature, is calculated as:

$$P = \dot{m} c_p (T_{set} - T_{return}) \quad \text{Equation 0-4}$$

The control actions of a PID controller are defined as:

$$u(t) = K_r \cdot \left( e(t) + \frac{\int e(t) dt}{T_i} + T_d \cdot \frac{d e(t)}{dt} \right) \quad \text{Equation 0-5}$$

Where  $e$  is the difference between the actual power  $P$  follows the set points defined by the central controller set point  $P^*$ .

### Configuration with central buffers

For the configuration where a central buffer is present, the approach becomes a lot simpler since the flexibility in the houses is no longer assumed to be controllable. Only the flexibility in the central storage system can be harvested.

As such also here we developed a MPC controller directly for the storage system where the control parameters is charging on/off. This results in the following optimization problem.

$$\begin{aligned} \mathbf{P}^* &= \arg \min_{\mathbf{P} \in \mathbb{R}^T} \mathbf{P}^T \boldsymbol{\lambda} \\ \text{s. t.} \\ P_t &\in \{0, P_{max}\}, \forall t \in \mathbf{T}, \\ T_t^{min} &\leq T_t \leq T_t^{max}, \forall t \in \mathbf{T}, \\ T_{t+1} &= \alpha T_t + \beta P_t \Delta t + \gamma D_t, \forall t \in \mathbf{T}. \end{aligned}$$

$$\text{Equation 0-6}$$

Here  $\mathbf{P}$  is the controller value indicating if the storage system has to be charged, i.e. an integer control variable.

The Temperature  $\mathbf{T}$  (average temperature in the storage) has to remain between the boundaries  $T^{min}$  and  $T^{max}$ . The parameters  $\alpha$ ,  $\beta$  and  $\gamma$  are determined on an independent training set using techniques similar as described In Annex C.

The thermal energy requested by the building is expressed through  $\mathbf{D}$ ,  $D$  is assumed known by the controller.



## Annex D: The buffer grey-box model

As was explained in section 0 the grey-box buffer model is the following form:

$$\frac{dT}{dt} = \underbrace{A(T - T_{\text{external}})}_{\text{heat exchange}} + \underbrace{m(BT + C)}_{\text{draining}} + \underbrace{Du}_{\text{heating}} + \underbrace{E\Delta T}_{\text{mixing}} \quad \text{Equation 0-1}$$

All symbols are explained in Table 0-1. The different components are discussed in more details. Heat exchange between the different layers is described by:

$$A = \begin{pmatrix} \alpha - \beta & \beta & & & \\ \beta & \alpha - 2\beta & \beta & & \\ & & \ddots & & \\ & & & \beta & \alpha - 2\beta & \beta \\ & & & & \beta & \alpha - \beta \end{pmatrix} \quad \text{Equation 0-2}$$

With  $A$  a  $M \times M$  matrix. These parameters are constraint by:

$$\begin{aligned} \alpha &\leq 0 \\ \beta &\geq 0 \\ \alpha - \beta &\leq 1 \end{aligned} \quad \text{Equation 0-3}$$

The parameter  $\alpha$  will be negative if heat loss is significant; otherwise it will be zero.  $\beta$  is always positive, since heat flows from the warmer layer to the colder layer, whereby the third constraint guarantees conservation of energy.

Draining is described by two terms and will only be active if water is tapped from the boiler (when  $m$  differs from zero). The first term describes the movement of water from each layer to the above layer:

$$B = \begin{pmatrix} -\gamma & & & & \\ \gamma & -\gamma & & & \\ & \gamma & -\gamma & & \\ & & \ddots & & \\ & & & \gamma & -\gamma \end{pmatrix} \quad \text{Equation 0-4}$$

with  $B$  an  $M \times M$  matrix. The second term takes the inlet temperature into account

$$C = (\gamma T_{\text{inlet}} \quad 0 \quad \dots \quad 0)^T \quad \text{Equation 0-5}$$

with  $C$  an  $M \times 1$  vector and  $T$  the transpose. The unknown parameter  $\gamma$  depends on the volume of the layers. The position and efficiency of the heating device will differ for each boiler. For that reason a flexible heating term is used

$$D = (\delta_1 \quad \delta_2 \quad \dots \quad \delta_M)^T \quad \text{Equation 0-6}$$

So heating is parametrized by  $M$  potentially different parameters. We have chosen for this type of parametrization, because many different heating systems are present in buffers. Some inject hot water from above, other have an internal hot water tank and some have an electrical heater installed. If the model has to be changed according to each new buffer design, this would cost too much effort to be used in practice.

Mixing will only occur when temperature inversions are present. The stratification effect in the boiler or buffer vessels works as follows: if the system is in a steady state the water temperature increases from bottom to top. However, this is not the case if an internal heat exchanger is injecting heat into the system. In this case, the warm water will rise and will mix with the colder layer on top of it. This is modelled as follows:

First, temperature inversions are detected with:

$$\Delta T = \max(0, FT) \quad \text{Equation 0-7}$$

With

$$F = \begin{pmatrix} 1 & -1 & & & \\ & 1 & -1 & & \\ & & \ddots & \ddots & \\ & & & 1 & -1 \end{pmatrix} \quad \text{Equation 0-8}$$

where  $F$  an  $(N-1) \times N$  matrix.  $\Delta T$  is zero in the absence of temperature inversions and quantifies the inversion when present.

Then, the mixing is modelled by

$$E = \begin{pmatrix} -\varepsilon & & & & \\ \varepsilon & -\varepsilon & & & \\ & \varepsilon & -\varepsilon & & \\ & & \ddots & \ddots & \\ & & & \varepsilon & -\varepsilon \\ & & & & \varepsilon \end{pmatrix} \quad \text{Equation 0-9}$$

with  $E$  an  $N \times (N-1)$  and with  $\varepsilon$  the unknown mixing parameter. If  $\varepsilon$  is small ( $\varepsilon \ll 0.5$ ) almost no heat is exchanged. If  $\varepsilon \approx 0.5$ , both layers end up with equal temperatures after mixing.

Table 0-1: *Symbol list.*

Symbol	Description	Unit & dimension
Counters		
$N$	Number of time steps	(scalar)
$M$	Number of layers in the buffer model	(scalar)
$S$	Number of sensors	(scalar)
Model variables		
$T$	Temperatures inside buffer	K ( $M \times N$ matrix)
$t$	Time	s ( $N \times 1$ vector)
$\Delta T$	Temperature difference between the layers ( $(M-1) \times N$ matrix)	K ( $(M-1) \times N$ matrix)
$m$	Tap water flux	l/s ( $N \times 1$ vector)
$u$	Heating	J/s ( $N \times 1$ vector)

$T_{\text{inlet}}$	Inlet temperature	K ( $M \times N$ matrix)
Model Matrices		
$A$	Heat exchange matrix	( $M \times M$ matrix)
$B$	First draining matrix	( $M \times M$ matrix)
$C$	Second draining matrix	( $M \times M$ matrix)
$D$	Heating matrix	( $M \times 1$ matrix)
$E$	Mixing matrix	( $M \times (M-1)$ matrix)
$F$	Temperature difference matrix	(( $M-1$ ) $\times M$ matrix)
Unknown model parameters		
$\alpha$	Heat loss parameter	1/s (scalar)
$\beta$	Heat exchange parameter (between the layers)	1/s (scalar)
$\gamma$	Heat convection parameter (due to draining)	1/l (scalar)
$\delta$	Heating parameter (layer dependent)	K s/J ( $M \times 1$ vector)
$\varepsilon$	Mixing parameter	1/s (scalar)
$T_0$	External temperature (room temperature of the laboratory)	°C (scalar)
Estimator parameters		
$C, C_0$	Least squares cost function (no index: cost function of the test; index zero: reference cost function)	(scalar)
$\theta, \theta_0$	Vector with all model parameters (no index: tested parameter values; index zero: reference parameter values)	(( $M+4$ ) $\times 1$ vector)

## Annex E: Identification of the buffer parameters

In section 0 the Markov-chain-monte-carlo (MCMC) method is described. This method is used to estimate the buffer model parameters. For every set of parameters, a cost function is calculated. The objective is to find the set with the lowest cost function, i.e. the set of parameters whereby the model simulation results correspond best to the measurements.

In the following figures, the mean root-mean-square (RMS) error is used instead of the cost function, because the cost function scales with the number of measurements and is expressed in °C squared. The mean RMS error is a measure for the mean deviation between the measured and modelled temperatures in the buffer at each sampling moment. This makes this measure independent of the number of observations. The relation between both is:

$$RMS = \sqrt{\frac{C}{NM - n_{\theta}}} \quad \text{Equation 0-1}$$

With  $n_{\theta}$  the number of parameters.

### **Domestic hot water cylinder 1**

The first DHWC is a tank-in-tank system. The model is executed 220.000 times. Figure 0-1 shows the parameter values with a mean RMS value below 20 °C. This is only about 1% of all model runs and mean RMS errors up to one thousand have been scanned. This broad search range is used to ensure that the algorithm did not found only the nearest local optimum in the cost function.

The under bound of error  $\alpha$  follows a relatively smooth line, leading to a single optimum parameter value. This indicates that the identification procedure was probably not stuck in a local optimum. Heat loss has the lowest error for a value close to, but different from, zero per second. The error doubles almost when zero is approached. The second parameter is the heat exchange parameter  $\beta$ . It may be possible that this one is indeed zero per second, since the minimum error remains constant around zero per second. The heat convection parameter  $\gamma$  is effectively zero, as can be seen in the small spread of the lowest error around zero. This means that the heat convection process, as modelled here, is not necessary to describe the measured variations. This does not mean that such processes are not present. As will be shown later, this process is sometimes significant, depending on the experimental set-up and maybe on the geometry of the buffer. The mixing parameter  $\varepsilon$  has a most likely value close to zero. This can be interpreted as follow: including this mixing process does not improve the match of the model on the measurements. For that reason this process can be neglected.

For the heating parameters  $\delta(1)$  to  $\delta(5)$  the error distribution is well defined and significantly different from zero. In addition, these are probably equal to each other, which are not surprisingly for a tank-in-tank DHWC, since the heat flow from the internal tank to the external one is almost identical for each layer.

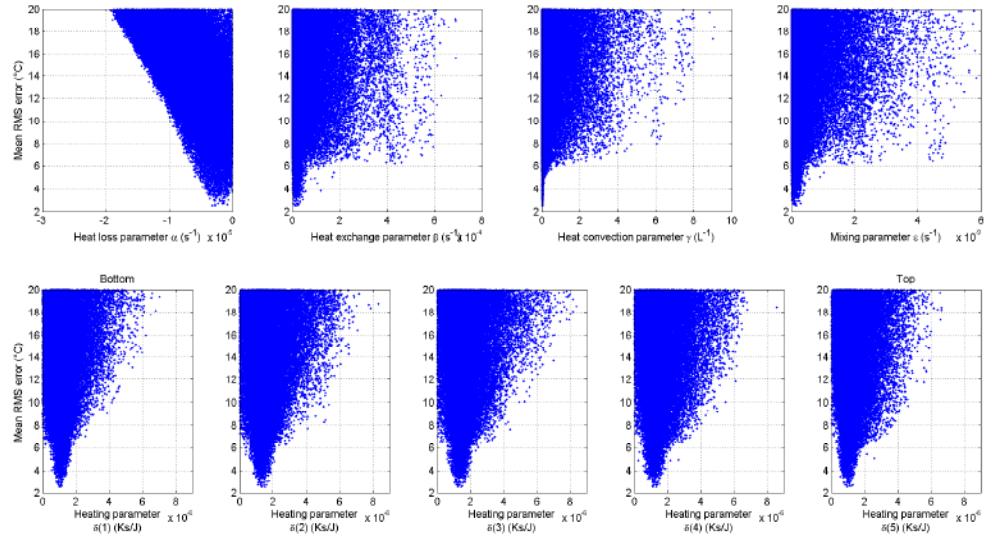


Figure 0-1: *parameter distributions for DHWC 1.*

### **Domestic hot water cylinder 2**

The second DHWC is heated by a spiral internal heat exchanger. Parameter distributions are shown in Figure 0-2.

All distributions have a single clear minimum. Heat loss  $\alpha$  and heat exchange  $\beta$  are possibly zero in this experiment, meaning that the first term in the model is not significantly contributing. The heat convection parameter  $\gamma$  has a well-defined value, different from zero. Just as in the previous experiment, all heating parameters  $\delta$  are identical, which is in agreement with the geometry of the vessel. This is not surprising because the internal heating device in this case is a spiral shaped heat exchanger located at the first lower half of the tank. So the model complexity coincides very well with this particular DHWC.

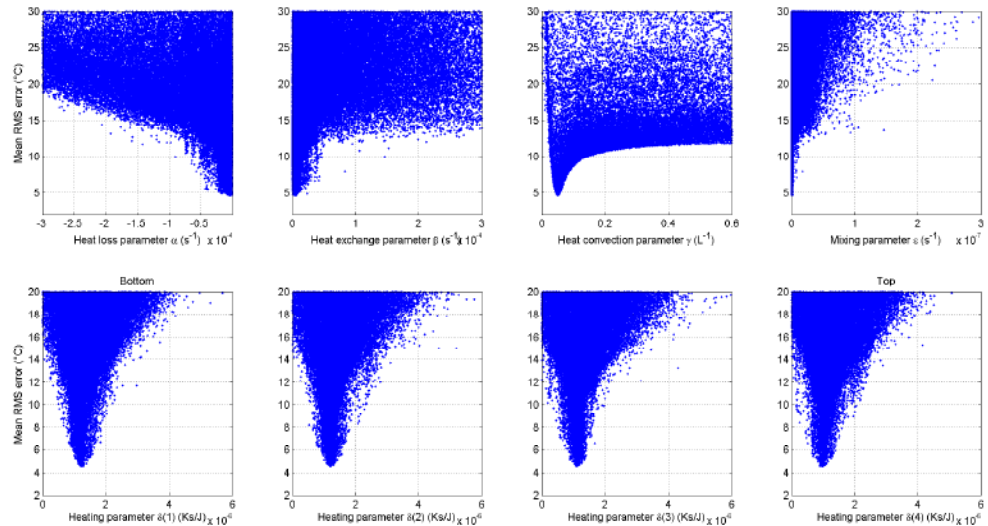


Figure 0-2: *parameter distribution for DHWC 2.*

### Hot water storage buffer 1

The two HWSB installations do not have an internal heating system. Heat is added to the buffer by injecting hot water at the top of the vessel. We modelled this as heating and let the identification procedure identify the layer where heat is injected. If this procedure works correctly the top layers should be chosen.

The parameter distributions are shown in Figure 0-3. None of the parameters are as sharp defined as in the previously discussed DHWC installations. The heat loss and heat exchange parameter have a non-zero value, but the heat convection parameter can have almost any value between zero and ten  $L^{-1}$ . This can be explained as follows: the temperature differences between the layers are small and almost negligible. If cold water is injected from below, this does not cause a well-defined temperature difference between the layers. For that reason, the identification procedure is not able to identify this parameter clearly.

The heating parameters nicely reflect the system. Hot water is injected from above and actually only the top layer is heated in the model. All other layers account for only about 1% of the injected heat.

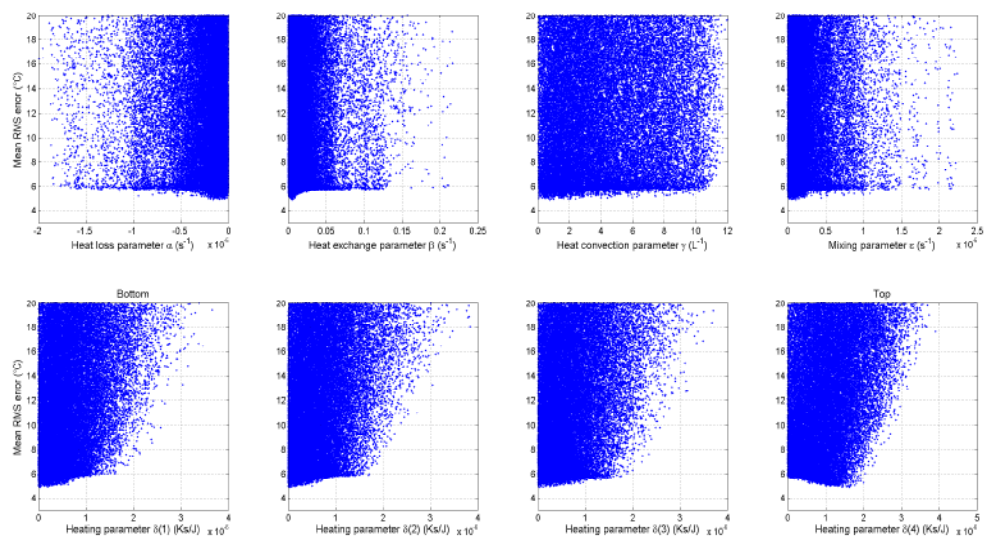


Figure 0-3: *parameter distributions for HWSB 1.*

### Hot water storage buffer 2

In this last experiment a second HWSB is tested. Like with the previous buffer, the stored water is not heated directly, but hot water is injected on top.

The characterization is again less clear than in the DHWC installations. Except for the heating parameters all system parameters are close to zero. Thereby, heat loss is probably not a significant process when describing the variations in the layer temperatures. Heat exchange and mixing have also a minimum that cannot be distinguished from zero. The magnitude of heat loss is comparable with the two DHWCs, but the heat exchange is much larger in this HWSB. This might be due to the fact that hot water is injected, which is a much more disturbing process than providing heat with an internal heat exchanger.

The heat convection parameter is a special case. The model is insensitive to any perturbation of this parameter in the range of 0 to 550  $/L$ , but if the parameter exceeds this threshold value, the error suddenly increases rapidly. So we cannot conclude that this process is absent in this experiment, but nor can we identify a particular value inside this large range.

The heating parameters are all identical and a small decrease in the error function can be found around the optimal value. The heating parameter of the top layer is indeed slightly larger, but one can doubt if this is significant. Especially compared to the two DHWC experiments, the range of acceptable parameter values is much broader.

Errors are not significantly larger than in the experiments with distinct parameter values.

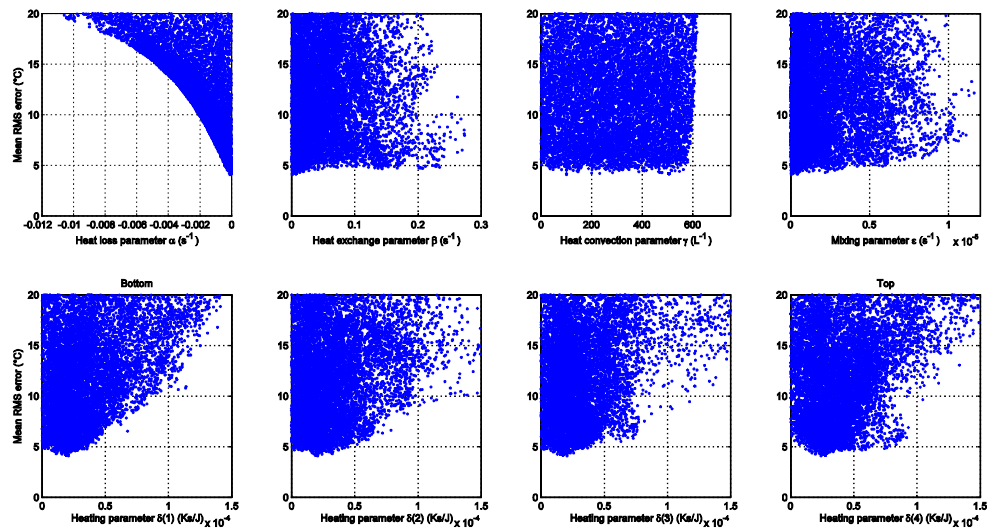


Figure 0-4: parameter distribution for HWSB 2.

## Discussion

### Calculation times

A disadvantage of this MCMC algorithm compared to other methods, like Levenberg-Marquardt, is that the model has to be called many times and therefore, the calculation times may be considerably larger. However, in each of these experiments, the computer runs were performed overnight and were finished within 24h, which is of the same order of magnitude as the experiments themselves. From this point of view, calculation times are acceptable. In addition, these MCMC-like search algorithms, but also genetic algorithms and many others, are more robust against local minima in the cost function surfaces and the resulting parameters can thus be interpreted with much more confidence than local search algorithms.

### Parsimony

Several parameters have an optimal value which is close to zero, as can be seen in Table 3-5. In fact, the residual cost function values with these parameter values present and with the parameter values set to zero are very similar. Therefore, one can wonder if we should include these processes. One argument for not including such processes is parsimony. It states that among competing hypotheses, the hypothesis with the fewest assumptions should be selected and is also called Ockham's razor. Projected on this case, the models which include processes that are in fact insignificant need additional parameters. These additional parameters lead to larger model variability. This necessarily results in less precise predictions. In addition, this additional process is not able to increase the accuracy of the model, since the cost functions (with and without this process) are comparable.

Algorithms are available which can optimize the balance between accuracy (including more processes in the model) and precision (minimizing the uncertainty on the parameters and thus on predictions). In brief, Akaike has formulated a rationale, which minimizes the error between the model and data if these data were resampled with the same set-up [125]. A different school of thought aims at finding the model with the largest probability to be the 'true' model [126, [127]. An overview between these model selection criteria is given in references [128] and [129]. Applied in this context of automated modelling, we compared the model with full complexity with the model where some parameters are set to zero. If cost functions are comparable this process is left out. The remaining significant parameter values are shown in bold in Table 3-5.



#### *Parameter comparison of the different systems*

The heat loss parameter is of the same order of magnitude for both DHWCs and for the first HWSB. The second HWSB has a larger value, as can be seen in Table 3-5. Heat exchange between the layers is comparable for respectively the two DHWCs and the two HWSBs. Evidently, it is much larger in the HWSB systems, since hot water is injected for heating, which causes unavoidably additional mixing between the layers. Heat convection is absent in the first DHWC and well defined in the second one. For both HWSBs the heat convection parameter can have any value in a broad range. Once a certain threshold is exceeded, higher values for this parameter become rapidly unlikely. The mixing parameter is negligible in all experiments. In both DHWCs all layers are heated almost identically. Maybe the top layer has a slightly lower value, but one can doubt if this is significant. The first HWSB is clearly heated in the top layer. This effect should also be present in the second HWSB, but is less pronounced. All layers are heated here. Numerically the top layer has a slightly larger parameter value, but one can doubt its significance.

#### **References**

- [125] H. Akaike, New look at statistical-model identification, IEEE Transaction on Automatic Control 19(6) (1974) 716– 723.
- [126] G. Schwarz, Estimating the dimension of a model, Ann. Stat. 6 (2) (1978) 461– 464.
- [127] J. Rissanen, Modeling by shortest data description, Automatica 14 (5) (1978) 465– 471.
- [128] F. De Ridder, R. Pintelon, J. Schoukens, D.P. Gillikin, Modified AIC and MDL Model Selection Criteria for Short Data Records, IEEE Transactions on Instrumentation and measurement 54(1) (2005) 144-150.
- [129] A. de Brauwere, F. De Ridder, R. Pintelon, M. Elskens, J. Schoukens, W. Baeyens, Model selection through a statistical analysis of the minimum of a weighted least squares cost function, Chemometrics and Intelligent Laboratory Systems 76 (2005) 163– 173.

## Annex F: Kalman filter procedure

To implement the Kalman filter, a number of matrices are defined:

$$\begin{aligned} A_{\text{Kalman}} &= I_N + A^{\text{conduction}} \Delta t + \dot{m} A^{\text{convection}} \Delta t + A^{\text{mix}} \phi F \\ B_{\text{Kalman}} &= A^{\text{heating}} u \Delta t + \dot{m} B^{\text{convection}} \Delta t \\ \phi &= (Fx > 0) \\ H &= \text{diag}(h_1 \quad h_1 \quad \dots \quad h_N) \end{aligned} \quad \text{Equation 0-1}$$

Where  $(Fx > 0)$  is the logical expression which can have values (0 or 1) and where  $h_i$  is one if a sensor is present in layer  $i$  and zero otherwise.

At every time step a prediction is made from the previous time step, a covariance matrix of this prediction is made and the state spaces are updated by combining this prediction and the observed values.

### Prediction of the state and Covariance of the prediction

The next state is estimated by:

$$\begin{aligned} x^+ &= A_{\text{Kalman}} x + B_{\text{Kalman}} \\ C^+ &= A_{\text{Kalman}} C A_{\text{Kalman}}^T + Q \end{aligned} \quad \text{Equation 0-2}$$

Where  $Q$  is a tuning parameter, called the process noise. It should take model uncertainty into account.

### Measurement Update

The Kalman gain is calculated as

$$K = \frac{C^+ H^T}{H C^+ H^T + R} \quad \text{Equation 0-3}$$

With  $R$  the measurement covariance matrix. The states are updated by

$$x = x^+ + K(s - Hx^+) \quad \text{Equation 0-4}$$

With  $s$  the observations.

## Annex G: Supporting information for design, modeling, construction and testing of the closed sorption TCS system

### Summary of design specifications for prototype

Table 0-1. General system requirements.

Quantity	Symbol	Value	Unit
Heat storage capacity	Q	3	kWh
Output power	P	800	W
HX temperature loss	$\Delta T$	5	°C
Water temperature Space Heating (SH)	$T_{SH}$	40	°C
Hydration temperature	$T_H = T_{SH} + \Delta T$	45	°C
Boiler temperature dehydration 1	$T_{B1}$	90	°C
Boiler temperature dehydration 2	$T_{B2}$	140	°C
Dehydration temperature 1	$T_{D1} = T_{B1} - \Delta T$	85	°C
Dehydration temperature 2	$T_{D2} = T_{B2} - \Delta T$	135	°C
Evaporator temperature	$T_E$	10	°C
Condenser temperature	$T_C$	30	°C
Maximum pressure loss liquid H <sub>2</sub> O HX	$\Delta p_{hx}$	0.2	bar
Maximum pressure loss vapour	$\Delta p_v$	1	mbar

Table 0-2. Evaporator properties & dimensioning.

Quantity	Symbol	Value	Unit
Required output power	P	800 (3000)	W
Evaporation enthalpy of water at 25°C	$\Delta h_w$	44	kJ/mol
Molar mass of water	$M_W$	0.018	kg/mol
Required evaporation mass rate	$M_t$	0.327	g/s
Evaporator temperature	$T_E$	10	°C
Evaporator vapour pressure	$p_E$	1221	Pa
Vapour molecular density	$n_E$	$3.12 \times 10^{23}$	m <sup>-3</sup>
Vapour mass density	$\rho_E$	9.4	g/m <sup>3</sup>
Volume flow rate	$V_t$	0.0348	m <sup>3</sup> /s
Maximum evaporation rate 10°C in vacuum	$\phi_{e,m}$	1.35	kgm <sup>-2</sup> s <sup>-1</sup>
Maximum evaporation rate 10°C in vacuum	$Z_{t,m}$	1.35	mm/s
Maximum evaporation rate 10°C, $\Delta p = 1$ mbar	$\phi_{e,\Delta}$	0.11	kgm <sup>-2</sup> s <sup>-1</sup>
Maximum evaporation rate 10°C, $\Delta p = 1$ mbar	$Z_{t,\Delta}$	0.11	mm/s
Minimum evaporator area, 10°C, $\Delta p = 1$ mbar	$A_{E,min}$	30	cm <sup>2</sup>
Minimum temperature evaporator for $\Delta p = 1$ mbar	$T_{E,min}$	8	°C

Table 0-3. Condenser properties & dimensioning.

Quantity	Symbol	Value	Unit
Condenser temperature	$T_C$	30	°C
Condenser pressure	$p_C$	4231	Pa

Table 0-4. Connecting tube between evaporator and reactor.

Quantity	Symbol	Value	Unit
Vapour density, 10°C, 1221kPa	$\rho_E$	9.4	g/m <sup>3</sup>
Vapour mass flow	$M_t$	0.327	g/s
Vapour volume flow	$V_t$	0.0348	m <sup>3</sup> /s
Tube diameter	$D_{tube}$	4	cm
Vapour speed in tube	$v_{tube}$	27.7	m/s

Drag coefficient, inflow, sharp edges	$\zeta_{in}$	0.34	-
Pressure drop inflow tube	$\Delta p_{in}$	1.24	Pa
Molecular velocity at 25°C	$v$	591	m/s
Mean free path ambient air	$\lambda_0$	68	nm
Mean free path at 1221Pa	$\lambda$	5.6	$\mu\text{m}$
Viscosity	$\mu$	$1.0 \times 10^{-5}$	kg/sm
Reynolds number	Re	1079 (laminar)	-
Pressure drop along tube (laminar)	$\Delta p_{tube}$	5.3	Pa

Table 0-5. Heat storage densities and reactor dimensioning for two dehydration temperatures.

Quantity	Symbol	Value	Unit
Density Zeolite (bulk, measured)	$\rho_z$	750	kg/m <sup>3</sup>
Porosity (bulk, measured)	$\varepsilon$	0.73	-
Average evaporation enthalpy	$\Delta h_m$	3.0	MJ/kg H <sub>2</sub> O
Beladung hydration, 45°C, 1221Pa	$B_H$	0.250	g H <sub>2</sub> O/g Z13X
Beladung dehydration 85°C, 4231Pa	$B_{D1}$	0.225	g H <sub>2</sub> O/g Z13X
Difference in beladung, $T_D = 85^\circ\text{C}$	$\Delta B_1$	0.015	g H <sub>2</sub> O/g Z13X
Storage density, $T_D = 85^\circ\text{C}$	$\Delta h_v$	0.038	GJ/m <sup>3</sup> Z13X
Required TCM volume, $T_D = 85^\circ\text{C}$	$V_{TCM1}$	0.28	m <sup>3</sup>
Required TCM mass, $T_D = 85^\circ\text{C}$	$M_{TCM1}$	210	kg
Beladung dehydration 135°C, 4231Pa	$B_{D2}$	0.145	g H <sub>2</sub> O/g Z13X
Difference in beladung $T_D = 135^\circ\text{C}$	$\Delta B_2$	0.105	g H <sub>2</sub> O/g Z13X
Storage density, $T_D = 85^\circ\text{C}$	$\Delta h_v$	0.236	GJ/m <sup>3</sup> Z13X
Required TCM volume, $T_D = 135^\circ\text{C}$	$V_{TCM2}$	0.046	m <sup>3</sup>
Required TCM mass, $T_D = 135^\circ\text{C}$	$M_{TCM2}$	34.5	kg
TCM module height	$L_{z,mod}$	1	m
TCM module width	$L_{y,mod}$	38	mm
TCM module depth	$L_{x,mod}$	33	mm
Number of TCM modules, $T_D = 85^\circ\text{C}$	$N_{mod1}$	32	-
Number of TCM modules, $T_D = 135^\circ\text{C}$	$N_{mod2}$	32	-

Table 0-6. Pressure drop along TCM bed.

Quantity	Symbol	Value	Unit
Vapour density, 10°C, 1221kPa	$\rho_E$	9.4	g/m <sup>3</sup>
Vapour flow in tube, 10°C, 1221Pa	$M_t$	0.327	g/s
Vapour flow in tube, 10°C, 1221Pa	$V_t$	0.0348	m <sup>3</sup> /s
Viscosity	$\mu$	$1.0 \times 10^{-5}$	kg/sm
Module dimension along vapour flow	$L_{x,bed}$	33	mm
Module width	$L_{y,bed}$	76	mm
Module height	$L_{z,bed}$	1	m
Number of modules	$N_m$	32	-
Flow cross-section	$A_{bed}$	2.432	m <sup>2</sup>
Darcy speed	$v_D$	0.014	m/s
HX coolant tube diameter	$D_{HXC}$	12.5	mm
Distance vapour channel to HX coolant	$L_{TCM}$	10.25	mm
TCM diameter, Zeolite 13X	$D_{TCM}$	2	mm
Open volume fraction Bed (HCP spheres)	$\varepsilon$	0.260	-
Permeability bed	$k$	$7.1 \times 10^{-10}$	m <sup>2</sup>
Mean Free Path vapour, 10°C, 1221Pa	$\lambda$	5.4	$\mu\text{m}$
Reynolds number	Re	0.028 (laminar flow)	-
Pressure drop TCM bed	$\Delta p_{TCM}$	2.1	Pa

Table 0-7. Heat transfer coefficient TCM-HX Coolant.

Parameter	Value determined from	Value	Unit
$D_{TCM}$	TCM grain diameter	2	mm
$L_{TCM}$	TCM transport length, TCM grain radius	1	mm
$L_{x,cell}$	Unit cell of module, x-dimension	33	mm
$L_{y,cell}$	Unit cell of module, y-dimension	38	mm
$D_{HXC}$	HX Coolant tube diameter	12.5	mm
$A_{TCM}$	TCM contact area with vins above and below	11.4	cm <sup>2</sup>
$F_{contact}$	Contact fraction of TCM and vins	0.1	-
$\lambda_{TCM}$	Heat conductivity TCM	0.1	W/mK
$H_{TCM,c}$	Heat conductance TCM = $1/R_{TCM,c}$	0.0113	W/K
$D_H$	Hydraulic diameter unit cell	3.5	cm
$L_{vin}$	Average distance from TCM grain to HX coolant tube	6.6	mm
$A_{vin}$	Contact area vin and HX coolant tube	7.854	mm <sup>2</sup>
$\lambda_{vin}$	Heat conductivity TCM	0.1	W/mK
$H_{vin}$	Heat conductance vinplate = $1/R_{vin}$	0.281	W/K
$L_{HXC}$	Wall thickness HX coolant tube	0.5	mm
$A_{HXC}$	Contact area HX coolant tube and coolant	1.57	cm <sup>2</sup>
$S_{HX,wall}$	Heat conductance tube wall = $1/R_{HX,wall}$	122.5	W/K
$e$	Emissivity TCM to vin plate	1	-
$T_{avg}$	Average temperature TCM	305.5	K
$H_{TCM,rad}$	Radiation heat conductance TCM = $1/R_{TCM,rad}$	0.00073	W/K
$H_{TCM}$	Total heat conductance TCM	0.0120	W/K
$H_{cell}$	Total heat conductance cell	0.0115	W/K
$h_{TCM,HXC}$	Heat transfer coefficient TCM to HX Coolant	73.5	W/m <sup>2</sup> K
$h_{TCM,HXC,meas}$	Heat transfer coefficient TCM to HX Coolant, measured	30	W/m <sup>2</sup> K

Table 0-8. HX Coolant tube dimensioning.

Quantity	Symbol	Value	Unit
Output power	P	800	W
HX input temperature	$T_0$	20	°C
HX output temperature	$T_L$	40	°C
Temperature difference TCM – HX output	$\Delta T$	5	°C
TCM temperature	$T_r$	45	°C
Heat transfer coefficient TCM – HX Coolant	h	30	W/m <sup>2</sup> K
Density liquid water	$\rho$	1000	kg/m <sup>3</sup>
Specific heat capacity water	$c_p$	4181	J/kgK
Viscosity liquid water	$\mu$	$7 \times 10^{-4}$	kg/sm
Maximum pressure drop HX Coolant tube	$\Delta p_{HX}$	0.2	bar
HX Coolant tube diameter	$R_{HX}$	6	mm
HX Coolant tube length	$L_{\Delta T}$	67	m
HX Coolant speed	v	12	cm/s
Reynolds number	Re	2057 (laminar)	-
Pressure drop HX Coolant tube	$\Delta p_{HX,true}$	1800	Pa

## Sensor positioning in the reactor

The position of sensors in the reactor, including labeling, is given below.

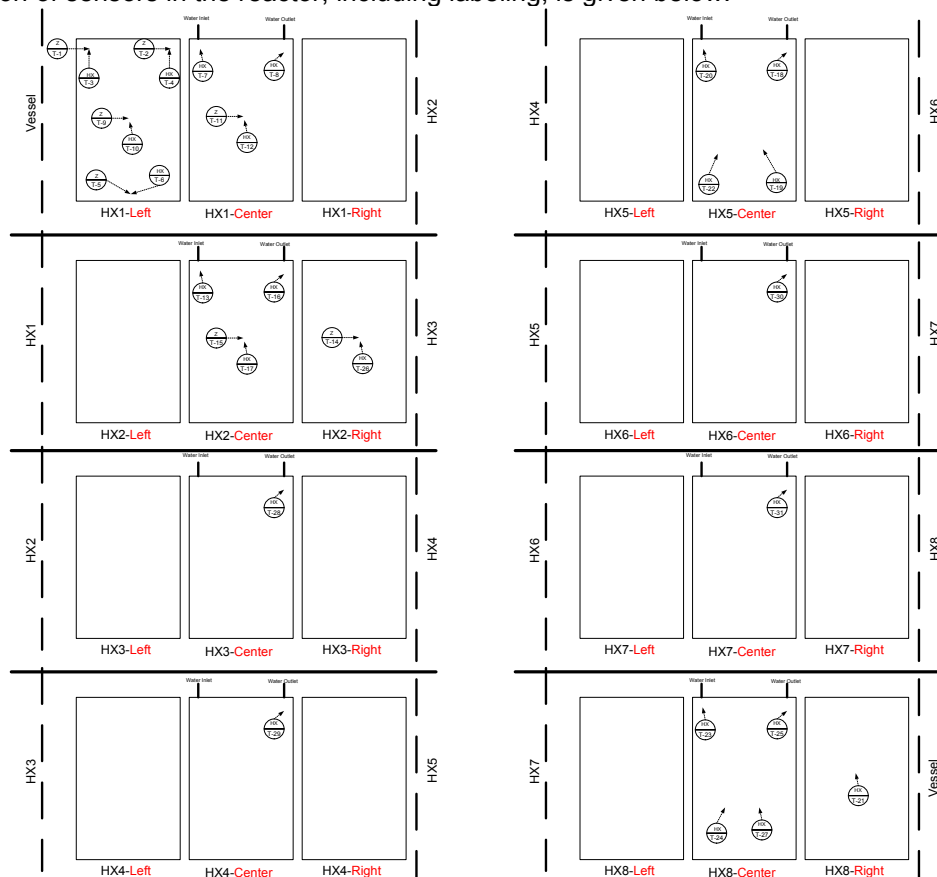


Figure 0-1. Sensor positioning inside the adsorber/desorber in a typical measurement set-up.

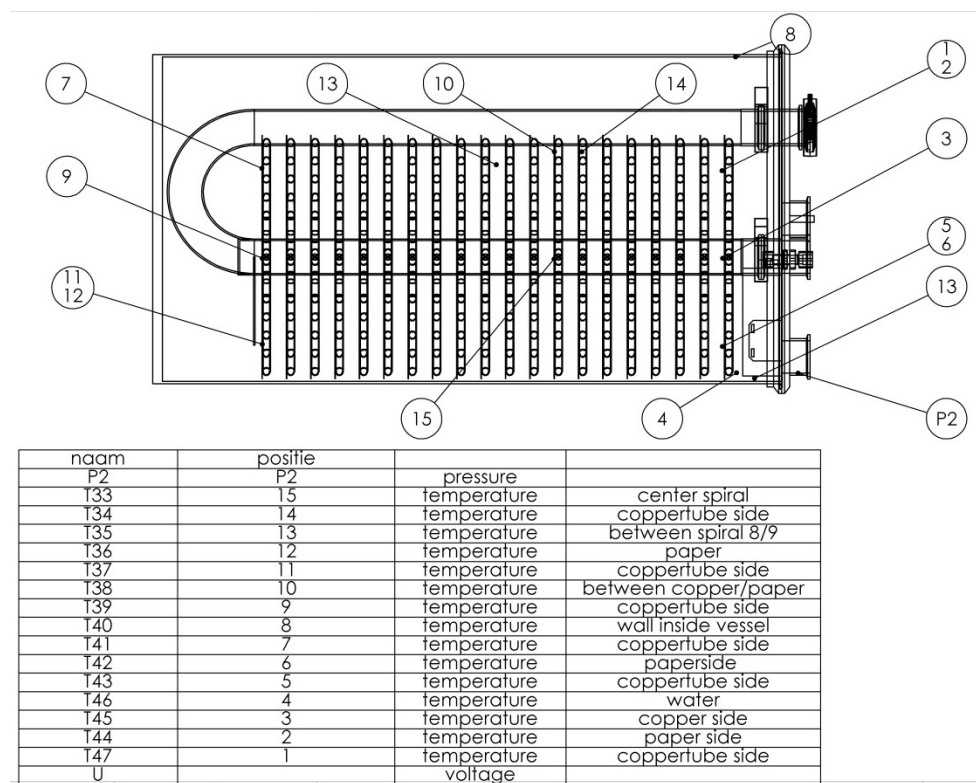


Figure 0-2. Sensor positioning inside the evaporator/condenser in a typical measurement set-up.

## Modelling parameters

Following are the modelling parameters used for simulation.

### %Time loop parameters

- Nt = 1000; %Number of time steps for simulation
- dt = 1; %[s] Time Step

### %Water vapour pressure parameters (Antoine equation)

- Wa = 101300/760; Wb = 8.07131; Wc = 1730.63;
- Wd = 233.426; We = 273.15;

### %Zeolite vapour pressure parameters (Toth equation)

- Za0 = 1.106e-8; %[mol kg<sup>-1</sup> kPa<sup>-1</sup>]
- Zb0 = 4.714e-10; %[kPa<sup>-1</sup>]
- ZE = 9.955e3; %[K]
- Zt0 = 3.548e-1; %[-]
- Zc = -5.114e1; %[K]

### %Mass flow parameters

- MW = 0.018; %[kg/mol] Water molar mass
- RB = 8.314; %[J/molK] Gas constant = Boltzmann constant per mol
- MtotZ = 41; %[kg] Total Z5A mass
- RhoZ = 700; %[kg/m<sup>3</sup>]
- VtotZ = MtotZ / RhoZ; %[m<sup>3</sup>] Z5A volume
- RZ = 0.001; %[m] Z5A spherical grain radius
- NZ = VtotZ / ( (4/3)\*pi\*RZ<sup>3</sup> ); %Number of Z5A spheres
- AZ = NZ \* 4\*pi\*RZ<sup>2</sup>; %[m<sup>2</sup>] Total Z5A area
- AW = 1.4; %[m<sup>2</sup>] Water area evaporator
- TauZ = 75; %[s] Time constant diffusion into Zeolite (probably diffusion into grains of radius RZ)
- Zeta = 1; %[-] Aerodynamics valve + friction factor tubing
- AV = pi \* (0.04/2)<sup>2</sup>; %[m<sup>2</sup>] Valve & tube cross section, E-hub diameter = 4cm
- GW = 1.33; %[-] cp/cv ratio for De Saint Venant equation
- pRpEc = (2/(GW+1)) ^ ( GW/(GW-1) ); %[-] Critical ratio pR/pE for choked flow
- Nit = 10; ConvRatio = 0.1; %Initialize iteration loop

### %HX parameters

- HHX = 30; %[W/m<sup>2</sup>K] Ikon reactor 30W/m<sup>2</sup>K, good value would be 300W/m<sup>2</sup>K
- cpW = 4181; %[J/kgK] Specific heat capacity flow
- RhoW = 1000; %[kg/m<sup>3</sup>] Flow density
- NP = 8; %TCM array of Np x Np = 8x8=64 pipes of 1m, 8 parallel going back&forth through TCM
- LP = 8; %[m] Pipe length through TCM, pipes of 1m going back&forth through TCM
- DP = 0.01; %[m] Pipe diameter
- SP = pi\*DP; %[m] Pipe circumference
- AP = pi\*(DP/2)<sup>2</sup>; %[m<sup>2</sup>] Pipe cross section
- VP = 0.12; %[m/s] Default flow speed through HX pipes => Time constant HX = LP/VP = 67s (85s?)
- LPmin = RhoW\*cpW\*AP\*VP / (HHX\*SP); %[m] Minimum pipe length for saturation
- VPmax = HHX\*SP\*LP / (RhoW\*cpW\*AP); %[m/s] Maximum flow speed pipe for saturation

### %Sensible heat storage and loss Reactor

- TA = 273 + 10; %[K] Ambient temperature
- LxR = NP\*0.038; %[m] Reactor width, 8 pipes, 4 times back&forth through TCM
- LySp = 0.008; %[m] Spacing between rows



- $LyR = NP \cdot 0.033 + (NP - 1) \cdot LySp$ ; %[m] Reactor depth, 8 rows of 8 pipes back&forth through TCM
- $LzR = 1$ ; %[m] Reactor height
- $cpZ = 750$ ; %[J/kgK] Specific heat of Z5A, take value of quartz [BINAS]
- $MtotCu = 0.5 \cdot MtotZ$ ; %[kg] Estimate on 20% of Z5A
- $cpCu = 390$ ; %[J/kgK]
- $Cp = cpZ \cdot MtotZ + cpCu \cdot MtotCu$ ; %[J/K] Heat capacity of reactor
- $AR = 2 \cdot LxR \cdot LyR + 2 \cdot LxR \cdot LzR + 2 \cdot LyR \cdot LzR$ ; %[m<sup>2</sup>] Reactor Area
- $LabdaRW = 0.1$ ; %[W/mK] Thermal conductivity of insulated reactor wall, minimally about 0.04W/mK
- $DRW = 0.03$ ; %[m] Thickness insulated reactor wall
- $UR = LabdaRW / DRW$ ; %[W/m<sup>2</sup>K] Heat conductance reactor wall
- $RA = 1 / (UR \cdot AR)$ ; %[K/W] Heat resistance reactor to ambient environment

%HXE parameters (Evaporator HX with reservoir)

- $HHXE = 300$ ; %[W/m<sup>2</sup>K] Ikon reactor 30W/m<sup>2</sup>K, good value would be 300W/m<sup>2</sup>K
- $NPE = 20$ ; %Number of pipes, 20 spirals of 3.1m
- $LPE = 3.1$ ; %[m] Pipe length through evaporator
- $DPE = 0.008$ ; %[m] Pipe diameter
- $SPE = \pi \cdot DPE$ ; %[m] Pipe circumference
- $APE = \pi \cdot (DPE/2)^2$ ; %[m<sup>2</sup>] Pipe cross section
- $dVdtE = 0.145e-3$ ; %[m<sup>3</sup>/s] Debit HXE
- $VPE = dVdtE / (NPE \cdot APE)$ ; %[m/s] Flow speed HXE
- $LPEmin = \rho W \cdot cpW \cdot APE \cdot VPE / (HHXE \cdot SPE)$ ; %[m] Minimum pipe length for saturation
- $VPEmax = HHXE \cdot SPE \cdot LPE / (\rho W \cdot cpW \cdot APE)$ ; %[m/s] Maximum flow speed pipe for saturation
- $MtotWE = 12$ ; %[kg] Total water mass Evaporator
- $CpE = cpW \cdot MtotWE$ ; %[J/kgK] Heat capacity evaporator
- $LzE = 0.77$ ; %[m] Evaporator length
- $RzE = 0.20$ ; %[m] Evaporator radius
- $AE = 2 \cdot \pi \cdot RzE \cdot LzE$ ; %[m<sup>2</sup>] Evaporator area
- $LabdaEW = 0.1$ ; %[W/mK]
- $DRE = 0.03$ ; %[m]
- $UE = LabdaEW / DRE$ ; %[W/m<sup>2</sup>K] Heat conductance reactor wall
- $RAE = 1 / (UE \cdot AE)$ ; %[K/W] Heat resistance reactor to ambient environment

## Reactor testing procedures

### Vacuum test

Procedure:

- Seal the reactor as it will be normally used;
- Turn on vacuum pump;
- Measure internal pressure ;
- Heat up reactor vessel in order to evaporate any adsorbed gases on internal reactor wall. Use heating lint on exterior of reactor vessel;
- At minimum pressure, seal vacuum pump connection and shut down vacuum pump;
- Leave sealed system for 12-24hrs;
- Monitor any increase of internal pressure.

Interpretation:

If internal pressure increases substantially while 'sealed', a leak is possible and should be fixed.

### **Test thermocouples of the evaporator / condenser**

#### **Procedure:**

- Connect all thermocouples to the appointed locations within the evaporator;
- Connect all thermocouples to the data logger, add a calibrated temperature sensor to the setup;
- Prevent direct external effects on local temperatures (position setup including calibrated sensor within vessel);
- Monitor the measured temperatures;
- Next, use hositrade coupling device to connect thermocouple to the outside;
- Re-connect thermocouples with the data logger;
- Repeat the monitoring test of the thermocouples together with the calibrated temperature sensor.

#### **Interpretation:**

- Measured temperatures should be the same or near the temperature reported by the calibrated temperature sensor. If not, investigate possible causes of error (check connections);
- If no errors found for thermocouples that report different temperatures, consider replacing the thermocouple ;
- Clearly report any measurement errors of the different thermocouples;
- If errors are found after connecting through the hositrade couple piece, this is where the source of the error is likely to be found.

### **Optional: Test evaporator / condenser on leakages**

#### **Procedure:**

- Connect evaporator at gas outlet to medium/high pressure generator;
- Minimize distance between pressure generator and evaporator, double check possible weak spots;
- Leave water cycle inlet / outlet open, i.e. allow free connection to atmosphere;
- Increase (air) pressure within evaporator (2 bar);
- Seal separate evaporator system;
- Monitor system pressure for >2hrs;
- Treat the evaporator carefully to prevent any new leaks.

#### **Interpretation:**

- The internal volume of the evaporator is brought at an increased pressure;
- If the pressure falls (considerably) when sealed, gas is able to leak from the system;
- Water inlet / outlet could be sealed, if pressure keeps decreasing with sealed water inlet / outlet, the leak is positioned at the connection between the top lid of the evaporator and main vessel.

### **Evaporator test**

#### **Procedure:**

- Place evaporator setup on automatic weighing device (scale);
- Connect scale to measuring setup (PC);
- Measure empty (dry) weight of the condenser / evaporator setup;
- Check water content of the evaporator;
- Connect evaporator to vacuum pump;
- Seal setup from environment;
- Start cold water cycle, i.e. condition water temperature within evaporator at evaporating temperature (10°C);
- Measure temperature uniformity through evaporator cycle and water content;
- Put system under vacuum;
- Measure temperatures, pressure and mass decrease of the total system;
- Repeat experiment with dripping plate equipment.

Interpretation:

- A sealed system should end up in equilibrium state, i.e. no water evaporates as no water can leave the system;
- Within a vacuum, system moves to a non-equilibrium. Water can evaporate and leave the system through the vacuum pump;
- Temperatures are expected to be constant;
- Pressure will first sharply decrease and move to some low constant (vapour pressure water at specific temperature?);
- Of interest is the system mass decrease while under constant low pressure and constant temperature, this indicates how fast water evaporates from the whole setup.

### **Condenser test**

Procedure:

- Keep condenser setup on scale and connected to PC;
- Check water content of the condenser (appropriate level);
- Connect evaporator to water bath with controllable temperatures (10 degrees and a little higher should be possible);
- Connect vacuum pump to the system;
- Seal the condenser from the environment;
- Start water flow, wait for evaporator to reach a specific constant temperature (10°C);
- Condition water bath also at 10°C (equal to evaporator so no mass transport occurs);
- Turn on vacuum pump, reduce pressure until water vapour pressure at 10°C & vacuum;
- Disconnect vacuum pump from system while keeping total system sealed from environment;
- Measure specific weights & temperatures of evaporator & water bath;
- Increase temperature water bath such that water vapour pressure is the same as would be in zeolite reactor (33mbar);
- Now that vapour pressure in both components is different, a mass transport should occur. Measure the mass increase of the condenser.

Interpretation:

- Theoretically, the mass decrease of the water bath should be equal to the mass increase of the evaporator. Errors could occur because of water condensation in the piping system. Keeping piping system as short as possible and non-horizontal could minimize these errors;
- Of interest is how much water is condensed by the condenser at the foreseen conditions.

### **Test thermocouples**

Procedure:

- Connect thermocouples to the fixed positions on the reactor heat exchanger;
- Connect thermocouples to the Agilent data logger;
- Position calibrated thermocouple / Pt100 next to (not connected to) heat exchanger;
- Block heat exchanger from any air flows (walls / box);
- Compare measured thermocouple temperatures with value calibrated thermocouple.

Interpretation:

- Thermocouples placed on the heat exchanger are to provide temperatures that are (at least) close to the calibrated (i.e. real) temperature;
- If not, seek source of difference, check connection spots and tip of thermocouple;
- Ultimately replace the thermocouple if source of error remains unclear.

### **Optional: Test heat exchanger leakages before zeolite loading (8x)**

Procedure:

- Connect heat exchanger to medium/high pressure generator;
- Minimize distance between pressure generator & heat exchanger, double check possible weak spots;
- Increase (air) pressure within heat exchanger (choose limit);

- Seal separate heat exchanger system;
- Monitor system pressure for >2hrs;
- Treat the heat exchangers carefully to prevent any new leaks;

Interpretation:

- Connection weak spots should be double checked, if pressure in system falls while system is supposed to be sealed, this indicates a leakage in the heat exchanger;
- Leaking systems are to be replaced with new ones.

### **Loading zeolite in heat exchanger**

Procedure:

- First the dry weight of the heat exchanger is to be measured (before loading);
- Get a clean & dry box that can withstand high temperatures of drying. Weigh the empty dry weight of this box + lid + labeling;
- Load zeolite in the heat exchanger with glue;
- Let heat exchanger dry (carefully), retrieve zeolite that is not mounted into the heat exchanger;
- Weigh the new mass of the loaded heat exchanger;
- Weigh the new mass of the remaining zeolite that is not added to the heat exchanger;
- Calculate the respective masses of the zeolite added to the heat exchanger and the zeolite taken from the initial amount;
- Take an amount (ca. 50g) of 'wet' zeolite of the remainder zeolite and weigh this;
- Dry the specific amount of 'wet' zeolite for (>24hr, >150 degrees) in order to evaporate any adsorbed water;
- Get mass of the 'dry' zeolite. Calculate mass difference between 'wet' and 'dry' zeolite, calculate the amount of dry zeolite in the heat exchanger system;
- Treat the loaded heat exchangers carefully to prevent any loss of zeolite from the heat exchanger.

Interpretation:

- The mass of glue in the heat exchanger is considered insignificant and neglected;
- Mass of loaded heat exchanger and mass of test sample should be taken in the same time frame in order to prevent weather changes to be of any effect on the test;
- Mass of the dry zeolite should be measured shortly after removal from the oven, as to prevent the adsorption of water. Consider a closable box / unit to prevent the adsorption of atmospheric water on dry zeolite.

In order to make a careful prediction of the theoretic system performance, it is essential to know the amount of zeolite that is present in the reactor. Inaccuracy will lead to an error of the system performance, thereby increasing the gap between system measured performance and system theoretical performance.

### **Test thermocouples after zeolite loading**

Procedure:

- Position all thermocouples at the preferred location in the heat exchanger (note that each heat exchanger is to be labeled properly in order to prevent any later mistakes);
- Connect all thermocouples (including the ones fixed at the heat exchanger surface) to an data logger;
- Add 'gaas' (wire mesh) to the setup and connect / fix thermocouples to this. The 'gaas' is used to 'carry' the main mass of the thermocouple in order to reduce any stress on the glued zeolite in the system;
- Connect an calibrated environment temperature sensor (Pt100?) to the data logger;
- Block heat exchanger from any air flows (walls / box);
- Compare measured thermocouple temperatures with value calibrated thermocouple.

Interpretation:

- Thermocouples placed on the heat exchanger are to provide temperatures that are (at least) close to the calibrated (i.e. real) temperature;
- Thermocouples measured at an earlier stage are not likely to yield new significant errors;
- If errors are measured, seek source of difference, check connection spots and tip of thermocouple;
- Ultimately replace the thermocouple if source of error remains unclear.

#### **Optional: Test heat exchanger on leakages after zeolite loading**

Procedure:

- Connect loaded heat exchangers with known amount of zeolite with the header;
- Connect headers with the reactor top;
- Load the heat exchangers / header / top combination into the reactor;
- Connect pressure generator to the headers / top outlets;
- Increase gas pressure in heat exchangers;
- Seal heat exchangers;
- Monitor pressure possible drop over time (>2hrs).

Interpretation:

- Separate heat exchangers were tested on leaks. Considered they have been treated carefully, no leaks should occur within the heat exchanger;
- Any currently exposed leak is likely to be located in connection between heat exchangers with headers or headers with top.

#### **Test performance in case of idle system**

Procedure:

- Reactor is loaded with zeolite and heat exchangers;
- Connect thermocouples through connector elements (hositrade);
- Connect connector outputs to the agilent data logger ;
- Connect data logger to the computer;
- Connect and check the reading of the weighing scales with the computer;
- Connect all system components (reactor, evaporator, vacuum pump, water flow unit);
- Check if all sensors work and initiate data sampling;
- Turn on vacuum pump / create vacuum, monitor vacuum (pump) influence on sensor data output;
- Fix any not performing sensor,

Interpretation:

- Final check if all system components (sensors etc.) produce an output while system is still at rest;
- Up to this point, everything should work as intended. After this, the system is not supposed to be opened up again (on a short notice).

#### **Test performance in case of system in operation**

Procedure:

- If not, seal system from environment (close lids, etc.);
- If not, put system under vacuum;
- If not, close valves to vacuum pump, turn off vacuum pump;
- If not, close valve between adsorber and condenser;
- Initiate cold water cycle at 10°C and start flow through the condenser (Tcondenser should stabilize at 10 °C);
- Monitor the sensors output (should be stable / become stable over time);
- Open connection between condenser & adsorber;
- Monitor sensor outputs (might change due to water transport from adsorber to condenser);

- Get hot water cycle at 90°C, without flow through the adsorber;
- Initiate hot water flow through the adsorber;
- Monitor sensor outputs (should change due to desorption zeolite);
- Check if all sensor yield outputs that are expected;
- After 30min, close valve between adsorber & condenser;
- Disconnect hot water flow through adsorber;
- Cool hot water cycle to 20°C;
- When adsorber water cycle is at 20°C, initiate flow through adsorber;
- Cool adsorber to 20°C until stable temperature;
- Maintain water temperature of evaporator at 10°C;
- Open connection adsorber & evaporator;
- Monitor sensor output while water adsorbs again on surface zeolite;
- Measure until system stabilizes (zeolite fully adsorbed with water, no mass flow from evaporator to adsorber, i.e. no mass decrease evaporator).

Interpretation:

- Short check is sensors give expected results while system in operation. Not intended as full first cycle.

## List of performed experiments with their respective parameters

Following is the list of performed experiments, and their respective parameters.

Table 0-9. *List of performed experiments, and their respective parameters (1/5).*

Experiment	remarks	T desorption	T condenser	T adsorption	T evaporator	dT desorption - condensation
[#]		[Celsius]	[Celsius]	[Celsius]	[Celsius]	[Kelvin]
1	short term exp.	90.0	10.0	20.3	18.1	80.0
2	short term exp.	80.0	12.0	21.5	19.4	68.0
3	short term exp.	95.0	12.0	24.7	14.8	83.0
4	short term exp.	80.0	12.0	21.3	12.3	68.0
5	short term exp.	91.0	11.0	21.4	7.8	80.0
6	short term exp. / air in heat exchanger	91.0	11.0	21.6	14.9	80.0
7	short term exp.	91.0	11.0	21.3	14.8	80.0
8	short term exp.	97.0	11.0	21.9	14.8	86.0
9	short term exp.	97.0	20.0	20.7	14.8	77.0
10	short term exp.	102.0	20.0	22.0	14.8	82.0
11	short term exp.	100.9	13.6	30.0	15.3	87.3
12	long term exp.	101.4	12.6	29.9	15.3	88.8
13	long term exp.	112.6	6.3	20.6	15.2	106.3
14	long term exp.	94.5	14.9	20.8	15.3	79.5
15	long term exp.	89.6	13.6	20.7	15.3	76.0
16	long term exp.	91.3	17.3	21.1	15.2	74.0
17	long term exp. / vapor valve partly open	90.0	14.5	20.9	15.4	75.5
18	long term exp.	111.5	7.0	20.7	15.2	104.5
19	long term exp.	102.4	6.9	20.6	15.4	95.5
20	long term exp.	103.5	12.9	20.9	15.4	90.6
21	long term exp.	103.3	20.7	21.0	15.3	82.6
22	long term exp.	96.1	11.1	20.9	15.3	85.0
23	long term exp.	103.7	19.9	20.4	8.4	83.9
24	long term exp. / higher flow adsorber	103.6	20.5	29.5	15.3	83.1
25	long term exp.	103.6	20.5	20.8	15.3	83.1
26	long term exp. / focus on pressure drop	104.1	16.3	20.8	49.6	87.8
27	long term exp.	103.6	23.1	30.1	20.2	80.5
28	experiment focus on pressure drop between adsorber and evaporator / 30 s open valve					
29	experiment focus on pressure drop between adsorber and evaporator / 5 min open valve					
30	short term exp. / change vapor valve setting	104.4	20.6	20.1	20.2	83.8
31	long term exp. / higher flow adsorber	104.8	18.6	20.2	20.3	86.1
32	long term exp. / higher flow adsorber	104.6	20.7	19.6	20.3	83.9



Table 0-10. List of performed experiments, and their respective parameters (2/5).

Experiment	Pressure evaporator at start	dT adsorption max	Power max	Q adsorber max	Q adsorber max	Q evaporator max	Power evaporator max
[#]	[mbar]	[Kelvin]	[Watt]	[MJ]	[kWh]	[MJ]	[Watt]
1	10.9	22.2	1040	6.31	1.75	-5.38	-3181
2	23.6	20.6	828	4.20	1.17	-3.02	-1991
3	19.8	30.9	1500	5.20	1.44	-2.87	-2888
4	12.1	24.2	800	3.50	0.97	-2.86	-1746
5	12.5	21.9	731	2.69	0.75	-2.14	-1674
6	17.9	16.3	517	3.17	0.88	-2.36	-2480
7	15.8	28.0	904	5.19	1.44	-3.93	-2042
8	12.6	33.1	1050	5.30	1.47	-2.44	-2171
9	12.5	25.6	877	6.00	1.67	-4.17	-2089
10	13.0	29.2	948	6.93	1.93	-5.06	-2047
11	19.3	26.5	877	6.35	1.76	-4.01	-2143
12	18.4	34.1	1143	8.41	2.34	-5.21	-1909
13	20.1	50.6	1613	13.05	3.62	-9.25	-2902
14	19.9	30.9	1040	9.72	2.70	-5.96	-2267
15	19.9	27.5	857	8.40	2.33	-6.27	-2365
16	18.4	27.0	841	8.53	2.37	-5.87	-1894
17	19.2	15.1	465	8.28	2.30	-6.44	-485
18	19.2	50.0	1563	14.33	3.98	-12.11	-2792
19	20.3	43.8	1368	13.18	3.66	-9.85	-2469
20	20.8	37.9	1168	10.48	2.91	-8.23	-1964
21	19.9	31.2	971	9.28	2.58	-6.66	-2266
22	19.6	34.4	1059	10.16	2.82	-7.35	-2046
23	14.4	29.7	928	7.79	2.16	-4.62	-1716
24	9.9	18.7	2199	7.39	2.05	-6.19	-2130
25	15.1	33.8	1085	9.67	2.69	-7.09	-2608
26	118.7	48.2	1536	9.18	2.55	-12.65	-8658
27	25.7	23.9	775	6.09	1.69	-5.79	-2640
28							
29							
30	23.8	28.9	909	3.70	1.03	-3.39	-2368
31	24.4	27.9	1786	11.61	3.22	-10.75	-2065
32	24.2	22.7	2132	8.84	2.46	-8.74	-2494

Table 0-11. List of performed experiments, and their respective parameters (3/5).

Experiment	heat flow density evaporator max	Flow adsorber avg	Flow evaporator avg	Peak Power adsorption	Time	<dT> adsorber for dT > 20K	<Power> for dT > 20K
[#]	[W/m <sup>2</sup> ]	[l/s]	[l/s]	[W/kg]	[s]	[Kelvin]	[Watt]
1	-2272	0.0090	0.1460	25.37	2665	23.4	880
2	-1422	0.0085	0.1430	20.20	955	20.4	729
3	-2063	0.0109	0.1670	36.59	2090	26.3	1197
4	-1247	0.0080	0.1650	19.51	2635	22.5	745
5	-1196	0.0080	0.1400	17.83	1115	21.1	705
6	-1771	0.0078	0.1870	12.61	840	15.7	514
7	-1459	0.0079	0.1780	22.05	3275	24.6	811
8	-1551	0.0078	0.1440	25.61	4730	26.4	867
9	-1492	0.0083	0.1370	21.39	3370	23.5	818
10	-1462	0.0078	0.1250	23.12	4176	25.0	812
11	-1530	0.0079	0.1339	21.38	2382	24.0	793
12	-1364	0.0080	0.1450	27.88	4098	27.2	910
13	-2073	0.0076	0.1744	39.34	6234	32.9	1048
14	-1619	0.0080	0.1445	25.36	4698	25.8	867
15	-1689	0.0075	0.1458	20.89	3576	24.3	757
16	-1353	0.0075	0.1455	20.51	3912	24.1	752
17	-346	0.0074	0.1457	11.34	11868	13.4	414
18	-1994	0.0075	0.1443	38.12	7398	32.8	1024
19	-1764	0.0075	0.1456	33.36	6948	30.4	951
20	-1403	0.0074	0.1437	28.48	4524	29.2	900
21	-1619	0.0074	0.1442	23.69	4656	25.5	794
22	-1462	0.0074	0.1441	25.83	5142	26.5	814
23	-1226	0.0075	0.1417	22.63	3858	25.4	795
24	-1522	0.0282	0.1445	53.64	1266	15.0	1763
25	-1863	0.0077	0.1743	26.46	5100	26.9	861
26	-6184	0.0076	0.1805	37.47	7890	29.7	946
27	-1886	0.0078	0.1473	18.90	2370	22.6	732
28							
29							
30	-1691	0.0075	0.1176	22.17	1824	25.3	796
31	-1475	0.0153	0.1186	43.57	1578	24.8	1588
32	-1782	0.0225	0.1189	52.00	726	21.7	2043

Table 0-12. List of performed experiments, and their respective parameters (4/5).

Experiment	Q	Average Power	Energy	Energy	Time	<dT> adsorber
	for dT > 20K	for dT > 20K	for dT > 20K	max	for <dT> = 20K	for <dT> = 20K
[#]	[MJ]	[W/kg]	[J/g]	[J/g]	[s]	[Kelvin]
1	2.35	21.46	57.20	153.90	5605	20.0
2	0.70	17.78	16.98	102.44	1545	20.0
3	2.50	29.20	61.02	126.83	4775	20.0
4	1.96	18.17	47.88	85.37	4915	20.0
5	0.79	17.20	19.17	65.61	2090	20.0
6	0.43	12.54	10.53	77.32	1390	15.0
7	2.66	19.78	64.78	126.59	6955	20.0
8	4.10	21.14	99.99	129.27	9875	20.0
9	2.75	19.94	67.19	146.34	6490	20.0
10	3.39	19.81	82.75	169.02	8448	20.0
11	1.89	19.34	46.07	154.84	4500	20.0
12	3.73	22.20	90.96	205.18	8982	20.0
13	6.53	25.55	159.29	318.28	15744	20.0
14	4.07	21.14	99.32	237.13	9462	20.0
15	2.71	18.46	66.02	204.77	7116	20.0
16	2.94	18.33	71.72	208.02	7590	20.0
17	4.92	10.11	119.94	202.01	22044	10.0
18	7.58	24.98	184.78	349.54	19488	20.0
19	6.61	23.19	161.10	321.38	17328	20.0
20	4.07	21.95	99.32	255.49	10752	20.0
21	3.70	19.36	90.14	226.25	9696	20.0
22	4.19	19.86	102.11	247.83	11388	20.0
23	3.07	19.38	74.78	190.07	7794	20.0
24	2.23	42.99	54.42	180.29	3342	10.0
25	4.39	21.00	107.11	235.88	10746	20.0
26	7.47	23.08	182.11	223.99	11376	25.2
27	1.73	17.85	42.31	148.46	4392	20.0
28						
29						
30	1.45	19.41	35.41	90.16	3600	20.0
31	2.51	38.74	61.13	283.07	3114	20.0
32	1.48	49.83	36.18	215.71	1200	20.0

Table 0-13. *List of performed experiments, and their respective parameters (5/5).*

Experiment	<Power>	Q	Average Power	Energy
	for <dT> = 20K	for <dT> = 20K	for <dT> = 20K	for <dT> = 20K
[#]	[Watt]	[MJ]	[W/kg]	[J/g]
1	713	4.00	17.39	97.47
2	716	1.11	17.46	26.98
3	913	4.36	22.27	106.33
4	660	3.24	16.10	79.12
5	667	1.39	16.27	34.00
6	493	0.69	12.02	16.71
7	659	4.58	16.06	111.72
8	657	6.48	16.01	158.14
9	697	4.52	16.99	110.25
10	649	5.49	15.84	133.79
11	661	2.97	16.11	72.51
12	670	6.02	16.33	146.71
13	637	10.03	15.54	244.70
14	673	6.37	16.41	155.29
15	623	4.43	15.20	108.15
16	623	4.73	15.20	115.38
17	309	6.81	7.54	166.11
18	625	12.17	15.23	296.85
19	625	10.82	15.24	264.02
20	616	6.63	15.03	161.63
21	622	6.03	15.18	147.14
22	615	7.01	15.01	170.96
23	625	4.87	15.24	118.74
24	1178	3.94	28.73	96.02
25	641	6.89	15.63	167.99
26	804	9.15	19.62	223.15
27	648	2.85	15.81	69.44
28				
29				
30	630	2.27	15.37	55.31
31	1284	4.00	31.33	97.55
32	1886	2.26	45.99	55.19